

Scalar Mixing and Coherent Structures in Simulations of the Plane Turbulent Mixing Layer

Thesis submitted for the degree of
Doctor of Philosophy
at the University of Leicester

by

Stephan Nicholas Hug BEng
Department of Engineering
University of Leicester

August 2017

Abstract

Scalar Mixing and Coherent Structures in Simulations of the Plane Turbulent Mixing Layer

Stephan Nicholas Hug

For more than half a century turbulent mixing layers have been the subject of intense experimental and numerical investigation. With the discovery of primary, spanwise aligned and secondary, streamwise oriented vortices the interest in low and high Reynolds number mixing layers has been invigorated. The immense increase of computational capabilities in recent years has lead to an ever growing number of numerical simulations of mixing layers. However, numerical simulations have had great difficulties in reproductions the structure dynamics and entrainment mechanisms observed in the experiments.

In this study Large Eddy Simulations of the low and high Reynolds number spatially developing, three-dimensional mixing layer are performed. At the heart of the presented studies lies the focus on the inlet conditions of the simulations. The effects of spatial and temporal correlation of the inlet conditions are studied for the low and high Reynolds number plane mixing layer. It is shown that physically correlated inlet fluctuations lead to the development of the spatially stationary, streamwise oriented vortices observed in experiments. The effects of the presence of the streamwise vortices on the momentum and passive scalar fields are investigated in detail.

In the latter parts of this work, the effects of varying the inlet fluctuation levels are reported. By altering the inlet fluctuation magnitudes the number and strength of the spatially stationary streamwise vortices can be controlled. The implications of this on the dynamics of the primary, spanwise aligned vortices are discussed. A change in the number and strength of the spatially stationary streamwise vortices is shown to be critical for the shape of the obtained probability density functions. If spatially stationary streamwise vortices are present, the obtained probability density functions are of the *non-marching* type. A lack of spatially stationary streamwise vortices produces *marching* probability density functions.

Acknowledgements

I would like to thank my supervisor Dr. Andrew McMullan for his incredible support throughout my studies. His knowledge and guidance during my Ph.D. were invaluable. His dedication to his work and the enjoyment he gets from it are truly exemplary.

I also want to thank my family who has supported me throughout my life and my studies without questioning me and always believing in my success. My heartfelt thanks and all my love go out to my wife for her support and understanding when I needed it the most.

Thanks also to Xingzhong for being a friend to me throughout my Ph.D. studies. Special mentions go to Franco and Jiang, my brothers from other mothers. Your friendships are some of the most precious things in my life. I hope we will remain the close friends we are today for the rest of our lives.

CONTENTS

1	Introduction	1
1.1	Turbulence	1
1.2	Numerical Simulation	2
1.2.1	Direct Numerical Simulation	2
1.2.2	Reynolds-Averaged Navier-Stokes (RANS)	3
1.2.3	Large Eddy Simulations (LES)	4
1.3	Mixing Layers	5
1.4	Aims and Objectives	8
2	Background Literature	10
2.1	Background of Large Eddy Simulation	10
2.2	Applications of Large Eddy Simulation	12
2.3	Mixing Layers	14
2.3.1	Mixing Layer Growth Rates	14
2.3.2	Coherent Structures	17

2.3.3	Secondary Streamwise Structures	19
2.3.4	Entrainment and Mixing	21
2.4	Numerical Simulation of Mixing Layers	24
2.4.1	Temporal Mixing Layers	25
2.4.2	Spatially Developing Mixing Layers	26
2.5	Chapter Summary	28
3	Numerical Methods	30
3.1	Navier-Stokes Equations	30
3.2	Sub-grid Scale Modelling	32
3.2.1	Smagorinsky	32
3.2.2	Wall Adapting Local Eddy-viscosity (WALE)	34
3.3	Code Description	35
3.3.1	Governing Equations	36
3.3.2	Time Advancement	36
3.3.3	Pressure Solver	37
3.3.4	Outflow Boundary Condition	38
3.3.5	Solid Wall Condition	39
3.3.6	Passive Scalar	39
3.4	Inlet Generation	40
3.4.1	White Noise (WN)	40
3.4.2	Recycling-Rescaling Method (RRM)	40

3.5	Structure Tracking	42
3.6	Chapter Summary	43
4	Inlet Fluctuation Correlation Effects	44
4.1	Low Reynolds Number Mixing Layer	44
4.1.1	Introduction	44
4.1.2	Reference Experiment	45
4.1.3	Simulation Setup	46
4.1.4	Results	49
4.1.5	Summary	59
4.2	High Reynolds Number Mixing Layer	60
4.2.1	Introduction	60
4.2.2	Reference Experiment	61
4.2.3	Simulation Setup	62
4.2.4	Grid validation	64
4.2.5	SGS Model Validation	65
4.2.6	Main Simulation Results	67
4.2.7	Flow Visualisation	69
4.2.8	Summary	81
4.2.9	Conclusions	83
4.3	Figures	84
5	Parametric Study of the High Reynolds Number Mixing Layer	110

5.1	Introduction	110
5.2	Inlet Fluctuation Magnitude	112
5.2.1	Simulation Setup	112
5.2.2	Results	113
5.2.3	Summary	119
5.3	Velocity Ratio Effects	120
5.3.1	Introduction	120
5.3.2	Simulation Setup	121
5.3.3	Results	121
5.3.4	Summary	128
5.4	Effects of High-Speed Boundary Layer Thickness	129
5.4.1	Introduction	129
5.4.2	Simulation Setup	129
5.4.3	Results	130
5.4.4	Summary	132
5.5	Conclusions	133
5.6	Figures	135
6	Elevated Inflow Fluctuation Magnitude Effects	160
6.1	Inlet Fluctuation Magnitude Effects	160
6.1.1	Introduction	160
6.1.2	Simulation Setup	161

6.1.3	Results	162
6.1.4	Summary	173
6.2	Velocity Ratio Changes	174
6.2.1	Introduction	174
6.2.2	Simulation Setup	174
6.2.3	Results	175
6.2.4	Summary	179
6.3	Discussion	179
6.4	Conclusions	181
6.5	Figures	183
7	Conclusions and Further Work	202
7.1	Conclusions	202
7.2	Further Work	205
	Bibliography	207

LIST OF TABLES

4.1	Flow properties	46
4.2	Measurement stations.	47
4.3	Simulation cases overview.	48
4.4	Experimental and simulation vorticity growth rates and growth constants.	50
4.5	Smallest length scale significant to passive scalar mixing, λ_D , and smallest resolved passive scalar length scale inside the mixing layer, Δ_{ave} , at measurement station 3.	53
4.6	Minimum, maximum and spanwise averaged values for the entrainment ratio at measurement station 3.	57
4.7	Summary of flow properties for reference dataset by Browand & Latigo [45].	62
4.8	Measurement stations.	63
4.9	Simulation cases overview.	64
4.10	Grid resolutions.	65
4.11	Model validation simulations.	67

4.12	Smallest length scale significant to passive scalar mixing, λ_D , and smallest resolved passive scalar length scale inside the mixing layer, Δ_{ave} , at measurement station 6.	74
4.13	Entrainment ratios at measurement stations 2 to 6 for BL-066-RRM-L and BL-066-WN-L.	79
5.1	Summary of flow properties for reference dataset by Browand & Latigo [45] and Meyer <i>et. al.</i> [94].	111
5.2	Simulation parameters.	112
5.3	Measurement stations.	112
5.4	Entrainment ratios in the pre-transition (MS3) and post-transition (MS5 & MS6) region of the mixing layer.	118
5.5	Simulation parameters.	121
5.6	Measurement stations.	123
5.7	Smallest length scale significant to passive scalar mixing, λ_D , and smallest resolved passive scalar length scale inside the mixing layer, Δ_{ave} , at measurement station 6.	126
5.8	Entrainment ratios at measurement station 6.	128
5.9	Simulation inlet boundary layers.	129
5.10	Measurement stations.	131
6.1	Simulation cases and inlet boundary layer fluctuation profiles.	161
6.2	Measurement stations.	162
6.3	Momentum thickness growth rates.	163
6.4	Entrainment ratios at measurement station 6.	170
6.5	Chosen spanwise locations for mixed fluid statistics.	171

6.6	Simulation cases and inlet boundary layer fluctuation profiles.	175
6.7	Momentum thickness growth rate constants.	176
6.8	Vorticity growth rate.	177

LIST OF FIGURES

1.1	Plane mixing layer.	5
1.2	Coherent structures in turbulent plane mixing layer, discovered by Brown & Roshko [9].	7
2.1	Vorticity growth rates reported by experiments.	17
2.2	Streamwise vortex structure topology (Bernal & Roshko [54]).	20
2.3	Examples of three-tiered and single row vorticity formations by Wiecek & Mehta [55].	20
2.4	‘Nibbling’ entrainment mechanism by Corrsin & Kistler [57] and ‘engulfment’ entrainment mechanism by Dimotakis [56].	21
2.5	Examples of <i>marching</i> and <i>non-marching</i> probability density function shapes (Karasso & Mungal [60]).	23
2.6	Example of a temporal DNS. (Lesieur <i>et al.</i> [65]).	25
3.1	Energy spectrum contained in a flow.	32
3.2	Examples of inlet velocity and inlet velocity fluctuation profiles.	40
3.3	Primary vortex in a spanwise averaged, instantaneous passive scalar flow visualisation with indicated points of interest.	42

4.1	Inlet conditions.	84
4.2	Mean streamwise velocity at measurement stations A and 3.	84
4.3	Mean streamwise velocity fluctuation magnitude at measurement station 2.	85
4.4	Power spectral density plots at measurement station MSA. Lines have been shifted in the vertical axis for clarity.	85
4.5	Instantaneous passive scalar contour maps of MAS-RRM-L.	85
4.6	Instantaneous passive scalar contour maps of MAS-WN-L.	86
4.7	Mean streamwise velocity for MAS-RRM-L at measurement stations 2 and 3.	86
4.8	Mean streamwise velocity for MAS-WN-L at measurement stations 2 and 3.	86
4.9	Mean secondary shear stress for MAS-RRM-L at measurement stations 2 and 3. Dashed lines denote negative values.	86
4.10	Mean secondary shear stress for MAS-WN-L at measurement stations 2 and 3. Dashed lines denote negative values.	87
4.11	Mean secondary shear stress and mean streamwise vorticity for MAS-RRM-L at measurement station 3.	87
4.12	Mixing layer centreline plots for MAS-RRM-L and MAS-WN-L at measurement stations 2 and 3.	87
4.13	Cross-stream passive scalar measurements during a primary structure passage for MAS-RRM-L at measurement station 2.	88
4.14	Cross-stream passive scalar measurements during a primary structure passage for MAS-WN-L at measurement station 2.	88
4.15	Spanwise averaged mean passive scalar concentration at measurement station 2. Error bars denote the <i>r.m.s.</i> value of the spanwise variation, not measurement error.	89

4.16 Spanwise averaged mean passive scalar fluctuation measurements at measurement stations 2. Error bars denote the <i>r.m.s.</i> value of the spanwise variation, not measurement error.	90
4.17 Entrainment ratio, E_v , and centreline locus, y_0 , plots at measurement station 2.	90
4.18 Probability density function plots for MAS-RRM-L at measurement station 3.	90
4.19 Probability density function plots for MAS-WN-L at measurement station 3.	91
4.20 Mean streamwise velocity statistics.	91
4.21 Power spectral density plots at MSA. Lines have been shifted in the vertical axis for clarity.	92
4.22 Instantaneous passive scalar contour maps for MAS-RRM-M and MAS-RRM-H.	92
4.23 Streamwise velocity $y - z$ cross-planes at measurement station 3.	92
4.24 Mean streamwise vorticity maps at measurement station 2. Dashed lines denote negative values.	93
4.25 Mean streamwise vorticity maps at measurement station 3. Dashed lines denote negative values.	93
4.26 Cross-stream passive scalar measurements during a primary structure passage for MAS-RRM-M at measurement station 3.	94
4.27 Cross-stream passive scalar measurements during a primary structure passage for MAS-RRM-H at measurement station 3.	94
4.28 Spanwise averaged mean passive scalar concentration and mean passive scalar fluctuations at measurement stations 3. For clarity spanwise variation bars are only shown for MAS-RRM-L.	95
4.29 Probability density function plots for MAS-RRM-M at measurement station 3.	95

4.30 Probability density function plots for MAS-RRM-H at measurement station 3.	96
4.31 Inlet velocity profiles and inlet velocity fluctuation profiles.	96
4.32 Velocity statistics for GR1 and GR2.	96
4.33 Local momentum thickness for GR1 and GR2.	97
4.34 Contour maps of instantaneous passive scalar concentration and contour lines of the ratio of the subgrid to molecular viscosity for (a) BL-066-WN-Cs010, (b) BL-066-WN-Cs018, (c) BL-066-WN-Cw030, and (d) BL-066-WN-Cw056.	98
4.35 Local momentum thickness and peak streamwise velocity fluctuation.	98
4.36 Local momentum thickness for BL-066-WN-L and BL-066-RRM-L	98
4.37 Flow statistics at $x/\theta_i = 1000$	99
4.38 Peak normalised streamwise velocity fluctuation.	99
4.39 Streamwise velocity fluctuation spectral plots along the mixing layer centreline. Spectra have been shifted along vertical axis for clarity.	99
4.40 Instantaneous, single plane and spanwise averaged passive scalar contour lines for BL-066-RRM-L.	99
4.41 Instantaneous, single plane and spanwise averaged passive scalar contour lines for BL-066-WN-L.	100
4.42 Perspective view of the mixing layer at measurement station 4.	100
4.43 Perspective view of the mixing layer at measurement station 5.	100
4.44 Structure diameter growth tracks.	101
4.45 Mean streamwise velocity and mean streamwise vorticity $y - z$ cross-planes for BL-066-RRM-L at measurement station 2.	101
4.46 Mean streamwise velocity and mean streamwise vorticity $y - z$ cross-planes for BL-066-WN-L at measurement station 2.	101

4.47 Mean streamwise velocity and mean streamwise vorticity $y - z$ cross-planes for BL-066-RRM-L at measurement station 3.	102
4.48 Mean streamwise velocity and mean streamwise vorticity $y - z$ cross-planes for BL-066-WN-L at measurement station 3.	102
4.49 Mean streamwise velocity and mean streamwise vorticity $y - z$ cross-planes for BL-066-RRM-L at measurement station 5.	102
4.50 Mean streamwise velocity and mean streamwise vorticity $y - z$ cross-planes for BL-066-WN-L at measurement station 5.	103
4.51 Centreline locus plots at measurement stations 1 to 6.	103
4.52 Passive scalar statistics for BL-066-RRM-L at measurement station 3 and 5.	103
4.53 Passive scalar statistics for BL-066-WN-L at measurement station 3 and 5.	104
4.54 Passage of primary roller structure in the BL-066-RRM-L simulation at measurement station 3.	104
4.55 Passage of primary roller structure in the BL-066-RRM-L simulation at measurement station 5.	105
4.56 Passage of primary roller structure in the BL-066-WN-L simulation at measurement station 3.	105
4.57 Passage of primary roller structure in the BL-066-WN-L simulation at measurement station 5.	106
4.58 Spanwise averaged passive scalar concentration during a structure passage at measurement station 5.	106
4.59 Entrainment ratio for BL-066-RRM-L.	107
4.60 Entrainment ratio for BL-066-WN-L.	107
4.61 Mixed fluid statistics at measurement station 6.	108
4.62 Probability density function for BL-066-RRM-L at measurement station 6 at two spanwise locations.	108

4.63	Probability density function for BL-066-WN-L at measurement station 6 at two spanwise locations.	109
5.1	High-speed stream inflow conditions for BL-066-RRM-L and BL-066-RRM-M.	135
5.2	Velocity statistics for BL-066-RRM-L and BL-066-RRM-M.	136
5.3	Vertically shifted, power spectral density plots at $x/\theta_i = 44$ and $x/\theta_i = 219$	136
5.4	Local momentum thickness of the mixing layer.	137
5.5	Instantaneous flow visualisations for BL-066-RRM-L.	137
5.6	Instantaneous flow visualisations for BL-066-RRM-M.	137
5.7	Perspective views for BL-066-RRM-L at measurement station 3 and 5.	138
5.8	Perspective views for BL-066-RRM-M at measurement station 3 and 5. For legend refer to Figure 5.7a.	138
5.9	Vertical structure size growth tracks.	138
5.10	Streamwise vorticity $y - z$ cross-planes for BL-066-RRM-L.	139
5.11	Streamwise vorticity $y - z$ cross-planes for BL-066-RRM-M.	139
5.12	Centreline evolution at measurement stations 2 through 6.	140
5.13	Streamwise vortex structure evolution.	140
5.14	Entrainment ratio at measurement stations 3 and 5.	140
5.15	Streamwise development of the entrainment ratio variation.	141
5.16	Mixed fluid statistics at measurement station 6.	142
5.17	Probability density functions for BL-066-RRM-L at measurement station 6.	143

5.18	Probability density functions for BL-066-RRM-M at measurement station 6. For legend refer to Figure 5.17a.	144
5.19	Mean flow statistics.	145
5.20	Power spectra density plots at $x/\theta_i = 44$ and $x/\theta_i = 217$. For clarity, spectra have been shifted along the vertical axis.	145
5.21	Local momentum thickness of the mixing layer.	145
5.22	Single plane, passive scalar flow visualisations.	146
5.23	Spanwise averaged, passive scalar flow visualisations.	146
5.24	Cross-plane maps at measurement station 2 for BL-039-RRM-M. . . .	147
5.25	Cross-plane maps at measurement station 2 for BL-052-RRM-M. . . .	147
5.26	Cross-plane maps at measurement station 2 for BL-066-RRM-M. . . .	148
5.27	Cross-plane maps at measurement station 4 for BL-039-RRM-M. . . .	148
5.28	Cross-plane maps at measurement station 4 for BL-052-RRM-M. . . .	149
5.29	Cross-plane maps at measurement station 4 for BL-066-RRM-M. . . .	149
5.30	Cross-plane maps at measurement station 6 for BL-039-RRM-M. . . .	150
5.31	Cross-plane maps at measurement station 6 for BL-052-RRM-M. . . .	150
5.32	Cross-plane maps at measurement station 6 for BL-066-RRM-M. . . .	151
5.33	Centreline evolution at measurement stations 1 through 6.	151
5.34	Streamwise vortex structure evolution.	152
5.35	Passive scalar statistics of BL-039-RRM-M at measurement station 6. . .	152
5.36	Passive scalar statistics of BL-052-RRM-M at measurement station 6. . .	153
5.37	Passive scalar statistics of BL-066-RRM-M at measurement station 6. . .	153
5.38	Mean flow statistics.	154

5.39	Local momentum thickness of the mixing layer.	154
5.40	Vertically shifted, power spectral density plots at $x/\theta_i = 44$ and $x/\theta_i = 444$	154
5.41	Secondary shear stress contour maps at measurement station 2.	155
5.42	Secondary shear stress contour maps at measurement station 3.	156
5.43	Secondary shear stress contour maps at measurement station 5.	156
5.44	Secondary shear stress contour maps at measurement station 6.	156
5.45	Centreline evolution at measurement stations 2 through 6.	156
5.46	Streamwise vortex structure evolution.	157
5.47	Probability density functions at measurement station 6.	158
5.48	Probability density functions at measurement station 6.	159
6.1	Streamwise velocity inlet profile and high-speed stream inflow fluctuation conditions.	183
6.2	Mean flow statistics.	184
6.3	Power spectral density of streamwise velocity fluctuations. Power spectral density shifted along vertical axis for clarity.	184
6.4	Local momentum thickness against downstream distance from the splitter plate trailing edge.	185
6.5	Instantaneous single plane and spanwise averaged passive scalar flow visualisations for BL-066-RRM-M.	185
6.6	Instantaneous single plane and spanwise averaged passive scalar flow visualisations for BL-066-RRM-H.	185
6.7	Instantaneous single plane and spanwise averaged passive scalar flow visualisations for BL-066-RRM-VH.	186
6.8	Perspective views at measurement station 3.	186

6.9	Perspective views at measurement station 4.	187
6.10	Cross-plane mean streamwise vorticity maps at measurement station A.	187
6.11	Cross-plane mean streamwise vorticity maps at measurement station 2.	188
6.12	Cross-plane mean streamwise vorticity maps at measurement station 3.	188
6.13	Cross-plane mean secondary shear stress maps at measurement sta- tion 5.	189
6.14	Centreline evolution at measurement stations 2 through 6.	189
6.15	Streamwise vortex spacing. Included data by Bell & Mehta [88] and Plesniak <i>et al.</i> [104].	190
6.16	Primary structure growth for BL-066-RRM-M. Dashed line indicates the visual thickness of the mixing layer. Filled symbols denote square root of time growth.	190
6.17	Primary structure growth for BL-066-RRM-H. Dashed line indicates the visual thickness of the mixing layer. Filled symbols denote square root of time growth.	190
6.18	Primary structure growth for BL-066-RRM-VH. Dashed line indicates the visual thickness of the mixing layer. Filled symbols denote square root of time growth.	191
6.19	Primary structure passage for BL-066-RRM-M at measurement plane 5.	191
6.20	Primary structure passage for BL-066-RRM-H at measurement plane 5.	192
6.21	Primary structure passage for BL-066-RRM-VH at measurement plane 5.	192
6.22	Typical spanwise averaged passive scalar concentration in a primary structure core at measurement station 5.	193

6.23	Entrainment ratio, E_v , and mixing layer centreline locus, y_0 , at measurement station 4.	193
6.24	Entrainment ratio, E_v , and mixing layer centreline locus, y_0 , at measurement station 6.	194
6.25	Standard deviation of the mixing layer entrainment ratio, E_v . Experimental data of Bell and Mehta [47] for the standard deviation of the mixing layer thickness.	195
6.26	Mixed fluid probability, P_m , and average mixed fluid concentration, ξ_m at measurement station 6.	196
6.27	Probability density functions for BL-066-RRM-M at measurement station 6.	196
6.28	Probability density functions for BL-066-RRM-H at measurement station 6. For legend refer to Figure 6.27a.	197
6.29	Probability density functions for BL-066-RRM-VH at measurement station 6. For legend refer to Figure 6.27a.	197
6.30	Local momentum thickness against downstream distance from the splitter plate trailing edge.	198
6.31	Vorticity growth rate as a function of velocity ratio.	198
6.32	Mixing layer centreline at measurement station 6 for varying inlet fluctuation levels and velocity ratios. For clarity the centrelines have been shifted in the vertical axis.	199
6.33	Primary structure growth tracks for $R = 0.39$ with varying inlet fluctuation magnitudes. Filled symbols denote square root of time growth.	199
6.34	Primary structure growth tracks for $R = 0.52$ with varying inlet fluctuation magnitudes. Filled symbols denote square root of time growth.	200
6.35	Mixed fluid probability, P_m , and average mixed fluid concentration, ξ_m , at measurement station 6.	200
6.36	Probability density function for $R = 0.39$ at measurement station 6, taken at an entrainment maximum.	201

6.37 Probability density function for $R = 0.52$ at measurement station 6,
taken at an entrainment maximum. 201

Nomenclature

Re	Reynolds number
u_i	Velocity field variable
$\langle u_i \rangle_t$	Time-averaged velocity field variable
u'	Velocity fluctuation
Δt	Time step
\bar{u}_i	Filtered velocity field variable
U_1	Mixing layer high-speed side velocity
U_2	Mixing layer low-speed side velocity
U_c	Convection velocity
ξ	Passive scalar
$\bar{\xi}$	Filtered passive scalar
R	Velocity ratio parameter
ΔU	Velocity difference
δ_ω	Vorticity thickness of the mixing layer
θ	Momentum thickness of the mixing layer
θ_1	Momentum thickness of high-speed inlet boundary layer
θ_2	Momentum thickness of low-speed inlet boundary layer
δ_{viz}	Visual thickness of the mixing layer
k_v	Visual thickness growth rate constant
k_m	Momentum thickness growth rate constant
k_o	Vorticity thickness growth rate constant
St	Strouhal number
f	Disturbance frequency
E_v	Entrainment ratio
ν	Kinematic viscosity
P	Pressure
ρ	Density
G	Filter function
D	Computational domain
$\bar{\Delta}$	Grid filter width
\bar{S}_{ij}	Filtered strain rate tensor
ν_{sg}	Sub-grid scale viscosity
ν_m	Molecular viscosity
C_s	Smagorinsky model coefficient
C_w	WALE model coefficient
δ_{ij}	Kronecker delta
α	Diffusivity coefficient

α_m	Molecular diffusivity
α_{sg}	Subgrid-scale diffusivity
\tilde{u}_i^*	Provisional velocity field variable
Sc	Schmidt number
x_0	Mixing layer virtual origin
y_0	Mixing layer centreline
δ_i	High-speed inlet boundary layer thickness
$\langle u'w' \rangle_t$	Mean secondary shear stress
Ω_x	Mean streamwise vorticity
λ_D	Smallest lengthscale significant to passive scalar mixing
Δ_{ave}	Smallest resolved length scale inside the mixing layer
V_l	Entrained low-speed fluid volume
V_h	Entrained high-speed fluid volume
M_l	Time averaged low-speed fluid fractional flux
M_h	Time averaged high-speed fluid fractional flux
E_c	Composition ratio
P_l	Low-speed fluid probability
P_h	High-speed fluid probability
P_m	Total probability of finding mixed fluid
x_i^*	Pairing parameter
ξ_m	Average concentration of mixed fluid
Δ_x	Grid spacing in dimension x
L_x	Domain extent of dimension x
N_x	Number of grid points in dimension x
H	Shape factor
η	Non-dimensional self-similar co-ordinate parameter
η'	Self-similar co-ordinate parameter

Chapter 1

Introduction

1.1 Turbulence

Turbulence is a phenomenon that surrounds us every day. Dissolving sugar in a cup of coffee, the flow around a car on the motorway or the combustion taking place inside a jet engine are just a few examples of flows that involve turbulence. Seemingly regardless of its abundance in our daily lives, turbulence remains one of the great mysteries that science is yet to solve.

The first formal recordings of turbulence were found in Leonardo Da Vinci's notebooks, evidencing that turbulence has been studied for the last 500 years [1]. The first formal description of turbulence came in 1883 when Osborne Reynolds formulated a set of conditions that are met when a pipe flow goes from an orderly and laminar state to a chaotic and turbulent one [2]. His dimensionless parameter, termed 'Reynolds number', remains the most critical parameter of any flow, more than 100 years later.

With the many types of turbulent flows surrounding us every day, one would be excused for thinking that we have long arrived at an analytical solution for turbulence. The closest we have come to do so are the incompressible Navier-Stokes equations named after Claude-Louis Navier and George Gabriel Stokes. The Navier-Stokes

equations are a set of equations describing the behaviour of incompressible turbulent flows by modelling the flow of every Newtonian fluid based on the principle of conservation of mass and momentum. However, even with the knowledge of the incompressible Navier-Stokes equations, no analytical solution for turbulence has been found. In fact, making progress towards a mathematical theory which will unlock the secrets in the Navier-Stokes equations remains one of the seven ‘Millennium Prize Problems’ with a prize fund of USD 1 million.

In the absence of a mathematical solution, scientists have to conduct experiments, or more recently, numerical simulations to increase our understanding of what turbulence is.

1.2 Numerical Simulation

With the rapid advancement of the modern computer, the numerical simulation of turbulence has become a reality; a practice which has been termed Computational Fluid Dynamics (CFD). Since the very first numerical simulations in the early 1970s, CFD has remained an active area of research, and it has more recently also become an important part of industrial research.

Researchers use a large number of different modelling techniques, and the three most common ones, Direct Numerical Simulation, Reynolds-Averaged Navier Stokes simulations and Large Eddy Simulations, are discussed here in more detail.

1.2.1 Direct Numerical Simulation

Direct Numerical Simulations get their name from the fact that they resolve and compute the Navier-Stoke equations to the smallest scale, explicitly. However, this comes at a great computational cost. At high Reynolds numbers, the computational resources required become unrealistic as the number of mesh points is a function of $Re^{9/4}$. An aeroplane at a typical cruise speed would require 7.5×10^{18} grid points.

If this number is compared to one of the most sophisticated DNS of our time which uses 3×10^9 grid points and 65536 processing cores [3], it becomes clear that DNS of engineering applications will not become a reality in the near future.

While DNS of engineering applications might remain out of reach, DNS have successfully been used to study different mixing layer properties and behaviours. The earliest DNS were of the temporal type in which the flow evolves inside a computational box in a temporal sense such as the ones performed by Rogers & Moser [4, 5, 6]. This approach is comparatively computationally affordable but suffers from inherent drawbacks which will be explored in more detail later in this chapter. With the increase in computational capabilities over the years the computational cost of DNS have also increased significantly. Very recently, a DNS of a spatially evolving mixing layer has been conducted which used approximately 10 million CPU hours [3]. However, DNS with such costs remain largely intractable. The high computational cost of DNS has led researchers and engineers to find other types of numerical simulations that are more affordable.

1.2.2 Reynolds-Averaged Navier-Stokes (RANS)

The most common type of numerical simulation used to model engineering applications today is the Reynolds-Averaged Navier-Stokes (RANS) model. RANS is based on the Reynolds decomposition, which states that any instantaneous quantity can be decomposed into its mean and fluctuation components

$$u = \langle u \rangle_t + u' \quad (1.1)$$

where u is the instantaneous value, $\langle u \rangle_t$, is the mean value and u' represents the fluctuation component of the variable. This decomposition can then be substituted into the Navier-Stokes equations. This procedure, however, introduces a component describing the fluctuation components, termed the Reynolds stress, into the Navier-Stokes equations. This component is given by

$$\tau_{ij} = \langle u_i u_j \rangle_t - \langle u_i \rangle_t \langle u_j \rangle_t. \quad (1.2)$$

To close the RANS equations the term τ_{ij} has to be modelled as a function of the mean flow. This modelling is known as the *closure problem*.

Regarding the closure problem, a large number of models have been proposed. Two of the most common ones are the $k - \epsilon$ and the $k - \Omega$ models. As this study will not use the RANS model in depth knowledge about these models is not required.

1.2.3 Large Eddy Simulations (LES)

Similarly to RANS, Large Eddy Simulation is also based on the Reynolds decomposition. However, unlike RANS which is based on averaging, in LES the flow is decomposed into large, energy-carrying scales of motion, the *resolved sub-filter scales* (SFS) and *unresolved sub-grid scales* (SGS). The assumption which makes this separation possible is the Kolmogorov theory in which the smallest scales of turbulent motions are assumed to be statistically isotropic. However, this assumption has not remained unchallenged [7]. The LES decomposition is therefore given by

$$u = \bar{u} + u' \quad (1.3)$$

where \bar{u} are the scales of motion larger than the smallest grid size (SFS) and u' are the scales smaller than the resolved grid (SGS). A low-pass spatial filter is used to separate the scales of motion. Like RANS, the effect of the subgrid scales has to be accounted for and is given by,

$$\tau_{ij} = \overline{u_i u_j} - \bar{u}_i \bar{u}_j. \quad (1.4)$$

A *sub-grid scale model* is used to close the Navier-Stokes equations. A large number

of such models exist, and two outlined ones are presented in more detail in Chapter 3.2.

The biggest advantage of LES compared to RANS is that it can provide information about time-dependent, unsteady turbulent flows. While temporal information is also produced by a DNS, LES can achieve similar results to a DNS, with a much smaller number of grid points which reduces computational costs but also allows for the simulation of flows at much greater Reynolds numbers.

1.3 Mixing Layers

A mixing layer is formed when two, parallel streams with differing velocities come in contact. There are numerous types of mixing layers, but jets and plane mixing layers are the most commonly studied ones. An illustration of a plane mixing layer developing between two fluids is shown in Figure 1.1. The high- and low-speed streams are located on the upper and lower side of the mixing layer, respectively and are separated by a thin splitter plate. In experimental setups, it is common practice to use a series of settling chambers to smoothen the flow before it is accelerated inside a contraction and then enters the test section.

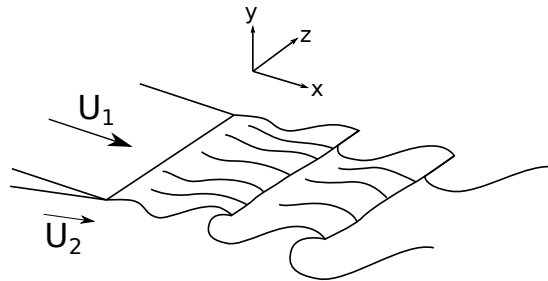


Figure 1.1: Plane mixing layer.

The Reynolds number, discovered by Osborne Reynolds [2] in 1883, remains a key property of any flow. The Reynolds number is defined as being the ratio of *inertial forces* to *viscous forces* within the fluid of interest. Inside the fluid, the *inertial forces* move a flow from the laminar state to the turbulent state while the *viscous forces* counteract this process.

The laminar flow state characterises a flow in which the *viscous forces* are dominating the *inertial forces*, resulting in a smooth fluid motion. The ratio between the different forces in the laminar state results in a low Reynolds number. In turbulent flows, occurring at high Reynolds numbers, the flow is dominated by the inertial forces and the flow is of an unorganised, chaotic appearance.

The Reynolds number is defined as,

$$Re = \frac{\rho u L}{\mu} = \frac{u L}{\nu} \quad (1.5)$$

where ρ is the density, u is the velocity, L is a characteristic length scale, μ is the dynamic viscosity, and ν is the kinematic viscosity.

Plane mixing layers are often classified into low and high Reynolds number mixing layers. The differentiation is done on the basis of whether the flow undergoes transition inside the test section of the experiment. Dimotakis [8] has shown the mixing layer transition to occur at a Reynolds number of $Re_\delta \approx 40000$, based on the local visual thickness and velocity difference across the mixing layer. While the mixing layer transition is a complex and interesting process, it is not a focus of the presented simulations, and a complete understanding of it is not required in this context.

Structures in mixing layer have long been a subject of interest. At the heart of the accepted origin of the primary structures found in mixing layers lie the Kelvin-Helmholtz (K-H) vortices. In experiments, it can be observed how a short distance downstream of the splitter plate trailing edge the mixing layer ‘rolls up’ into small scale Kelvin-Helmholtz vortices. After a given distance from the splitter plate, the first subharmonic of the primary instability causes the K-H vortices to undergo pairing in which a vortex starts to rotate around its downstream neighbour before amalgamation occurs. Some time afterwards, the first subharmonic of this instability causes a similar pairing again, which then spawns a new generation of vortices and so the cycle continues. The streamwise location of these pairings varies slightly; this gives rise to the self-similar growth of the mixing layer. Self-similarity is a crucial aspect of the mixing layer and means that self-similar quantities will collapse onto a single line if the velocity and length scales are taken into account. For a long time, the accepted

view of mixing layers has long been that a high Reynolds number mixing layer is initially in a laminar, organised state before it undergoes a transition into a turbulent, unorganised state. This turbulent state was thought to consist of a mean flow with a fluctuation component which is random in nature.

The discovery of large scale, quasi-two-dimensional, spanwise coherent structures by Brown & Roshko [9], shown in Figure 1.2, therefore, came as a great surprise. These large scale structures were shown to have significant lifespans and to grow and interact and pair as they convect downstream. It was subsequently proposed that the pairing of the large scale coherent structures gives rise to the growth of the mixing layer as a whole. However, some uncertainty about this remains as it has also been suggested that most of the mixing layer growth occurs not during interactions, but during the ‘normal life’ of structures between pairing events [10].

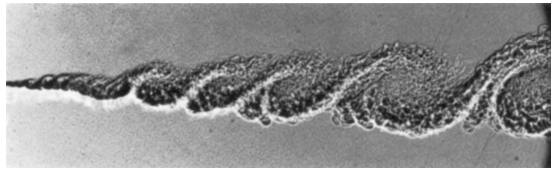


Figure 1.2: Coherent structures in turbulent plane mixing layer, discovered by Brown & Roshko [9].

With a lack of an alternative interpretation, the theory that the large scale, coherent structures, found in the post-transition, turbulent mixing layer, evolve based on the same K-H instability theory as their pre-transition cousins, has received widespread acceptance. It has, however, not remained unchallenged. Most recently D’Ovidio & Coats [11] have suggested that the mixing transition results in a change in growth mechanism. Their theory is that the coherent structures grow as K-H vortices in the pre-transition but in the post-transition, they grow continuously and linearly.

Recently, large scale coherent structures have been shown to be critical to mixing layers in real world engineering applications, particularly those related to entrainment, mixing and combustion. It follows therefore that a complete understanding of coherent structures will play a crucial part in meeting the ever increasing demand for improved efficiency and cleaner combustion.

While there are many aspects to mixing layers, one critical aspect of mixing layer ex-

periments and numerical simulations are the initial or inlet conditions from which the mixing layer develops. Particularly the pre-transition region of the mixing layer has shown a hypersensitivity to the inlet conditions [12, 13]. Even though inlet conditions are a crucial part of every mixing layer experiment, the author feels that their importance has been under-appreciated, particularly in the ever increasing number of numerical simulations. Considerable focus will, therefore, be paid to the study of inlet conditions and their effects, in this work.

1.4 Aims and Objectives

This chapter has served as a brief introduction into what mixing layers are and their importance in our lives. It has introduced the most common types of numerical simulations and has highlighted LES has been chosen in this particular study.

The aim of this project is to produce accurate numerical simulations of low and high Reynolds number mixing layers using LES. However, this approach will be taken further here; in the later chapters, LES will be used to try and advance our knowledge about mixing layers, expanding on available experimental results. Mixing layer inlet properties are varied and their effects are studied. In the last chapter, the effects of inlet fluctuation levels on structure dynamics and passive scalar entrainment and mixing are evaluated. The findings will be discussed in relation to experimental research and they will be used to shed light on some of the remaining uncertainties about mixing layers.

Chapter 2. Background Literature A review of the relevant literature to the studied topic.

Chapter 3. Numerical Methods An overview of the numerical methods and codes used for the presented simulations.

Chapter 4. Inlet Fluctuation Correlation Effects Numerical studies of the low and high Reynolds number mixing layer using spatially and temporally correlated and non-correlated inlet fluctuations.

Chapter 5. Parametric Study of the High Reynolds Number Mixing Layer Parameterised testing of mixing layer properties using LES.

Chapter 6. Elevated Inflow Fluctuation Magnitude Effects Study of high inlet fluctuation level effects on the high Reynolds number mixing layer.

Chapter 7. Conclusions and Future Work

Chapter 2

Background Literature

2.1 Background of Large Eddy Simulation

When the different types of numerical simulations are compared, it becomes clear that they all offer their own sets of benefits and drawbacks. While RANS is computationally affordable enough to offer solutions to engineering applications with an acceptable turnaround time, one problem is that it offers no information about the temporal evolution of the flow. This is particularly important in the prediction of noise generation and combustion processes. A DNS can offer this type of information by producing a ‘true’ numerical representation. However, this comes at a significant computational cost, especially at high Reynolds numbers, making DNS unsuitable for most engineering applications. In the spectrum of numerical simulations with RANS being on one end and DNS on the other end, LES sits somewhere in the middle. It offers all the advantages of a DNS, such as temporal information, and detailed simulation of flow structures, but avoids the computational cost associated with simulating all scales of turbulence present in a mixing layer. However, this separation of scales in LES implies the use of a sub-grid scale model to close the Navier-Stokes equations. Numerous sub-grid scale models have been proposed and two popular ones will be discussed in detail here.

The first sub-grid scale model was proposed by Smagorinsky in 1963 [14]. The model

was originally developed for the modelling of weather behaviour, and it was first used successfully by Deardroff [15] in a channel flow simulation. It has since been applied to many different types of LES. The Smagorinsky model is based on the idea that the rate of energy transferred from the resolved to the unresolved scales is equal to the rate of energy dissipated in the sub-grid scales. In the sub-grid scales, the energy is removed from the simulation instantaneously and entirely. The length scale cut off point has to be chosen carefully. Removing too much, or too little, energy from the flow can lead to erroneous results.

The choice of the sub-grid scale model constant, C_s , is critical to the successful application of the Smagorinsky model. C_s typically ranges between 0.005 for channel flows to 0.05 for simulations with isotropic turbulence [16]. For plane mixing layer simulations, a popular value of C_s falls between 0.10 and 0.18 [17]. One of the challenges in the application of the Smagorinsky model lies in the fact that the best model constant value changes for different applications. Often a number of simulations with varying model constants have to be run and evaluated to find the most suitable one for the problem at hand. However, recent LES have shown the Smagorinsky model to be of limited suitability to plane mixing layers as it predicts non-zero values for the eddy viscosity in regions of laminar flow [18] which can delay the transition to a turbulent state. Equally relevant, simulations have also shown the Smagorinsky model to be problematic in the treatment of near wall conditions [19] which is particularly problematic when trying to model a splitter plate as part of the computational domain.

To overcome the shortcomings of the standard Smagorinsky model, Germano *et al.* [20] proposed a dynamic eddy viscosity model in which the model constant is changed dynamically. This model has been compared to DNS simulations and shown good agreement but its implementation is challenging and altering the model constant dynamically can be costly in terms of computational resources. Additional problems arise from the model constant being negative, which can result in numerical instability.

The limitations of the Smagorinsky model have led to the development of a vast number of alternative models. Of particular interest to the simulation of mixing layers is the wall adapting local eddy viscosity (WALE) model proposed by Nicoud &

Ducroux [17]. The WALE model uses the square of the velocity gradient tensor to account for both strain and the rotation rate of the smallest resolved turbulent fluctuations. One advantage of the model is that the eddy viscosity tends to zero in the proximity of a wall, without the need for dynamic constant adjustment or artificial damping. Most importantly to this work, the model predicts zero eddy viscosity in pure shear. This property makes it possible to simulate the laminar to turbulent transition process without delaying the transition to a fully turbulent state [18]. The WALE model is discussed in detail in Section 3.2.2.

2.2 Applications of Large Eddy Simulation

The vast advances made concerning sub-grid scale models and meshing techniques have lead to LES being used in more and more varied research and engineering simulations. Examples of academic applications are plane mixing layer simulations [21], variable density simulations [22], compressible [23] and reacting flow simulations. In industry, LES has been used in numerous simulations ranging from jet engine geometry [24], and combustor simulations [25], to the noise prediction of chevron jets [26].

Large eddy simulations are particularly suited to engineering problems involving large scale structures and high Reynolds numbers. An example of this is jet noise prediction. Great advances have been made in this field, and the accuracy of predictions is as good as 1dB for high-speed jets. However, particularly for low-speed jets, producing accurate simulation data remains challenging. A possible reason for this is the uncertainty about the effect of sub-grid scale models [27]. Another challenge are the inlet or initial conditions of jet simulations. Bogey & Bailly [28] have done LES of jet noise simulations and have repeatedly shown the specification of accurate inlet conditions to be critical.

LES has also been used in industrial applications such as turbo machinery. While RANS has been the tool of choice in the design of turbo-machinery, the ever increasing demand for efficiency is driving the industry towards computational methods that offer good spatial resolution, as well as a time accurate simulation of the flow.

In particular, the recent development of multiple-injection sprays in Diesel engines [29] and auto-ignition inside engines [30] rely heavily on detailed temporal information about the flow. Of interest is also the work of Michelassi *et al.* [31, 32] who performed many LES of different types of turbo machinery.

The choice of a suitable sub-grid scale model and model constant is not the only criteria for a successful LES. The LES methodology with its filtering of scales depends heavily on the choice of a suitable mesh resolution. Vreman *et al.* [33] has studied different sub-grid scale models as well as mesh resolutions and found direct links between an increase in resolution and better agreement of LES data when compared to data produced by a DNS. Similar studies have also been conducted by Voke [34]. Particularly in flows with wall interactions, the mesh resolution near the wall becomes critical [35]. The combination of high Reynolds number flow with the adverse pressure gradients found in engineering applications makes the choice of a suitable mesh for LES challenging [35]. Of interest are also recent studies by McMullan [36] investigating the effects of spanwise domain confinement in mixing layer simulations. The study showed how spanwise confinement in a three-dimensional simulation results in primary structures that resemble those found in two-dimensional simulations.

Inlet conditions have repeatedly been shown to be critical for LES and DNS by various authors [21, 37]. Tabor & Baba-Ahmadi [38] investigated specifically the importance of the inlet conditions in LES. They reviewed ‘precursor simulation’, such as the recycling-rescaling method used in this study, and ‘synthesis’ methods, termed idealised or white-noise in this work. Tabor & Baba-Ahmadi found that while ‘synthesis’ methods are quick to develop and implement, they produce less accurate data compared to ‘precursor’ based simulations. They also suggested that the practice of using a feedback loop to drive the inlet conditions to a desired state can be a successful approach. While precursor based LES have become more numerous in recent years, idealised or synthesis type inlet conditions remain widely used in numerical studies.

To study the structure dynamics inside the mixing layer experiments and numerical simulations have used the practice of injecting a passive, non-reacting scalar into one or two streams of the mixing layer. This is particularly useful in the study of large scale structure interactions in the plane mixing layer [18]. Le Ribault *et al.* used

a passive scalar to study for incompressible [39] and compressible plane jets [23]. While the simulation of non-reacting scalars is comparatively trivial, the simulating reacting flows remains challenging. The simulation of a reacting flow can involve not only the tracking of the reactants, which can be modelled similarly to passive scalars but also the primary atomization, sub-filter scalar mixing and pollutant formation [25]. LES has been applied successfully to combustion problems, but there are comparably few simulations and a discussion of these lies outside the scope of this literature review and is not necessary for the understanding of the simulations presented in this study.

In the 40 years since the first LES by Deardroff [40], LES has advanced steadily. Today, LES is applied to every type of shear layer and is a useful tool for engineering simulations. This section is not intended as an exhaustive review of all the LES performed. Instead, it tries to highlight the broad spectrum of mixing layer flows and problems that are studied using LES today. The next section will review the experimental side of mixing layer research.

2.3 Mixing Layers

With the discovery of coherent structures in the turbulent region of mixing layers by Brown & Roshko in 1974 [9], there has been a resurgence of interest in the mixing layer. There are many aspects of the mixing layer that warrant careful examination. In this literature review, four mixing layer characteristics; the growth rate, large scale coherent structures, secondary streamwise oriented structures, and entrainment and mixing are studied in detail.

2.3.1 Mixing Layer Growth Rates

The growth rate of a mixing layer is considered to be one of its defining characteristics. Townsend proposed that every mixing layer eventually achieves a self-preserving, asymptotic state. In this asymptotic state, the mean growth of the mixing

layer is linear. The idea of a linear growth rate is an extension of this theory and was first proposed by Abramovich in 1963 [41]. Abramovich used earlier unpublished data by Zhestkov *et al.* to deduce a relationship for the growth rate of the mixing layer, given by

$$b = cx \frac{1-r}{1+r} \quad (2.1)$$

where b denotes the mixing layer width and $r = U_2/U_1$. U_1 and U_2 are the high- and low-speed inlet velocities, respectively. Abramovich found that a growth rate constant value of $c = 0.27$ approximated the self-similar growth rate of a turbulent mixing layer well.

Since then a number of measures for mixing layer growth have been proposed. In the literature, mixing layer width is commonly presented as *vorticity thickness* (2.2), *momentum thickness* (2.3) or *visual thickness* (2.4).

$$\delta_\omega = \frac{U_1 - U_2}{(\partial u / \partial y)_{max}} \quad (2.2)$$

$$\theta = \frac{1}{\Delta U^2} \int_{-\infty}^{+\infty} (U_1 - u)(u - U_2) dy \quad (2.3)$$

$$\frac{\delta_{viz}}{x - x_0} = k_v R \quad (2.4)$$

where R is the velocity ratio given by

$$R = \frac{U_1 - U_2}{U_1 + U_2} \quad (2.5)$$

and U_1 and U_2 are the high speed and low speed inlet velocities, respectively. x_0 is the streamwise component of the virtual origin of the mixing layer, found by tracing the visual outlines of the mixing layer.

From these relationships the respective growth rates can be derived

$$\frac{d\theta}{dx} = k_m R \quad (2.6)$$

which describes the *momentum growth rate* and

$$\frac{d\delta_\omega}{dx} = k_o R \quad (2.7)$$

which defines the *vorticity growth rate*. Some experiments, such as Brown & Roshko [9] recorded the growth rate as *visual thickness* which can be related to the vorticity thickness as being roughly double the vorticity thickness, as shown in Equation 2.8.

$$\delta_{viz} \approx 2\delta_\omega. \quad (2.8)$$

However, early on researchers noticed a large spread in the recorded growth rates. Figure 2.1 shows a selected number of vorticity growth rates reported in experiments. As an example, the difference in the growth rate recorded between Liepmann & Laufer [42] and Wygnanski & Fiedler [43] varied as much as 30% in measurements of a single stream mixing layer ($U_2 = 0$). This spread has been investigated throughout the years, and a number of possible causes have been suggested:

1. Free stream velocity fluctuation levels [44]
2. Residual pressure gradients [45]
3. Inlet boundary layer fluctuations [45, 46]

In particular, the inlet conditions have been studied in depth. Browand & Latigo [45] showed that a mixing layer developing from turbulent inlet conditions grows slower at first, but then relaxes to a growth rate similar to that, of a mixing layer evolving from laminar inlet conditions. Similar results were reported by Bell & Mehta [47] who reported a large difference between tripped and untripped inlet conditions in the near field but similar growth rates in the far-field, self-similar region. The

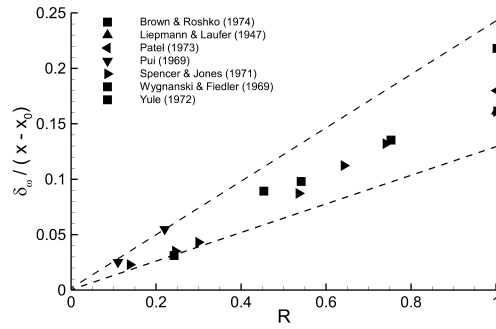


Figure 2.1: Vorticity growth rates reported by experiments.

uncertainty about a definitive growth rate constant has even been used to suggest that there is no self-similar asymptotic final state at all [7]. It is clear then that even after 40 years of research a definitive answer for the experimental spread in growth rates remains to be found.

2.3.2 Coherent Structures

Huerre & Monkewitz [48] studied instabilities in two stream mixing layers and found that the mixing layer can only grow if it is convectively unstable. They showed that mixing layers are convectively unstable if their velocity ratio reaches a critical number and that the most amplified disturbance can be predicted by

$$St = \frac{f\delta_\omega}{4(U_1 - U_2)} \approx \frac{0.017}{R} \quad (2.9)$$

where f is the disturbance frequency, δ_ω the local vorticity thickness and R is the velocity ratio.

Before the discovery of large coherent structures in the high Reynolds number mixing layer by Brown & Roshko [9], coherent structures were thought to be a feature of the low- and moderate Reynolds number mixing layers, exclusively. The most influential part of their work published in 1974 [9] were flow visualisations showing large scale, quasi-two-dimensional, spanwise coherent structures in the turbulent region

of the mixing layer that grew as they convected downstream.

Before Brown & Roshko, Winant & Browand [49] studied the growth rate of a liquid mixing layer at moderate Reynolds number and observed large scale, coherent structures. It was shortly after that Brown & Roshko [9] discovered large scale coherent structures in the post-transition, high Reynolds number mixing layer, which rotated around each other before amalgamating. As the rotation-amalgamation behaviour of structures was previously reported in low- and medium Reynolds number mixing layers, Brown & Roshko deduced that the large structures observed in turbulent mixing layers are therefore cousins of the laminar Kelvin-Helmholtz vortices and develop similarly. They also suggested that the mixing layer growth rate is driven primarily by the pairing interactions between the large scale, primary vortices.

A recent study of the high Reynolds number mixing layer was conducted by D'Ovidio & Coats [11]. Their key finding was a change of growth mechanism of the primary structures during the transition of the mixing layer. In the pre-transition, the primary structures grow based on the Kelvin-Helmholtz instability theory by rotation and amalgamation. In the post-transition, however, the coherent structures grow continuously and linearly. The observed self-similar growth of the mixing layer in the post-transition region has long been a point of contention. Some [9] have suggested that the pairing of primary vortices is responsible for the linear growth, while others [49] have argued that the linear growth results from continuous entrainment of fluid by the primary vortices. Of note is also the observation of two states of the mixing layer in the experiments by D'Ovidio & Coats; an organised state in which large scale coherent structures are present, and an unorganised state in which no structures are evident. The two states also differ in terms of growth rates and entrainment ratios. However, this *two state mixing layer* has not been reported by any other experimental or numerical study.

Although primary and secondary structures have been studied extensively, uncertainty about the primary vortices remains. The observations of a rotation-amalgamation type structure pairing mechanism of the primary vortices and the theory of the continuous, linear growth of the mixing layer [11] are seemingly incompatible. Similarly, the large spread of the mixing layer growth rates observed in experiments has remained a cause of concern.

2.3.3 Secondary Streamwise Structures

In experiments of two stream plane mixing layers, Konrad [50] discovered a secondary, streamwise oriented vortex structure which he suggested to appear during the mixing transition. This streamwise vortex structure was shown to be spatially stationary, and to persist into the self-similar, far field region of the mixing layer. Konrad described the secondary streamwise vortex structures as streamwise oriented hairpin vortices that lie between adjacent spanwise coherent structures. He also showed the rate of entrainment of free-stream fluid to increase with the appearance of the secondary streamwise vortex structures. Breidenthal [51] observed spatially stationary streamwise vortices in time averaged, long exposure flow visualisations. Breidenthal reported the secondary structure to appear just upstream of the mixing transition, in agreement with Konrad [50].

A few years later, Jimenez [52] showed the streamwise vortex structure to persist into the far field and to form long streamwise structures. Jimenez studied the development and evolution of the secondary structure and suggested that based on the amplitude and spacing, the streamwise vortex structure is the product of a secondary instability of the mixing layer. In a subsequent study, Jimenez [53] used digital image processing to analyse flow visualisations by Bernal & Roshko [54]. The study identified a system of streamwise oriented, counter-rotating vortices, residing on top of the primary, quasi-two-dimensional, spanwise coherent structures. Jimenez showed these secondary structures to have a significant effect on mixing in the near-field of the mixing layer and their effect on mixing to decrease in the far-field region.

The effect of the secondary streamwise vortex structure on local mixing was also shown by Bernal & Roshko [54]. They proposed a model in which the secondary, streamwise oriented vortex structures loop between the high-speed of a primary vortex and the low-speed side of the trailing primary vortex, illustrated in Figure 2.2. The spatial organisation of the secondary vortices was reported to produce a well-defined spanwise entrainment pattern in which fluid from either stream is entrained preferentially at different spanwise locations.

In 1992, Bell & Mehta [47] produced cross-plane ($y-z$) measurements of the streamwise vorticity generated by the spatially stationary streamwise vortices. In the near

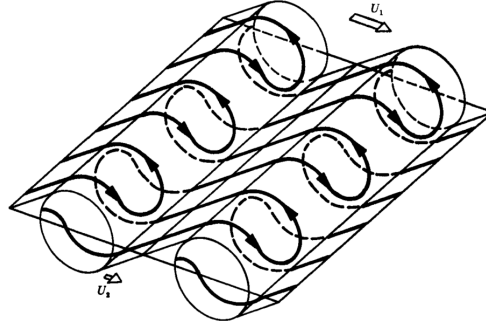


Figure 2.2: Streamwise vortex structure topology (Bernal & Roshko [54]).

field of the mixing layer, the vortices first appear in three-tiered vorticity clusters in which patches of patches vorticity surround a central patch of vorticity with an opposite sign. Figure 2.3a is an illustration of this. With an increase in downstream distance, the streamwise vorticity realigns into a single row of counter rotating streamwise vortices, illustrated in Figure 2.3b. Subsequently, the number of streamwise vortices is reduced in a step-wise fashion with increasing distance from the trailing edge of the splitter plate. While the streamwise vortices persist through the mixing transition into the self-similar region, their strength decreases rapidly and it has been suggested that the mixing layer becomes effectively two-dimensional in the far field [47].

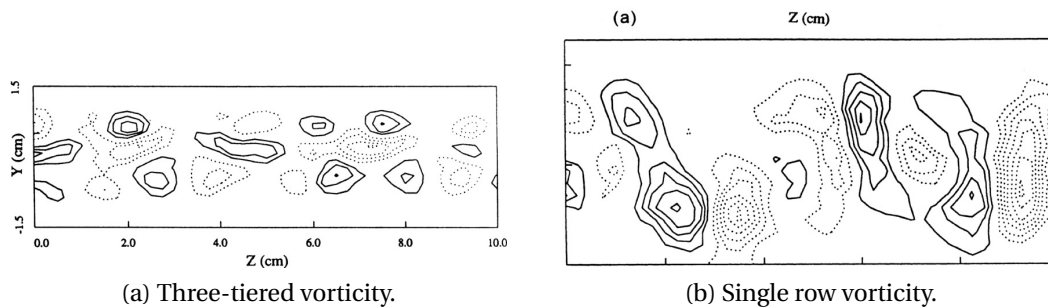


Figure 2.3: Examples of three-tiered and single row vorticity formations by Wiecek & Mehta [55].

2.3.4 Entrainment and Mixing

Entrainment broadly describes the process by which fluid from the irrotational free-streams is introduced to the rotational mixing layer [56] and a clear understanding of the entrainment process is critical to our understanding of shear layers. The earliest proposed entrainment mechanism was by Corrsin & Kistler [57]. The Corrsin & Kistler [57] entrainment mechanism describes a process in which rotational, turbulent fluid contained within the shear layer ‘nibbles’ away on the irrotational, surrounding, free-stream fluid. The two areas are separated by a ‘superlayer’ which is comprised of isotropic turbulence. This ‘superlayer’ will hereafter be referred to as an ‘interface zone’. Entrained fluid is, therefore, a flux of non-turbulent fluid that moves through the interface zone into the turbulent shear layer. An illustration of this entrainment mechanism is shown in Figure 2.4a.

However, in the light of the subsequent discovery of the large scale, quasi-two-dimensional coherent structure in the turbulent mixing layer, it was suggested that the ‘nibbling’ entrainment mechanism might be too simple. Broadwell & Breidenthal [58] proposed a model of mixing and chemical reaction in turbulent mixing layers based on the entrainment of the large scale, spanwise coherent primary vortices. Dimotakis [56] later reviewed performed experiments and proposed the formulation for entrainment which is largely driven by the large scale structures dynamics. The Dimotakis ‘gulping’ or ‘engulfment’ entrainment mechanism can be described as three separate phases, visualised in Figure 2.4b.

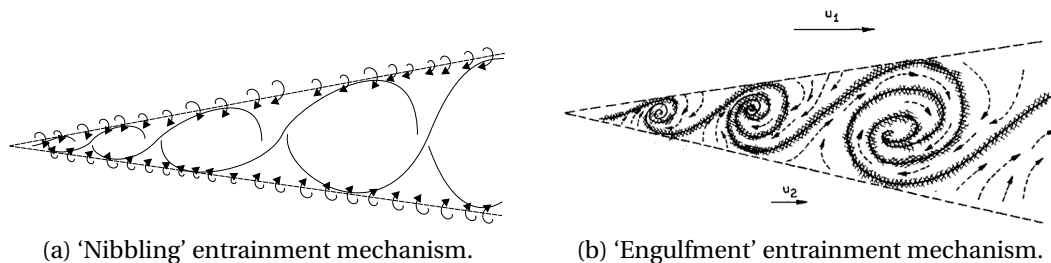


Figure 2.4: ‘Nibbling’ entrainment mechanism by Corrsin & Kistler [57] and ‘engulfment’ entrainment mechanism by Dimotakis [56].

In the first phase, free stream fluid in the vicinity of the spanwise vorticity bearing mixing layer fluid is being ‘dragged’ into motion by the Biot-Savart-induced velocity field. Dimotakis termed this first phase of the entrainment mechanism ‘induc-

tion'. Brown & Roshko [9] referred to this stage as 'entanglement'. The second phase strains the entangled fluid element until the spatial scale is small enough for the diffusive process to overcome the kinematic, 'induction' process. The third phase describes other diffusive processes such as molecular mixing or heat release and is termed 'infusion'. The Dimotakis entrainment model is formulated by

$$E_v(r, s) = s^{1/2} \left(1 + 0.68 \frac{1-r}{1+r} \right) \quad (2.10)$$

where s denotes the density ratio, $s = \rho_2/\rho_1$ and r is the velocity ratio, $r = U_2/U_1$. This model satisfies two key entrainment characteristics observed in experimental mixing layers:

- As the velocity ratio tends to unity, the entrainment ratio tends to unity.
- A decrease in the velocity ratio results in an increase of the high-speed fluid entrainment.

The model agrees well with experimental values for both uniform ($E_v = 1.3$) and non-uniform density entrainment ratios ($E_v = 3.4$ for $s = 7$) reported by Konrad [50]. The Dimotakis model is also based on the earlier findings of Winant & Browand [49] who reported the mixing layer entrainment to be a result of the rotation and amalgamation of the primary vortices. However, Hernan & Jimenez [10] later refuted this idea and instead showed that most of the entrainment occurs during normal structure life and not during vortex pairing events.

While an entrainment model describes how irrotational, free-stream fluid becomes part of the rotational mixing layer body, it does not give any information about the mixing process that occurs inside the mixing layer after the entrainment. Probability Density Functions (p.d.f.'s) are a commonly-used means to describe the mixing process inside the mixing layer. P.d.f.'s describe the probability of finding mixed fluid of a given concentration at any vertical location inside the mixing layer. The p.d.f. is defined as,

$$f(\alpha)d\alpha = \text{probability that } \alpha < \xi < \alpha + d\alpha, \quad (2.11)$$

and

$$\int_{-\infty}^{+\infty} f(\xi) d\xi = 1 \quad (2.12)$$

where ξ is the passive scalar and α is the spatial resolution of the passive scalar data.

P.d.f.'s are generally categorized into one of three distinct types; the first type is the *marching* type p.d.f, shown in Figure 2.5a. In a *marching* p.d.f. the preferred passive scalar concentration is equal to the average scalar at any given vertical location. The spikes at $\xi = 1$ and 0, indicate the presence of pure, unmixed free stream fluid. The width of these spikes results from the spatial resolution of the passive scalar data [59]. The second type is the *non-marching* p.d.f. which describes a p.d.f. with a preferred passive scalar concentration that is constant across the mixing layer width, shown in Figure 2.5b. The location of the peak in between the free stream peaks defines the *preferred concentration*. *Tilted* or *hybrid* p.d.f.s are the third kind and describe a mixing layer which has features of both the *marching* and *non-marching* p.d.f. *Tilted* p.d.f.'s differ from *marching* p.d.f.'s in that they have a preferred passive scalar concentration in the high-speed side but a *marching* characteristic in the low-speed side of the mixing layer.

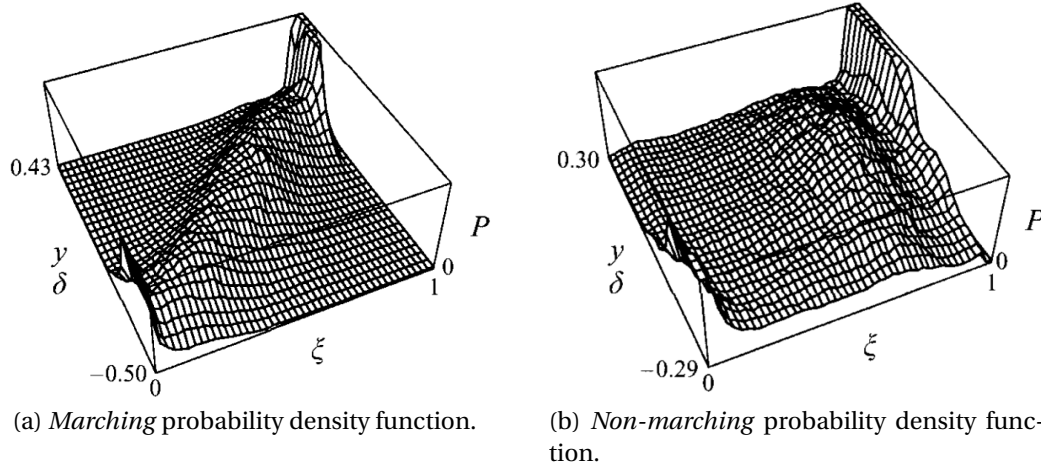


Figure 2.5: Examples of *marching* and *non-marching* probability density function shapes (Karasso & Mungal [60]).

For the low Reynolds number mixing layer, Masutani & Bowman [59] reported p.d.f.'s of the *non-marching* type. Recently Picket & Gandhi [61] reported *non-marching* type p.d.f.'s for moderate Reynolds numbers. For the p.d.f. shape in self-similar, far-field region of a high Reynolds number mixing layer some uncertainty remains. Post-

transition p.d.f.'s by Konrad for the uniform density case were exclusively of the *non-marching* type. Batt [62] performed single stream mixing layer ($U_2 = 0$) experiments and found the p.d.f.'s in the far-field to be of the *marching* type. Later experiments by Pickett *et al.* [63] showed that tripping the boundary layer of an inlet stream can change the p.d.f. shape from *non-marching* to *hybrid* or *marching*. This suggests that the *marching* p.d.f.'s observed by Batt could have been caused by very high inlet fluctuations caused by the 'flow over step' type flow configuration.

While the consensus has been that mixing layer entrainment is largely driven by primary structures, Lasheras & Choi [64] have shown spatially stationary streamwise vortices to contribute significantly to the overall entrainment of the mixing layer, particularly in the early stages of the mixing layer development. After many years, entrainment and mixing remain areas of active research and uncertainty about different entrainment mechanisms, p.d.f. shapes and changes with Reynolds number remain. LES is the optimal tool to investigate these processes as it suffers from none of the complications that are associated with passive scalar and reactant measurements in experiments while simultaneously allowing full control of the flow parameters and inlet conditions.

2.4 Numerical Simulation of Mixing Layers

Experimental studies of mixing layers are extremely challenging. The effects of inlet conditions, upstream boundary layers, exit conditions and density differences make experimental investigations costly and time-consuming. Numerical simulations allow parameterised studies at a fraction of the cost of a comparable experimental study. As a result of this, researchers are increasingly using numerical methods, instead of experiments, to study various aspects of the mixing layer. The first numerical simulations were of the temporal type, shown in Figure 2.6. A temporal simulation uses periodic boundary conditions in the streamwise and spanwise directions. This eliminates the difficulty of handling boundary conditions and allows the evolution of a mixing layer to be simulated with a smaller domain, and grid.

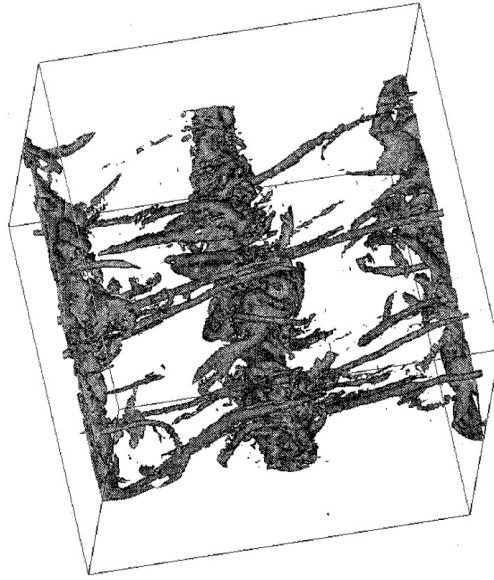


Figure 2.6: Example of a temporal DNS. (Lesieur *et al.* [65]).

2.4.1 Temporal Mixing Layers

One of the first temporal DNS was produced by Metcalfe *et al.* [66]. The primary objective of their DNS was to study the secondary, streamwise oriented vortex structure. It was found that depending on the initial conditions, the temporal analogue to inlet conditions in spatial simulations, the flow would either be ‘unorganised’ or ‘organised’ into large scale structures with spatially stationary streamwise vortices that loop between the primary, quasi-two-dimensional primary structures. The presence of the spatially stationary streamwise vortices significantly enhanced the overall spanwise coherence of the mixing layer.

Lesieur *et al.* [67] studied the primary vortex structure using a temporal LES. Unlike previous DNS by Metcalfe *et al.* [66], Lesieur *et al.* [67] did not observe any spatially stationary streamwise vortices in their simulations. Unlike the study by Metcalfe *et al.* [66] which used a largely two-dimensional initial disturbance field, the simulations by Lesieur *et al.* [67] used white noise type initial conditions.

The influence of two- and three-dimensionality of the initial conditions was later studied by Comte *et al.* [68]. It was found that if the three- and two-dimensional initial disturbances were combined the flow produced quasi-two-dimensional roller

structures with weak secondary streamwise vortices stretching between the primary vortices. If the two-dimensional initial disturbance was removed and the simulation used only three-dimensional disturbances, the flow produced helical-type instabilities, as observed by Nygaard & Glezer [69], and no streamwise vortices were present.

Three sets of initial conditions for a temporal DNS were investigated by Rogers & Moser [6]. The first set of initial conditions was based on velocity fields produced by a turbulent boundary layer DNS by Spalart [70]. Two additional simulations utilised the same inlet disturbance field but with superimposed two-dimensional disturbances of varying strengths. The simulation without, and low-level additional two-dimensional disturbances produced a lack of large-scale organised primary vortex pairings and a lack of streamwise vortices. The produced p.d.f.'s were of the *marching* type. The case with high additional two-dimensional disturbances showed organised primary vortex pairings, streamwise vortices and the obtained p.d.f.'s were of the *non-marching* type.

While attractive on the basis of computational cost, temporal mixing layer simulations suffer some limitations. The most critical limitation in the context of the simulations in this study, is the prediction of equal entrainment from the high- and low-speed streams in temporal simulations [18], while experiments have unequivocally shown entrainment to favour the high-speed stream.

2.4.2 Spatially Developing Mixing Layers

With the rapid advance of computational resources, the number of DNS and LES studies of spatially evolving mixing layers has increased rapidly. The number of spatially developing numerical studies is too large to be reviewed in its entirety. Therefore, a selection of the earliest, most relevant to this study, and most recent DNS and LES of spatially developing mixing layers will be reviewed.

The first spatially developing numerical simulations were limited to two dimensions. Ghoniem & Kenneth [71] produced a vortex simulation of a confined, two-dimensional, two-stream mixing layer. Large scale structure pairings were observed, and entrain-

ment was of the engulfment type. However, as two-dimensional simulations grow by primary vortex pairing, it has been suggested that entrainment can only happen by engulfment by definition.

A similar LES of a two-dimensional mixing layer was produced by Yang *et al.* [72]. The authors suggested that the observed large scale dynamics agree qualitatively with flow visualisations by Roshko [73]. The predicted peak velocity fluctuation magnitudes were considerably higher than those reported in the reference experiment, and the momentum growth rate does not show any evidence of a mixing layer transition. It has since been shown that the lack of a third-dimension results in unrealistic flow dynamics [36].

Baig & Milane [74] studied the Masutani & Bowman [59] dataset using a two-dimensional vortex-in-cell method for passive scalar transport. One key difference between the simulation and the experiment was the streamwise distance required for self-similarity. While the experiment reported self-similarity after 7cm from the trailing edge of the splitter plate, the simulations produced self-similarity after 21cm from the trailing edge of the splitter plate. The p.d.f.'s were of the *non-marching* type which was in agreement with the reference experiment. However, it has since been suggested that the engulfment entrainment mechanism present in spatially developing two-dimensional simulations produces *non-marching* p.d.f. by definition, which makes the *non-marching* p.d.f.'s a 'necessity' of the performed two-dimensional simulation.

More recently, a three-dimensional, spatially evolving LES based on white noise type inlet fluctuations has been used to investigate the large scale coherent structures in plane mixing layers [18]. These numerical studies were a recreation of earlier experiments by D'Ovidio & Coats [11]. The white noise based LES produced large scale coherent structures that grew continuously and linearly in the post-transition, in agreement with the reference dataset. The reference dataset nor the simulations reported any p.d.f.'s.

McMullan & Garrett [21] compared results between white noise type LES and an LES based on spatially and temporally correlated inlet fluctuations. While both simulations produced good agreement with reference mean statistics, the correlated inlet

fluctuations produced spatially stationary streamwise vortices, while the white noise based simulations did not. Particular interest was paid to the growth mechanism of the primary vortices. In the white noise type simulation the primary vortices were shown to be fully three-dimensional and grew continuously and linearly, in agreement with an earlier, white noise based LES by McMullan *et al.* [18] and experiments by D'Ovidio & Coats [11]. In the LES based on spatially and temporally correlated inlet fluctuations, the primary vortices were quasi two-dimensional and the primary vortex growth was best approximated by the square root of time. The square root of time growth was linked to the presence of the spatially stationary streamwise vortices.

A DNS of a spatially developing, mixing layer at Reynolds numbers up to 25000 has recently been reported by Attili *et al.* [3]. The main focus of the study was the investigation of the interface zones between the mixing layer and the free-streams. A passive scalar was included in the simulations and the reported p.d.f.'s were of the *marching* type which is in disagreement with the majority of experiments reporting *non-marching* p.d.f.'s.

Numerical simulations of shear layers have seen incredible developments in recent years, and today DNS and LES are used successfully to study various aspects of mixing layers. However, uncertainty about critical mixing layer aspects such as the growth rates, p.d.f. shapes, primary and secondary vortices, and inlet conditions remain. This study will use LES based on idealised and physically correlated inlet conditions to simulate and study low and high Reynolds number mixing layers. Unlike many of the studies reported in the literature which focus on momentum or passive scalar fields, the simulations presented in this work will pay attention to the accurate simulation of the momentum field as well as passive scalar entrainment and mixing.

2.5 Chapter Summary

In this literature review, the background and application of Large Eddy Simulations have been discussed. The experimental mixing layer was discussed with a focus on a few selected mixing layer properties which will be the main focus of this work. A

review of temporally and spatially developing Direct Numerical Simulations and LES has provided some insight into past and current numerical simulations.

With the presented previous research in mind, these key issues have been identified:

1. Three-dimensional LES of a low Reynolds number mixing layer

As of now, no three-dimensional simulations of the Masutani & Bowman [59] dataset have been reported. The effect of inlet conditions on a three-dimensional numerical simulation have to be investigated. The Masutani & Bowman [59] dataset has been chosen for further study as it contains detailed passive scalar statistics that can be used for validation. The target of the numerical simulations will be the reproduction of the *non-marching* probability density function shape reported in the experiment.

2. Passive scalar entrainment and mixing in a high Reynolds number mixing layer

While three-dimensional, spatially developing LES of high Reynolds number mixing layers are numerous by now, data on passive scalar entrainment and mixing are scarce. Numerical simulations comparing white noise and physically correlated inlet fluctuations exist [21] but no passive scalar statistics were reported. An LES investigating the links between physical correlation of the inlet conditions and passive scalar statistics including the probability density functions is currently outstanding.

3. Primary, spanwise oriented and spatially stationary streamwise vortices in the plane mixing layer

There is experimental evidence [46, 75, 76] for the links between inlet conditions and the spanwise and streamwise oriented vortex dynamics in the plane mixing layer. Numerical studies are the ideal candidate to investigate the links between different mixing layer properties and structure dynamics as they allow the careful isolation of individual simulation parameters [76].

Chapter 3

Numerical Methods

In this chapter an outline of the numerical methods is presented. The fundamental Navier-Stokes equations are discussed briefly. Sub-grid scale modelling is introduced and two sub-grid scale models, the Smagorinsky model and WALE model, are studied in detail. The used research code and the chosen numerical methods are explained and the white noise and recycling-rescaling inlet generation methods are discussed. The last part of this chapter describes a Matlab code that was developed to study the growth of large scale coherent structures.

3.1 Navier-Stokes Equations

The Navier-Stokes equations in tensorial notation for an incompressible fluid are given by

$$\frac{\partial u_i}{\partial t} + \frac{\partial u_i u_j}{\partial x_j} = -\frac{1}{\rho} \frac{\partial p}{\partial x_i} + \nu \frac{\partial^2 u_i}{\partial x_j \partial x_j} \quad (3.1)$$

$$\frac{\partial u_i}{\partial x_i} = 0 \quad (3.2)$$

where i and $j = 1, 2, 3$ correspond to the x, y and z axes. A repetition of the index indicates a summation. u_i is the velocity in the i -th direction, p is the pressure, ρ is the density and ν is the kinematic viscosity, $\nu = \mu/\rho$.

In Large Eddy Simulations, the resolved and unresolved scales are filtered using a filter function, G , defined as

$$\bar{f}(x) = \int_D f(x') G(x, x'; \bar{\Delta}) dx' \quad (3.3)$$

where D is the computational domain, G is the filter function and $\bar{\Delta}$ is the filter width. The filter width is the effective size of the smallest resolved scale. The most common form of filter is top-hat filter,

$$G(x) = \begin{cases} 1/\bar{\Delta}, & \text{if } |x| \leq \bar{\Delta}/2 \\ 0, & \text{otherwise.} \end{cases} \quad (3.4)$$

As the information contained in the unresolved, filtered scales is lost and therefore has to be modelled, the choice of the correct cut-off length is critical [77]. After application of the filtering equation to the Navier-Stokes equations (3.1, 3.2), the filtered equations of motion for an incompressible fluid are given by

$$\frac{\partial \bar{u}_i}{\partial t} + \frac{\partial}{\partial x_j} (\bar{u}_i \bar{u}_j) = -\frac{1}{\rho} \frac{\partial \bar{p}}{\partial x_i} - \frac{\partial \tau_{ij}}{\partial x_j} + \nu \frac{\partial^2 \bar{u}_i}{\partial x_j \partial x_j} \quad (3.5)$$

$$\frac{\partial \bar{u}_i}{\partial x_i} = 0. \quad (3.6)$$

The filtering operation introduces a new term, τ_{ij} , which accounts for the stresses generated for the filtered, sub-grid scale scales. This sub-grid scale tensor term is given by

$$\tau_{ij} = \overline{u_i u_j} - \bar{u}_i \bar{u}_j \quad (3.7)$$

τ_{ij} is computed from the unfiltered u variable which can not be done as the governing equations are functions of \bar{u} and therefore provide no information about the unfiltered variable u . This problem is known as the *closure problem* and is solved by using a sub-grid scale model. Two sub-grid scale models are discussed in the next section.

3.2 Sub-grid Scale Modelling

A figure illustrating the typical energy content of a turbulent flow is shown in Figure 3.1. Of interest is the separation between the resolved and unresolved regions of the energy spectrum. Figure 3.1 illustrates the energy contribution of the filtered equations which ends at the inertial region of scales of motion. The cutoff length applied by the filtering function should lie in the region of the energy containing scales, by definition. It can be seen, therefore, that the smallest scales of motion are not resolved explicitly, and have to be modelled to close the system. This is necessary to produce the correct dissipative behaviour required in turbulent flows.

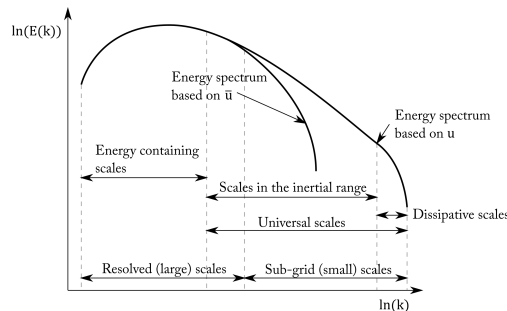


Figure 3.1: Energy spectrum contained in a flow.

3.2.1 Smagorinsky

The earliest proposed sub-grid scale model is the Smagorinsky model [14] and it has remained one of the most popular sub-grid scale models. The Smagorinsky gradient-diffusion type model takes the form

$$m_{ij} = -2\nu_{sg}\bar{S}_{ij} \quad (3.8)$$

where

$$\bar{S}_{ij} = \frac{1}{2} \left(\frac{\partial \bar{u}_i}{\partial x_j} + \frac{\partial \bar{u}_j}{\partial x_i} \right). \quad (3.9)$$

m_{ij} describes the effects of the filtered, small-scales, \bar{S}_{ij} is the filtered strain rate tensor and ν_{sg} is the sub-grid scale eddy viscosity.

A universal assumption of sub-grid scale models is the acceptance of the Kolmogorov theory that turbulence is isotropic at the smallest scales. Additionally, the Smagorinsky model assumes that energy transferred from the resolved to the unresolved scales is dissipated entirely and instantaneously. These assumptions are used to construct an expression for the sub-grid scale eddy viscosity, ν_{sg} ,

$$\nu_{sg} = (C_s \bar{\Delta})^2 |\bar{S}| \quad (3.10)$$

where $|\bar{S}|$ is given by

$$|\bar{S}| = (2S_{ij}S_{ij})^{1/2} \quad (3.11)$$

and $\bar{\Delta}$ is the filter width, determined by the computational grid. Typical values for C_s lie in the range of 0.05 for simulations of isotropic turbulence to 0.18 for plane mixing layer simulations [16].

In the Chapter 2 it was highlighted that the Smagorinsky model suffers from some drawbacks:

1. Incorrect near-wall behaviour

Due to the boundary layer present near a wall, a sub-grid model should predict zero eddy viscosity at the wall. This can not be done using the standard Smagorinsky model, and *ad hoc* corrections of the model constant have to be performed in near-wall regions.

2. Prediction of non-zero eddy viscosity in laminar flow

A major drawback of the Smagorinsky model in light of the presented simulations is the non-zero eddy viscosity predicted in laminar flow. Non-zero eddy viscosity in the near field can damp out fluctuations in the initial region, leading to a delay in the flow evolution. This is particularly problematic for the low Reynolds number flows presented in the first part of Chapter 4 as low Reynolds number mixing layers have shown a hypersensitivity to the inlet condition and the near field of the mixing layer.

3. Poor flow transition prediction

LES have shown the Smagorinsky model to delay the transition of the mixing layer to a fully turbulent flow [78]. This is due to the over- and under-dissipation of energy in the pre- and post-transition region that occurs if a Smagorinsky model with a fixed model constant is used [79].

3.2.2 Wall Adapting Local Eddy-viscosity (WALE)

The Wall Adapting Local Eddy-viscosity model (WALE) has been developed by Nicoud & Ducros [17] and addresses the drawbacks of the Smagorinsky model. In the WALE model, the sub-grid scale tensor, ν_{sg} is computed from

$$\nu_{sg} = (C_w \bar{\Delta})^2 \frac{(S_{ij}^d S_{ij}^d)^{3/2}}{(\bar{S}_{ij} \bar{S}_{ij})^{5/2} + (S_{ij}^d S_{ij}^d)^{5/4}}. \quad (3.12)$$

S_{ij}^d is computed from the traceless symmetric part of the square of the velocity gradient tensor:

$$S_{ij}^d = \frac{1}{2}(\overline{g}_{ij}^2 + \overline{g}_{ji}^2) - \frac{1}{3}\delta_{ij}\overline{g}_{kk}^2 \quad (3.13)$$

where $\overline{g}_{ij}^2 = \overline{g}_{ik}\overline{g}_{kj}$, δ_{ij} is the Kronecker delta and $\overline{g}_{ij} = \partial\overline{u}_i/\partial x_j$. The model constant C_w is chosen *a priori*. Typical values for C_w range between 0.55 to 0.60 [17]. Compared to the Smagorinsky model the WALE model offers a number of advantages:

- Local strain and local rotation are taken into account in the spatial operator. This means the model takes all turbulence producing structure into account for the kinetic energy dissipation modelling.
- The eddy-viscosity near a wall tends to zero making dynamics adjustment of the model constant or damping functions unnecessary.
- In regions of pure shear, the model predicts zero eddy-viscosity. This makes it suitable to simulate the transition from laminar to turbulent flow.

Since its formulation, the WALE model has been used successfully in many LES [21, 26, 80, 81, 82], and has become frequently used as a sub-grid scale model for low and high Reynolds number mixing layer simulations.

3.3 Code Description

Plane turbulent mixing layers have been studied extensively using the code employed in the presented simulations [18, 21, 78, 82]. This section provides a description of the research code.

3.3.1 Governing Equations

The used code has been used in jet flows [83], and plane mixing layer simulations [21, 84]. The code uses the spatially filtered analytical equations for conservation of momentum and mass of a uniform density fluid, given by

$$\frac{\partial \bar{u}_i}{\partial t} = -\frac{\partial \bar{p}}{\partial x_i} + \frac{\partial}{\partial x_j} (-\bar{u}_i \bar{u}_j + 2\nu \bar{S}_{ij}) \quad (3.14)$$

$$\bar{S}_{ij} = \frac{1}{2} \left(\frac{\partial \bar{u}_i}{\partial x_j} + \frac{\partial \bar{u}_j}{\partial x_i} \right) \quad (3.15)$$

$$\frac{\partial \bar{u}_i}{\partial x_i} = 0. \quad (3.16)$$

These equations are discretised on a staggered mesh [85]. The kinematic viscosity, ν , is given by

$$\nu = \nu_m + \nu_{sg} \quad (3.17)$$

where ν_m and ν_{sg} are the molecular and sub-grid scale components of the viscosity, respectively.

3.3.2 Time Advancement

Time advancement of the simulation is done using the second-order Adams-Bashforth method in which a provisional velocity field is computed from

$$\bar{u}_i^* = \bar{u}_i^n + \Delta t \left(\frac{3}{2} H_i^n - \frac{1}{2} H_i^{n-1} \right) \quad (3.18)$$

where

$$H_i = \frac{\partial}{\partial x_j} (-\bar{u}_i \bar{u}_j + 2\nu \bar{S}_{ij}). \quad (3.19)$$

The superscript $*$ denotes a temporary value, (n) are current values and $(n-1)$ are values obtained at the previous time step. The value of \bar{u}_i^* does not obey continuity,

and a pressure solver is used to compute a pressure field from which the velocity components are updated, and a value for \bar{u}_i^{n+1} is computed which obeys continuity.

3.3.3 Pressure Solver

The pressure field is solved explicitly using the continuity equation (3.2). The pressure field is used to calculate the provisional velocity field, \bar{u}_i^* , in Equation 3.18 using the gradient of an unknown pressure field $p^{n+\frac{1}{2}}$

$$u_i^{n+1} = u_i^* - \Delta t \frac{\partial p^{n+\frac{1}{2}}}{\partial x_i}. \quad (3.20)$$

Since the new pressure field u_i^{n+1} has to have zero divergence, a Poisson equation is used to compute the pressure field between the current and next time step

$$\nabla^2 p^{n+\frac{1}{2}} = \frac{1}{\Delta t} \frac{\partial \bar{u}_i^*}{\partial x_i} \equiv R. \quad (3.21)$$

For the Poisson equation to be applicable, one spatial dimension must be periodic. If this is true, a Fourier transform of Equation 3.21 gives a sequence of Helmholtz problems for each wavenumber k_z

$$\frac{\partial^2 \tilde{p}}{\partial x^2} + \frac{\partial^2 \tilde{p}}{\partial y^2} - k_z^2 \tilde{p} = \tilde{R}. \quad (3.22)$$

This Fourier transform is performed in the direction of the span and subsequently iterated by a multigrid method for the stream and vertical dimensions, respectively.

3.3.4 Outflow Boundary Condition

The only outflow boundary present in the presented simulations lies in the stream-wise, x , direction. A convective outflow boundary is used to fix an outflow velocity component \bar{u}_x , given by

$$\frac{\partial \bar{u}_x}{\partial t} = -U_c \frac{\partial \bar{u}_x}{\partial x}. \quad (3.23)$$

The outflow boundary condition only applies to the nodes $n_{i=N_x, j, k}$ where N_x is the number of nodes in the streamwise direction. U_c is the mean streamwise velocity averaged over the outflow plane and the time derivative is computed by

$$\frac{\partial \bar{u}_x}{\partial t} = (\bar{u}_x^{n+1} - \bar{u}_x^n) / \Delta t \quad (3.24)$$

accurate to the first order in time.

The pressure solver implies that the sum of the mass flux through the domain boundaries must be zero. However, a temporally and spatially correlated inlet condition does not guarantee a constant net inflow. Therefore the outflow velocity has to be rescaled to preserve the mass flux balance. This normalisation is done using the ratio between the fluxes, r , such that

$$\bar{u}_x \leftarrow r \bar{u}_x. \quad (3.25)$$

3.3.5 Passive Scalar

The computations include a passive scalar, $\bar{\xi}$. The filtered passive scalar field is solved by

$$\frac{\partial \bar{\xi}}{\partial t} = \frac{\partial}{\partial x_i} \left(-\bar{u}_i \bar{\xi} + \alpha \frac{\partial \bar{\xi}}{\partial x_i} \right) \quad (3.26)$$

α is the diffusivity and is given by

$$\alpha = \alpha_m + \alpha_{sg} \quad (3.27)$$

where α_m and α_{sg} are the molecular and sub-grid scale diffusivity, respectively. The α_{sg} is computed from μ_{sg} by

$$\alpha_{sg} = Sc_t \mu_{sg} \quad (3.28)$$

$$Sc = \nu / \alpha = 0.7 \quad (3.29)$$

where $Sc = 0.7$ is the chosen Schmidt number and ν is the kinematic viscosity. The scalar is discretised at the cell centre, and a third-order Total Variation Diminishing (TVD) scheme is used to control the scalar fluxes and ensure the values of $\bar{\xi}$ are bounded between 0 and 1. A zero-gradient condition is imposed at the outflow plane. Time advancement is done using the Adams-Bashforth method, explained in Section 3.3.2.

3.4 Inlet Generation

The subsequently presented simulations utilise one of two types of inlet generation methods. In this section, both inlet generation methods will be discussed in more detail.

3.4.1 White Noise (WN)

White Noise (WN) type inlet conditions use a velocity profile with superimposed pseudo random velocity fluctuations. In this study velocity profiles for u , v and w are specified. Superimposed on the velocity profiles are individually specified fluctuation profiles. Examples of such velocity and velocity fluctuation profiles are shown in Figure 3.2.

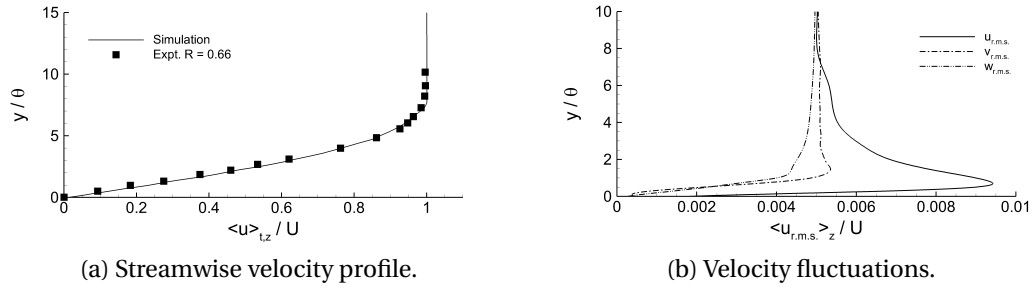


Figure 3.2: Examples of inlet velocity and inlet velocity fluctuation profiles.

3.4.2 Recycling-Rescaling Method (RRM)

The Recycling-Rescaling Method (RRM) type inlet condition generation is based the R^2M technique by Xiao *et al.* [37]. Similar to the WN inlet condition, mean velocity and velocity fluctuation profiles for u , v and w at the inlet plane of the domain are specified. However, these define target values, rather than absolute values. How the inlet fluctuations are generated is described below.

An additional, pre-cursor domain upstream of the inlet plane is created. The stream-wise domain size is a minimum of $14\delta_i$ where δ_i is the high-speed inlet boundary layer thickness. The pre-cursor domain is initialised with the chosen velocity profiles onto which fluctuations with a magnitude of $0.1U_1$ are superimposed. At each time step a $y-z$ plane a short distance upstream of the end of the pre-cursor domain is extracted. This $y-z$ plane is then recycled onto the inlet plane of the pre-cursor domain. For the duration of the simulation, a running average of the velocity field within the pre-cursor domain is computed using the equation

$$\bar{U}_i^{n+1}(y) = \alpha \langle U_i(x, y, z, t) \rangle_{x,z} + (1 - \alpha) \bar{U}_i^n(y) \quad (3.30)$$

$$U_{mean}^{n+1}(x, y, z, t) = \alpha \langle \bar{U}^{n+1}(x, y, z, t) \rangle_{x,z} + (1 - \alpha) U_{mean}^n(y) \quad (3.31)$$

where α is specified *a priori*. $\langle \rangle_{x,z}$ denotes streamwise and spanwise averaging and $\bar{U}^{n+1}(x, y, z, t)$ is the current velocity field. The r.m.s. fluctuations of the velocity are computed using the expression

$$u_i'^{n+1}(y) = (\alpha \langle [U_i(x, y, z, t) - \bar{U}_i^{n+1}(y)]^2 \rangle + (1 - \alpha) [u_i'^n(y)]^2)^{1/2} \quad (3.32)$$

The mean and r.m.s. velocity fields are rescaled within the virtual domain at a specified rescaling interval. The rescaling process creates a new instantaneous velocity field for the virtual domain, given by

$$U_i^r(x, y, z, t) = \frac{u_{target}'(y)}{u_i'^{n+1}(y)} [U_i(x, y, z, t) - \bar{U}_i^{n+1}(y)] + \bar{U}_{target}(y) \quad (3.33)$$

The components for v and w are rescaled using the same procedure.

The RRM inlet generation procedure produces spatially and temporally correlated inlet fluctuations with a small increase in computational cost. The increased computational cost is offset by using additional CPU cores resulting in similar run times compared to the WN type simulations.

3.5 Structure Tracking

The vertical size of a structure can be used as a means to track structure growth. An example of a structure with indicated vertical points, the centre of location and

saddle points is shown in Figure 3.3a. The manual tracking of primary structures in simulations is time intensive and involves multiple steps; first stream traces are used on an instantaneous or spanwise averaged flow field to locate a primary structure. Once a structure has been identified, additional stream traces are plotted to establish if the structure is not undergoing any type of interaction. If this is not the case, the centre of rotation of the structure has to be found, and the vertical size can be measured.

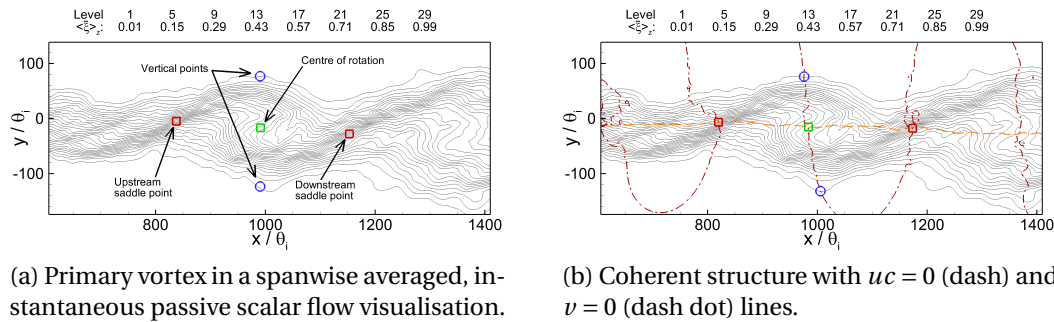


Figure 3.3: Primary vortex in a spanwise averaged, instantaneous passive scalar flow visualisation with indicated points of interest.

The time intensity of this activity limits the analysis to a low number of structures. To enable quantitative analysis and to reduce the time requirement to produce vertical structure growth tracks, a Matlab code was written. That code will be presented here in detail.

To track primary vortices instantaneous, spanwise averaged flow fields, sampled at a given frequency are analysed. The first step in this process is to read a single time instance of the spanwise averaged flow field into memory. The imported variables are x, y, uc, ν and $\bar{\xi}$ where x, y are the streamwise and vertical coordinates, uc is the convection velocity and is given by $uc = u - (U_1 + U_2)/2$ and $\bar{\xi}$ is the passive scalar concentration.

Figure 3.3b shows an example structure and the $uc = 0$ and $\nu = 0$ lines which pinpoint a structure centre of rotation. Matrix comparison is used to identify the sign changes in uc and ν . Matrix operations are parallelised effectively in Matlab which allows the code to process flow fields with more than 500000 nodes in 2 seconds per time step. Further matrix comparison is done to categorize points of interest into centres of rotations and saddle points. A clustering algorithm is used to cluster very

small structures and introduced false positives into the primary vortices that would be observed if the flow field was to be investigated manually.

The vertical size is computed by linearly interpolating the x and y coordinates of the identified structures back onto the passive scalar grid and finding the vertical distance between the $\bar{\xi} = 0.01$ and $\bar{\xi} = 0.99$ passive scalar concentrations in the vertical plane of the centre of rotation.

The array of the identified primary vortices and vertical size is written out into a plain text data file, and the next flow field is read in. The described Matlab code has been used to compute the presented primary vortex growth tracks in the later chapters.

3.6 Chapter Summary

In this chapter, a short overview of the LES code and two sub-grid scale models has been presented. The Smagorinsky and WALE models have been compared and the implementation of both has been shown. An analysis code written in Matlab has been presented. The described code has been used to identify and track structures in instantaneous flow fields presented in the later chapters of this thesis.

Chapter 4

Inlet Fluctuation Correlation Effects

In this chapter the effects of temporal and spatial inlet fluctuation correlation are studied. The chapter is divided into two sections; the first part of this chapter is based on a low Reynolds number, plane mixing layer dataset by Masutani & Bowman [59]. The latter part of this chapter studies inlet correlation effects in simulations of high Reynolds number mixing layers, based on a reference dataset by Browand & Latigo [45].

4.1 Low Reynolds Number Mixing Layer

4.1.1 Introduction

The low Reynolds number mixing layer has long been an area of active research and is considered a canonical test case. One key aspect identified early on is its hypersensitivity to initial conditions, i.e., the state of the boundary layer that departs the splitter plate [86]. It has been suggested that the hypersensitivity of the mixing layer to its initial conditions has led to a large spread in experimental measurements of similar mixing layers [42, 43]. The combination of the experimental difficulty in obtaining accurate flow data inside the inlet boundary layer, and its hypersensitivity to

initial conditions, makes producing physically realistic inlet conditions for numerical simulations particularly challenging [84]. Numerical inlet conditions have traditionally utilised pseudo random velocity fluctuations imposed onto a mean inlet profile. This type of simulation is referred hereafter as white-noise (WN), or idealised simulation, and remains common today. More recently the practice of producing spatially and temporally correlated inlet fluctuations utilising an additional domain located upstream of the inlet plane has become more common [37, 21]. This type of inlet condition is referred here as the recycling-rescaling method (RRM).

The presented simulations are compared against an experimental dataset of the low Reynolds number mixing layer by Masutani *et al.* [59]. The Masutani dataset is one of the few datasets available which includes both velocity as well as passive scalar data. Of particular interest is the reproduction of the *non-marching* type probability density functions (p.d.f.s) reported by the experiment. *Non-marching* p.d.f.s have, as of yet, not been reproduced in any three-dimensional numerical simulation of this dataset. While the initial conditions have been reported to some extent, insufficient information is available about the state of the boundary layer at the inlet plane, permitting scope for a parametrised study of the effects of varying the inlet boundary layer fluctuation magnitude.

The presented results aim to investigate the effect of inlet conditions and inlet boundary layer conditions on a low Reynolds number mixing layer using numerical simulations with particular attention paid to passive scalar data.

4.1.2 Reference Experiment

The test section in the reference experimental setup was 20cm long, 4cm high, and 10cm wide. The two free-streams were separated by a tapered Teflon-coated brass splitter plate with an edge thickness of 0.1mm. The free-stream velocity of the high-speed inlet, U_1 , was recorded as 6.0m/s and the low-speed inlet, U_2 , as 3.0m/s. The chosen inlet velocities result in a velocity ratio, R , given by $R = (U_1 - U_2)/(U_1 + U_2)$, of $R = 0.333$. For both inlets, the boundary layer was laminar with a momentum thickness of 0.24mm, and 0.26mm, on the high- and low-speed side, respectively.

U_1 (m/s)	θ_1 (mm)	U_2 (m/s)	θ_2 (mm)	R	u'_{\max}/U (%)
6.0	0.24	3.0	0.28	0.333	0.5

Table 4.1: Flow properties

The free-stream fluctuation magnitude in the free-stream, $u_{r.m.s.}$, was recorded as 0.5% of the convection velocity U_c given as $U_c = (U_1 + U_2)/2$. No streamwise velocity boundary layer fluctuation profiles were recorded. To reduce the adverse pressure gradient present, an angled bottom wall was used. For the passive scalar measurements, the reference experiment measured non-reacting O_3 , injected into the low-speed inlet stream at a concentration of 1000 p.p.m. A summary of the flow properties is given in Table 4.1.

The streamwise velocity data presented was measured at the streamwise locations of $x = 0.07, 0.12, 0.15$, and 0.18 m using a single-wire, gold-plated hot wire probe and a TSI anemometer and linearizer [59]. The passive scalar measurements were obtained by seeding one stream with O_3 while the other stream consisted of pure N_2 . A fibre-optic absorption probe was traversed vertically through the layer at the streamwise locations of $x = 0.07, 0.11$ and 0.15 m. For the passive scalar measurements, the spanwise location was kept constant as $z = 0.04$ m. The spanwise location of the velocity measurements was not reported.

4.1.3 Simulation Setup

The reference experiment reported an incomplete description of the initial conditions and as such any numerical simulation of the reference data set is a representation of the experimental conditions, at best. Figure 4.1b shows the low-level inlet boundary layer fluctuation profile, denoted in the simulations as -L. The specified inlet fluctuation levels are imposed onto a Blasius type mean streamwise velocity profile, shown in Figure 4.1a, at the trailing edge of the splitter plate. Similar profiles are imposed in the low-speed stream. Table 4.3 shows a complete overview of the presented simulations.

Station	Streamwise location (m)
MS1	0.07
MS2	0.11
MS3	0.15
MSA	0.12
MSB	0.18

Table 4.2: Measurement stations.

The outflow conditions is a standard advective condition which ensures global mass conservation in the computational domain. The upper and lower guide walls of the domain are modelled as free-slip boundaries, and the lower guide wall is angled to minimise any pressure gradient present inside the computational domain. The simulation time step is kept constant at $\Delta t = 5 \times 10^{-6}$ s producing a CFL number which remains below 0.35 throughout the entire computation. After the simulations have a statistically stationary state, statistical samples are accumulated over a period equating to 18 convective flow-through times, based on the convection velocity, $U_c = 0.5(U_1 + U_2)$. Cross-plane $y - z$ data is recorded at three measurement locations, and velocity data was reported by the reference experiment at two streamwise locations. Measurement stations 1 to 3 denote data computed from $y - z$ cross-planes while data at measurement stations A and B is computed from spanwise averaged data. Spanwise averaged data is computed from 168 individual spanwise measurements. Table 4.2 lists all measurement stations. At least 1500 samples are ensemble averaged to produce the presented scalar statistics and probability density functions. Passive scalar is given a value of unity in the low-speed stream and zero in high-speed stream, mimicking the O_3 concentration in the experiment. The Schmidt number is chosen as $Sc = 0.7$, and the viscosity is specified as $\nu = 1.8 \times 10^{-5}$.

Statistics are normalised by the similarity variables, $\eta = (x - x_0)/(y - y_{uc})$ for mean flow data and $\eta' = (x - x_0)/(y - y_{\bar{\xi}=0.5})$ for passive scalar data. x_0 is the streamwise location of the virtual origin, found by overlaying a large number of instantaneous passive scalar $x - y$ plots and tracing the outlines of passive scalar lines of $\bar{\xi} = 0.01$ and $\bar{\xi} = 0.99$. The resulting intersection produces the streamwise coordinate, x_0 . y_{uc} is the vertical location at which the local streamwise velocity, u , is equal to the centreline streamwise velocity, $\bar{u}_{uc} = 0.5(U_1 - U_2)$.

Case	Inlet type	High-speed fluctuations	Low-speed fluctuations
MAS-WN-L	WN	Fig. 4.1b	Fig. 4.1b
MAS-RRM-L	RRM	Fig. 4.1b	Fig. 4.1b

Table 4.3: Simulation cases overview.

4.1.3.1 Idealised Simulations (WN)

The computational domain extends from the trailing edge of the splitter plate to the advective outflow boundary. No solid geometry is included inside the domain. In the idealised simulations, pseudo-random, white noise fluctuations are imposed on a mean inflow velocity profile. The resulting inlet fluctuations are temporally and spatially uncorrelated.

4.1.3.2 Correlated Inflow Simulations (RRM)

The correlated inflow simulations use two virtual domains placed upstream of the main computational domain to produce temporally and spatially correlated inlet fluctuations. For both inlet streams, the virtual domains extend 0.026m upstream of the trailing edge of the splitter plate. The recycling plane at which information about the flow is extracted to be recycled, is located $10\theta_i$ upstream of the splitter plate trailing edge, where θ_i is the high speed inlet boundary layer momentum thickness, $\theta_i = 0.24\text{mm}$. Rescaling of the flow inside the virtual domain is done at an interval of every 50 iterations. The splitter plate is modelled as a solid boundary layer with infinitesimal thickness. The virtual domains contain $256 \times 128 \times 152$ cells and the grid spacing matches that of the main computational domain near the trailing edge of the splitter plate. For a detailed description of the RRM method, see Xiao *et al.* [37].

4.1.4 Results

4.1.4.1 Mean Flow Statistics

Figure 4.2 shows the spanwise-averaged normalised streamwise velocity. MAS-WN-L and MAS-RRM-L show good agreement with the reference experimental data at measurement stations A, 3 and C and both simulations show self-similarity.

The mean streamwise velocity fluctuation data are shown in Figure 4.3. In the presented figures, the variation bars are a measure of spanwise variation in terms of the standard deviation. They do not represent measurement errors. The predicted peak mean streamwise velocity fluctuation magnitudes are shown in Figure 4.3. Both simulations over-predict the peak fluctuation magnitude in the core of the mixing layer and under-predict it in the free-streams. It has to be noted that the reference experiment quoted a free-stream turbulence level of $\approx 0.5\%$, but the reported values are $\approx 5\%$. Due to the small vertical test section extent, it is likely that the top and bottom walls had an effect on the mixing layer [87]. The MAS-RRM-L simulation shows a very large spanwise variation compared to MAS-WN-L. When the spanwise variation is taken into account, the MAS-RRM-L matches the reference data well. The cause of this spanwise variation is discussed in detail in Section 4.1.4.4.

The growth rate of the mixing layer in the reference experiment was reported in terms of the local vorticity thickness. The vorticity thickness is defined in Equation 2.2. Table 4.4 lists the vorticity thickness growth rate and the vorticity growth rate constant, k_o (Equation 2.7) for the reference study and the simulations. The vorticity thickness is obtained by following the procedure of the reference study. The vorticity growth rate is over-predicted by 23% and 14% compared to the experimental value for MAS-RRM-L and MAS-WN-L, respectively.

4.1.4.2 Frequency Spectra

Spectral plots of the streamwise velocity fluctuations in the plane of the splitter plate at measurement station MSB are shown in Figure 4.4. The presented spectral plots

Case	R	\mathbf{k}_o	$d\delta_\omega/d\mathbf{x}$
Masutani & Bowman	0.333	0.211	0.0706
MAS-RRM-L	0.333	0.250	0.0860
MAS-WN-L	0.333	0.240	0.0832

Table 4.4: Experimental and simulation vorticity growth rates and growth constants.

have been computed from 120000 data points, taken at a frequency of 200kHz. For clarity, the power spectra have been shifted in the vertical axis. Both simulations show a straight roll-off with no spectral peak. All plots follow the decay law, k^n , with $n = -3$, indicative of a laminar mixing layer [59]. Similar observations were made in the power spectra obtained in the centre of the mixing layer of the reference experiment at the same streamwise location.

4.1.4.3 Flow Visualisation

Instantaneous, single plane and spanwise averaged passive scalar measurements are used to produce flow visualisations of the mixing layer. Data is sampled at a rate of 2kHz.

Typical single plane and spanwise averaged instantaneous passive scalar contour plots for MAS-RRM-L are shown in Figure 4.5a and 4.5b, respectively. Individual structures cores separated by braid regions are easily identifiable in the single plane and spanwise averaged plots. Similar flow visualisations for MAS-WN-L are shown in Figure 4.6. Unlike the recycling-rescaling simulation, structures become indiscernible downstream of $x \approx 0.1\text{m}$.

4.1.4.4 Streamwise Vortex Structure

Cross-plane plots of the mean streamwise velocity for MAS-RRM-L are shown in Figure 4.7. The presented cross-plane mean data is computed from a minimum of 1500 individual $y - z$ planes recorded at a frequency of 2.0kHz. At measurement station 2, shown in Figure 4.7a, strong wrinkling of the mean streamwise velocity contour

lines is visible. This wrinkling persists to the most downstream measurement station 3, shown in Figure 4.7. Wrinkling of the streamwise momentum field, such as the one observed in MAS-RRM-L is caused by spatially stationary, streamwise oriented vortex structures [88]. Increasing the number of samples causes the undulations to become ‘clearer’, which is an indication of the spatially stationary nature of the streamwise oriented vortices. At multiple spanwise locations, individual undulations can be traced between the two measurement stations. An example of this is the upwards wrinkling of the lower edge of the mixing layer at $z = 0.054\text{m}$ which can be identified in both plots. Figure 4.8 shows the mean streamwise velocity field for MAS-WN-L. No wrinkling of the mean streamwise velocity field is evident. The mean streamwise velocity field is devoid of any undulations and is largely statistically two-dimensional.

Quantitative data of spatially, stationary streamwise oriented vortex structures have been obtained in experiments through the interrogation of mean secondary shear stress, $\langle u'w' \rangle_t$. The mean secondary shear stress data is normalised by the square of the high-speed inlet velocity, U_1^2 .

Cross-plane maps of the mean secondary shear stress for MAS-RRM-L at measurement stations 2 and 3 are shown in Figure 4.9. At station 2 alternating sign clusters of positive and negative shear stress are present. Vertical stacking of differing sign clusters is also present. Further downstream at measurement station 3 the number of alternating sign clusters has decreased markedly. A three-tiered cluster, in which four positive clusters surround a central patch of negative shear stress, is visible at $z = 0.038\text{m}$. Individual clusters can easily be tracked between the measurement stations. Two examples of this are the positive clusters at $z = 0.042\text{m}$ and 0.052m . The peak shear stress magnitude decreases from measurement station 2 to 3. The observed clusters of mean secondary shear stress and their spatially stationary nature are evidence for the presence of a spatially stationary, streamwise oriented vortex structure in the MAS-RRM-L simulation. The observed clusters are qualitatively similar to comparable cross-planes obtained in experiments Bell *et al.* [88].

The mean secondary shear stress cross-plane data for MAS-WN-L shown in Figure 4.10 is markedly different. No clustering is visible at either measurement station at the shear stress of a random appearance. Unlike in the recycling-rescaling sim-

ulation, there is no evidence of a spatially stationary streamwise vortex structure. Similar observations have been made in comparable numerical simulations [21].

The mean streamwise vorticity is computed from

$$\Omega_x = \frac{\partial \langle w \rangle_t}{\partial y} - \frac{\partial \langle v \rangle_t}{\partial z} \quad (4.1)$$

where $\langle v \rangle_t$ and $\langle w \rangle_t$ are the mean vertical and spanwise velocities, respectively. The presented streamwise vorticity data have been partially normalised by U_1 , as an appropriate normalising lengthscale is not known [47].

A comparison of mean secondary shear stress and mean streamwise vorticity for MAS-RRM-L at MS3 is shown in Figure 4.11. When individual clusters of mean secondary shear stress and mean streamwise vorticity are compared, an anti-correlation becomes apparent. An anti-correlation between the mean secondary shear stress and mean streamwise vorticity has been observed by Wiecek *et al.* [55] while Bell & Mehta [88] observed a one-to-one correlation.

A quantitative measure of the wrinkling of the mixing layer is obtained by plotting the mixing layer centreline as a function of downstream distance from the splitter plate. The centreline of the mixing layer, y_0 , is defined as the vertical location at which the mean streamwise velocity is equal to the convection velocity U_c , $\langle u \rangle_t = U_c$. The mixing layer centreline at measurement stations 2 and 3 for MAS-RRM-L is shown in Figure 4.12a. An easily discernible pattern of peaks and troughs is apparent at both measurement stations. Individual maxima and minima can be traced between the two measurement stations. In experiments, peaks and troughs of the mixing layer centreline have indicated the presence of a pair of spatially stationary streamwise vortices with a common upflow and downflow, respectively [88]. The shift of the centreline towards the low-speed side of the mixing layer is in agreement with experimental observations [88].

The centrelines for MAS-WN-L at measurement station 2 and 3 are shown in Figure 4.12b. At MS2 small scale undulations are visible. Further downstream the amplitude of the undulations increases but no regular spanwise wavelength is apparent.

Case	Re_δ	λ_D (mm)	Δ_{ave} (mm)
MAS-RRM-L	4327	0.522	0.120
MAS-WN-L	3920	0.510	0.116

Table 4.5: Smallest length scale significant to passive scalar mixing, λ_D , and smallest resolved passive scalar length scale inside the mixing layer, Δ_{ave} , at measurement station 3.

At both measurement stations, the amplitudes of the undulations are significantly lower for MAS-WN-L than MAS-RRM-L.

4.1.4.5 Passive Scalar Mixing

The velocity statistics suggest that spatially and temporally correlated inlet fluctuations lead to the development of a spatially stationary, streamwise vortex structure. In this section, the effects of the spatially stationary streamwise structure on the passive scalar field are studied. Table 4.5 shows the local Reynolds number based on the visual thickness, $Re_{\delta_{vis}}$, smallest length scale significant to passive scalar mixing, λ_D , and the smallest resolved scalar based on the average spacing of the mesh inside the mixing layer, Δ_{ave} . The smallest length scale significant to passive scalar mixing is given by,

$$\lambda_D = 11.2\delta_{vis}Re_{\delta_{vis}}^{-3/4}Sc^{-1/2} \quad (4.2)$$

The average mesh spacing, is a factor of 4 smaller than the smallest scale significant to passive scalar mixing, indicating that passive scalar mixing is resolved completely.

To visualise the passive scalar entrainment and mixing during a primary structure passage, time series of three instantaneous passive scalar concentration cross-planes at measurement station 2 are presented. A primary structure passage for MAS-RRM-L is shown in Figure 4.13. Figure 4.13a shows the braid, leading the investigated primary structure. The mixing layer is consists of a single interface zone separating the free-streams. Undulations caused by spatially stationary streamwise vortex struc-

tures are visible throughout the entire spanwise extent of the interface zone. The second plot in the series, shown in Figure 4.13b, is taken in the core of the primary structure. Two interface zones separate the core of the structure which is comprised of mixed fluid. At $z \approx 0.032\text{m}$ a patch of unmixed high-speed fluid near the low-speed interface zone is visible. This patch of unmixed high-speed fluid has most likely been engulfed rapidly by the mixing layer, as suggested by the Dimotakis engulfment entrainment mechanism. The cross-plane of the trailing braid region is shown in Figure 4.13c. The mixing layer has returned to a single interface zone. Individual undulations can easily be traced through the time series, evidencing the spatially stationary nature of the secondary, streamwise oriented vortex structures.

Flow visualisations of typical primary structure passage for MAS-WN-L are shown in Figure 4.14. The qualitative differences between the recycling-rescaling and white noise based simulations are immediately evident. Single and dual interface zones are evident in all time instances. A lack of a spatially stationary streamwise vortex structure leads to a lack of undulations that are observed in MAS-RRM-L. Unlike the physically correlated simulation, it is not possible to trace individual undulations from one image to the next.

Spanwise averaged mean passive scalar data at measurement station 2 for MAS-RRM-L are shown in Figure 4.15a. The variation bars are the *r.m.s.* value of the spanwise variation of the mean passive scalar measurement. MAS-RRM-L reproduces the passive scalar measurements in both the high- and low-speed sides of the mixing layer well. The spanwise variation observed in MAS-RRM-L, permits the experimental profile to be closely replicated at particular spanwise planes. Figure 4.15b shows the spanwise averaged mean passive scalar data for MAS-WN-L. The passive scalar concentration is over-predicted in the low-speed and under-predicted in the high-speed sides of the mixing layer. The lack of a secondary, spatially stationary streamwise vortex structure produces no significant spanwise variation, resulting in very small variation bars. Overall agreement of the spanwise averaged passive scalar concentration for MAS-WN-L is worse than for MAS-RRM-L.

Figure 4.16 shows the spanwise averaged mean passive scalar fluctuations at measurement station 2. The passive scalar fluctuation magnitude is an indication of the degree of homogeneity of the flow. If for the duration of the statistical sampling,

a location in the mixing layer only observes homogeneous fluid, then $\bar{\xi}_{r.m.s.} = 0.0$ [59]. Conversely, for a mixing layer location that measures only immiscible fluid, $\bar{\xi}_{r.m.s.} = 0.5$ [59]. Both simulations reproduce the ‘bi-modal’ shape that has been observed in studies of the low and high Reynolds number mixing layer [50, 62, 59]. From the large spanwise variation in MAS-RRM-L, it can be seen that the spatially stationary streamwise vortex structure has a measurable effect on the mean passive scalar fluctuations.

The time-averaged fractional volume of entrained low-speed volume, V_l , can be calculated from

$$V_l = \frac{1}{|\delta_h - \delta_l|} \int_{\delta_l}^{\delta_h} \bar{\xi}(\eta') d\eta' \quad (4.3)$$

where, δ_h and δ_l , are the upper and lower extends of the time averaged mixing layer; e.g. the vertical location where $\bar{\xi} = 0.01$ and 0.99 , respectively [59]. Alternatively, the time-averaged fractional flux of low-speed fluid is given by

$$M_l = \frac{\int_{\delta_l}^{\delta_h} \overline{\xi(\eta') u(\eta')} d\eta'}{\int_{\delta_l}^{\delta_h} \overline{u(\eta')} d\eta'} \quad (4.4)$$

where M_l is the average fraction of the total flow crossing a plane normal to the streamwise axis that originated from the low-speed stream. Using Equation 4.4, a composition ratio, E_c can be calculated by

$$E_c = \frac{V_h}{V_l} = \frac{\text{average volume of high-speed fluid}}{\text{average volume of low-speed fluid}} \quad (4.5)$$

and corresponding entrainment ratio

$$E_v = \frac{M_h}{M_l} = \frac{\text{average fractional flow rate of high-speed fluid}}{\text{average fractional flow rate of low-speed fluid}} \quad (4.6)$$

Figure 4.17 shows the entrainment ratio as a function of spanwise location at measurement station 2. A strong anti-correlation between the centreline and the entrainment ratio is evident in the MAS-RRM-L data, shown in Figure 4.17a. When the plots are compared to the mean secondary shear stress plot at MS2, shown in Figure 4.9a, it can be seen how a local entrainment minimum is the product of an interface between a pair of spatially stationary streamwise vortices with a common upflow. A local entrainment maximum is produced by an interface between a pair of streamwise vortices with a common downflow. This illustrates the importance of the spatially stationary streamwise vortex structure in the entrainment of the passive scalar in the presented simulations. A peak in the entrainment ratio is representative of an area where more high speed, high concentration fluid is entrained which produces a centreline trough. This anti-correlation also visualises the coupling between the momentum and passive scalar fields reported in experiments [59].

The entrainment ratio and centreline data for MAS-WN-L are shown in Figure 4.17. The axis scales have been kept constant to visualise the stark contrast in the magnitudes of the undulations observed in the two simulations. While the centreline and entrainment ratios do show some undulations, they are of a low magnitude, and no spanwise wavelength is evident. No anti-correlation between the mean entrainment ratio and the centreline is seen.

Table 4.6 compares the minimum, maximum and spanwise averaged entrainment ratio values for MAS-RRM-L and MAS-WN-L together with the value reported by the reference experiment. It was not reported if the experimental value was based on a single spanwise measurement station or was the product of the averaging of multiple spanwise locations, but it can be assumed that this value is based on a single spanwise location. The experimental value of $E_v = 1.36$ is about 10% higher than predicted by the Dimotakis entrainment model, Equation 2.10. However, experiments of liquid mixing layers by Koochesfahani & Dimotakis [89, 90] have shown the entrainment ratio in the pre- and transition region of the mixing layer to be higher than predicted by the Dimotakis model which is based on post-transition data by Konrad [50].

The spanwise averaged value of the entrainment ratio is identical in both simulations. However, the large undulations of the entrainment ratio and centreline in Fig-

Case	$E_{v,\min}$	$E_{v,\max}$	$\langle E_v \rangle_z$
Masutani & Bowman	-	-	1.36
MAS-RRM-L	0.92	1.46	1.22
MAS-WN-L	1.08	1.33	1.22

Table 4.6: Minimum, maximum and spanwise averaged values for the entrainment ratio at measurement station 3.

ure 4.17a are reflected in a much larger range of entrainment ratio values. Depending on the spanwise location of the measurement, the reference entrainment ratio value can be obtained in both simulations. It is reasonable to assume the experiment to have been host to similar spatially stationary streamwise vortex structures observed in MAS-RRM-L and therefore to have been susceptible to similar spanwise variations.

The entrainment ratio provides information about the volume ratio of high- to low-speed free stream fluid. However, in many practical engineering applications more detailed knowledge about the preferred concentration in the mixing layer is required. This is particularly true for diffusion controlled combustion processes. Probability density functions plots (p.d.f.'s) give an indication of the preferred concentration as well as the probability of finding fluid at a certain concentration at any vertical location in the mixing layer. The different types of p.d.f.'s are reviewed in Section 2. In the pre-transition mixing layer, experiments have reported p.d.f.'s of the *non-marching* type [59, 90]. The presented p.d.f.'s have been computed from a minimum of 1600 individual cross-planes, sampled at a frequency of 2.0kHz.

The presented p.d.f.'s are computed in the usual manner [60, 90]. The probability density function of the passives scalar fraction, $\bar{\xi}$, at any given vertical location, y , is denoted by $p(\xi, y)$. Normalisation of the p.d.f. requires that

$$\int_0^1 p(\xi, y) d\xi = 1. \quad (4.7)$$

The average concentration of high-speed fluid, $\bar{\xi}$, is therefore given by

$$\bar{\xi}(y) = \int_0^1 \bar{\xi} p(\xi, y) d\xi. \quad (4.8)$$

The probabilities of finding unmixed fluid from the low-speed, P_l , and high-speed, P_h , are given by

$$P_l(y) = \int_0^\delta p(\xi, y) d\xi \quad (4.9)$$

$$P_h(y) = \int_{1-\delta}^1 p(\xi, y) d\xi \quad (4.10)$$

where δ is the binning width of the passive scalar data.

The integrated area in the mixed fluid p.d.f. gives the total probability of finding mixed fluid at any concentration and is given by

$$P_m(y) = \int_\delta^{1-\delta} p(\xi, y) d\xi. \quad (4.11)$$

For the reported p.d.f.s the passive scalar range between $0 \leq \bar{\xi} \leq 1$, is divided into 40 levels resulting in a delta value of $\delta = 0.025$. The reference study reported p.d.f.'s of the *non-marching* type with a preferred concentration of $\bar{\xi} \approx 0.27$ at measurement station 3. The reference measurements were taken at an unspecified spanwise location. For each simulation p.d.f.'s at two spanwise locations are presented. The spanwise locations have been chosen to show p.d.f.'s at an entrainment maximum and minimum, respectively.

Figure 4.18 shows the p.d.f.'s for MAS-RRM-L at measurement station 3. The shown p.d.f.'s are of the *non-marching* and *hybrid* type. In Figure 4.18a, the preferred concentration value of $\bar{\xi} \approx 0.33$ is close the experimental value of $\bar{\xi} \approx 0.27$. The very high value of the probability density at the peak and its isolation are suggestive of the presence of a strong pair of spatially stationary vortex structures with a common downflow that continuously entrain high-speed fluid into the core of the mixing layer.

The p.d.f. in Figure 4.18b, shows an elevated value of the probability density for the

high-speed fluid but no preferred concentration. Taken at a local entrainment minimum, the spanwise location for this p.d.f. is located between a pair of streamwise vortices with a common upflow. The increase in the entrainment of low-speed fluid by the spatially stationary streamwise vortices with a common upflow, dilutes the preferred concentration value, resulting in a *hybrid* p.d.f.

Figure 4.19 shows the p.d.f.'s for MAS-WN-L at measurement station 3. Both p.d.f.'s are of the *hybrid* with a plateau of slightly elevated probability density values in the high-speed side of the mixing layer. Due to the lack of a spatially stationary, streamwise vortex structure, the produced p.d.f.'s in the WN simulation are always of the *hybrid* type, regardless of spanwise location. This is reflective of the statistically two-dimensional entrainment ratio plot in Figure 4.17b.

4.1.5 Summary

A simulation originating from idealised, white noise inlet conditions, and a simulation utilising spatially- and temporally-correlated inlet fluctuations, have been compared to a reference data set of a low Reynolds number mixing layer by Masutani *et al.* [59].

Simulations based on white noise (WN) type inlet conditions are shown to be largely statistically two-dimensional with little variation of the momentum and passive scalar field across the spanwise domain extent. The recycling-rescaling simulation (RRM) uses correlated inlet fluctuations and produces spatially stationary streamwise vortex structures. These structures have strong effects on the momentum and passive scalar field in the mixing layer. The local entrainment ratio value is found to be strongly linked to the geometry of the secondary, spatially stationary streamwise vortex structures. The interface between a pair of streamwise vortices with a common downflow produces a local entrainment maximum while a pair of streamwise vortices with a common upflow produces a local entrainment minimum. Overall agreement with reference data is better in RRM, particularly for the probability density functions. The RRM simulation produces *non-marching* probability density functions, in agreement with the reference data, while the idealised simulation produces

hybrid probability density functions.

The presented results show a very large spanwise dependency of the mixing layer in the presence of spatially stationary streamwise vortex structures. This spanwise dependence has to be accounted for in measurements taken in experimental studies. The data also indicates that correlated inlet fluctuations are required for the accurate simulation of a spatially developing low Reynolds number mixing layer. Without a secondary, spatially stationary vortex structure the mixing layer dynamics are not reproduced adequately.

4.2 High Reynolds Number Mixing Layer

4.2.1 Introduction

The previous section has investigated the effects of the nature of the imposed inlet fluctuations on a low Reynolds number mixing layer. While low Reynolds number mixing layers are an interesting test case, they are not commonly found in engineering applications. The high Reynolds number mixing layer has been an area of active research for more than half a century, yet a large spread in the reported growth rates remains [92]. Two- and three-dimensional numerical simulations have had difficulties matching experimental data, particularly passive scalar measurements [93].

Within the modelling of a high Reynolds number mixing layer lie a number of challenges, one of which is the simulation of the large, spanwise coherent structures that have been observed in experimental studies [9, 49]. The reproduction of the behaviour of the large scale structures is crucial as they have been shown to be driving mixing layer entrainment and growth. However, the mechanism with which the high Reynolds number mixing layer entrains fluid remains a topic of debate [10, 11, 56].

Another challenge is the simulation of the secondary, spatially stationary streamwise oriented structures developing from upstream streamwise vorticity present in laminar inlet conditions that have been observed in high Reynolds number mixing layers [47, 50]. In Section 4.1, spatially and temporally correlated inlet fluctuations have

produced these secondary, spatially stationary streamwise vortex structures. One of the aims of this section is to investigate if the streamwise structures are present in simulations of the high Reynolds number mixing layer based on spatially and temporally correlated inlet fluctuations and if they persist through the mixing transition.

As in the previous section, particular attention will be paid to the investigation of passive scalar entrainment and mixing. Experimental studies of the high Reynolds number mixing layer have reported probability density functions (p.d.f.'s) in the post-transition region of the *non-marching* type [50, 90]. However, *hybrid* [94, 60] and *marching* [62] type p.d.f.'s have also been reported. These differing p.d.f.'s have been attributed to a number of mixing layer properties such as the local Reynolds number or the pairing parameter [60]. A dependence on the initial conditions has also been proposed [60, 63].

Due to the lower computational cost compared to DNS, large eddy simulations offer the optimal tool to investigate the dependence of the mixing layer, and in particular the passive scalar entrainment and mixing, to mixing layer properties. This chapter will focus on the investigation of the effects of the nature of the inflow conditions. For this, physically correlated and white noise type simulations will be compared and validated against an experimental dataset by Browand & Latigo [45].

4.2.2 Reference Experiment

The reference wind tunnel was driven by a blower, located 7m upstream of the splitter plate, trailing edge. A 3×3 m settling chamber was divided into two equal parts by a 10cm splitter plate. The splitter plate extended through the contraction section with an angle of two degrees. The trailing edge of the splitter plate extended 46cm into the test section with an edge thickness of 0.5mm. The test section was 120cm long, 91.4cm wide and 61cm high.

The free stream velocity of the high-speed inlet, U_1 was typically 25m/s with a free stream streamwise velocity fluctuation magnitude, $u'/\Delta U$, of less than 0.1%. The lower inlet velocity was reported as 5.2m/s. The inlet velocities of the reference experiment result in a velocity ratio of $R = 0.66$ at the trailing edge of the splitter plate.

U_1 (m/s)	U_2 (m/s)	θ_1 (mm)	θ_2 (mm)	R
25.5	5.2	0.457	0.86	0.66

Table 4.7: Summary of flow properties for reference dataset by Browand & Latigo [45].

The momentum thickness was 0.457mm for the high-speed side and 0.81mm for the low-speed side. The initial momentum thickness of the mixing layer, θ_i , was shown to be similar to the momentum thickness of the high-speed boundary layer, θ_1 , in the experiment. The maximum velocity fluctuation magnitudes in the inlet boundary layer were recorded as 2.5% and 2.0% of the high- and low-speed free stream velocities, respectively. Noise introduced during the recording process lead to an 1% measurement error of the fluctuation magnitudes in the experiment. A summary of flow properties is given in Table 4.7.

4.2.3 Simulation Setup

The time step is chosen as $\Delta t = 6 \times 10^{-7}$ s and is identical in both simulations. Statistical data is accumulated at every time step, while cross-planes, spanwise averaged and single plane flow visualisations are acquired every 500 time steps. The CFL number is kept below 0.35 for the entire duration of the simulation. The presented mean flow data has been computed from a minimum of 1000000 iterations, equating to approximately 15 flow through times based on the convective velocity, $U_c = 0.5(U_1 + U_2)$ where U_1 and U_2 are the high- and low-speed inlet velocities, respectively. Data produced from $y-z$ cross-planes has been computed from a minimum of 1200 individual cross-planes. The Schmidt and viscosity are chosen as $Sc = 0.7$ and $\nu = 1.8 \times 10^{-5}$, respectively.

A total of 6 measurement stations have been chosen along the streamwise domain extent. Measurement stations 1 to 3 are located in the pre-transition region of the mixing layer and measurement station 4 is located approximately in the transition region. Measurement stations 5 and 6 are located in the far-field, self-similar region of the mixing layer. Table 4.8 lists the measurement stations in terms of streamwise distance from the splitter plate in metres, normalised by the high-speed inlet mo-

Station	x (m)	x/θ_i	x_i^*	$Re_{\delta_{vis}}$ (WN)	$Re_{\delta_{vis}}$ (RRM)
MS1	0.0180	40	0.88	13488	7342
MS2	0.0380	83	1.86	19455	15043
MS3	0.0690	151	3.37	28018	26326
MS4	0.1330	291	6.50	39596	51040
MS5	0.2695	590	13.17	87549	103693
MS6	0.5390	1180	26.35	166810	207028

Table 4.8: Measurement stations.

mentum thickness, pairing parameter, as well as the local Reynolds number based on the visual thickness, $Re_{\delta_{vis}}$.

The local pairing parameter, x_i^* [91], given by

$$x_i^* = \frac{Rx}{30\theta_i} \quad (4.12)$$

where R is the velocity ratio, and θ_i is the high-speed inlet momentum thickness. The first, second and third pairing events occur at values of $x_i^* = 4, 8,$ and $16,$ respectively [91].

4.2.3.1 Idealised Simulation (WN)

For the idealised, white-noise (WN) simulation, the mean streamwise velocity profile, shown in Figure 4.31a, are specified at the inlet plane of the computational domain. Pseudo-random velocity fluctuations, shown in Figure 4.31b, are superimposed onto the mean inflow velocity plane. Similar inlet conditions are specified for the low-speed inlet stream. This type of inlet condition results in temporally- and spatially-uncorrelated inlet fluctuations.

4.2.3.2 Recycling-Rescaling Simulation (RRM)

The recycling-rescaling (RRM) simulation uses two auxiliary domains placed upstream of the inlet plane to produce spatially and temporally correlated inlet fluctuations. The virtual domains extend a streamwise distance of $x/\theta_i = 333$ upstream

Case	Inlet type	u'_{\max}/U_1 (%)	v'_{\max}/U_1 (%)	w'_{\max}/U_1 (%)
BL-066-WN-L	WN	0.95	0.55	0.50
BL-066-RRM-L	RRM	0.95	0.55	0.50

Table 4.9: Simulation cases overview.

of the trailing edge of the splitter plate, where θ_i denotes the high-speed inlet momentum thickness. At a recycling plane, located $10\theta_i$ upstream of the main computational domain, the flow is extracted, rescaled and remapped to the inlet of the virtual domains as explained in detail in Section 3.4.2. At an interval of 50 iterations the flow inside the virtual domain is rescaled to match the desired fluctuation levels. The splitter plate separating the two virtual domains is modelled as a no-slip solid boundary of infinitesimal thickness.

4.2.4 Grid validation

The main computational domain is of dimensions $1630 \times 1326 \times 392\theta_i$ in the streamwise (x), vertical (y) and spanwise (z) directions, respectively. The vertical domain size has been chosen to match the experimental facility. The main computational domain commences at the trailing edge of the splitter plate and includes no splitter plate geometry. The main domain has been discretised into $768 \times 256 \times 256$ cells in the vertical, streamwise and spanwise directions respectively. An identical mesh resolution has been utilized in a comparable LES of the same reference experimental facility [21, 78, 95]. This grid will hereafter be referred to as GR1. The minimum grid spacing is $\Delta x_{\min}/\theta_i = 0.44$ and $\Delta y_{\min}/\theta_i = 0.086$ in the streamwise and vertical directions respectively. The grid has been stretched in the streamwise and vertical directions utilising a geometric expansion, while the spanwise nodes are distributed with a constant spacing. A total of 42 and 46 nodes lie within the high- and low-speed boundary layers, respectively.

To validate the computational grid, a low resolution simulation utilising a lower resolution grid (GR2) is compared with the preferred grid (GR1). The simulations use the WALE model with a model constant of $C_w = 0.56$. The inlet conditions are kept constant. Table 4.10 summarise the specifications for the main computational grid

Grid	N_x	N_y	N_z	$\Delta x_{\min}/\theta_i$	$\Delta y_{\min}/\theta_i$	$\Delta z_{\min}/\theta_i$
GR1	768	256	256	0.44	0.09	1.57
GR2	512	224	224	0.88	0.18	1.78

Table 4.10: Grid resolutions.

and the low resolution grid.

Figure 4.32 shows mean flow statistics differences between the two compared grids. The mean streamwise velocity at $x/\theta_i = 1000$ is shown in Figure 4.32a. Both simulations collapse onto a single line and agree well with the reference data, indicating self-similarity. The mean streamwise velocity fluctuations are shown in Figure 4.32b. The GR1 data captures the shape and peak value very well. The peak in the GR2 simulation is shifted towards the high-speed side of the mixing layer. Figure 4.32c shows the peak streamwise velocity fluctuation as a function of distance from the splitter plate. The peak magnitude and location is reproduced well in the GR1 simulation. The simulation utilising the GR2 grid over-predicts the peak streamwise velocity fluctuation.

The local momentum thickness graph is shown in Figure 4.33. Both simulations achieve self-similarity, characterised of a linear growth rate, at $x/\theta_i \approx 500$. The GR1 simulation is self-similar for the entire streamwise domain extent. The low resolution simulation starts to show a decrease in the growth rate at $x/\theta_i \approx 1000$.

Overall the GR1 mesh shows better agreement with the reference data, particularly for the growth of the mixing layer, and is therefore chosen for all subsequently presented simulations.

4.2.5 SGS Model Validation

To validate the choice of the subgrid-scale (SGS) model, five simulations are presented; two simulations utilise the Smagorinsky model with a model constant of $C_s = 0.10$ and $C_s = 0.18$, and two simulations employ the WALE model with model constants of $C_w = 0.30$ and $C_w = 0.56$. An overview of the naming convention for the model validation simulations is shown in Table 4.11. Instantaneous passive scalar

concentration with the ratio between the subgrid to molecular viscosity, μ_{sgs}/μ , as contour lines, are shown in Figure 4.34. In the initial region of the mixing layer, both Smagorinsky model constants predict non-zero values for the eddy viscosity, shown in Figure 4.34a and 4.34b as contour lines. An increase in the model constant from $C_s = 0.10$ to $C_s = 0.18$ increases the magnitude of the predicted eddy viscosity. Previous numerical studies have observed similar results for the Smagorinsky model [84]. The WALE model simulations, shown in Figure 4.34c and 4.34d, produce zero eddy viscosity in the initial region with the only viscosity produced being located inside the cores of the emerging vortex core, as desired.

The momentum thickness is a measure of the integral thickness of the mixing layer and is defined in Equation 2.3. Figure 4.35a shows the local momentum thickness from each simulation together with reference data. The reduction in growth rate observed near the end of the computational domain is commonly observed in numerical simulations [84, 96] and is a product of large scale structure leaving the computational domain. The momentum thickness appears to be largely insensitive to the choice of SGS model, and agreement with the reference data is generally good. Upstream of $x/\theta_i \approx 500$ the mixing layer development is delayed in the BL-066-WN-Cs018 simulation, resulting from the over-prediction of eddy viscosity in the near field of the mixing layer. In the self-similar region of the mixing layer the momentum growth rate is very similar between the simulations. Figure 4.35b shows the maximum streamwise velocity fluctuation as a function of downstream distance from the splitter plate trailing edge. All simulations produce an overshoot in the peak fluctuation magnitude which is located further downstream from the trailing edge of the splitter plate. This type of overshoot is commonly observed in numerical simulations based on white noise type inlet conditions [21, 78]. The delayed development observed for the momentum thickness in BL-066-WN-Cs018 is also evident here, where the peak is located much further downstream compared to the experiment and the other simulations. The asymptotic final state value of the maximum streamwise velocity fluctuation magnitude is in good agreement with the reference value for all simulations. Based on the presented results the WALE model with a model constant of $C_w = 0.56$ is chosen for the subsequently presented idealised and physically correlated simulations.

Name	Model	Model constant
BL-066-WN-Cs010	Smagorinsky	0.10
BL-066-WN-Cs018	Smagorinsky	0.18
BL-066-WN-Cw030	WALE	0.30
BL-066-WN-Cw056	WALE	0.56

Table 4.11: Model validation simulations.

4.2.6 Main Simulation Results

4.2.6.1 Mean Flow Statistics

Figure 4.36 shows the normalised momentum thickness growth for BL-066-WN-L and BL-066-RRM-L. The simulations show extremely good agreement with the reference data. Self-similarity is evident for both simulations.

In the self-similar region, the relationship between the momentum thickness and the velocity ratio is linear and given by Equation 2.6. The reference experiment reported a momentum growth rate of $k_m = 0.0357$ based on the velocity ratio, $R = 0.66$. For case BL-066-RRM-L, the momentum growth rate constant is predicted to be $k_m = 0.0364$, 1.9% higher than the experiment but in good agreement with the linear relationship. For BL-066-WN-L, $k_m = 0.0341$, which is 4.5% lower than the reported experimental value. A change in the nature of the inlet fluctuations changes the momentum growth rate constant by 7%.

The visual thickness of the mixing layer is computed by super-imposing a large number of instantaneous, spanwise averaged passive scalar contour plots. The outlines of the mixing layer are traced, resulting in the visual thickness of the mixing layer [9, 60]. The linear relationship for the visual thickness and velocity ratio is given in Equation 2.4. For BL-066-WN-L, $k_v = 0.318$ or $k_v \approx 1/\pi$ which is a relationship that has been observed in comparable numerical simulations based on idealised inlet conditions [18]. For BL-066-RRM-L, $k_v = 0.366$ which is higher than the idealised simulations but in good agreement with the comparable experimental data. The visual growth rate constant of the physically correlated simulation is 15% higher than that of the idealised simulation.

Mean velocity data have been normalised by the velocity difference across the mixing layer, $U_0 = U_1 - U_2$, in accordance with the reference experimental data [45]. Local velocity values are used due to the pressure gradient that is present in experiments and simulations of mixing layers with fixed horizontal guide walls.

The mean streamwise velocity profiles for BL-066-RRM-L and BL-066-WN-L at the streamwise location of $x/\theta_i = 1000$ are shown in Figure 4.37a. This streamwise location has been chosen to allow comparison with reference data. Both simulations show self-similar shapes, matching that of the reference experimental data well. The mean streamwise fluctuation magnitudes at $x/\theta_i = 1000$ shown in Figure 4.37b are in good agreement with the reference data. In both simulations the maximum fluctuation magnitude and shape at this streamwise location is captured very well.

Figure 4.38 shows the maximum streamwise velocity fluctuation as a function of the streamwise distance from the splitter plate trailing edge. While the maximum intensity of the reference experiment is matched well in the BL-066-RRM-L simulation, this maximum is located slightly closer to the splitter plate than the reference data. The BL-066-WN-L simulation over-predicts the maximum fluctuation magnitude slightly. In the self-similar region of the mixing layer, both simulations match the reference value well. Self-similarity is attained at approximately $x/\theta_i \approx 450$ in both simulations which is in good agreement with the $x/\theta_i \approx 1000$ criteria that have been suggested in experimental studies [75].

Streamwise velocity fluctuation spectral plots taken along the mixing layer centreline are shown in Figure 4.39. Linear stability theory predicts the most amplified disturbance in a two-stream mixing layer to be given by

$$St \approx \frac{f\delta_\omega}{4(U_1 - U_2)} \approx \frac{0.017}{R} \quad (4.13)$$

where f is the frequency, δ_ω is the local vorticity thickness, and R , the velocity ratio [97]. For the presented simulations this results in a Strouhal number of $St \approx 0.0258$. At $x/\theta_i = 44$ peaks in the power spectral density are observed in both simulations. BL-066-RRM-L predicts a peak Strouhal number of $St \approx 0.0248$ which is in good agreement with the value predicted by Equation 4.13. The peak Strouhal number for

BL-066-WN-L is $St \approx 0.0187$ which is lower than calculated by Equation 4.13. At the downstream measurement stations the power spectra approaches the $k^{-5/3}$ slope, indicative of fully developed turbulent flow [21].

4.2.7 Flow Visualisation

Up to 2000 individual single plane and spanwise averaged flow visualisation images, sampled at 3.33 kHz, are recorded from both simulations. The sampling frequency results from the time step of the simulation and a chosen output frequency. The entrainment and mixing of the passive scalar allows the visualisation of the primary, spanwise oriented structures. This approach is based on similar passive scalar measurements performed in experimental studies [59]. After an initial wash-out, spanwise averaged data is computed from 256 individual nodal values, spaced uniformly in the spanwise direction. Ensemble average data is computed at every time step.

Figure 4.40a shows an instantaneous passive scalar contour plot taken at the midspan of the domain in BL-066-RRM-L. Near the splitter plate, a vortex sheet is visible. After the roll-up, which occurs at $x_i^* \approx 2$ or $x/\theta_i \approx 90$, large scale, spanwise vortices occupy the entire vertical extent of the mixing layer. As the vortices convect downstream they increase in size thereby increasing the mixing layer thickness. Structure interactions are seen to be of the pairing type as observed in experiments by Winant & Browand [49]. The vortices persist through the mixing transition into the self-similar far field of the mixing layer. Throughout the entire streamwise extent structures show a high degree of circularity. Examples of this are visible at $x/\theta_i \approx 600$ and 900. A spanwise averaged passive scalar contour plot taken at the same time instant is shown in Figure 4.40b. The structures that have been identified in the single plane contour plot are easily recognisable in the spanwise averaged contour plot as well. The qualitative similarity between the single plane and the spanwise averaged flow visualisations suggests that the vortex structures are quasi-two-dimensional.

Similar flow visualisations for BL-066-WN-L are shown in Figure 4.41. In the single plane flow visualisation, Figure 4.41a, some large scale structures are identifiable at $x/\theta_i \approx 950$ and 1400. However, identifying the individual structures is subjectively harder than in BL-066-RRM-L. The process of spanwise averaging, shown in Figure

4.41b, leaves only two large scale structures, at $x/\theta_i = 950$ and 1400, identifiable. In the pre-transition region no individual structures are easily discernible.

Cross-plane ($y - z$) data, sampled at a frequency of 3.3 kHz are used to compute pseudo-three-dimensional perspective views. The iso-surfaces at $\bar{\xi} = 0.99$ and $\bar{\xi} = 0.01$ define the upper and lower boundaries of the mixing layer, respectively. The grey scale colouring is based on the streamwise velocity where white and black colours indicate streamwise velocity values that are higher and lower than the high-speed free stream velocity, respectively. Local streamwise velocity over-speeds indicate the presence of concentrated spanwise vorticity inside the vortex core [21].

Perspective views for BL-066-RRM-L at measurement station 4 are shown in Figure 4.42a. The structures passing through the measurement plane that are not undergoing any type of interaction are of a quasi-two-dimensional appearance. Small scale undulations ‘riding’ on the high-speed interface zones are visible. The perspective view of BL-066-WN-L at measurement station 4 is shown in Figure 4.42b. Undulations on the high-speed interface are present but there appears to be no temporal correlation, meaning it is not possible to track individual undulations between passing structures. Branches between the primary vortices and localised pairings are visible, and the mixing layer appears less quasi-two-dimensional than BL-066-RRM-L.

Perspective views at measurement station 5 are shown in Figure 4.43. Measurement station 5 is located in the self-similar, far-field region of the mixing layer, and the local Reynolds number is above the $Re \approx 10^4$ criterion for fully developed, post-transitional flow that has been stipulated by experimental research [8]. Figure 4.43a shows that even in the fully developed region of the mixing layer, the flow field in BL-066-RRM-L is dominated by large scale, spanwise coherent vortices of a quasi-two-dimensional appearance. The perspective view for BL-066-WN-L at measurement station 5, shown in Figure 4.43b, is qualitatively similar to that observed at measurement station 4. Some large scale structures show branching type structures that connect passing structures. Branching between primary vortices indicates that localised pairings are taking place [21]. This type of structure branching has been observed in experimental studies [44] as well as numerical simulations which utilised comparable, idealised inlet conditions [18, 21].

Figure 4.44 shows the vertical diameter of individually tracked structures. The vertical size of a structure is defined by the $\bar{\xi} = 0.01$ and 0.99 contour lines. This approach has previously been used in experimental [11] and numerical studies [18]. The difference in the primary structure observed in the perspective views is also evident in the structure growth tracks. Figure 4.44a shows individual structure tracks for BL-066-RRM-L. The growth of the primary vortices is best approximated by what has been termed ‘square root of time growth’ by McMullan & Garrett [21]. In experiments, square root of time growth has been observed in vortical structures growing continuously through irrotational roll-up [98] and turbulent diffusion [99]. Square root of time growth has also been reported in recent RRM-type numerical simulations by McMullan & Garrett [21]. Figure 4.44b shows the growth of the primary vortices in BL-066-WN-L. The growth is best approximated as linear growth as observed by D’Ovidio & Coats [11] in experiments and by McMullan *et al.* [78] in LES based on white noise type inlet conditions. Primary structure growth is discussed in more detail in Chapter 6.

4.2.7.1 Streamwise Structure

The primary structures present in the two types of simulation have been shown to have different internal geometries. The simulation utilising spatially- and temporally-correlated inlet fluctuations produces large scale structures with a high degree of spanwise coherence, resulting in a quasi-two-dimensional flow field and structures that grow as the square root of time. In the perspective views small scale undulations are seen to be located on top of the primary structures. Previous experimental [55, 47] and numerical [21] have shown these undulations to be a result of spatially stationary vortex structures. The structures in the idealised simulation, in contrast, show little spanwise regularity and branching between neighbouring structures is observed. In this section cross-plane data are used to investigate the origin and effect of the spatially stationary streamwise structures.

Figure 4.45 shows the mean streamwise velocity and mean streamwise vorticity $y-z$ cross-planes for BL-066-RRM-L at measurement station 2. A local pairing parameter of $x_i^* \approx 1.86$ indicates that MS2 lies in the region of the first roll up. Any streamwise vorticity present therefore originates in the upstream boundary layers [21]. The

mean streamwise velocity field, shown in Figure 4.45a, shows wrinkling which is particularly evident in the low-speed interface zone. The corresponding mean streamwise vorticity map, shown in Figure 4.45b, shows multiple clusters of three tiered vorticity patches with opposing signs. This type of clustering has been observed in experiments and is referred to as vorticity ‘quadrupoles’ or ‘three-tiered clustering’ [88]. The spanwise location of $z/\theta_i = 45$ lies between two patches of negative and positive vorticity, indicating a common downflow which produces a trough in the mean streamwise velocity lines in Figure 4.45a at the same spanwise location. At $z/\theta_i = 55$, a common upflow is observed which wrinkles the low-speed interface zone heavily towards the centre of the mixing layer. The effect of the present vorticity appears to be weaker in the high-speed interface zone, which could be a result of the balance of the momentum of the streamwise structures compared to the momentum contained in the free stream fluid.

The mean streamwise velocity for BL-066-WN-L is shown in Figure 4.46a. A distinct lack of undulations is observable. The vorticity map shown in Figure 4.46b, does not contain any evidence of the presence of any spatially stationary streamwise oriented vorticity and is essentially random in nature. This allows the link between a lack of spatially stationary streamwise vorticity and undulations of the mean streamwise velocity field to be made.

Mean streamwise velocity and mean streamwise vorticity contour maps for BL-066-RRM-L at measurement station 3 are shown in Figure 4.47. The local pairing parameter for MS3 is $x_i^* = 3.37$ which is in the region of the second pairing event. The mean streamwise velocity map of BL-066-RRM-L, shown in Figure 4.47a, shows heavy wrinkling of the velocity contour lines. The undulations have increased in magnitude compared to MS2. The mean streamwise vorticity is shown in Figure 4.47b. The three-tiered cluster formations have disappeared, and the streamwise vorticity has realigned itself into a single row of alternating sign vortices. Peaks and troughs of the the mean streamwise velocity field contour lines are at their extreme at the interface between particularly strong streamwise vortices. Examples of this are the interfaces at $40 < z/\theta_i < 60$, and $130 < z/\theta_i < 150$.

In comparison, the mean streamwise velocity contour maps for BL-066-WN-L, shown in Figure 4.48a, show little spanwise variation. The streamwise vorticity shown in

Figure 4.48b, shows no evidence of any type of spatially stationary streamwise vortex structure.

Post transition mean streamwise velocity and mean streamwise vorticity plots for BL-066-RRM-L at measurement station 5 are shown in Figure 4.49. Wrinkling of the mean streamwise velocity field is still present but with a reduced magnitude. The streamwise vorticity map in Figure 4.49b, shows evidence of spatially stationary streamwise vortex structures but at a reduced number compared to measurement station 3.

The BL-066-WN-L maps shown in Figure 4.50 are of particular interest as the mean streamwise velocity map starts to show some weak undulations in the low-speed interface zone. The mean streamwise vorticity also appears to be more organised than any of the shown upstream locations but no preferred spanwise wavelength is evident.

The wrinkling of the mixing layer can be studied using mixing layer centreline locus plots, shown in Figure 4.51, at every measurement station. The mixing layer centreline, y_0 , is defined as the vertical location at which the local streamwise velocity is equal to the convection velocity, U_c . In the pre-transition region which includes measurement stations 1 to 3, a regular spanwise wavelength is evident in the recycling-rescaling based simulation peaks and troughs data. Centreline wrinkling is greatest at spanwise locations which lie between high strength patches of streamwise vorticity, similar to what is observed in the mean streamwise velocity data. In the post-transition region the number of undulations decreases while the magnitude increases between measurement station 5 and 6. The spacing increase of the peaks and troughs with streamwise distance will be discussed in Chapter 5. The centreline locus plots for BL-066-WN-L in Figure 4.51b show no clear spanwise wavelength in the pre-transition region. At measurement stations 5 and 6 the centreline does show peaks and troughs but the magnitude of the wrinkling is less than in BL-066-RRM-L.

Case	x_i^*	Re_δ	λ_D (mm)	Δ_{ave} (mm)
BL-066-RRM-L	26.35	207028	0.171	0.668
BL-066-WN-L	26.35	166810	0.183	0.619
Meyer Case 3B <i>et al.</i> [94]	28.1	103000	0.096	0.245

Table 4.12: Smallest length scale significant to passive scalar mixing, λ_D , and smallest resolved passive scalar length scale inside the mixing layer, Δ_{ave} , at measurement station 6.

4.2.7.2 Passive scalar Mixing and Entrainment

The velocity statistics show that a change in the nature of the imposed inlet fluctuations has an effect on the momentum field in both the pre- and post-transition regions of the mixing layer. In this section the effect of the inlet fluctuation nature and the presence, or lack, of a spatially stationary streamwise vortex structure on the passive scalar field is studied. Whilst no scalar data was recorded in Browand & Latigo [45], data by Meyer *et al.* [94] which were recorded at $R = 0.60$, $x_i^* = 28.1$, $Re_\delta = 103000$ have been included in some graphs. The Meyer *et al.* [94] data has been included for guidance purposes rather than a like-for-like comparison. The smallest resolved passive scalar length scale significant to mixing at measurement station 6 is shown in Table 4.12. As the average grid spacing in the mixing layer is larger than the size of the smallest passive scalar length scale significant to mixing by a factor of 4, the passive scalar is well resolved even at the most downstream measurement station.

Figure 4.52a and 4.52b show the mean passive scalar concentration at measurement stations 3 and 5, located in the pre- and post-transition of the mixing layer, respectively. Three distinct lines are shown; spanwise averaged data and data for the two additional lines, taken spanwise locations lying between two streamwise vortices with a common downflow and upflow, respectively. The variation bars shown on the spanwise averaged data denote a ± 1 standard deviation in the spanwise variation of the computed flow statistics. At measurement station 3, shown in Figure 4.52a, the streamwise vortices have a strong effect on the mean passive scalar concentration. At the spanwise plane with a common downflow, $z/\theta_i = 41$, more high-speed fluid is entrained, increasing the passive scalar concentration throughout the entire ver-

tical extent of the mixing layer. At $z/\theta_i = 54$, a spanwise location with a common upflow, the reverse is observed and the mean passive scalar values decrease overall. The spanwise variation, denoted with variation bars, of the spanwise averaged data is greatest in the mixing layer centre with a reduction towards the free streams. Figure 4.52b shows the mean passive scalar concentration at measurement station 5. The mean passive scalar data shows an increased concentration of high-speed fluid in the low-speed side of the mixing layer, producing a ‘hump’ in the low-speed side of the mixing layer. This triple inflection passive scalar profile has also been observed in experiments [50, 59]. The spanwise variation has reduced greatly compared to measurement station 3 and the two spanwise locations are very similar to the spanwise averaged measurement. The reduction in spanwise variation could be linked to the decreased maximum magnitude of the streamwise vorticity as well as the reduced relative strength of the undulations observed in the centreline at greater downstream locations.

Figure 4.52c shows the mean passive scalar fluctuations at measurement station 3 for BL-066-RRM-L. As observed in the mean passive scalar measurements, the choice of spanwise location shifts the fluctuation profile along the vertical axis depending on the flow orientation of the streamwise vortex structures influencing the chosen spanwise plane. At measurement station 5, shown in Figure 4.52d, the two spanwise locations agree well with the spanwise averaged data and the variation bars have decreased in size compared to MS3. The ‘bi-modal’ shape produced by the simulations is in good agreement with experimental data of both, the low Reynolds number mixing layer [59], and the high Reynolds number mixing layer [50].

The mean passive scalar concentration for BL-066-WN-L at MS3 and MS5 is shown in Figure 4.53a and 4.53b. The measurements taken at an entrainment maximum and minimum show no discernible difference compared to the spanwise averaged data. This is also evident in the passive scalar fluctuation plots shown in Figure 4.53c and 4.53d, where no difference between the different spanwise positions and the spanwise averaged data is evident.

A series of instantaneous passive scalar concentration cross-planes for BL-066-RRM-L at measurement station 3 are shown in Figure 4.54. The series investigates the behaviour of the passive scalar in the leading braid region, inside the structure core and

in the trailing braid region. Figure 4.54a is taken in the leading braid region before the passage of the investigated structure. The free streams are separated by a narrow interface region with a large number of regularly spaced undulations. Inside the core of the structure, depicted in Figure 4.54b, two interface regions separated by the structure core are visible. After the structure has left the measurement plane, shown in Figure 4.54c, the flow returns to a single interface region. At several spanwise locations individual undulations can be tracked throughout the structure passage. Examples of this are seen at $z/\theta_i = 220, 240$ and 280 .

Instantaneous passive scalar concentration plots of BL-066-RRM-L at measurement station 5 are shown in Figure 4.55. In Figure 4.55a, the two free streams carrying passive scalar with values of 1 and 0 are separated by a thin interface region in which kinks and ‘mushroom’ shaped instabilities visible. Figure 4.55b shows the cross-plane passive scalar map as the primary structure passes the measurement station. The free streams are now separated by a large structure core in which mixing is taking place. Of particular interest is a thin pocket of unmixed high-speed fluid is present near the low-speed stream, most notable in the region of $40 < z/\theta_i < 200$. The observed pocket of unmixed fluid must have been entrained or engulfed rapidly by the mixing layer, as opposed to having been continually entrained by the interface zones. After the core of the structure has left the measurement station depicted in Figure 4.55c, the upper interface moves downwards towards the low-speed stream. The presented cross-planes are qualitatively very similar to flow visualisations by the Bernal & Roshko [54].

Instantaneous cross-planes of the passive scalar concentration during a structure passage at MS3 for BL-066-WN-L are shown in Figure 4.56. The cross-planes in the braid region are qualitatively different to their BL-066-RRM-L counterparts. Unlike the RRM simulation, there is less spanwise coherence and at multiple spanwise locations, such as at $z/\theta_i \approx 120$ the free streams are separated only by a very thin interface region. The co-existence of single and double interface zones during the structure passage is a result of the branching between primary vortices observed in the perspective views. In contrast the RRM simulation produces an almost uniform flow field with a constant visual thickness across the entire span. The cross-plane map taken in a structure core is shown in Figure 4.56b. The spanwise incoherence is also evident in this map. At some spanwise locations, $z/\theta_i \approx 100$ and 350 what appears

to be a structure core is evident while at other spanwise locations at the same time instance, the free streams are only separated by a very thin interface zone, such as at $z/\theta_i \approx 170$. Similar observations can be made for the cross-planes at MS5, shown in Figure 4.57. Most notable is the qualitative similarity between the braid and core maps. Even in the structure core plot, Figure 4.57b, a braid region type flow arrangement is evident at $z/\theta_i \approx 180$. The observed engulfment of fluid in which unmixed, high-speed fluid is found near the low-speed free stream is not evident in any of the plots. The passive scalar concentration inside the primary vortex in Figure 4.57b is largely homogeneous. Undulations of the interface zones are present, but they are of a low magnitude and do not show the characteristic ‘mushroom’ shape that is observed in the recycling-rescaling based simulation.

Quantitative data on the internal mixing process in the core of a primary structure and the braid regions between two neighbouring structures in the post-transition region of the mixing layer can be obtained from instantaneous, spanwise averaged, passive scalar concentrations taken through the core and braid regions of typical passing structures, shown in Figure 4.58.

Spanwise averaged, passive scalar profiles in a typical structure passing through measurement station 5 in BL-066-RRM-L, are shown in 4.58a. The passive scalar concentration profiles in the leading and trailing braid regions are of a similar shape but shifted in the horizontal axis. The concentration profile inside the structure core shows a reversal. It has been suggested that this passive scalar reversal is connected to the *non-marching* probability density functions observed in experimental studies [18]. The reversal is also a good indication of the engulfment entrainment mechanism.

Similar profiles for BL-066-WN-L are shown in Figure 4.58b. The passive scalar profiles at the three distinct stages of a structure passage are very similar. The width of the mixing layer, ie the horizontal distance between $0.01 < \langle \bar{\xi} \rangle_z < 0.99$, is similar for both simulations. Unlike the recycling-rescaling based simulation, the idealised simulation does not show a reversal of the passive scalar concentration inside the structure core. The presented plots are in agreement with passive scalar concentration plots for a white noise type simulation by McMullan *et al.* which have shown a ‘plateau’ of the passive scalar inside a primary vortex but no reversal [18].

To further investigate the entrainment of passive scalar into the mixing layer, the entrainment ratio at measurement stations 3 to 6 are presented. The entrainment ratio has been computed as described in Section 4.6. The variation of the entrainment ratio, E_v , across the span in BL-066-RRM-L and BL-066-WN-L at measurement station 3 is shown in Figure 4.59a and 4.60a, respectively. The peak and troughs of the entrainment ratio plot in Figure 4.59a correspond to interface zones of mean streamwise vorticity, similar to what has been observed for the mixing layer centreline locus plots in Figure 4.51. A clear anti-correlation for BL-066-RRM-L between the centreline, shown in Figure 4.51a, and the entrainment ratio is evident. The entrainment values for BL-066-RRM-L range from 0.98 to 1.52 compared to 1.23 to 1.34 for BL-066-WN-L, reflecting the greater spanwise variation present in the recycling-rescaling based simulation. The large variation is also evidence of the strong effects that the spatially stationary streamwise vortices have on the flow in the initial region. A lack of spatially stationary streamwise structures results in an entrainment ratio with little spanwise variation as is the case in Figure 4.60a for BL-066-WN-L.

A similar trend is observed in the entrainment ratio at measurement station 4, shown in Figure 4.59b and 4.60b. The number of undulations has decreased compared to MS3 a result of the rearrangement process of the streamwise vortex structures which will be discussed in more detail in Section 5. Compared to MS3, the peak entrainment ratio value for BL-066-RRM-L has decreased. As the streamwise structures are spanwise stationary, individual peaks and troughs can easily be traced between Figure 4.59a and 4.59b which is not possible for BL-066-WN-L.

Figure 4.59c and 4.60c show the entrainment ratio at measurement station 5, located in the self-similar, far field region of the mixing layer. At measurement station 5 the entrainment ratio in the two presented simulation starts to be qualitatively similar. The entrainment ratio at the last measurement station is shown in Figure 4.59d and 4.60d. The regular spaced undulations observed at measurement stations 1 to 4 have become less pronounced, and the entrainment ratio plots for BL-066-RRM-L and BL-066-WN-L are now qualitatively similar.

Table 4.13 summarises the entrainment ratio at measurement stations 2 to 6. In both simulations the entrainment ratio decreases in the transition zone before it asymptotes to a final state which is comparable for both simulations. Notable are the large

Simulation	Measurement station	$E_{v,\max}$	$E_{v,\min}$	$\langle E_v \rangle_z$
BL-066-RRM-L	MS 2	1.65	1.18	1.39
BL-066-RRM-L	MS 3	1.52	0.98	1.25
BL-066-RRM-L	MS 4	1.47	1.14	1.33
BL-066-RRM-L	MS 5	1.41	1.24	1.33
BL-066-RRM-L	MS 6	1.42	1.25	1.31
BL-066-WN-L	MS 2	1.76	1.59	1.69
BL-066-WN-L	MS 3	1.35	1.24	1.30
BL-066-WN-L	MS 4	1.43	1.32	1.37
BL-066-WN-L	MS 5	1.43	1.32	1.37
BL-066-WN-L	MS 6	1.43	1.31	1.36

Table 4.13: Entrainment ratios at measurement stations 2 to 6 for BL-066-RRM-L and BL-066-WN-L.

differences in the spanwise variation of the entrainment ratio. Particularly in the pre-transition, the spanwise variation is very large for BL-066-RRM-L but even in the self-similar, post-transition region the spanwise variation in the physically correlated simulation remains much higher than in the idealised one.

For the presented velocity ratio, $R = 0.66$, the Dimotakis entrainment model (Equation 2.10) predicts a value of $E_v = 1.44$. McMullan *et al.* found the entrainment ratio in their idealised simulations to be approximated well by $E_v = 1 + 0.5R$ which for the presented velocity ratio results in an entrainment ratio value of $E_v = 1.33$. This value is very close to the spanwise averaged entrainment values reported in these simulations. However, it has to be noted that depending on the chosen spanwise location, agreement for both simulations is good with both entrainment ratio relations. Meyer *et al.* [94] reported an entrainment ratio value of $E_v = 1.24$ for a comparable mixing layer.

While the entrainment ratio gives information about how much high-speed fluid is being entrained into the mixing layer, it offers no insight into the mixing process. The mixing process can be quantified using the probability of finding mixed fluid of any composition, P_m , which is given by

$$P_m(y) = \int_c^{1-c} p(\bar{\xi}, y) d\bar{\xi} \quad (4.14)$$

where ϵ is the the measurement resolution of the passive scalar. In this study, $\epsilon = 0.025$, a value based on comparable experiments [59]. Therefore, passive scalar values of $0 \leq \bar{\xi} \leq 0.025$ denote pure low-speed fluid and passive scalar values of $0.975 \leq \bar{\xi} \leq 1$ denote pure high-speed fluid.

Another quantification can be made using the average concentration of high-speed mixed-fluid, ξ_m , given by

$$\xi_m(y) = \frac{\int_{\epsilon}^{1-\epsilon} \bar{\xi} p(\bar{\xi}, y) d\bar{\xi}}{P_m(y)} \quad (4.15)$$

For each simulation P_m and ξ_m at two distinct spanwise locations are presented. These spanwise locations have been chosen to correspond to entrainment ratio maxima and minima values at measurement station 6. The vertical variable, y , is normalised by the local mixing layer visual thickness, δ_{vis} . P_m and ξ_m for BL-066-RRM-L at measurement station 6 are shown in Figure 4.61a. The P_m curve for BL-066-RRM-L agrees extremely well with the reference data. Like the experiment, P_m approaches values of unity but is not attained in the mixing layer. This indicates that at every point in the vertical extent of the mixing layer unmixed fluid can be found. Similarly good agreement is seen for the average mixed fluid concentration found at any vertical location, ξ_m . The rise in concentration in the low-speed side of the mixing layer shows how, relatively, unmixed high-speed fluid is found on the low-speed side of the mixing layer. The presented P_m and ξ_m measurements together with the cross-planes of $\bar{\xi}$ are a strong indication of the engulfment entrainment mechanism, described in detail in Section 2.3.4 [56].

The P_m data for BL-066-WN-L is shown in Figure 4.61b. At both spanwise measurement locations values of unity for P_m are found in the mixing layer, indicating that at no time instant unmixed free stream fluid can be found in the core of the mixing layer. The idealised simulation does not reproduce the increase in the average mixed fluid concentration seen in the low-speed side of the mixing layer in the reference data. In the centre of the mixing layer the gradient for ξ_m is steeper than BL-066-RRM-L, describing a mixing layer which entrains and mixes high-speed fluid gradually and continuously. The slight rise in ξ_m at the very edge of the mixing layer is explained by occasional entrainment of fluid during interactions between primary

structures of the very largest scale. The over-mixing observed in P_m as well as the shape of ξ_m , combined with the instantaneous vertical passive scalar concentration in Figure 4.58 suggest entrainment by the nibbling mechanism. The nibbling or Corrsin & Kistler [57] entrainment mechanism describes a mixing layer in which entrainment is produced by the nibbling of irrotational free-stream fluid by small-scale eddies in the interface zones of the mixing layer. The nibbling entrainment mechanism is commonly observed in DNS based on idealised inlet conditions [100, 101]. It has even been suggested that the engulfment entrainment mechanism [56] is an artifact of experimental studies and not representative of some practical applications [101].

The entrainment mechanism is also reflected in the probability density function (p.d.f.). Probability density functions give information about the probability of finding mixed fluid of any concentration at every vertical location in the mixing layer. The engulfment entrainment mechanism has previously been connected to p.d.f.'s of the *non-marching* type [50]. P.d.f.'s at measurement station 6 are presented in Figure 4.62 and 4.63. Two spanwise locations are shown for both simulations. The spanwise locations have been chosen to represent a spanwise location with an entrainment maximum and minimum value, respectively. Figure 4.62 shows the p.d.f.'s for BL-066-RRM-L. At both locations the p.d.f.'s are of the *non-marching* type. The preferred concentration, $\bar{\xi} \approx 0.6$ is in excellent agreement with p.d.f.'s of comparable mixing layers at $R = 0.38$ for which a preferred concentration of $\bar{\xi} \approx 0.6$ was reported [50]. The p.d.f.'s for BL-066-WN-L are shown in Figure 4.63. Both p.d.f.'s are of the *marching* type which describes a p.d.f. in which the preferred concentration is a function of the vertical location. *Marching* type p.d.f.'s have been observed in a number of DNS of a spatially evolving mixing layer [102].

4.2.8 Summary

In this chapter large eddy simulations of a high Reynolds number, spatially developing mixing layer have been performed. Two types of inlet fluctuation methods have been compared. The first type of inlet generation method, termed white-noise (WN), produces pseudo-random three-dimensional velocity fluctuations and was used for the BL-066-WN-L simulation. An alternative inlet generation method, recycling-

rescaling (RRM), produces physically correlated inlet fluctuations [37]. The RRM inlet generation method was used for the BL-066-RRM-L simulation. By keeping the inlet condition statistics constant for both simulations, the effects of spatial and temporal correlation of the inlet boundary layer fluctuations have been evaluated.

Using mean secondary shear stress and streamwise vorticity, cross-plane plots, a secondary, spanwise stationary, streamwise oriented structure is identified in the simulation based on the recycling-rescaling inlet generation method in BL-066-RRM-L. In contrast, BL-066-WN-L does not show any evidence of such a structure. Pseudo-perspective views of the idealised simulation, show large scale primary structures with branching between neighbouring structures. This is in agreement with comparable numerical simulations based on similar idealised inlet conditions [18]. In BL-066-RRM-L, the perspective views show quasi-two-dimensional, Brown-Roshko type primary structures with undulations that ‘ride’ on top of the primary roller structures.

Investigation of cross-plane data suggests the presence of spatially stationary streamwise vortex structures in the BL-066-RRM-L simulation, similar to ones observed by experimental studies [54]. Subsequent analysis of passive scalar data shows a strong link between the presence or lack of a streamwise oriented structure and passive scalar entrainment and mixing. The streamwise oriented structures present in BL-066-RRM-L, lead to large undulations of the entrainment ratio and mixing layer centreline along the span. BL-066-WN-L does show similar undulations, however, their respective magnitudes are much lower. The probability density functions (p.d.f.’s) for BL-066-WN-L are of the *marching* type. Spanwise interrogation finds that the p.d.f.’s for BL-066-WN-L show little spanwise variation and are always of the *marching* type. The spatially and temporally correlated inlet fluctuations used in BL-066-RRM-L, produce p.d.f.’s which are of the *non-marching* type. The preferred concentration and shape of the presented p.d.f.’s is in very good agreement with experimental data.

The presented data suggests that passive scalar in the BL-066-WN-L is entrained by a nibbling mechanism while the BL-066-RRM-L simulation entrains fluid by engulfment. This is evident in cross-plane passive scalar visualisations which show unmixed high-speed fluid in the low-speed side of the mixing layer in BL-066-RRM-L.

Instantaneous passive scalar measurements taken inside primary structures cores show similar trends and support entrainment by engulfment while the same data suggests a nibbling entrainment mechanism for the idealised simulations. This is a novel finding of this thesis.

Experimental evidence for the presence of a secondary, streamwise oriented vortex structure which persists into the self-similar region of the mixing layer is strong and numerous. The presented simulations show that depending on the type of inlet condition that is used, extremely good agreement with experimental data can be achieved for mean flow as well as passive scalar data. The large spanwise variation observed in some of the measurements also suggests that the choice of the spanwise location in experimental studies can be critical, even in a fully developed mixing layer.

4.2.9 Conclusions

In this chapter simulations of low and high Reynolds number mixing layers have been used to investigate the effects of spatial and temporal correlation of inlet conditions.

The presented simulations illustrate the need to model inlet conditions accurately. In particular, the spatial and temporal correlation of the inlet conditions has been shown to be critical in producing primary and secondary structure dynamics in agreement with experiments. Results from a recent DNS by Attili *et al.* [3] of a spatially developing mixing layer from idealised inlet conditions have shown that the problem of accurate passive scalar entrainment and mixing is not solved by resolving all scales of motion. Accurate passive scalar statistics are the result of simulating physically realistic primary and secondary vortex dynamics which can only be done by using physically realistic inlet conditions.

4.3 Figures

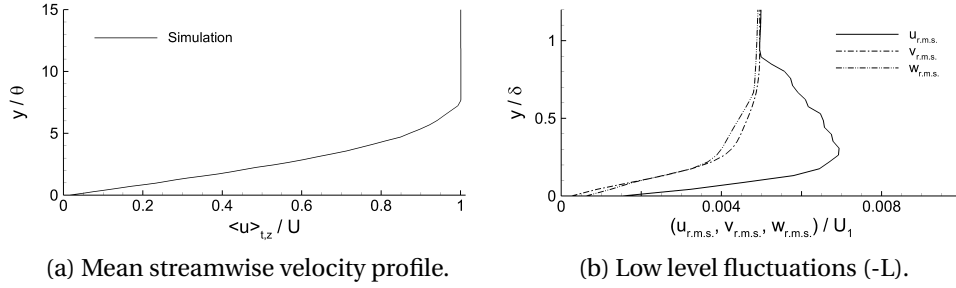


Figure 4.1: Inlet conditions.

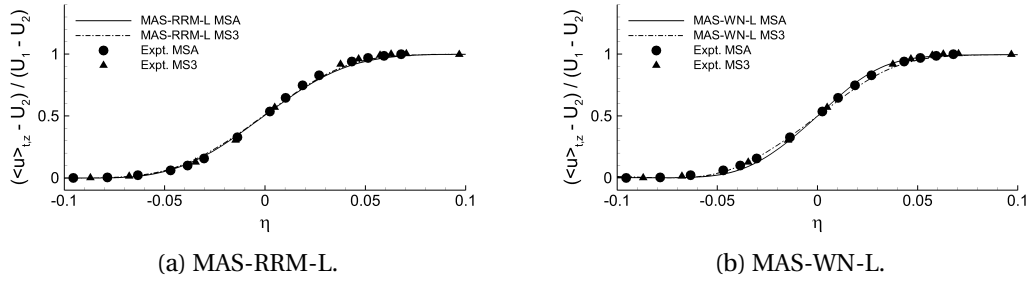


Figure 4.2: Mean streamwise velocity at measurement stations A and 3.

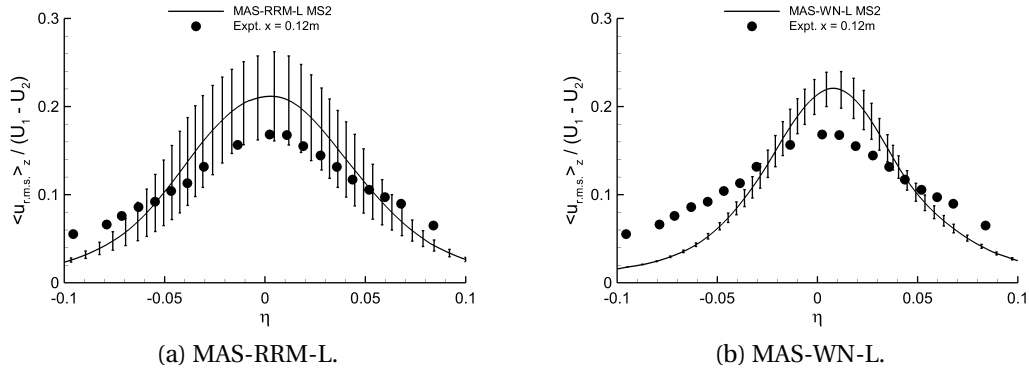


Figure 4.3: Mean streamwise velocity fluctuation magnitude at measurement station 2.

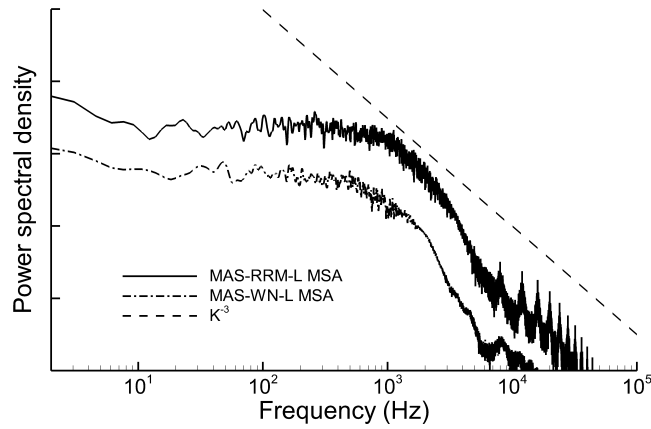


Figure 4.4: Power spectral density plots at measurement station MSA. Lines have been shifted in the vertical axis for clarity.

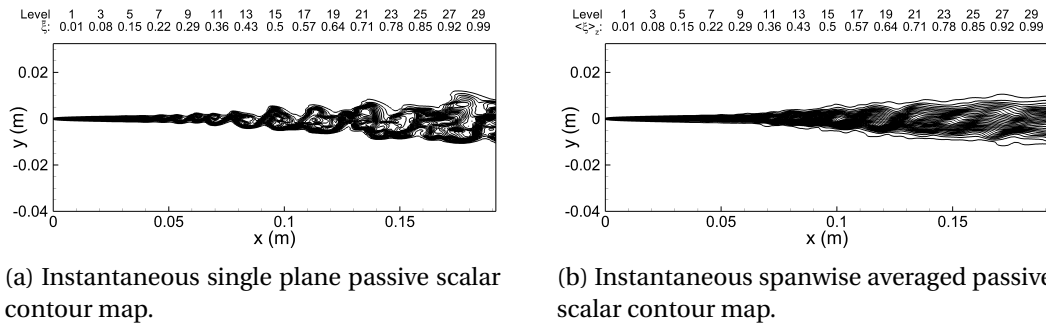
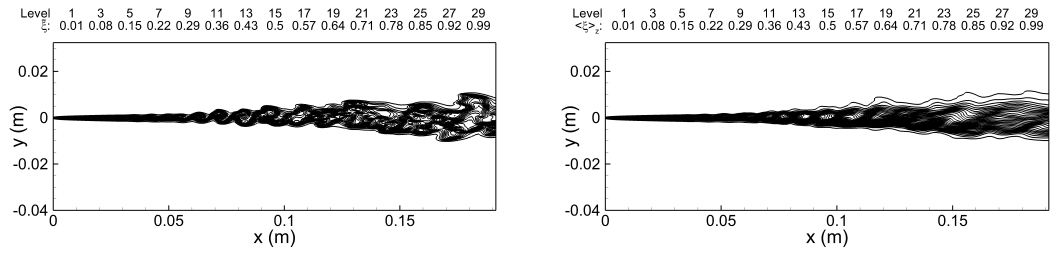


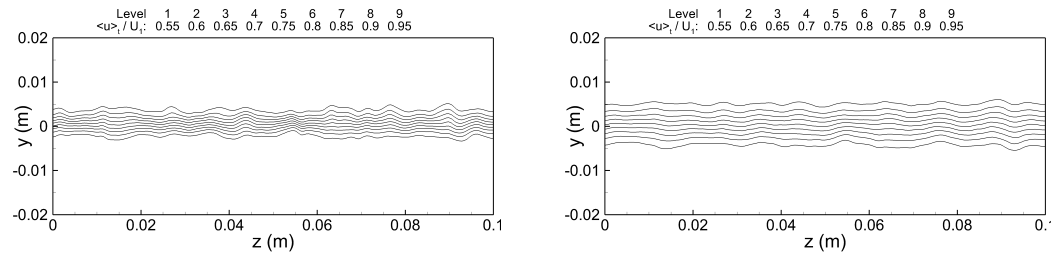
Figure 4.5: Instantaneous passive scalar contour maps of MAS-RRM-L.



(a) Instantaneous single plane passive scalar contour map.

(b) Instantaneous spanwise averaged passive scalar contour map.

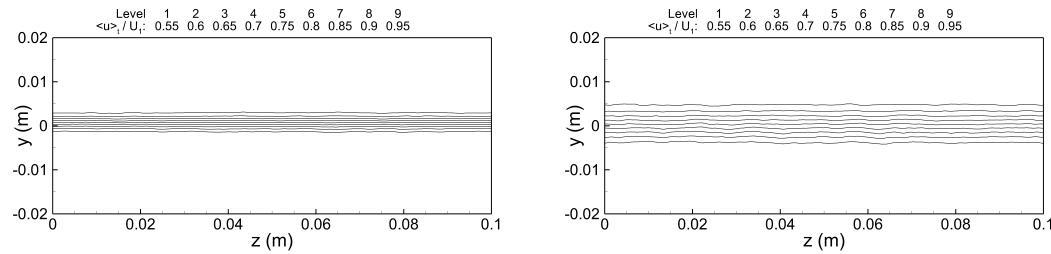
Figure 4.6: Instantaneous passive scalar contour maps of MAS-WN-L.



(a) MAS-RRM-L MS2.

(b) MAS-RRM-L MS3.

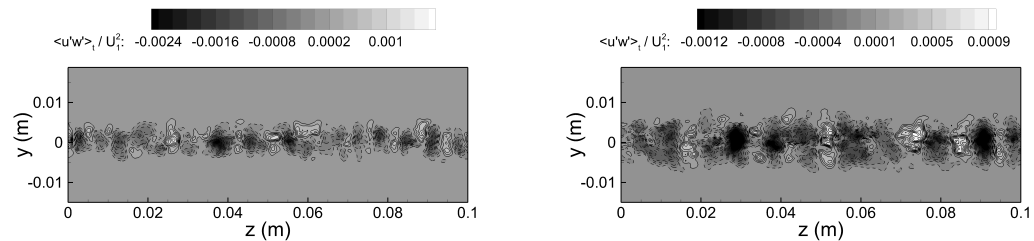
Figure 4.7: Mean streamwise velocity for MAS-RRM-L at measurement stations 2 and 3.



(a) MAS-WN-L MS2.

(b) MAS-WN-L MS3.

Figure 4.8: Mean streamwise velocity for MAS-WN-L at measurement stations 2 and 3.



(a) MAS-RRM-L MS2.

(b) MAS-RRM-L MS3.

Figure 4.9: Mean secondary shear stress for MAS-RRM-L at measurement stations 2 and 3. Dashed lines denote negative values.

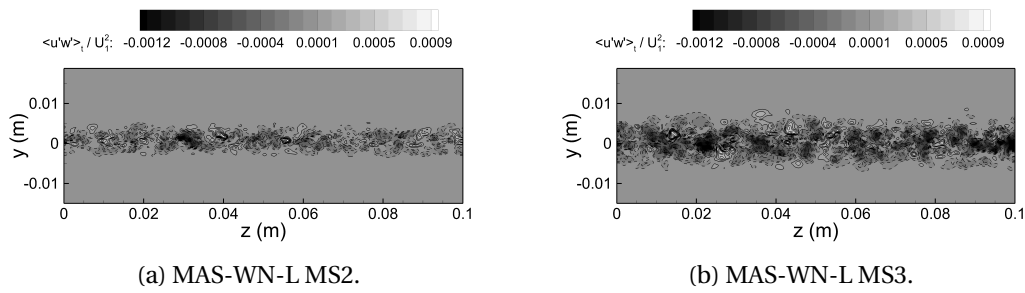


Figure 4.10: Mean secondary shear stress for MAS-WN-L at measurement stations 2 and 3. Dashed lines denote negative values.

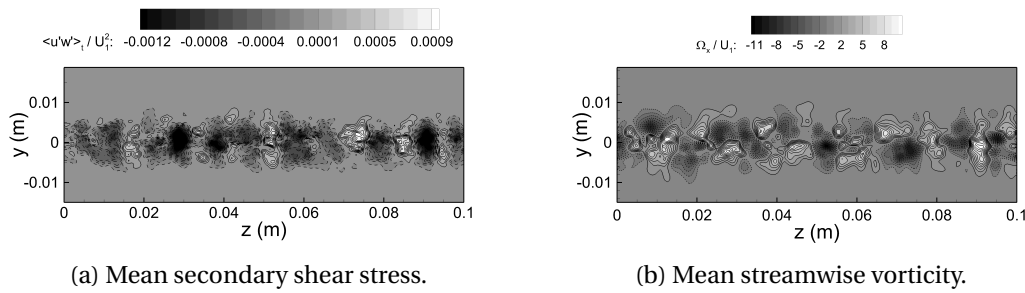


Figure 4.11: Mean secondary shear stress and mean streamwise vorticity for MAS-RRM-L at measurement station 3.

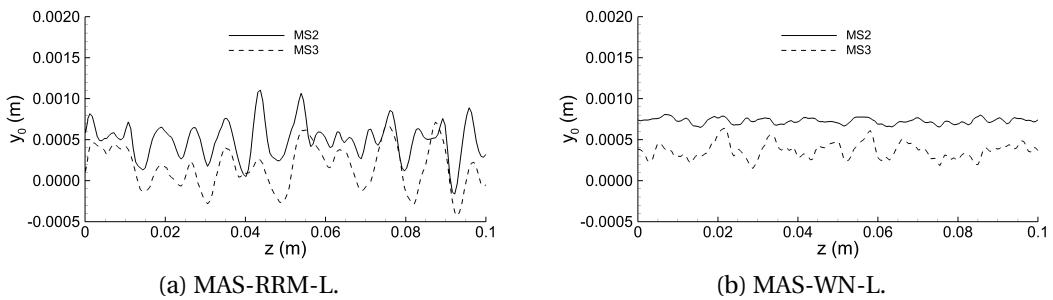


Figure 4.12: Mixing layer centreline plots for MAS-RRM-L and MAS-WN-L at measurement stations 2 and 3.

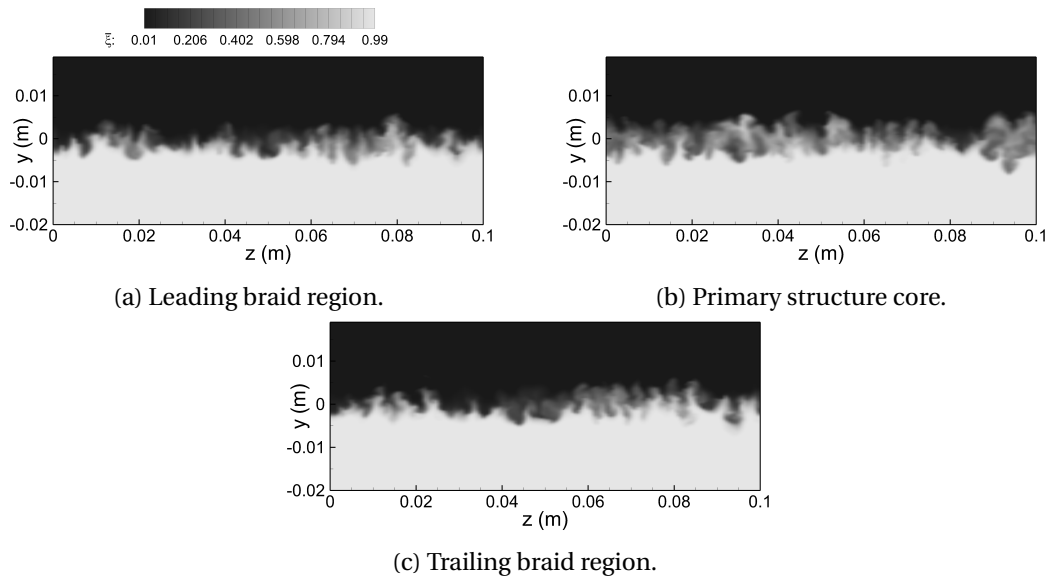


Figure 4.13: Cross-stream passive scalar measurements during a primary structure passage for MAS-RRM-L at measurement station 2.

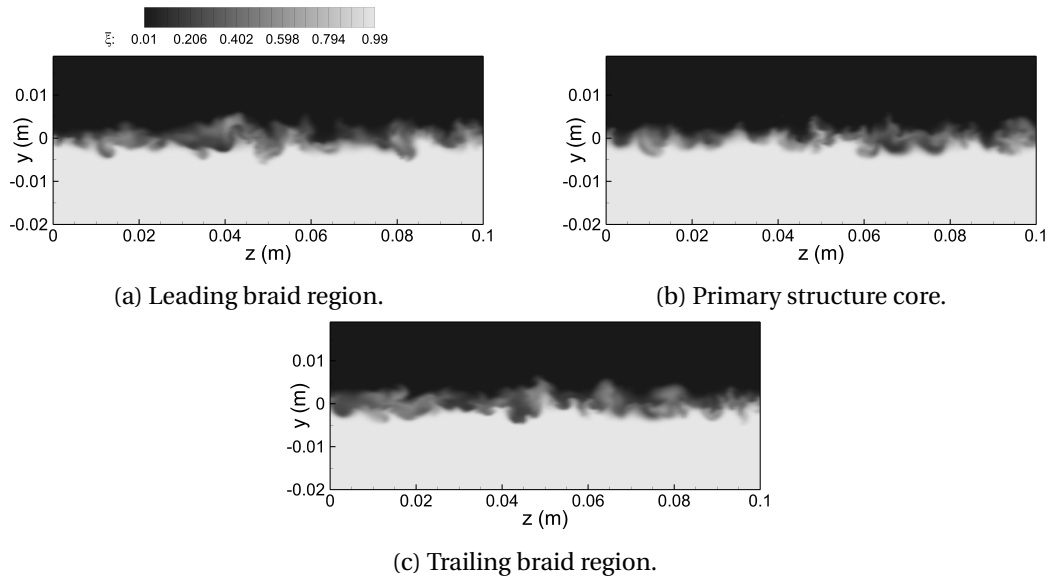


Figure 4.14: Cross-stream passive scalar measurements during a primary structure passage for MAS-WN-L at measurement station 2.

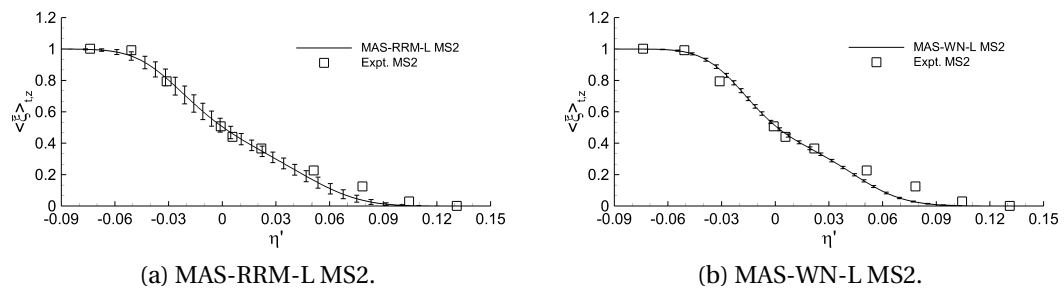


Figure 4.15: Spanwise averaged mean passive scalar concentration at measurement station 2. Error bars denote the *r.m.s.* value of the spanwise variation, not measurement error.

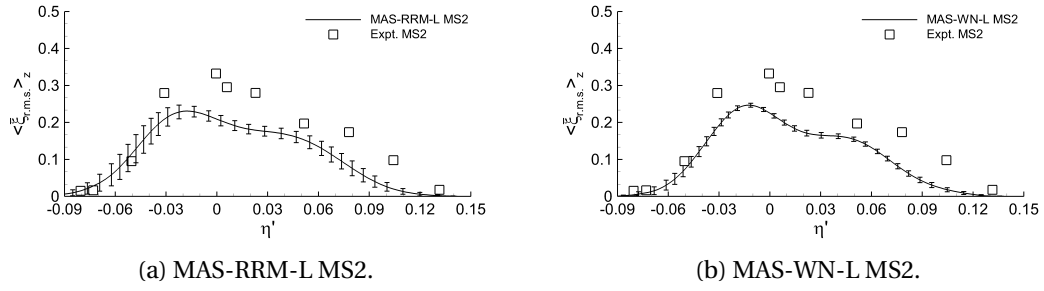


Figure 4.16: Spanwise averaged mean passive scalar fluctuation measurements at measurement stations 2. Error bars denote the *r.m.s.* value of the spanwise variation, not measurement error.

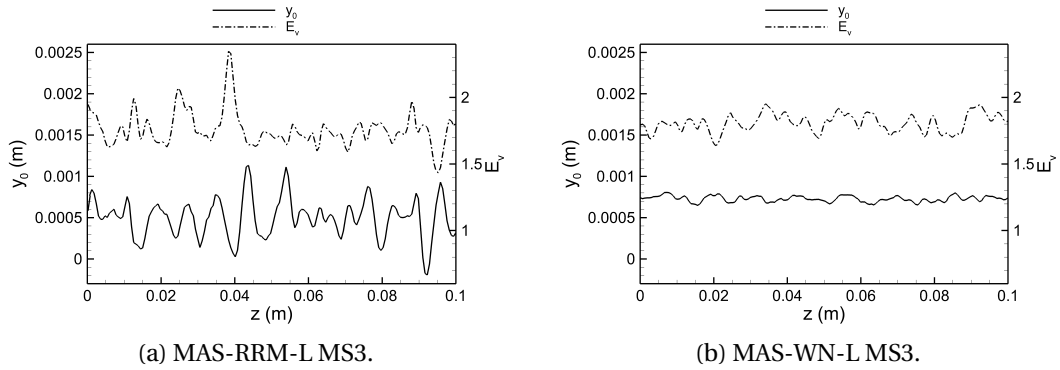


Figure 4.17: Entrainment ratio, E_v , and centreline locus, y_0 , plots at measurement station 2.

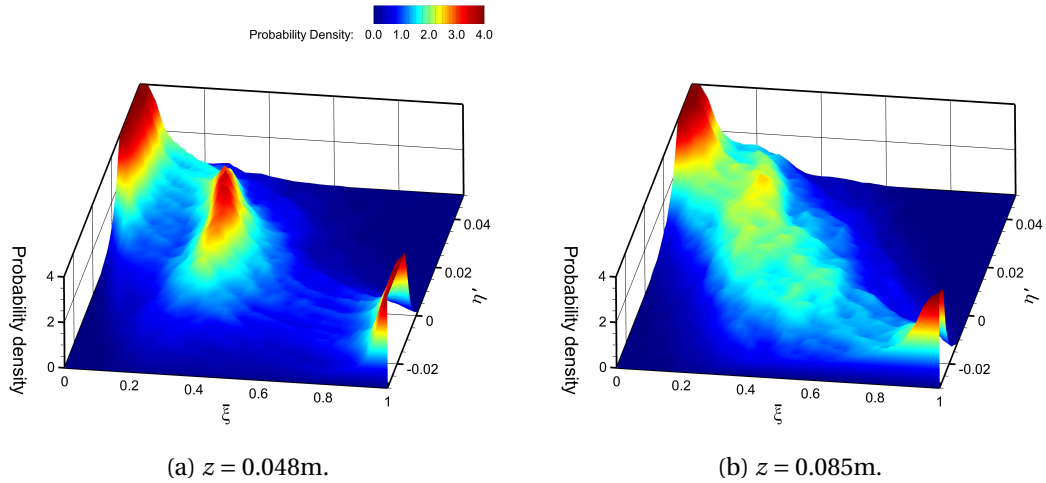


Figure 4.18: Probability density function plots for MAS-RRM-L at measurement station 3.

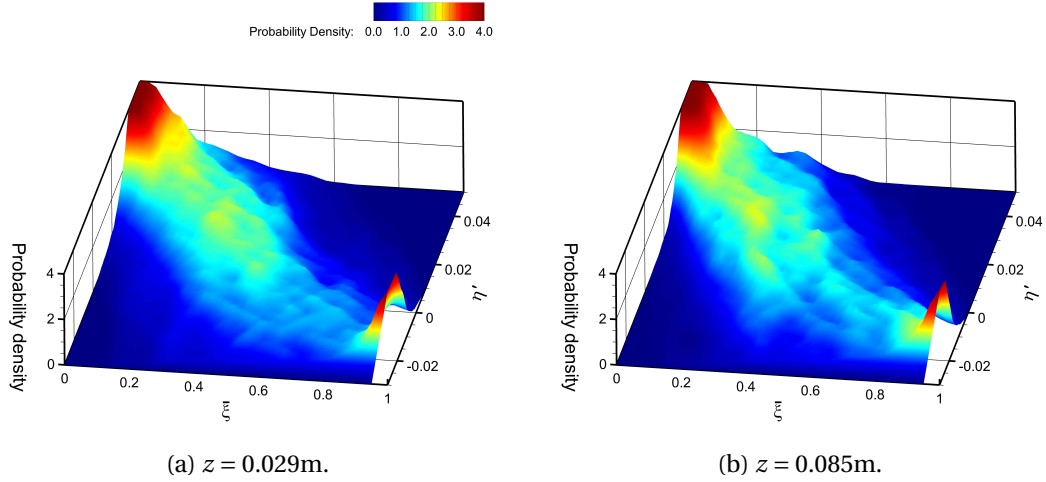


Figure 4.19: Probability density function plots for MAS-WN-L at measurement station 3.

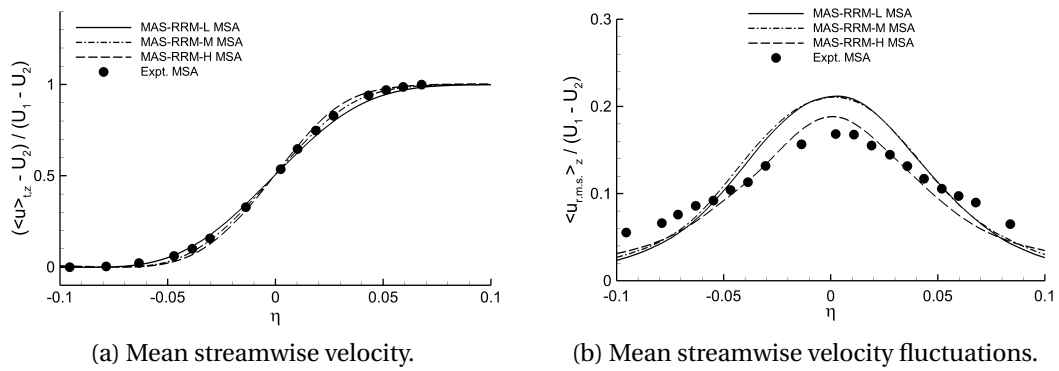


Figure 4.20: Mean streamwise velocity statistics.

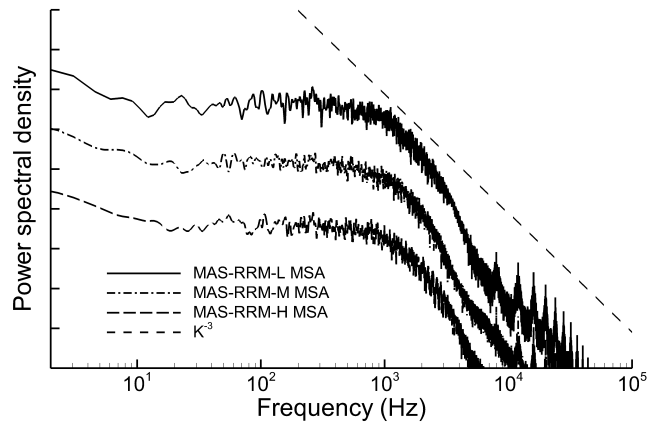


Figure 4.21: Power spectral density plots at MSA. Lines have been shifted in the vertical axis for clarity.

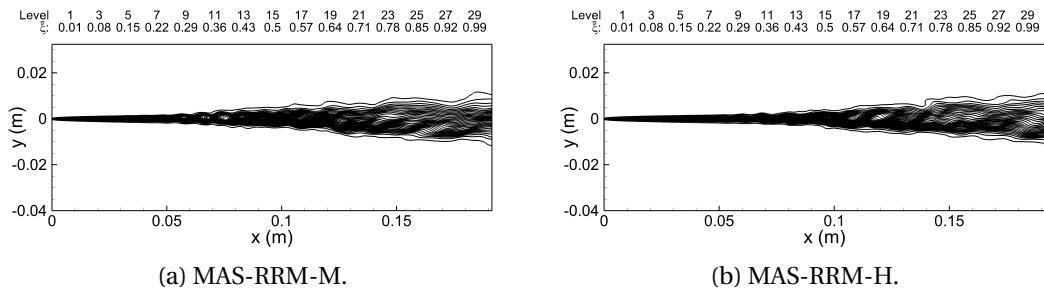


Figure 4.22: Instantaneous passive scalar contour maps for MAS-RRM-M and MAS-RRM-H.

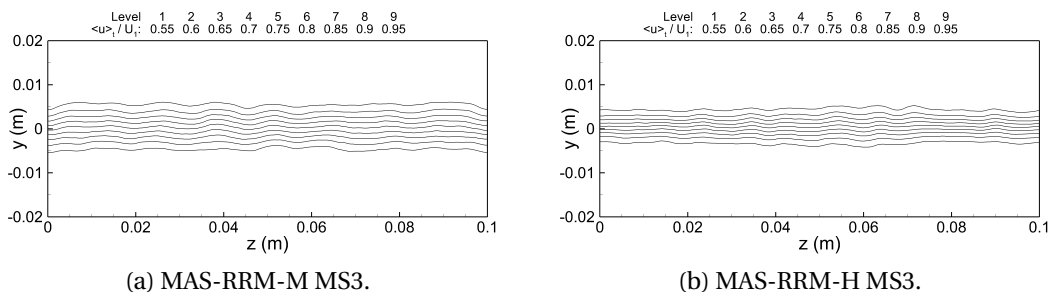


Figure 4.23: Streamwise velocity $y - z$ cross-planes at measurement station 3.

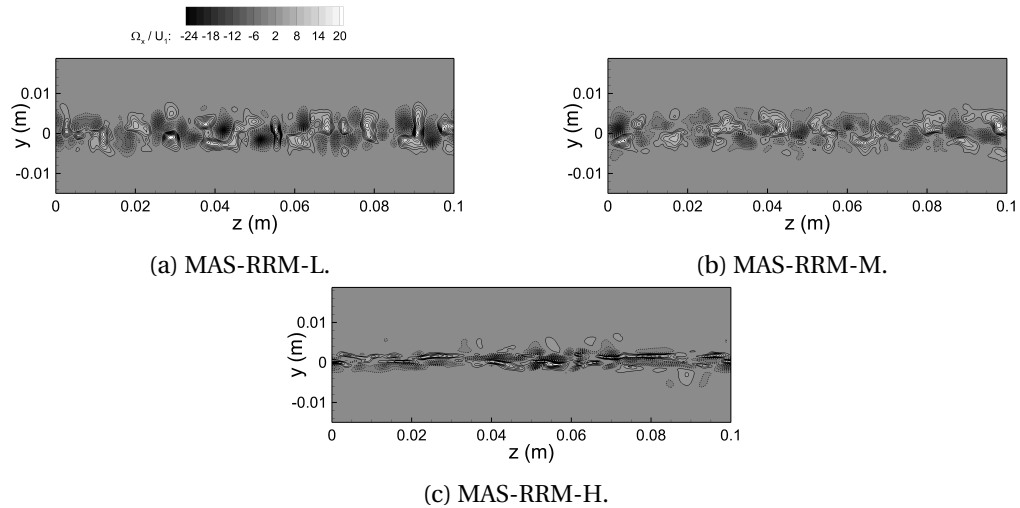


Figure 4.24: Mean streamwise vorticity maps at measurement station 2. Dashed lines denote negative values.

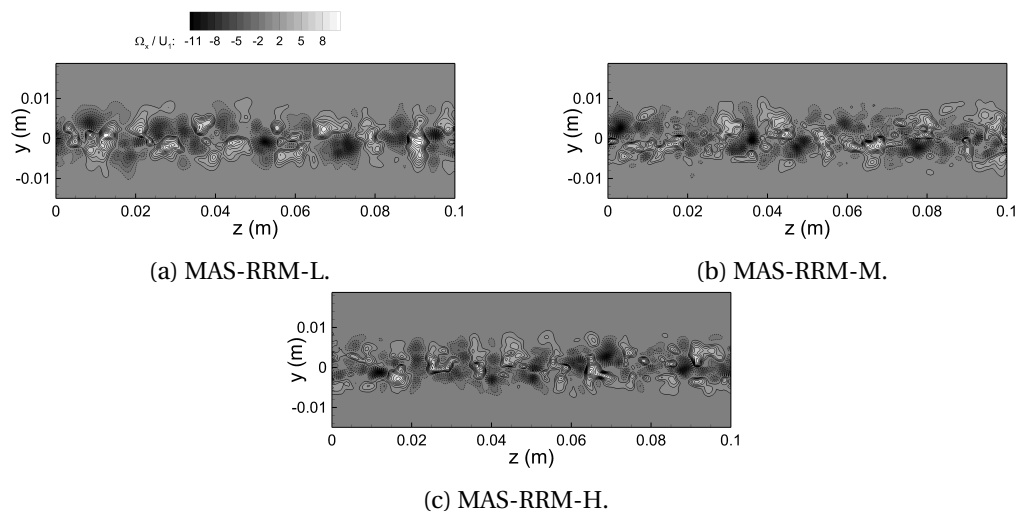


Figure 4.25: Mean streamwise vorticity maps at measurement station 3. Dashed lines denote negative values.

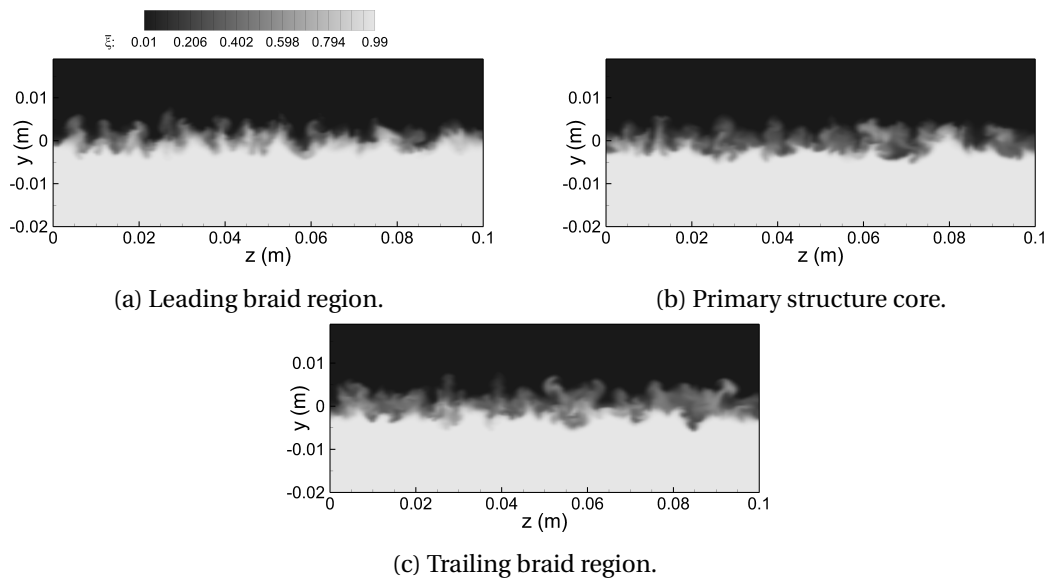


Figure 4.26: Cross-stream passive scalar measurements during a primary structure passage for MAS-RRM-M at measurement station 3.

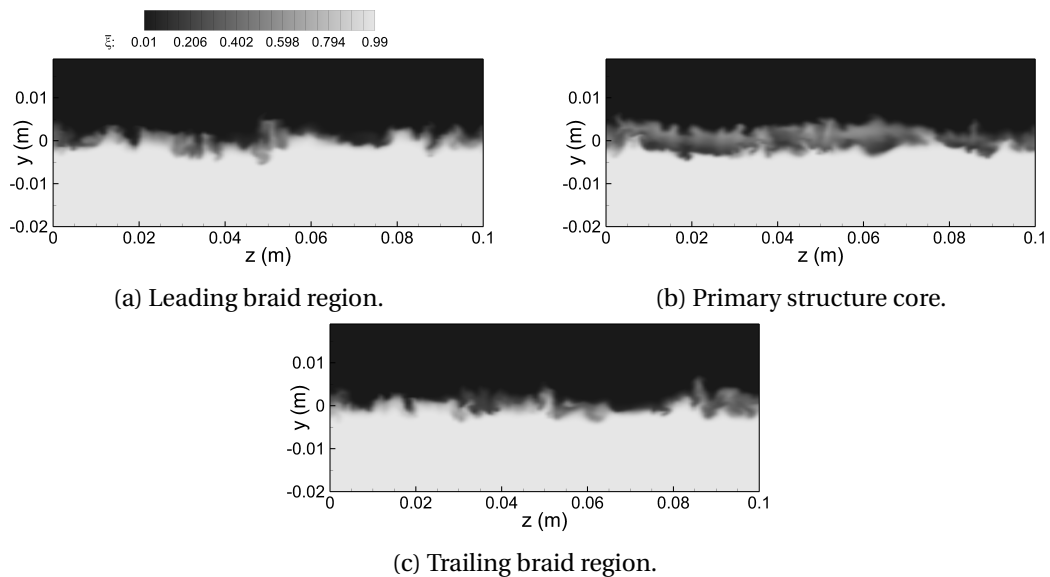


Figure 4.27: Cross-stream passive scalar measurements during a primary structure passage for MAS-RRM-H at measurement station 3.

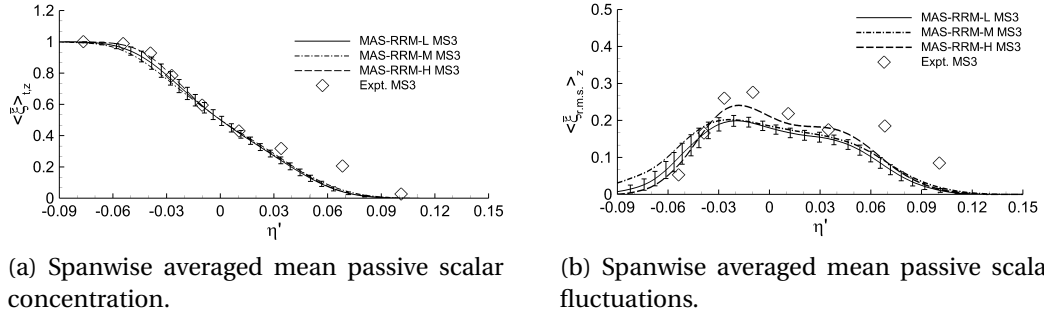


Figure 4.28: Spanwise averaged mean passive scalar concentration and mean passive scalar fluctuations at measurement stations 3. For clarity spanwise variation bars are only shown for MAS-RRM-L.

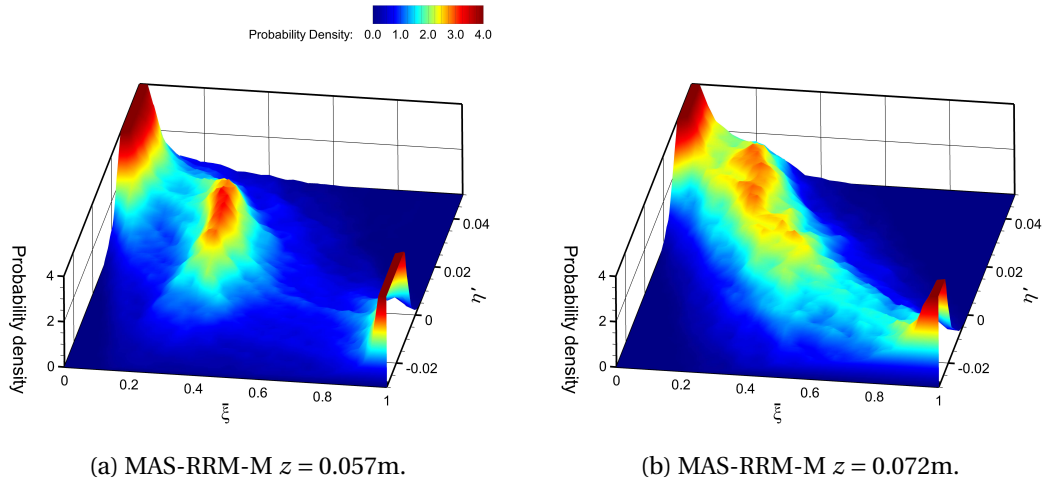


Figure 4.29: Probability density function plots for MAS-RRM-M at measurement station 3.

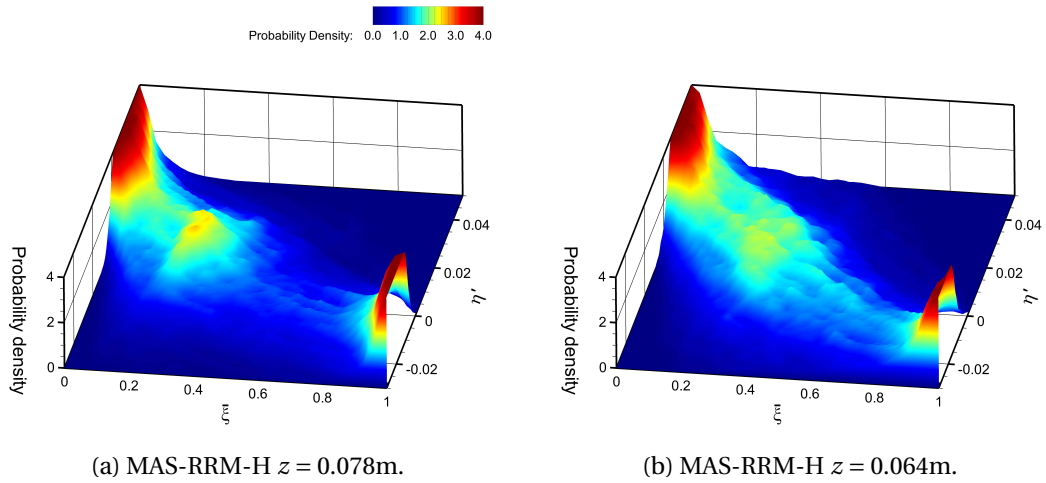


Figure 4.30: Probability density function plots for MAS-RRM-H at measurement station 3.

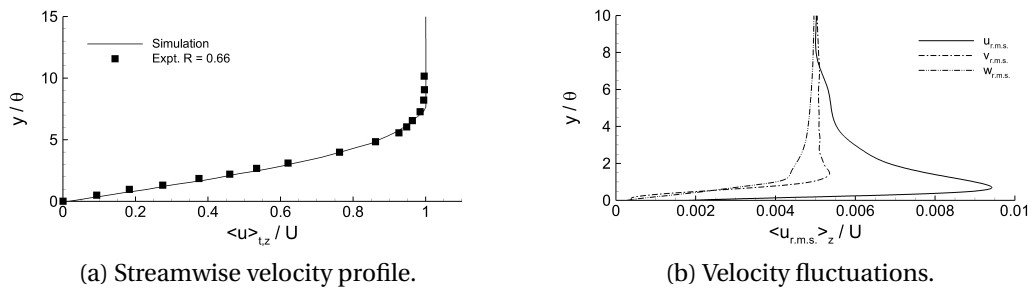


Figure 4.31: Inlet velocity profiles and inlet velocity fluctuation profiles.

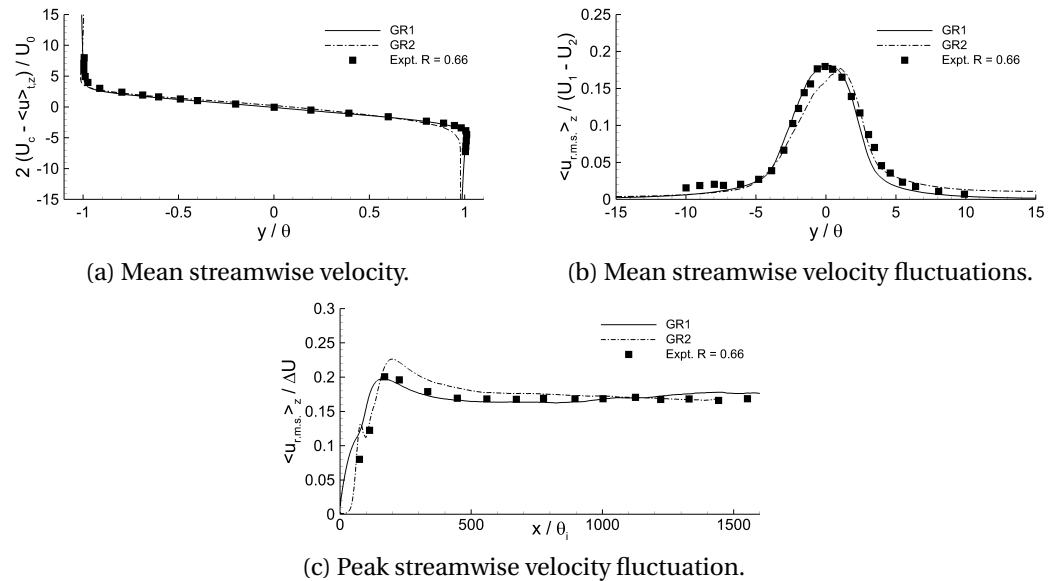


Figure 4.32: Velocity statistics for GR1 and GR2.

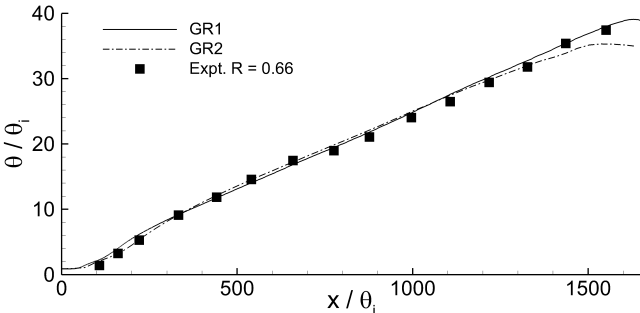


Figure 4.33: Local momentum thickness for GR1 and GR2.

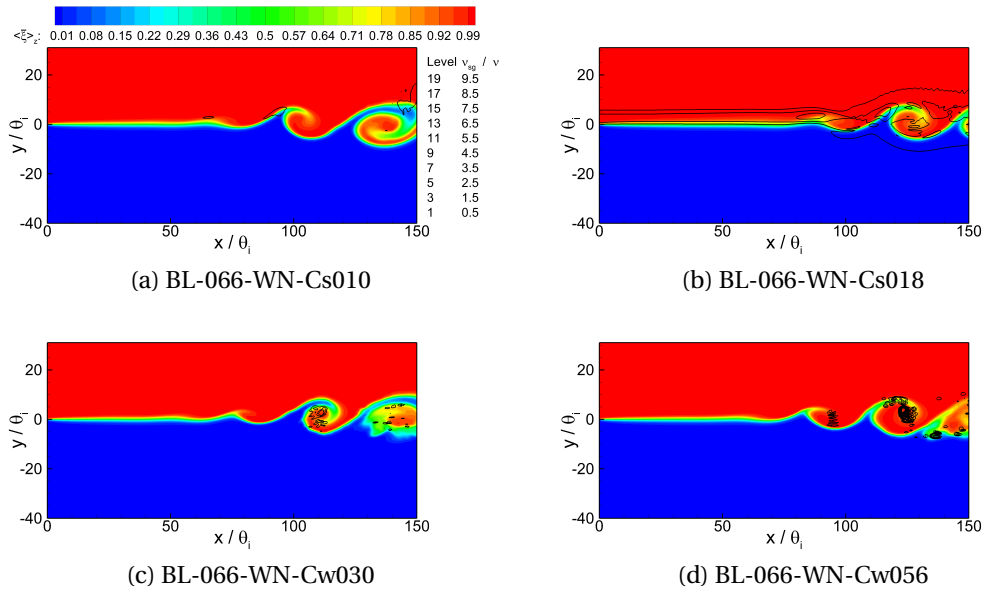


Figure 4.34: Contour maps of instantaneous passive scalar concentration and contour lines of the ratio of the subgrid to molecular viscosity for (a) BL-066-WN-Cs010, (b) BL-066-WN-Cs018, (c) BL-066-WN-Cw030, and (d) BL-066-WN-Cw056.

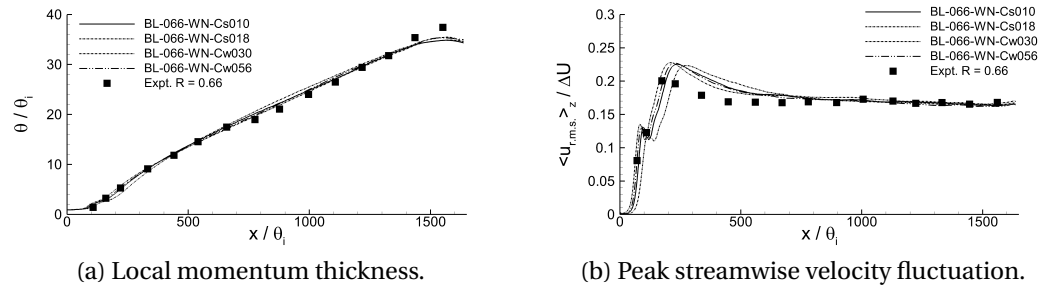


Figure 4.35: Local momentum thickness and peak streamwise velocity fluctuation.

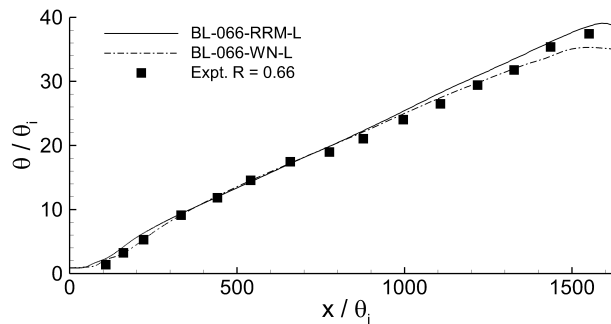


Figure 4.36: Local momentum thickness for BL-066-WN-L and BL-066-RRM-L

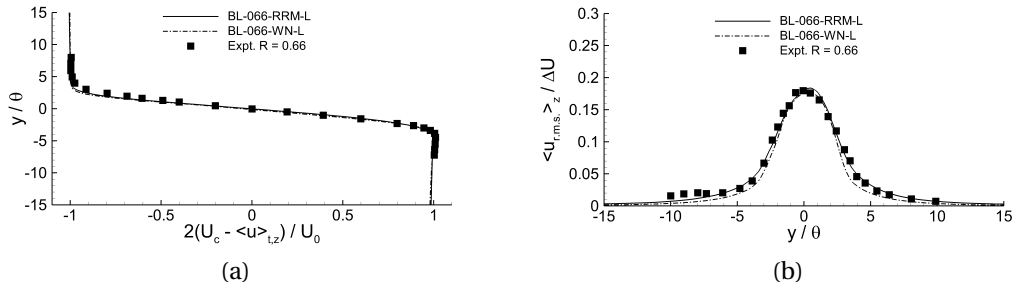


Figure 4.37: Flow statistics at $x/\theta_i = 1000$.

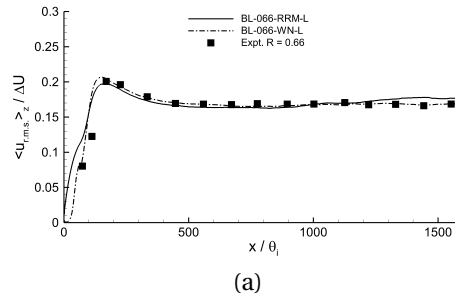


Figure 4.38: Peak normalised streamwise velocity fluctuation.

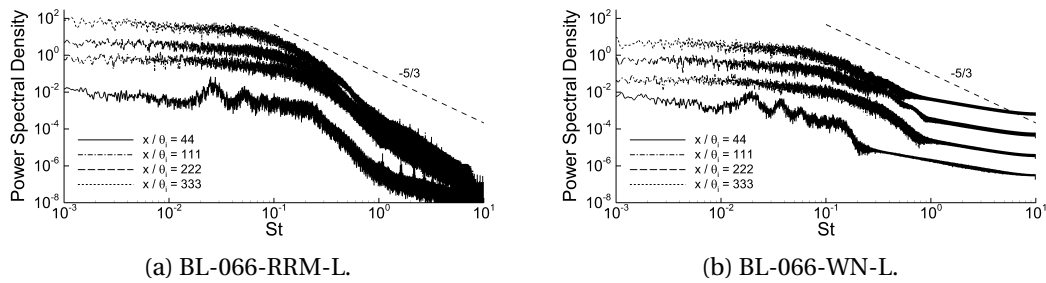


Figure 4.39: Streamwise velocity fluctuation spectral plots along the mixing layer centreline. Spectra have been shifted along vertical axis for clarity.

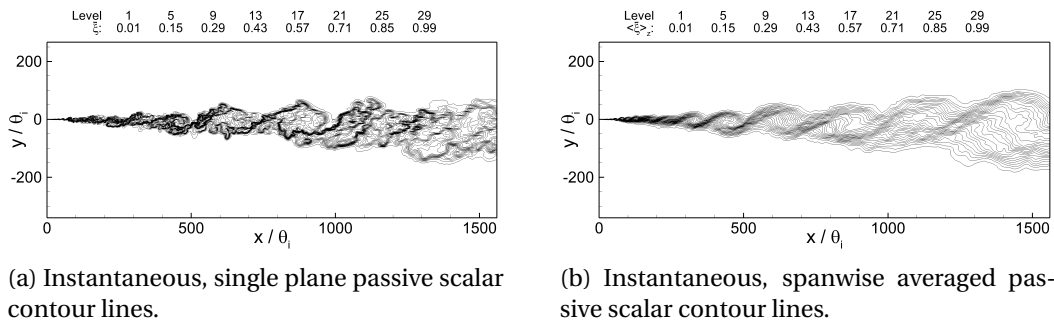


Figure 4.40: Instantaneous, single plane and spanwise averaged passive scalar contour lines for BL-066-RRM-L.

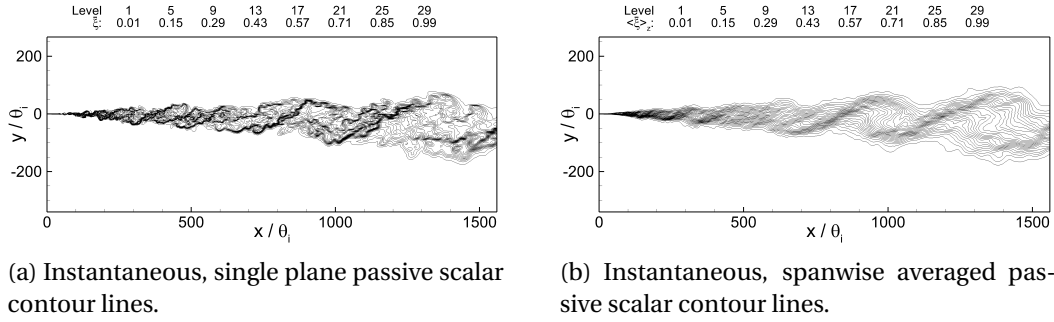


Figure 4.41: Instantaneous, single plane and spanwise averaged passive scalar contour lines for BL-066-WN-L.

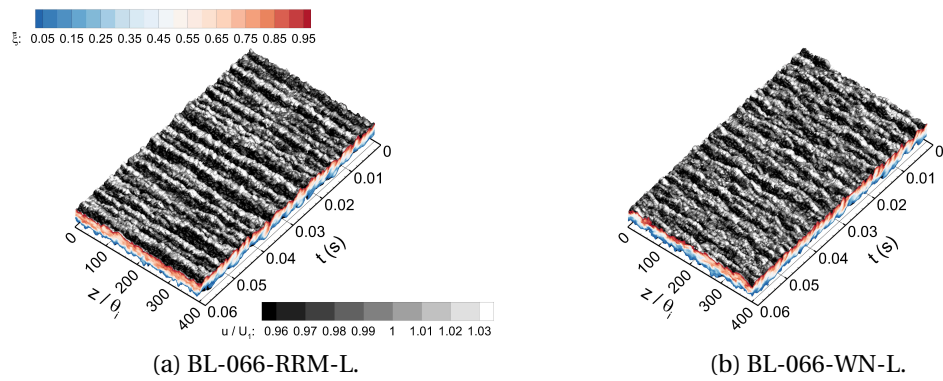


Figure 4.42: Perspective view of the mixing layer at measurement station 4.

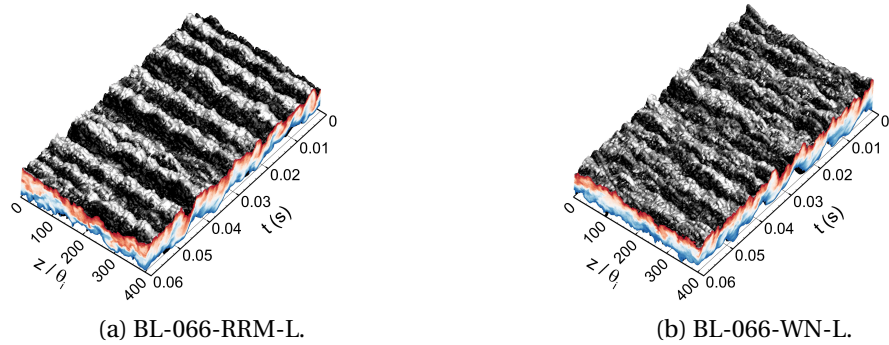


Figure 4.43: Perspective view of the mixing layer at measurement station 5.

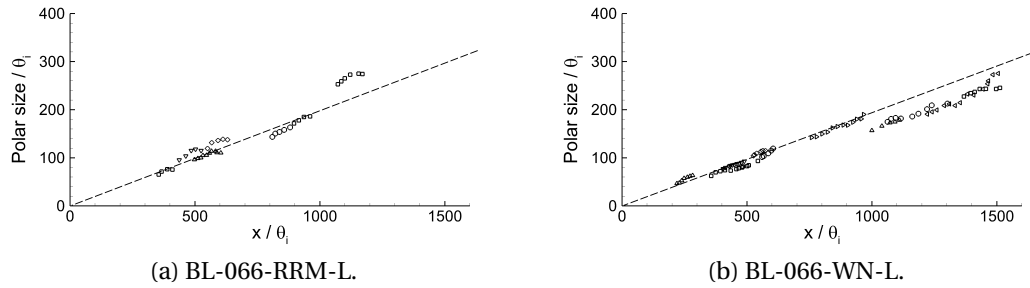


Figure 4.44: Structure diameter growth tracks.

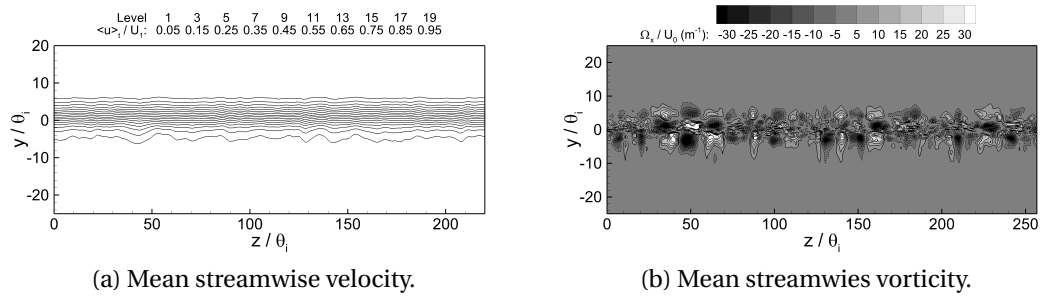


Figure 4.45: Mean streamwise velocity and mean streamwise vorticity $y - z$ cross-planes for BL-066-RRM-L at measurement station 2.

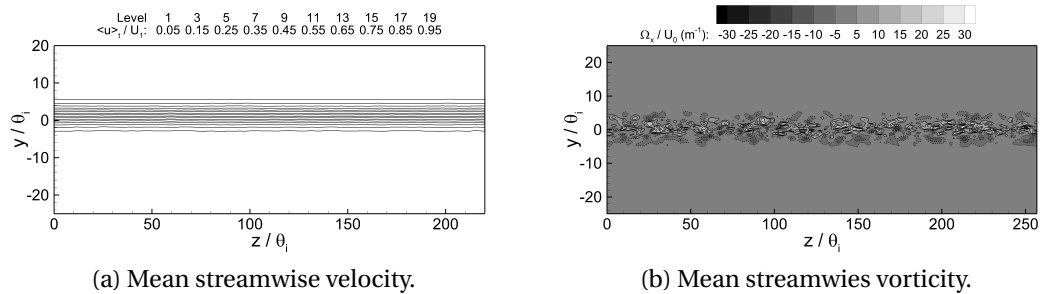


Figure 4.46: Mean streamwise velocity and mean streamwise vorticity $y - z$ cross-planes for BL-066-WN-L at measurement station 2.

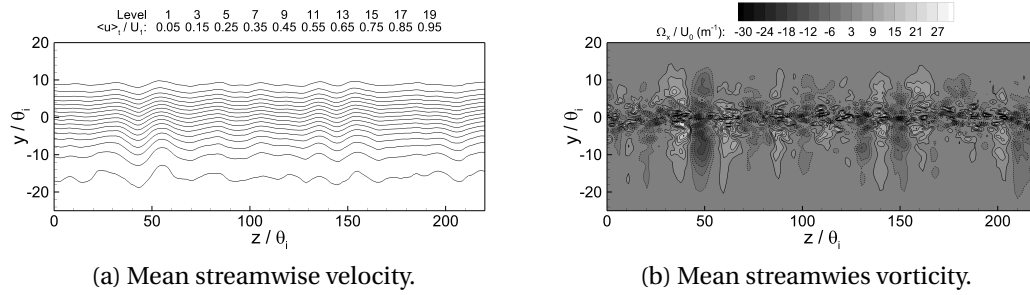


Figure 4.47: Mean streamwise velocity and mean streamwise vorticity $y - z$ cross-planes for BL-066-RRM-L at measurement station 3.

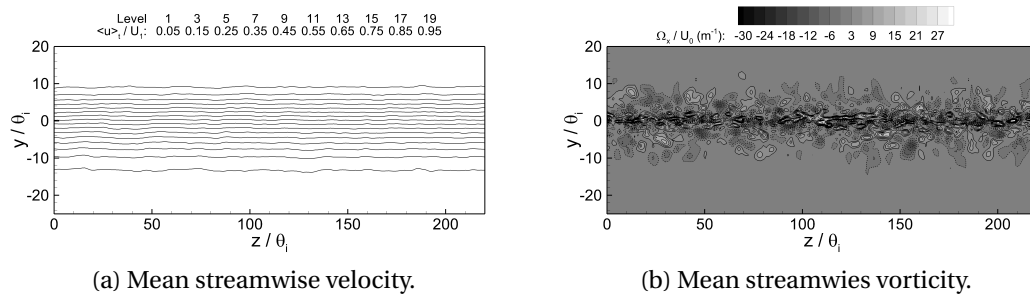


Figure 4.48: Mean streamwise velocity and mean streamwise vorticity $y - z$ cross-planes for BL-066-WN-L at measurement station 3.

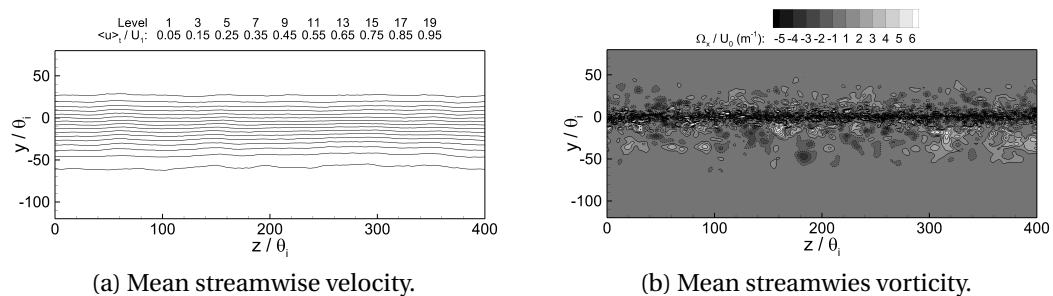


Figure 4.49: Mean streamwise velocity and mean streamwise vorticity $y - z$ cross-planes for BL-066-RRM-L at measurement station 5.

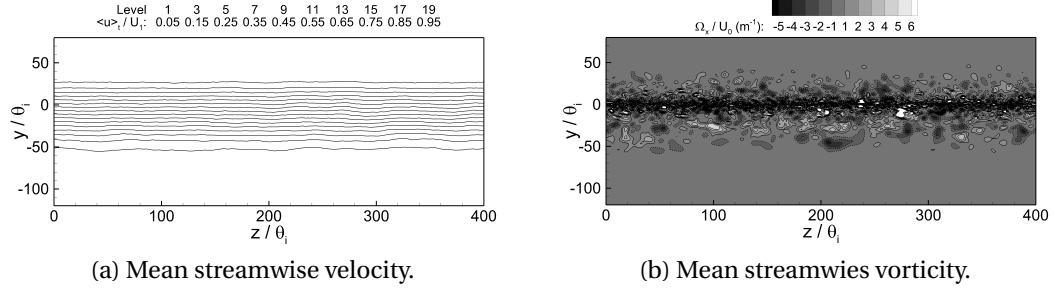


Figure 4.50: Mean streamwise velocity and mean streamwise vorticity $y - z$ cross-planes for BL-066-WN-L at measurement station 5.

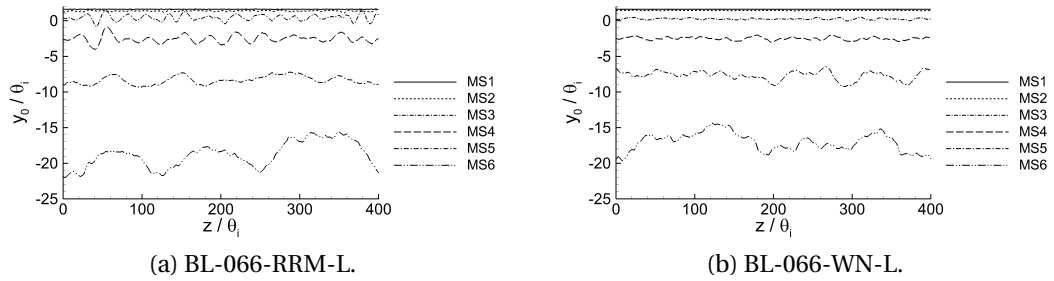


Figure 4.51: Centreline locus plots at measurement stations 1 to 6.

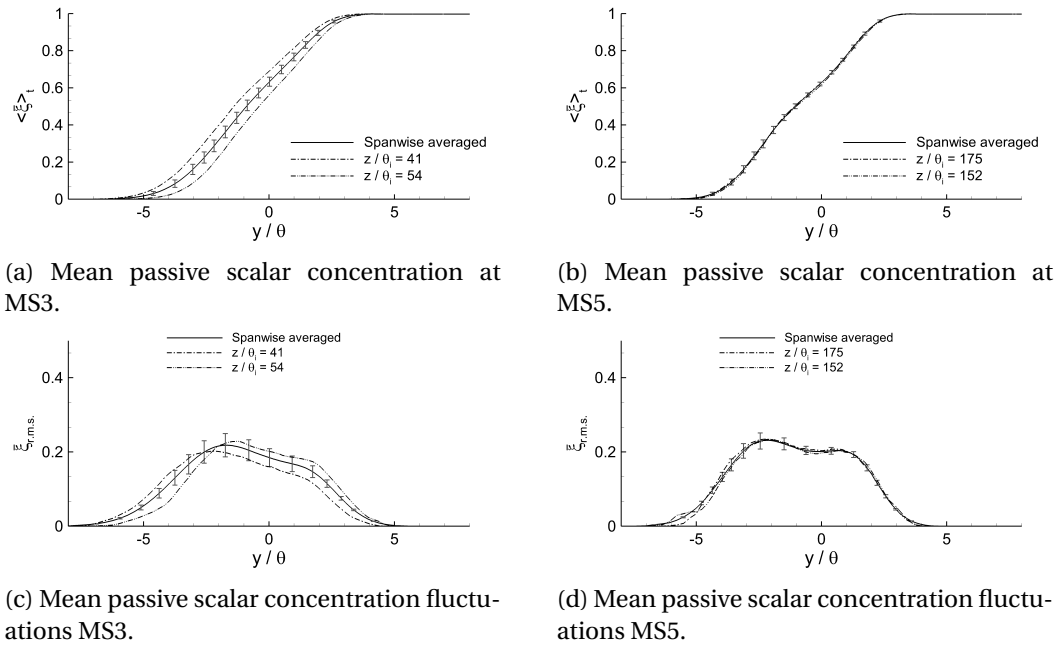


Figure 4.52: Passive scalar statistics for BL-066-RRM-L at measurement station 3 and 5.

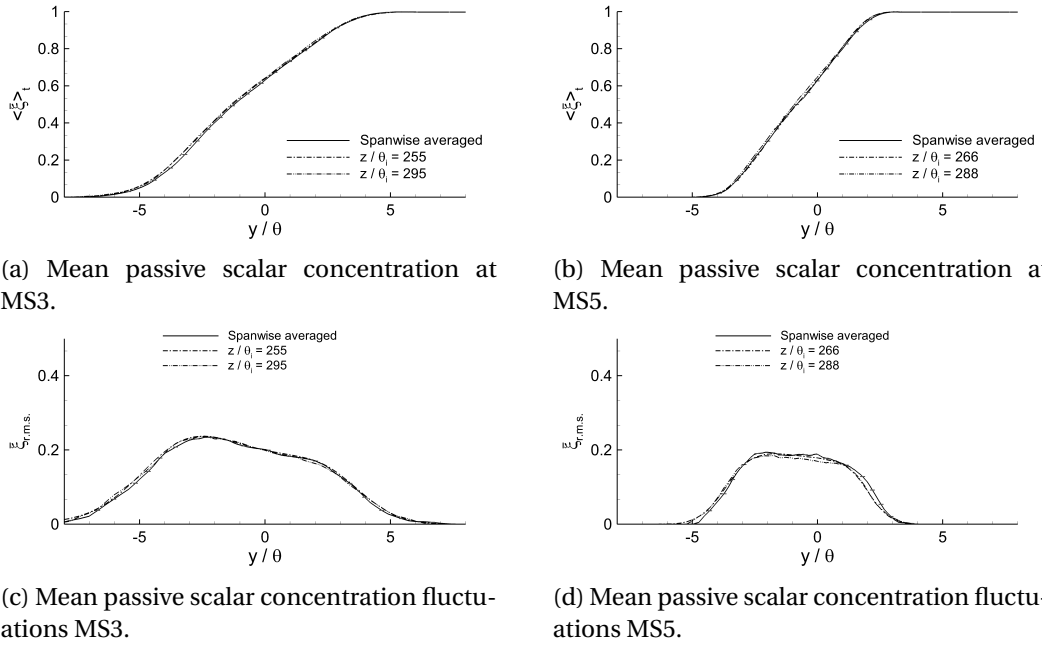


Figure 4.53: Passive scalar statistics for BL-066-WN-L at measurement station 3 and 5.

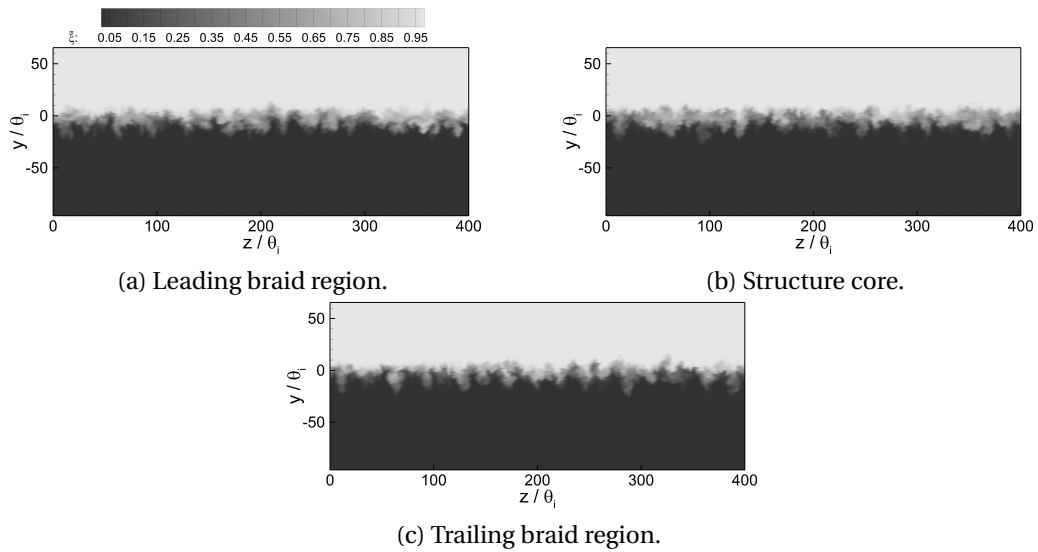


Figure 4.54: Passage of primary roller structure in the BL-066-RRM-L simulation at measurement station 3.

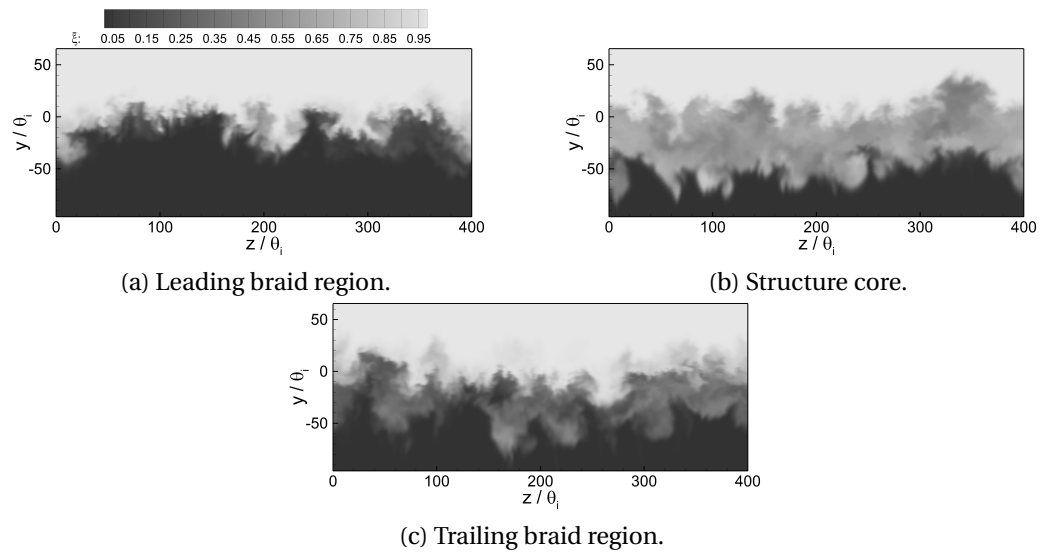


Figure 4.55: Passage of primary roller structure in the BL-066-RRM-L simulation at measurement station 5.

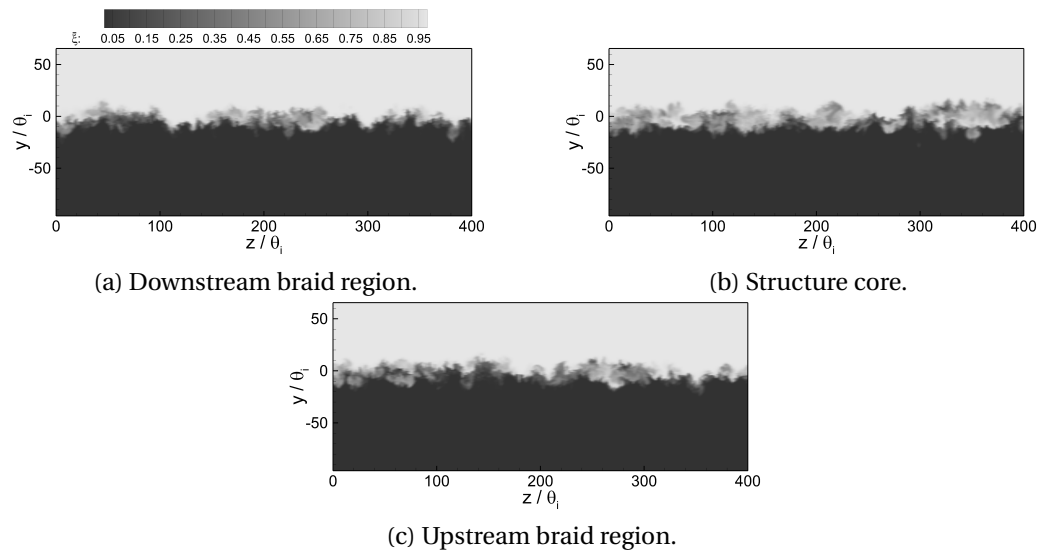


Figure 4.56: Passage of primary roller structure in the BL-066-WN-L simulation at measurement station 3.

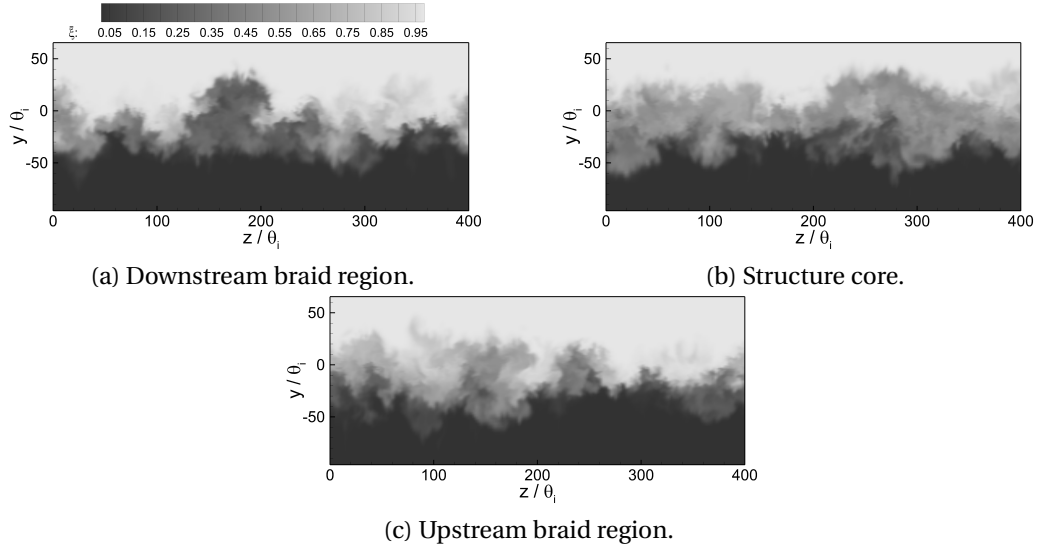


Figure 4.57: Passage of primary roller structure in the BL-066-WN-L simulation at measurement station 5.

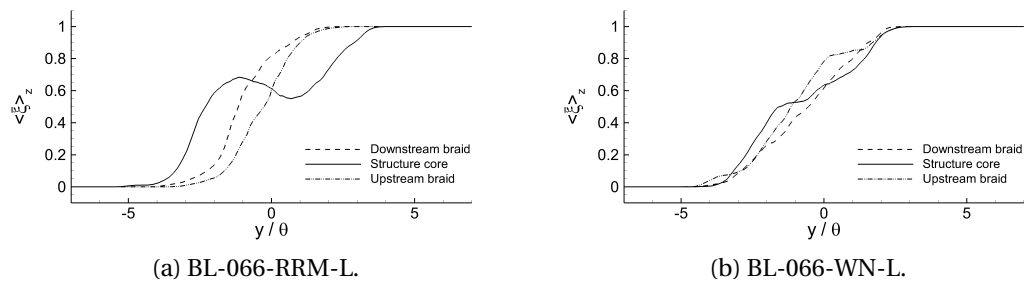


Figure 4.58: Spanwise averaged passive scalar concentration during a structure passage at measurement station 5.

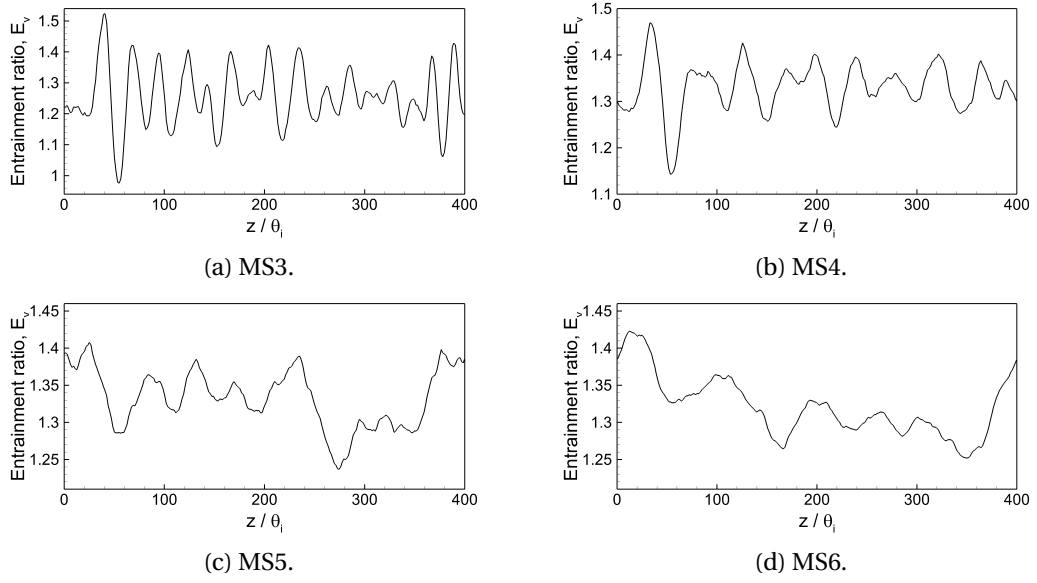


Figure 4.59: Entrainment ratio for BL-066-RRM-L.

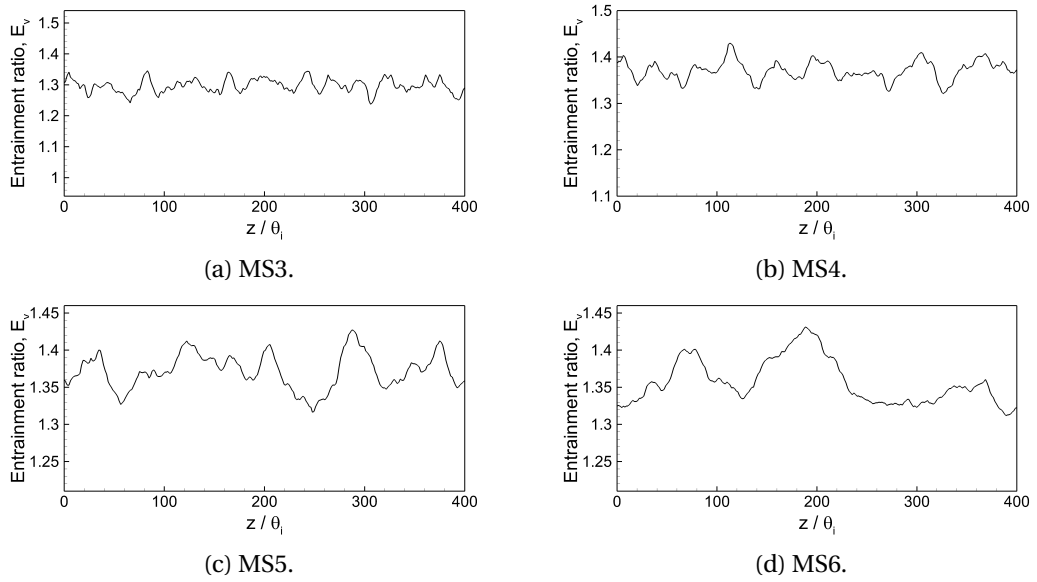


Figure 4.60: Entrainment ratio for BL-066-WN-L.

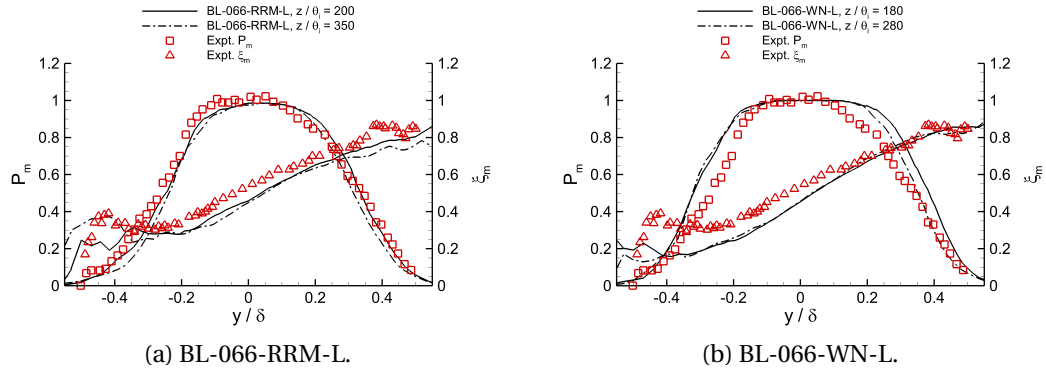


Figure 4.61: Mixed fluid statistics at measurement station 6.

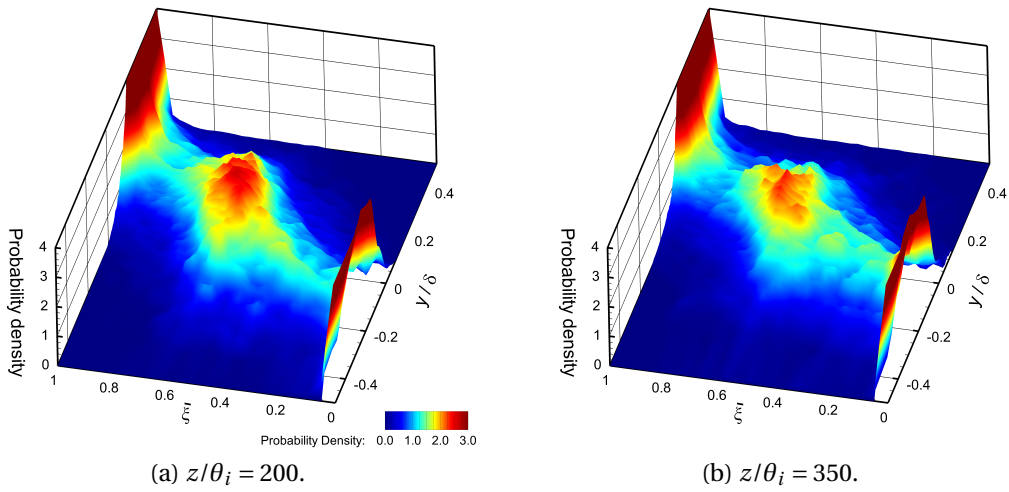


Figure 4.62: Probability density function for BL-066-RRM-L at measurement station 6 at two spanwise locations.

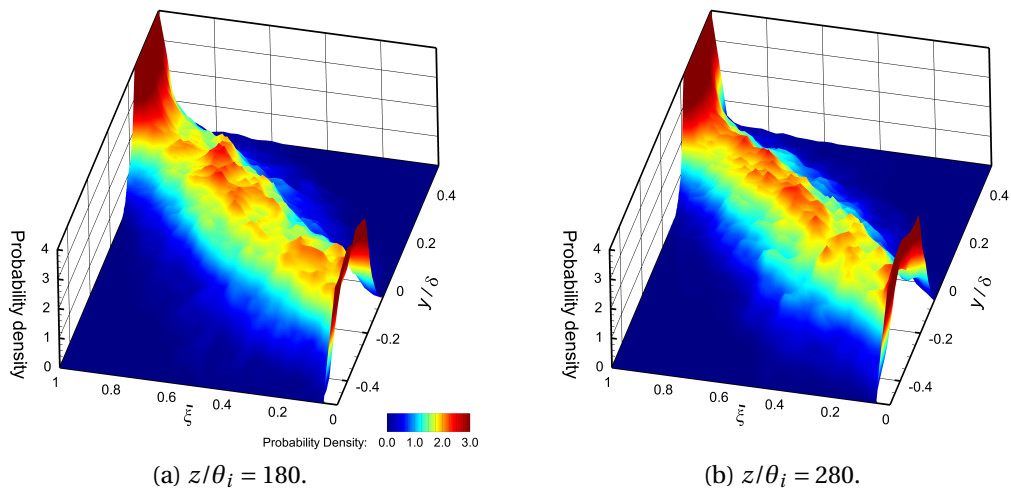


Figure 4.63: Probability density function for BL-066-WN-L at measurement station 6 at two spanwise locations.

Chapter 5

Parametric Study of the High Reynolds Number Mixing Layer

In this chapter small changes in the inlet boundary layer fluctuation magnitude, velocity ratio and the high-speed inlet boundary layer momentum thickness are investigated using simulations based on physically correlated inlet fluctuations. The simulations with varying velocity ratio values agree well with experimental data and theories. A critical aspect of the inlet condition is shown to be the inlet boundary layer fluctuation magnitude which affects the streamwise vortex structure persisting into the self-similar, far-field region of the mixing layer.

5.1 Introduction

In Chapter 4.2, two large eddy simulations with differing inlet conditions have been presented. The first simulation, BL-066-WN-L, was based on inlet conditions with pseudo random velocity fluctuations that matched a desired profile and intensity. The second simulation, BL-066-RRM-L was based on an inlet generation method which uses a recycling-rescaling method by Xiao *et al.*[37], that produces spatially correlated inlet fluctuations. Besides the spatial correlation of the inlet fluctuations, all other simulation parameters were kept constant.

Case	R	U_1 (m/s)	U_2 (m/s)	θ_1 (mm)	θ_2 (mm)
Browand & Latigo [45]	0.69	25.5	4.6	0.457	0.86
Meyer <i>et al.</i> [94] Case 1	0.44	29.5	12.8	0.179	0.32
Meyer <i>et al.</i> [94] Case 2	0.49	42.0	14.1	0.140	0.32
Meyer <i>et al.</i> [94] Case 3	0.60	50.5	12.8	0.140	0.32

Table 5.1: Summary of flow properties for reference dataset by Browand & Latigo [45] and Meyer *et al.* [94].

It was found that the spatial and temporal correlation of inlet fluctuations in the inlet boundary layer, leads to stationary, streamwise oriented vortex structures. Such streamwise oriented vortices have previously been observed in experiments, in the pre- and post-transition region of comparable mixing layers [47]. Overall, the simulation utilising spatially correlated inlet fluctuations showed agreement with experimental data than the idealised simulation. Special attention was paid to the effect of these secondary structures on passive scalar transport and mixing. Interestingly, the presence of secondary structures lead to a change in the probability density function from a *marching* to a *non-marching* type with a preferred concentration which showed very good agreement to comparable p.d.f.'s observed in experiments. Based on the conclusion that spatial correlation of the inlet boundary layer fluctuation is necessary to produce spatially stationary, streamwise oriented vortex structures, the presented simulations in this chapter exclusively use the recycling-rescaling inlet generation method.

The aim of this chapter is to investigate the effect of changing inlet conditions in a high Reynolds number mixing layer. Particular attention is paid to the secondary, streamwise oriented vortex structure and passive scalar mixing. The chapter is divided into three sections; the first section investigates the effect of the inlet boundary layer fluctuation magnitude. The second section is a parameter testing of the velocity ratio, R , and the final section investigates the role of the inlet boundary layer momentum thickness.

Simulation	R	U_1 (m/s)	U_2 (m/s)	θ_1 (mm)	θ_2 (mm)	u'/U_1 (%)
BL-066-RRM-L	0.66	25.6	5.2	0.457	0.81	1.0
BL-066-RRM-M	0.66	25.6	5.2	0.457	0.81	1.8

Table 5.2: Simulation parameters.

Station	x (m)	x/θ_1	x_1^*	Re_δ
MS1	0.0180	40	0.88	7342
MS2	0.0380	83	1.86	15043
MS3	0.0690	151	3.37	26326
MS4	0.1330	291	6.50	51040
MS5	0.2695	590	13.17	103693
MS6	0.5390	1180	26.35	207028

Table 5.3: Measurement stations.

5.2 Inlet Fluctuation Magnitude

5.2.1 Simulation Setup

The presented simulations are based on the experiments by Brown & Latigo [45] of high Reynolds number mixing layers. The experimental conditions were described in Chapter 4.2, Section 4.2.2. The mean streamwise velocity profile and the mean velocity fluctuations at the splitter plate trailing edge are shown in Figure 5.1. In both simulations, the low-speed stream utilises the BL-066-RRM-L velocity fluctuation profiles. The inlet mean streamwise velocity profile, shown in Figure 5.1a, matches the experimental data well and is a good approximation of a Blasius profile. The inlet velocity fluctuations for BL-066-RRM-L and BL-066-RRM-M are shown in Figure 5.1b and 5.1c, respectively. The peak streamwise velocity fluctuation magnitude is $\approx 1.0\%U_1$ for the BL-066-RRM-L simulation and $\approx 1.8\%U_1$ for BL-066-RRM-M.

The outflow condition is of a standard advective type and ensures global mass conservation inside the computational domain. In line with the reference experiment, the upper and lower guidewalls are unangled and are modelled as free-slip boundaries. The spanwise domain boundaries are periodic. The time step for the pre-

sented simulations is chosen as $\Delta t = 6 \times 10^{-7}$ s and the maximum CFL number is kept below 0.35 during the entire simulation. The passive scalar has a value of unity and zero in the high- and low-speed inlet stream, respectively.

The presented simulation utilise the same grid dimensions and grid resolutions as the simulations in Chapter 4.2. The WALE sub-grid scale model with a model constant value of $C_w = 0.56$ has been chosen based on the sub-grid scale validation results in Section 4.2. A detailed grid and model validation is presented in Section 4.2.

The reported statistics data have been obtained over a period of fifteen convective flow-through times, where one flow-through time is based on the convection velocity of the flow, $U_c = (U_1 + U_2)/2$. Single plane and spanwise averaged, $x - y$ flow visualisations are recorded at a frequency of 3.3 kHz. At five streamwise measurement stations, cross-planes ($y - z$) are recorded at a frequency of 3.3 kHz. The measurement stations are listed in 5.3. Spatial coordinates have been normalised with respect to the initial momentum thickness of the flow, θ_i which was reported to be identical to the momentum thickness of the high-speed boundary layer, θ_1 [45]. Furthermore, the streamwise distance from the splitter plate trailing edge is also expressed in terms of the local pairing parameter, $x_i^* = Rx/30\theta_i$ [60, 91].

5.2.2 Results

5.2.2.1 Velocity Statistics

Normalised mean streamwise velocity profiles recorded, at $x/\theta_i = 1000$, are shown in Figure 5.2a. Both simulations show very good agreement with the reference dataset and a typical self-similar velocity profile. Streamwise velocity fluctuations at $x/\theta_i = 1000$ are shown in Figure 5.2b. Both simulations capture the peak velocity fluctuation magnitude as well as the free-stream velocity fluctuation levels well. The peak streamwise velocity fluctuation magnitude, as a function of streamwise distance from the splitter plate trailing edge, is shown in Figure 5.2c. The value of the maximum streamwise velocity fluctuation is predicted well, but the peaks in the simulations are located slightly closer to the trailing edge of the splitter plate than was

reported in the reference data. Similar observations have been made in comparable numerical simulations [21]. In the far-field, asymptotic region of the mixing layer both simulations reproduce the experimental value well.

Power spectra density plots taken at $x/\theta_i = 44$ and $x/\theta_i = 219$ for BL-066-RRM-L and BL-066-RRM-M, are shown in Figure 5.3a and Figure 5.3b, respectively. The peak in the spectra at $x/\theta_i = 44$ occurs at $St \approx 0.0284$ in both simulations. Further downstream, at $x/\theta_i = 219$, the spectra in both simulations, approaches the $k^{-5/3}$ slope, indicative of a fully developed turbulent flow.

The local momentum thickness for both simulations are shown in Figure 5.4, together with the reference data. Both simulations produce an initially flat region, followed by a short region of high momentum growth, followed by an asymptotic, linear region of growth. Self-similarity is attained in both simulations at $x/\theta_i \approx 350$. Both simulations produce a growth rate value of $k_m \approx 0.036$ which is in very good agreement with the reference value of $k_m \approx 0.0357$.

From analysis of the mean statistics the two simulations are virtually identical. In the next section the flow structure and passive scalar data is investigated in more detail.

5.2.2.2 Flow Visualisation

Instantaneous single-plane and spanwise averaged passive scalar flow visualisations for BL-066-RRM-L and BL-066-RRM-M are shown in Figure 5.5 and Figure 5.6, respectively. Qualitatively similar, spanwise coherent, primary vortex structures are easily identified in both simulations. Individual primary structures can easily be recognised in both, the single-plane and spanwise averaged visualisations.

Perspective views for BL-066-RRM-L at measurement stations 3 and 5 are shown in Figure 5.7. At measurement station 3, shown in Figure 5.7a, roller type structures are visible. At measurement station 5, located downstream of the transition, the primary structures have increased in size but are still of a quasi-two-dimensional appearance. Streamwise velocity over-speeds on top of the structures and dark braid

regions indicate that the spanwise vorticity is contained inside the primary vortices.

The perspective views for BL-066-RRM-M at measurement station 3, shown in Figure 5.8, are qualitatively similar to those for BL-066-RRM-L. At measurement station 5 the perspective view is qualitatively less regular and an increased number of structure interactions are visible. During time instances without vortex interactions the flow is well organised into regular primary vortices and regular braid regions.

Figure 5.9 shows the vertical diameter of individually tracked structures. Individual structures have been tracked from their ‘birth’ to an eventual interaction with a neighbouring structure. The growth of the primary vortices is similar in both simulations and best approximated by a square root of time growth [21]. Square root of time growth has been observed in experiments [98] and numerical simulations based on recycling-rescaling type inlet fluctuations [21].

5.2.2.3 Streamwise Vortex Structure

The primary vortex structure in both simulations has shown to be qualitatively similar. In this section the effect of a small inlet fluctuation change on the secondary, spatially stationary streamwise vortex structure is evaluated.

In addition to the previously listed measurement stations, an additional cross-plane ($y - z$) is placed $26\theta_i$ upstream of the splitter plate trailing edge. Mean streamwise vorticity plots, Ω_x , at this location are shown in Figure 5.10a and 5.11a. In comparison, the mean streamwise vorticity patches in BL-066-RRM-L are seen to be fewer in number and lower in magnitude, compared to BL-066-RRM-M. The peak streamwise vorticity in BL-066-RRM-M is about 14% higher than that in BL-066-RRM-L. In the RRM inlet generation method the inlet fluctuations are rescaled based on the spanwise averaged value of the streamwise velocity fluctuation magnitude. This allows larger streamwise vortices to grow while still satisfying the desired spanwise averaged inlet fluctuation magnitude. This explains the 14% higher peak streamwise vorticity from a 1% increase in the spanwise averaged inlet streamwise velocity fluctuation magnitude. Mean streamwise vorticity planes at measurement station 2, located in the region of the first roll-up which occurs at $x_i^* \approx 2$, are shown in Figure

5.10b and 5.11. Three-tiered vorticity clustering is evident in both simulations. The peak magnitudes of the streamwise vorticity are higher in the BL-066-RRM-M simulation. Careful investigation of the vorticity data shows that strong vorticity clusters observed at MSA have remained spatially stationary and developed into three-tiered clusters.

Cross-planes at measurement station 3 are shown in Figure 5.10c and 5.11c. MS3 is located in the region of the second pairing interaction at $x_i^* \approx 4$. The streamwise vorticity has unwrapped from three-tiered clusters at MS3 into a single row of alternating sign vorticity clusters. This rearrangement process has been observed in experiments [88] as well as numerical simulations [21]. Individual vorticity clusters can easily be traced through the upstream measurement stations beginning at MSA. Figure 5.10d and 5.11d show Ω_x at measurement station 4, located in the post-transition region of the mixing layer. Clusters of mean streamwise vorticity are still present, showing the persistence of the streamwise vortices through the mixing transition. Direct comparison between BL-066-RRM-L and BL-066-RRM-M suggests that the increased energy contained in the BL-066-RRM-M streamwise structures helps to stabilise them through the mixing transition.

The effect of the secondary, spatially stationary streamwise vortices on the velocity field can be quantified using mixing layer centreline locus plots, shown in Figure 5.12. While the number of undulations is similar for both simulations, the undulation magnitudes are considerably higher for BL-066-RRM-M than BL-066-RRM-L. At MS4 the peak amplitude in BL-066-RRM-M is approximately double of that in BL-066-RRM-L. After the mixing layer transition, individual peaks and troughs of the centreline are visible for both simulations. At the last measurement station the undulation amplitudes are similar for both simulations.

Quantitative data on the secondary, streamwise oriented vortex structure is produced by measuring the average streamwise structure spacing, s . Figure 5.13a shows the streamwise structure spacing with increasing distance from the splitter plate trailing edge. As the spatially stationary streamwise vortices re-arrange themselves from three-tiered clusters to a single row of alternating sign vortices, the streamwise structure spacing decreases [88], this process is captured well in both simulations. After the transition which occurs between MS4 and MS5, the number of streamwise

oriented vortices is larger in the BL-066-RRM-L than the BL-066-RRM-M simulation. The ratio of the spanwise wavelength of the streamwise vortices and the vorticity thickness of both simulations as a function of pairing parameter, is shown in Figure 5.13b. In the pre-transition region, the difference between the two simulations is small. In the post-transition, self-similar region of the mixing layer, $\Lambda/\delta_\omega \approx 0.95$ for BL-066-RRM-L and $\Lambda/\delta_\omega \approx 1.0$ for BL-066-RRM-M. These values are in the range reported in experiments of $\Lambda/\delta_\omega \approx 0.8 - 1.28$ [54, 47, 52].

5.2.2.4 Passive Scalar Mixing

The presented mean flow statistics and cross-plane data suggest that the spatially stationary streamwise vortex structures are stronger in the higher fluctuation simulation. In this section, the effect of the inlet fluctuation magnitude on the passive scalar entrainment and mixing is investigated.

The entrainment ratio as a function of spanwise location at measurement stations 3 and 5 is shown in Figure 5.14. The vertical axis is kept constant to visualise the decrease in the entrainment ratio amplitude between the pre- and post-transition. At measurement station 3, BL-066-RRM-M shows larger variations than BL-066-RRM-L, likely as a result of the stronger spatially stationary streamwise vortex structures. In both simulations, the amplitude of the entrainment ratio variations across the span decreases rapidly during the mixing transition. Table 5.4 lists the maximum, minimum, and spanwise averaged entrainment ratios. The spanwise averaged entrainment ratio values at measurement station 5, of $E_\nu = 1.33$ and 1.32 for BL-066-RRM-L and BL-066-RRM-M, respectively, are lower than the value of $E_\nu = 1.45$ predicted by the Dimotakis [56] model for the presented flow parameters. However, for a single spanwise location, the simulations are within 2% and 5% of the Dimotakis model for BL-066-RRM-L and BL-066-RRM-M.

The effect of the spatially stationary streamwise vortex structures on the entrainment ratio in a spanwise sense can be quantified by comparing the standard deviation of the entrainment ratio as a function of downstream distance, shown in Figure 5.15. In both simulations the entrainment ratio variation peaks in between the primary roll-up at $x_i^* \approx 2$ and the third pairing event at $x_i^* \approx 8$. An increase in the

Simulation	Measurement station	$E_{v,\min}$	$E_{v,\max}$	$E_{v,z}$
BL-066-RRM-L	MS3	0.98	1.52	1.25
BL-066-RRM-L	MS5	1.24	1.41	1.33
BL-066-RRM-L	MS6	1.25	1.42	1.31
BL-066-RRM-M	MS3	0.95	1.62	1.26
BL-066-RRM-M	MS5	1.23	1.41	1.32
BL-066-RRM-M	MS6	1.21	1.38	1.28

Table 5.4: Entrainment ratios in the pre-transition (MS3) and post-transition (MS5 & MS6) region of the mixing layer.

inlet fluctuation magnitude moves the peak downstream. The peak in the variation magnitude corresponds to the area in which the secondary spatially stationary streamwise vortex structures re-arrange themselves from three-tiered clusters into a single row of counter rotating vortices. The data suggests that the increase in the inlet fluctuation magnitude leads to stronger, spatially stationary streamwise vortices that take a longer time to re-arrange from three-tiered type vorticity arrangements to a single row of counter rotating vortices. In self-similar region the streamwise vortices are arranged in a single row of counter rotating vortices and both simulations asymptote to a similar level of entrainment ratio variation.

Figure 5.16 shows the mixed fluid statistics for both simulations at measurement station 6. Experimental data by Meyer *et al.* [94], recorded at $R = 0.60$, $x_i^* = 28.1$, $Re_\delta = 103000$ have been included for guidance purposes and should not be understood as a like-for-like comparison. For each simulation, two spanwise locations are reported; one where the local entrainment is at a maximum and the other where the local entrainment is at a minimum. In both simulations the mixed fluid probability, P_m , does not attain a value of unity. This demonstrates that unmixed high-speed fluid penetrates across the mixing layer centreline. A non-unity peak value of P_m is evidence of the engulfment entrainment mechanism. At the peak entrainment location, BL-066-RRM-M reproduces the experimental mixed fluid probability better than BL-066-RRM-L.

ξ_m denotes the average mixed fluid concentration found at any vertical location in the mixing layer. Both simulations show an increase in the passive scalar concentration in the low-speed outer region of the mixing layer. This reversal is indicative of

disproportionately high amounts of high-speed fluid being entrained into the low-speed side of the mixing layer. This is another good indicator of the engulfment entrainment mechanism.

Probability density functions for BL-066-RRM-L are shown in Figure 5.17. At both spanwise locations the p.d.f.'s are of the *non-marching* type. At the entrainment peak location the preferred concentration is $\bar{\xi} = 0.58$. At the second spanwise location the peak in the preferred scalar value is broader with lower probability density values but is still of the *non-marching* type. The p.d.f.'s for BL-066-RRM-M at measurement station 6 are shown in Figure 5.18. At both spanwise locations the p.d.f.'s are of the *non-marching* type but compared to those for BL-066-RRM-L, the probability density values are higher at the peaks. The preferred concentration is $\bar{\xi} = 0.60$ which is in very good agreement with comparable data by Konrad [50] who measured a preferred concentration of $\xi = 0.60$ for a mixing layer of $R = 0.38$. The observed *non-marching* p.d.f.'s are also an indication of the engulfment entrainment mechanism [50]. It has been suggested that the *non-marching* p.d.f. shape is linked to the engulfment entrainment mechanism. The reasoning behind this is that rapid engulfment of free-stream fluid is required to produce a clearly preferred concentration value inside the mixing layer [47].

5.2.3 Summary

The effect of a small change in the streamwise velocity fluctuation in the high-speed inlet boundary layer has been investigated. The peak streamwise velocity fluctuation in the high-speed boundary layer has been chosen as 1.0% and 1.8% for the BL-066-RRM-L and BL-066-RRM-M simulations, respectively. With the exception of the streamwise velocity fluctuation in the high-speed boundary layer, all other simulation parameters have been kept constant.

A small change in the streamwise velocity fluctuation magnitude does not result in a measurable difference in the mean flow statistics. Single plane and spanwise averaged imagery of the primary flow structure are qualitatively similar in the presented simulations. However, the small change in the inlet condition has a quantifiable ef-

fect on the secondary, streamwise vortex structure. The measured changes are small in the near-field of the mixing layer. In the transition and post-transition region, an increase of the inlet fluctuation magnitude increases the strength of the individual streamwise oriented vortex structures.

The small change in the inlet condition is also shown to affect the passive scalar field. While the presented p.d.f.'s are all of the *non-marching* type, and show a similar preferred concentration, the p.d.f.'s for BL-066-RRM-M show a higher value for the probability density and more distinct peaks, compared to BL-066-RRM-L.

The simulations have shown that even very small changes in the inlet boundary layer conditions have a quantifiable effect on the momentum and passive scalar fields. For both simulations, large spanwise variations are observed and even a very small increase in the inlet fluctuation magnitude leads to a further increase in the spanwise variation. It has previously been suggested by Bell *et al.* [103] that the spanwise variation of mixing layer data might lead to significant misinterpretations of the results. The author agrees with Bell *et al.* [103] regarding the importance of accounting for spanwise variations. Higher levels of inlet boundary layer fluctuation magnitudes are investigated further in Chapter 6.

5.3 Velocity Ratio Effects

5.3.1 Introduction

In this section, the effect of changes of the inlet velocity ratio is investigated. To vary the velocity ratio, the low-speed inlet velocity is changed while keeping the high-speed inlet velocity constant. In the previous section, the -M inlet fluctuation magnitude has shown better agreement with experimental data and has therefore been chosen as the desired fluctuation magnitude for the hereafter presented simulations. Data obtained in the BL-066-RRM-M simulation is compared against reference data by Browand & Latigo [45].

Simulation	R	U_1 (m/s)	U_2 (m/s)	θ_1 (mm)	θ_2 (mm)	u'_{\max}/U_1 (%)
BL-039-RRM-M	0.39	25.6	11.2	0.457	0.81	1.8
BL-052-RRM-M	0.52	25.6	8.0	0.457	0.81	1.8
BL-066-RRM-M	0.66	25.6	5.2	0.457	0.81	1.8

Table 5.5: Simulation parameters.

5.3.2 Simulation Setup

The presented simulations are summarised in Table 5.5. The high-speed velocity is kept constant for all simulations, and the low-speed inlet velocity is altered to vary the resulting velocity ratio, R . To isolate the effect of changing the velocity ratio, all other simulation parameters are kept constant. The -M, $1.8\%U_1$, inlet fluctuation magnitude is shown in Figure 5.1c and is used for all hereafter presented simulations.

5.3.3 Results

5.3.3.1 Velocity Statistics

The mean streamwise velocity profiles, recorded at $x/\theta_i = 1000$, are shown in Figure 5.19a. The simulations show very good agreement with experimental data for $R = 0.66$. Figure 5.19b shows the mean streamwise velocity fluctuation at $x/\theta_i = 1000$. In the centre of the mixing layer, the simulations match the experimental data for $R = 0.66$ closely. In the outer regions of the mixing layer, BL-066-RRM-M shows some over-prediction of the fluctuation magnitude. The maximum streamwise velocity fluctuation with downstream distance from the splitter plate is shown in Figure 5.19c. The trend of a peak with a subsequent relaxation to an asymptotic value is similar for all the presented velocity ratios. The maximum value of the streamwise velocity fluctuation is captured well in the BL-066-RRM-M simulation, however, the peak is located slightly closer to the splitter plate than in the reference data. The self-similar, asymptotic value of the maximum streamwise velocity fluctuation is very similar in each simulation and in good agreement with the reference data.

The mean flow statistics suggest that, for the imposed inlet conditions, the simulations asymptote to a particular self-similar state.

Power spectral density plots of the streamwise velocity fluctuations recorded at $x/\theta_i = 44$, are shown in Figure 5.20a. The power spectral density peaks are located at $St \approx 0.044, 0.045$ and 0.0284 for BL-039-RRM-M, BL-052-RRM-M and BL-066-RRM-M, respectively. Agreement with theoretical values of the Strouhal number is good for BL-039-RRM-M and BL-066-RRM-M, while BL-052-RRM-M over-predicts the most amplified Strouhal number slightly. At $x/\theta_i = 217$, shown in Figure 5.20b, all three simulations approach the $-5/3$ slope indicative of a fully developed turbulent flow.

Figure 5.21 shows the momentum thickness of the mixing layer for the presented simulations together with experimental data of $R = 0.66$. The momentum thickness of BL-066-RRM-M shows very good agreement with the experimental data, both in the near-field and the far-field, self-similar region of the mixing layer. The presented simulations achieve self-similarity at $x/\theta_i \approx 350$, a value which is constant for all simulations. All simulations produce a momentum growth rate constant of $k_m \approx 0.036$ which is close to the reported value of $k_m \approx 0.0357$ for $R = 0.66$ by Browand & Latigo [45] and satisfies the linear relationship in Equation 2.6.

5.3.3.2 Flow Visualisation

Single plane passive scalar flow visualisation images, taken at mid-span, are shown in Figure 5.22. The simulations show large scale vortex structures throughout the entire streamwise domain extent. Close to the splitter plate trailing edge, a single vortex sheet is visible. After the roll-up, the vortices grow and occupy the entire vertical extent of the mixing layer in the self-similar, far-field region of the mixing layer. Spanwise averaged passive scalar flow visualisation images are shown in Figure 5.23. Individual large scalar structures identified in the single plane visualisations can easily be identified in the spanwise averaged planes. The relationship between R and mixing layer growth is visually represented in the increasing size of the primary vortices.

Measurement station	x/θ_i	x_i^* ($R = 0.39$)	x_i^* ($R = 0.52$)	x_i^* ($R = 0.66$)
MS1	39	0.5	0.7	0.9
MS2	83	1.1	1.4	1.8
MS3	151	1.9	2.6	3.3
MS4	291	3.8	5.0	6.4
MS5	590	7.6	10.2	12.9
MS6	1180	15.2	20.3	25.8

Table 5.6: Measurement stations.

5.3.3.3 Streamwise Vortex Structure

As the simulations are based on different values of R , the local pairing parameter, x_i^* , at every measurement station is different for each simulation. Table 5.6 lists the measurement stations in terms of their normalised downstream distance, x/θ_i , and the local pairing parameter value. The data is normalised against U_1 which is constant for all simulations. The mean streamwise vorticity has been partially normalised by U_1 .

Cross planes ($y - z$) data at measurement station 2 for BL-039-RRM-M are shown in Figure 5.24. Small scale undulations are visible in the mean streamwise velocity and the mean passive scalar fields, shown in Figure 5.24. The mean secondary shear stress and the mean streamwise vorticity shown in Figure 5.24c and 5.24d, respectively, show an anti-correlation, evident at $z/\theta_i = 70$, which is in agreement with Wiecek *et al.* [55]. Three-tiered vorticity clustering is present in the streamwise vorticity in Figure 5.24d. The cross-plane data for BL-052-RRM-M at measurement station 2 is shown in Figure 5.25. Some wrinkling is present in the mean streamwise velocity and mean passive scalar contour plots. The secondary shear stress and streamwise vorticity plots in Figure 5.25c and 5.25d are qualitatively similar to those of BL-039-RRM-M. Two clusters of three-tiered streamwise vorticity are visible. The wrinkling in the mean streamwise velocity and mean passive scalar concentration maps for BL-066-RRM-M at MS2, shown in Figure 5.26a and 5.26b, is much more pronounced than in the other two simulations. Particularly in the low speed interface zones, several undulations of large amplitude are observable. The mean secondary shear stress plot in Figure 5.26c shows a large number of shear stress patches with high intensities. Three-tiered clustering of mean streamwise vorticity, shown in

Figure 5.26d, is also evident for BL-066-RRM-M.

Cross-plane data for BL-039-RRM-M at measurement station 4 are shown in Figure 5.27. The wrinkling of the mean streamwise velocity and the mean passive scalar fields is stronger compared to those at MS2 in Figure 5.24. The secondary shear stress and streamwise vorticity plots, shown in Figure 5.27c and 5.27d respectively, show a single row of alternating sign banding. From the mean streamwise vorticity plot, it is evident how an interface between positive to negative vorticity distorts the velocity field in Figure 5.27a, and the passive scalar field in Figure 5.27b, towards the low-speed stream. This can be observed at $z/\theta_i = 30$ and 60 . For a negative to positive change in the streamwise vorticity, the momentum and passive scalar fields are undulated towards the high-speed stream, examples of this are visible at $z/\theta_i = 40, 80$ and 210 . Undulations in the mean streamwise velocity and mean passive scalar concentration maps at measurement station 4 are also present for BL-052-RRM-M, shown in Figure 5.28a and 5.28b. Single row banding of the secondary shear stress and streamwise vorticity are also visible. Figure 5.29 shows the cross-plane data for BL-066-RRM-M at MS4. Heavy wrinkling of the mean streamwise velocity and mean passive scalar concentration fields is evident. The wrinkling in BL-066-RRM-M at MS4 is stronger compared to the other velocity ratio values. Inspection of the mean secondary shear stress in Figure 5.29c reveals a single row of alternating sign shear stress with very high peak intensities. The mean streamwise vorticity map in Figure 5.29d is reflective of the secondary shear stress map, however, the derivative nature of the streamwise vorticity maps makes their interpretation more challenging than the secondary shear stress data.

BL-039-RRM-M cross-plane data at measurement station 6 are shown in Figure 5.30. The observed undulations of the mean streamwise velocity and the mean passive scalar concentration fields suggest that the effect of the streamwise vortex structures persists into the self-similar, far-field of the mixing layer. This is shown by the mean secondary shear stress in Figure 5.30c which shows a single row type arrangement of spatially stationary streamwise structures. Compared to the upstream measurement stations the number of structures and their respective strength has decreased. Comparison of the mean passive scalar concentration plot in Figure 5.30b and the shear stress data in Figure 5.30c shows the spatially stationary streamwise structures to occupy the entire visual thickness of the mixing layer. The cross-plane data for

BL-052-RRM-M at measurement station 6, shown in Figure 5.31, shows the same trends as those observed in BL-039-RRM-M. The secondary shear stress plots suggest that fewer structures are present in BL-052-RRM-M than BL-039-RRM-M at the same measurement station. BL-066-RRM-M cross-plane data at measurement station 6 is shown in Figure 5.32. The magnitudes of the secondary shear stress, shown in Figure 5.32c, are considerably higher than those observed for the other simulations.

The centreline loci for all simulations are shown in Figure 5.33. Starting at measurement station 3, all simulations show undulations in the centreline of the mixing layer. The effect of the spatially stationary streamwise vortex structures on the momentum field is evident. The similarity between the presented centrelines and experimental streamwise velocity data, taken in the plane of the splitter plate by Bell & Mehta [47] is striking.

Quantitative data about the number of streamwise vortices is computed by calculating the mean streamwise structure spacing, s , with downstream distance from the splitter plate, shown in Figure 5.34a. As the secondary, streamwise oriented vortex structures unwrap from three-tiered formations to a single row of alternate sign vortices the streamwise structure spacing decreases. In the re-arrangement phase, the simulations show slight differences in the absolute spacing value, but the overall trend is similar. With increasing distance, the simulations start to diverge and at measurement station 6, located in the far-field, self-similar turbulent region of the mixing layer, the three simulations show significantly different values for the streamwise structure spacing. The data suggests that in the self-similar region of the mixing layer the spanwise spacing of the streamwise vortex structures is a function of the velocity ratio parameter, R .

When comparing the streamwise structure spacing as a function of downstream distance, the difference in the mixing layer growth rate, a function of R , is not taken into account. To isolate the effect of an increase in the growth rate with an increase in R , the ratio of the spanwise wavelength of the streamwise vortex structures to the local vorticity thickness is computed, shown in Figure 5.34b. After the re-organisation of the streamwise vortices, the simulations asymptote to a value of approximately unity, showing a linear relationship between the local vorticity thickness and the

Case	x_i^*	Re_δ	λ_D (mm)	Δ_{ave} (mm)
BL-039-RRM-M	15.2	64 243	0.260	0.464
BL-052-RRM-M	20.3	136 073	0.182	0.553
BL-066-RRM-M	25.8	166 810	0.183	0.619
Meyer <i>et al.</i> Case 1B [94]	14.8	34 300	0.164	0.245
Meyer <i>et al.</i> Case 2B [94]	21.3	65 400	0.117	0.245
Meyer <i>et al.</i> Case 3B [94]	28.1	103 000	0.096	0.245

Table 5.7: Smallest length scale significant to passive scalar mixing, λ_D , and smallest resolved passive scalar length scale inside the mixing layer, Δ_{ave} , at measurement station 6.

spanwise wavelength of the streamwise vortices. At measurement station 6, $\Lambda/\delta_\omega = 1.0, 0.97,$ and 1.02 for BL-039-RRM-M, BL-052-RRM-M and BL-066-RRM-M, respectively. The obtained values lie in the range of recorded experimental data; Jimenez [52] reported $\Lambda/\delta_\omega \approx 1 - 1.25$, Bernal & Roshko [54] obtained $\Lambda/\delta_\omega \approx 0.8 \pm 0.14$, and Bell *et al.* [88] reported $\Lambda/\delta_\omega \approx 1.28 \pm 0.21$. The spanwise wavelength of the streamwise vortex structures to the local vorticity thickness shows that the spatially stationary, streamwise structures are dynamically similar and independent of R .

5.3.3.4 Passive Scalar Mixing

Table 5.7 shows the smallest passive scalar length scale significant to mixing and the smallest resolved scalar length scale at measurement station 6. The ratio of Δ_{ave}/λ_D is 1.8, 3.0 and 3.4 for $R = 0.39, 0.52$ and 0.66 , respectively. This indicating that passive scalar mixing is well resolved in the simulations.

Passive scalar statistics of BL-039-RRM-M at measurement station 6 are shown in Figure 5.35. For each simulation two p.d.f.'s taken at an entrainment maximum and minimum are reported. The p.d.f.'s shown in Figure 5.35a and 5.35b are of the *non-marching* type. The preferred concentration is $\bar{\xi} \approx 0.60$ with a peak probability density value of $P \approx 2.6$. The vertical extent of the mixing layer is similar at both spanwise measurement stations. Figure 5.35c shows the local entrainment ratio and the mixing layer centreline across the spanwise extent of the mixing layer. A clear anti-correlation between the entrainment ratio and the centreline is evident. The en-

trainment ratio ranges between $E_v = 1.18$ and 1.46 with a mean value of $\langle E_v \rangle_z = 1.37$. The mixed fluid probability, P_m , approaches unity, but is not equal to, in the centre of the mixing layer, indicating that unmixed fluid is being entrained deep into the mixing layer. The simulation captures the averaged mixed fluid concentration, ξ_m extremely well.

Figure 5.36 shows the passive scalar statistics of BL-052-RRM-M at measurement station 6. The presented p.d.f.'s are both of the *non-marching* type with a preferred concentration of $\bar{\xi} \approx 0.59$ at both spanwise measurement locations. The peak visible in the p.d.f. in Figure 5.36b, is slightly more defined and has higher value for the probability density. The entrainment ratio and centreline plots shown in Figure 5.36c are quantitatively similar to those of BL-039-RRM-M. An anti-correlation is also observed and the entrainment ratio ranges between a minimum of $E_v = 1.24$ and a maximum of $E_v = 1.37$ with a spanwise averaged value of $\langle E_v \rangle_z = 1.35$. The mixed fluid statistics of BL-052-RRM-M agree well with the general shape of the experimental data, and as in the experiment, the peak value of $P_m < 1$.

The passive scalar statistics of BL-066-RRM-M are shown in Figure 5.36. The p.d.f. taken at a spanwise plane between two vortices with a common downflow, shown in Figure 5.36a, is broader than observed in the other simulations but is still of the *non-marching* type. The preferred concentration is $\bar{\xi} \approx 0.58$ and the peak probability is ≈ 2.7 . The p.d.f. shown in Figure 5.36b, taken at an entrainment ratio minima, shows a very clearly defined peak surrounded by very low probability density values. The preferred concentration is $\bar{\xi} \approx 0.60$. Figure 5.36c shows the entrainment ratio and centreline at measurement station 6. The minimum and maximum values of the entrainment ratio are $E_v = 1.21$ and $E_v = 1.37$, respectively with a mean value of $\langle E_v \rangle_z = 1.32$. The mixed fluid statistics, shown in Figure 5.36d, match those of the reference data very well. The mixed fluid probability, P_m , data taken at the entrainment ratio minima matches the experimental data very well, both in shape and magnitude. Good agreement is seen in the average mixed fluid composition, ξ_m , particularly in the low-speed side of the mixing layer where the characteristic peak is captured very well.

Table 5.8 shows the maximum, minimum and spanwise averaged entrainment ratios. Predicted entrainment ratio values by Dimotakis [56] (Equation 2.10) have been

Simulation	$E_{v,\min}$	$E_{v,\max}$	$E_{v,z}$	Dimotakis [56]
BL-039-RRM-M	1.18	1.46	1.37	1.27
BL-052-RRM-M	1.24	1.37	1.35	1.35
BL-066-RRM-M	1.21	1.37	1.32	1.45

Table 5.8: Entrainment ratios at measurement station 6.

included. The Dimotakis [56] entrainment model is based on high Reynolds number mixing layer experiments by Konrad [50]. The values predicted by the Dimotakis model for $R = 0.39$ and 0.52 lie in the range of the entrainment ratio values observed in the simulations. The maximum entrainment value for BL-066-RRM-M is 6% smaller than predicted by Equation 2.10.

5.3.4 Summary

Three LES of varying velocity ratios of $R = 0.39, 0.52$ and 0.66 have been performed. The mean flow statistics show self-similarity to be obtained in all simulations. The momentum growth rate of BL-066-RRM-M shows good agreement with reference data and BL-039-RRM-M and BL-052-RRM-M follow the linear momentum growth relationship. The simulations attain self-similarity at similar streamwise locations.

Streamwise oriented vortex structures are observed in all three simulations. The streamwise structure spacing is shown to be dependent on the velocity ratio. When the velocity ratio difference is taken into account, all three simulations asymptote to a similar value of the ratio between the spanwise wavelength of the streamwise structure and the local vorticity thickness. While the number of spatially stationary streamwise vortices changes, the underlying flow dynamics of the spatially stationary streamwise vortex structures appear to remain unchanged with a change of R .

After normalisation, the passive scalar statistics for all simulations agree well with comparable experimental data by Meyer *et al.* [94].

Simulation	θ_1 (mm)	θ_2 (mm)
BL-039-RRM-L	0.45	0.81
BL-039-LBL-RRM-L	0.69	0.81

Table 5.9: Simulation inlet boundary layers.

5.4 Effects of High-Speed Boundary Layer Thickness

5.4.1 Introduction

In the previous parts of this chapter, the inlet boundary layer fluctuation magnitude and the velocity ratio have been studied. In this last part, the inlet boundary layer thickness is studied to complete the study of effects of small inlet condition changes on the high Reynolds number mixing layer.

5.4.2 Simulation Setup

For this section the $R = 0.39$ velocity ratio and the -L inlet fluctuation magnitude are chosen. The normalised inlet profile shown in Figure 5.1a is applied as the high-speed inlet boundary condition for the BL-039-RRM-L simulation. For the large boundary layer simulation, BL-039-LBL-RRM-L, the high-speed boundary layer is $\approx 50\%$ larger than that of BL-039-RRM-L. Table 5.9 lists both simulations with their respective inlet boundary layers. All other simulation parameters are kept constant. The grid and sub-grid scale model remain unchanged. Experimental data for $R = 0.66$ has been included to guide as a reference rather than as a like-for-like comparison.

5.4.3 Results

5.4.3.1 Mean Flow Statistics

Mean streamwise velocity data at $x/\theta_i = 1000$ is shown in Figure 5.38a. After normalisation, the agreement with reference data is good for both simulations indicating that self-similarity is achieved in both. The spanwise averaged, mean streamwise velocity fluctuations at $x/\theta_i = 1000$ are shown in Figure 5.38b. The peak values and shape of the curves are similar for both simulations. Figure 5.38c shows the peak streamwise velocity fluctuation with downstream distance from the splitter plate. Although the inlet fluctuation magnitude has not been changed, the peak fluctuation magnitude is $\approx 19\%$ lower in BL-039-LBL-RRM-L compared to BL-039-RRM-L. Self similarity is obtained at $x/\theta_i \approx 750$ in both simulations which is within the $x/\theta_i = 1000$ criteria stipulated by experimental research [75]. The asymptotic final state value is similar in both simulations and is similar to that of the included guidance data.

Figure 5.39 shows the momentum thickness for BL-039-RRM-L and BL-039-LBL-RRM-L, normalised by the respective inlet momentum thickness. The higher boundary layer thickness simulation rolls up further downstream and has a lower growth rate than BL-039-RRM-L. The momentum growth rate constants are $k_m = 0.036$ and $k_m = 0.028$ for BL-039-RRM-L and BL-039-LBL-RRM-L, respectively.

Streamwise velocity fluctuation spectra, recorded in the plane of the splitter plate ($y = 0$), are shown in Figure 5.40. Linear stability theory, based on Equation 4.13, suggests the most amplified disturbance to be $St = 0.044$. At $x/\theta_i = 44$, shown in Figure 5.40a, the peak Strouhal number of $St = 0.044$ for BL-039-RRM-L is in good agreement with the theory. The power spectral density peak for BL-039-LBL-RRM-L is at a slightly increased Strouhal number of $St = 0.051$ which is 15% higher than predicted by Equation 4.13. At $x/\theta_i = 444$, shown in Figure 5.40b, both simulations are approaching the $-5/3$ slope, characteristic of fully developed turbulent flow.

Measurement station	x (m)	x/θ_i	x_i^*	x/θ_i LBL	x_i^* LBL
MS1	0.0180	40	0.52	3	0.03
MS2	0.0380	84	1.1	55	0.7
MS3	0.0690	153	2.0	100	1.3
MS4	0.1330	296	3.8	192	2.5
MS5	0.2695	598	7.8	391	5.1
MS6	0.5390	1198	15.6	781	10.2

Table 5.10: Measurement stations.

5.4.3.2 Streamwise Vortex Structure

The cross-planes ($y - z$) of the secondary shear stress, $\langle u' w' \rangle_t$, presented here, have been normalised by the high speed inlet velocity, U_1 . Table 5.10 lists the measurement stations in terms of non-dimensional distance from the splitter plate as well as a function of the local pairing parameter, $x_i^* = Rx/(30\theta_i)$.

Secondary shear stress cross-planes at measurement station 2 are shown in Figure 5.41. Three-tiered cluster formations of secondary shear stress are present in the BL-039-RRM-L simulation while the delayed development in BL-039-LBL-RRM-L leads to a secondary shear stress plot with very low magnitudes. At measurement station 3, shown in Figure 5.42, the BL-039-RRM-L simulation has started to unwrap into a single row of alternating sign shear stress. Shear stress levels for BL-039-LBL-RRM-L are still considerably lower. Measurement station 5 is shown in Figure 5.43. In both simulations regularly spaced patches of secondary shear stress are present. At the last measurement station, both simulations still show evidence of spatially stationary streamwise oriented vortices. The shear stress magnitude remains higher in BL-039-RRM-L than BL-039-LBL-RRM-L.

The centreline loci for BL-039-RRM-L, shown in Figure 5.45a, shows a large number of undulations that decrease in number and increase in strength with increasing downstream distance in agreement with previously presented results for different values of R . The centreline loci for BL-039-LBL-RRM-L shown in Figure 5.45 are quantitatively different to any previously reported centreline plots. The centreline at MS2 shows two relatively large undulations at $z/\theta_i = 50$ and 230. At MS3 more wrinkling of the centreline is present, and the two undulations present at MS2 are

amplified. MS4 follows this pattern as well, and the magnitude of the two large scale undulations has increased even further. At the penultimate measurement station, a larger number of undulations are present, and a spanwise wavelength is evident but compared to the BL-039-RRM-L simulation their amplitudes are 40% smaller. At measurement station 5 the centreline locus plot is similar to BL-039-RRM-L, but the amplitude is still smaller.

The number of secondary structures can be evaluated using the streamwise structure spacing, s , shown in Figure 5.46a. If the inlet momentum thickness is accounted for both simulations, show similar trends for the streamwise structure spacing. This is also evident in the ratio of the spanwise wavelength of the streamwise vortices to the local vorticity thickness, shown in Figure 5.46b. From Figure 5.46b it can be seen that the streamwise structure spacing is dependent on the local vorticity thickness.

5.4.3.3 Passive Scalar Mixing

Probability density functions at measurement station 6 are shown in Figure 5.47 and 5.48 for BL-039-RRM-L and BL-039-LBL-RRM-L, respectively. The p.d.f.'s for both simulations are of the *non-marching* type with a preferred concentration of $\bar{\xi} \approx 0.58$ which is in good agreement with comparable experimental values [50]. Notable is the higher probability density value of the preferred concentration for BL-039-RRM-L compared to BL-039-LBL-RRM-L.

5.4.4 Summary

Two large eddy simulations with a varying high-speed inlet boundary layer momentum thickness have been compared. BL-039-RRM-L uses a high-speed boundary layer momentum thickness value reported by a comparable high Reynolds number mixing experiment [45]. BL-039-LBL-RRM-L uses a high-speed inlet boundary layer 0.5 times larger than that in BL-039-RRM-L. All other simulation parameters have been kept constant.

The mean flow statistics are shown to be heavily influenced by the momentum thickness in the near field and transition region of the mixing layer. An increase in the inlet boundary layer thickness effectively delays the roll up of the mixing layer. In the self-similar region of the mixing layer, the two simulations show very similar values for the momentum growth rate and velocity profiles.

The delay in the development is also evident in the secondary, streamwise oriented vortex structures which are present in both simulations. The streamwise structure spacing is shown to grow at a similar rate between the two simulations. If the delayed development is accounted for, the presented mixing layers are dynamically similar in the far-field and asymptote to similar final states.

5.5 Conclusions

In this chapter the influence of small changes in the flow conditions on the simulated mixing layer has been assessed. The small changes include small inlet fluctuation changes, velocity ratio effects, and the effect of the high-speed boundary layer thickness.

To study the effect of very small inlet fluctuation changes, simulations with high-speed boundary layer inlet fluctuation magnitudes of 1% and 1.8% of the high-speed inlet velocity have been compared. If the velocity ratio is accounted for in the normalisation, the mean flow statistics are shown to be largely unaffected by this small change in fluctuation magnitude. When perspective views are compared, slight differences in the streamwise oriented vortex structures are apparent. Further investigation reveals that even a very small change in the inlet fluctuation magnitude has a measurable effect on the intensity of the secondary, streamwise vortex structure which is shown to affect the momentum and the passive scalar fields. This finding is supported by Plesnika *et al.* [104], and it is the first time that this has been observed in numerical simulations.

The second part of this chapter is a parametrised study of the velocity ratio, R , by varying the high-speed inlet velocity while keeping all other inlet conditions con-

stant. In total three values of R are compared, $R = 0.39, 0.52$ and 0.66 . It is found that changing R results in a change of the streamwise vortex structure spacing as a result of the change in the vorticity thickness growth rate, which is a function of the velocity ratio. It is shown that if the change in the vorticity growth rate is accounted for, the streamwise vortex structure spacing for all R values asymptotes to a value of $\Lambda/\delta_\omega \approx 1$.

In the final section of this chapter, a change in the high-speed inlet boundary layer momentum thickness is studied. One simulation utilises a value of the high-speed inlet boundary layer momentum thickness of $\theta_i = 0.45\text{mm}$, based on the value reported by the reference experiment [45]. The large boundary layer simulation, -LBL, uses an increased boundary layer momentum thickness of $\theta_i = 0.69\text{mm}$. It is shown that an increase of the boundary layer momentum thickness leads to a delay in the development of the mixing layer due to the increased streamwise distance of the roll up location from the splitter plate trailing edge. The simulation with the larger inlet boundary layer shows a reduced momentum growth rate compared to the reference case. Passive scalar measurements are shown to be insensitive to the inlet boundary layer momentum thickness.

Arguably, the most interesting of the inlet parameters investigated in this chapter is the inlet boundary layer fluctuation magnitude. The presented simulations show that even very small changes in the fluctuation level have a significant effect on the streamwise vortex structure which is shown to persist into the self-similar, far-field region of the mixing layer. This novel finding is in agreement with experimental results by Plesniak *et al.* [104]. Higher inlet boundary layer fluctuation magnitudes will be investigated in the next chapter.

5.6 Figures

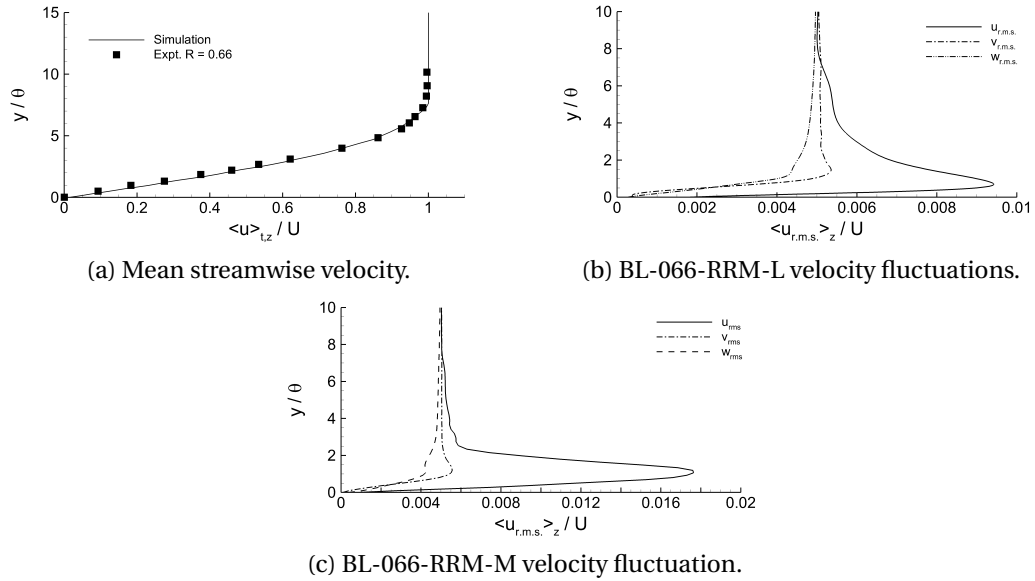


Figure 5.1: High-speed stream inflow conditions for BL-066-RRM-L and BL-066-RRM-M.

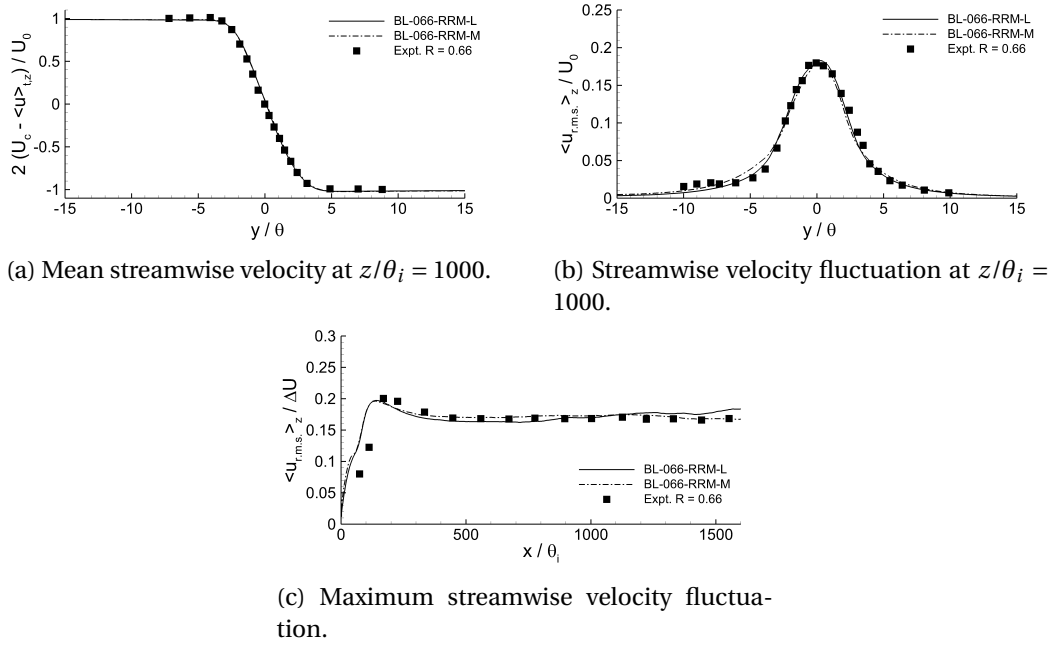


Figure 5.2: Velocity statistics for BL-066-RRM-L and BL-066-RRM-M.

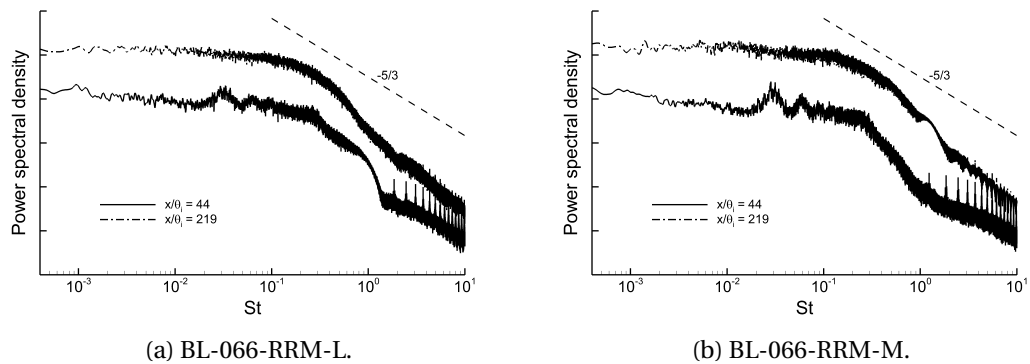


Figure 5.3: Vertically shifted, power spectral density plots at $x/\theta_i = 44$ and $x/\theta_i = 219$.

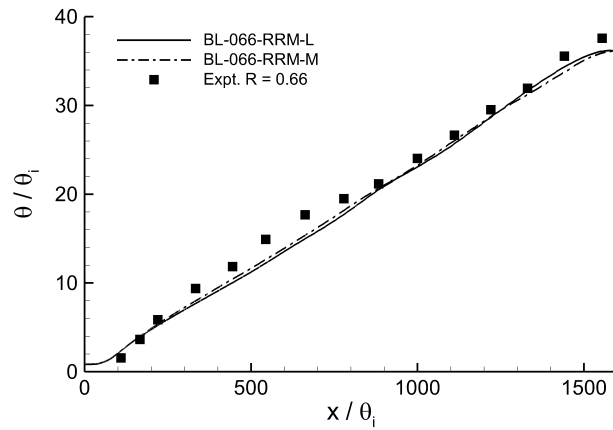


Figure 5.4: Local momentum thickness of the mixing layer.

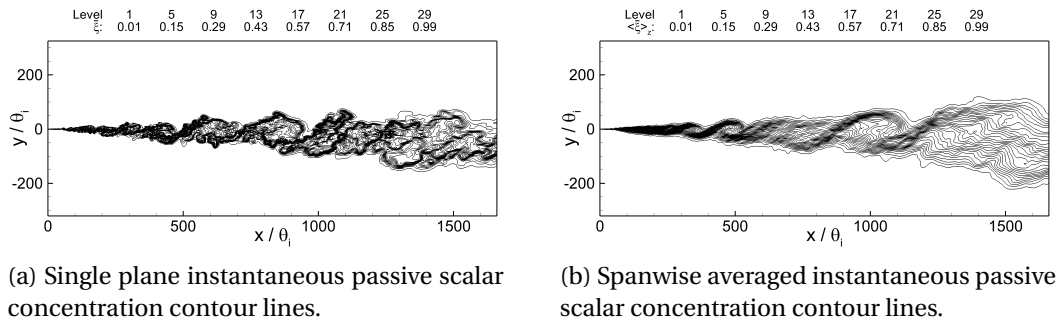


Figure 5.5: Instantaneous flow visualisations for BL-066-RRM-L.

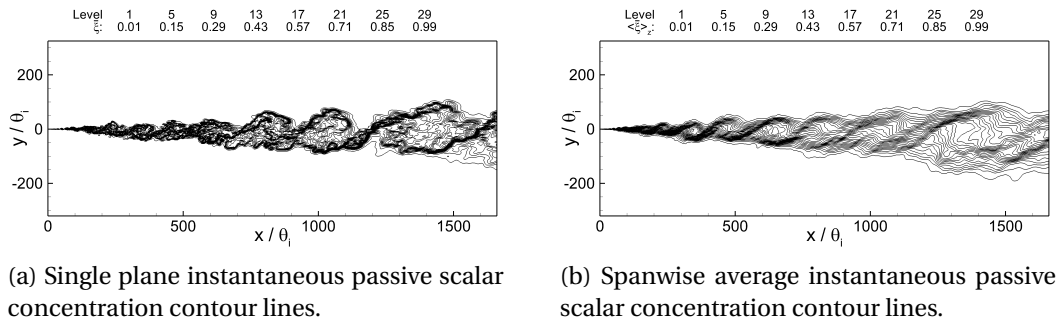


Figure 5.6: Instantaneous flow visualisations for BL-066-RRM-M.

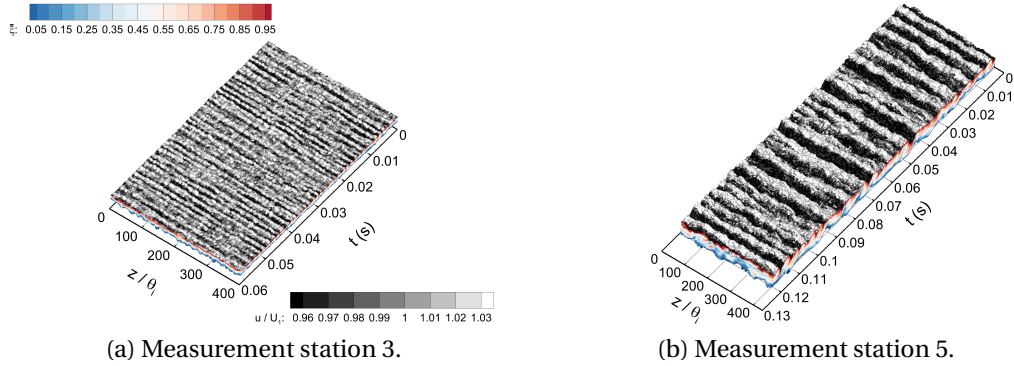


Figure 5.7: Perspective views for BL-066-RRM-L at measurement station 3 and 5.

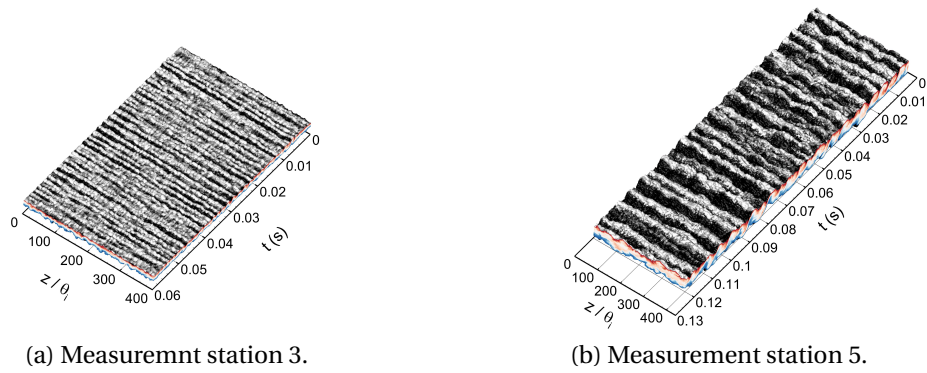


Figure 5.8: Perspective views for BL-066-RRM-M at measurement station 3 and 5. For legend refer to Figure 5.7a.

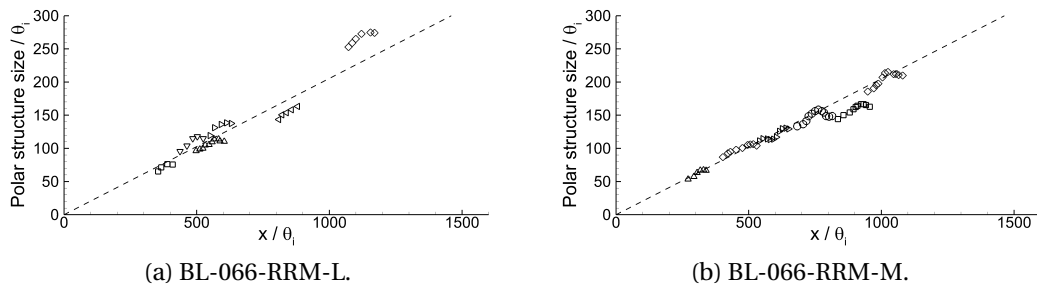


Figure 5.9: Vertical structure size growth tracks.

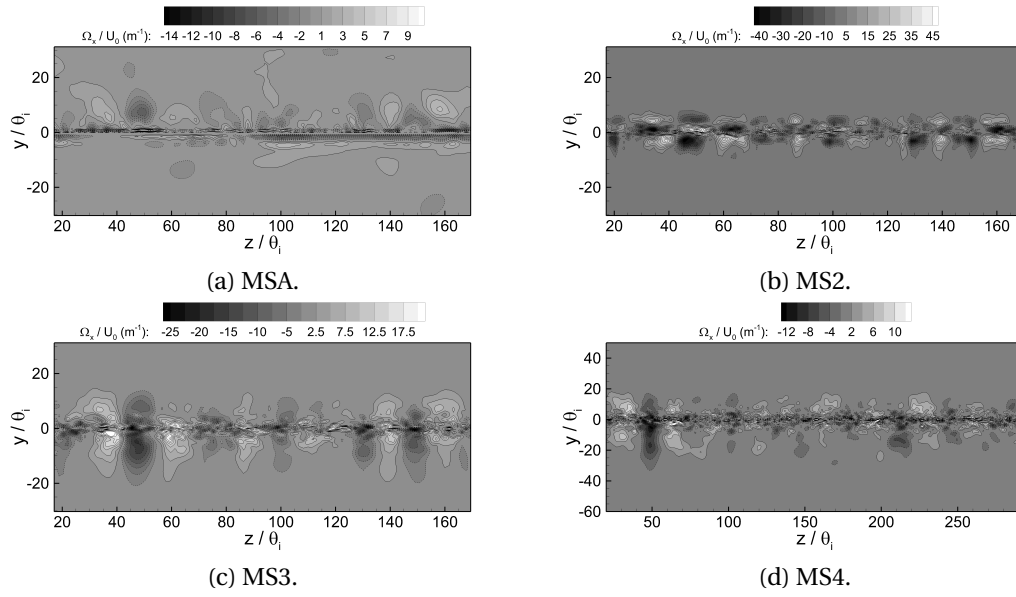


Figure 5.10: Streamwise vorticity $y - z$ cross-planes for BL-066-RRM-L.

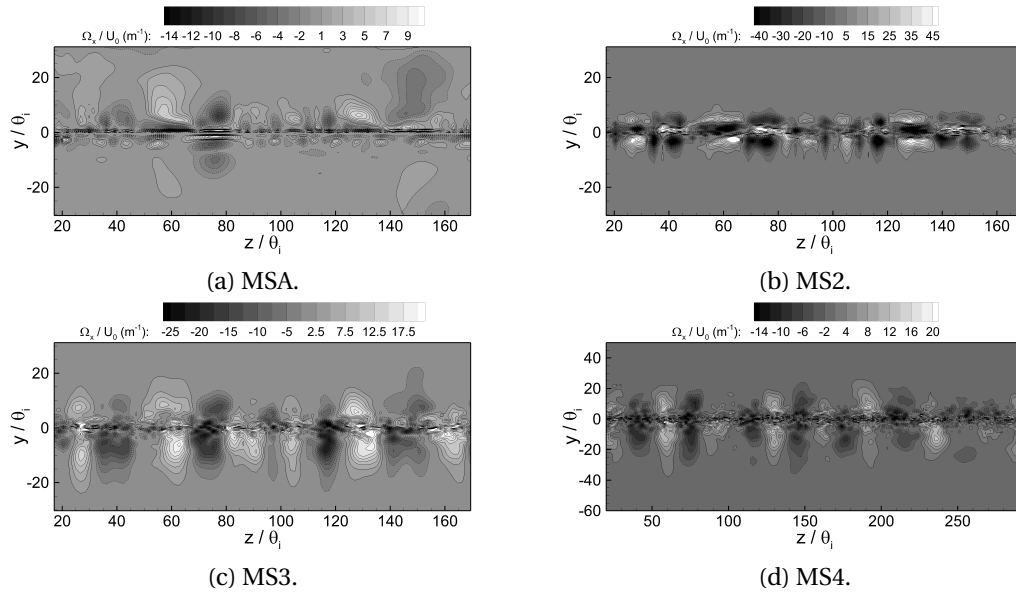


Figure 5.11: Streamwise vorticity $y - z$ cross-planes for BL-066-RRM-M.

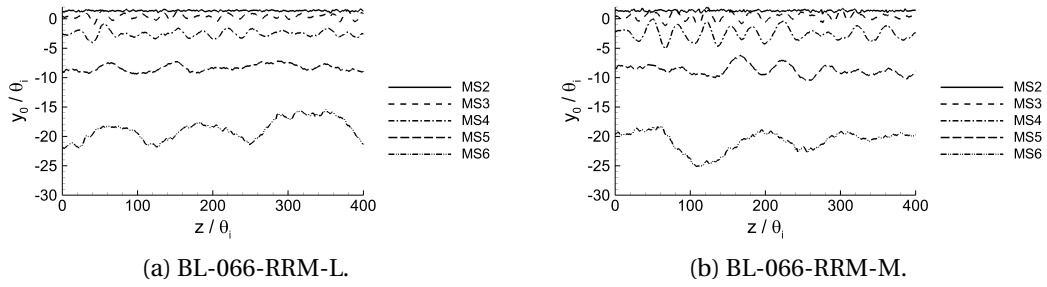


Figure 5.12: Centreline evolution at measurement stations 2 through 6.

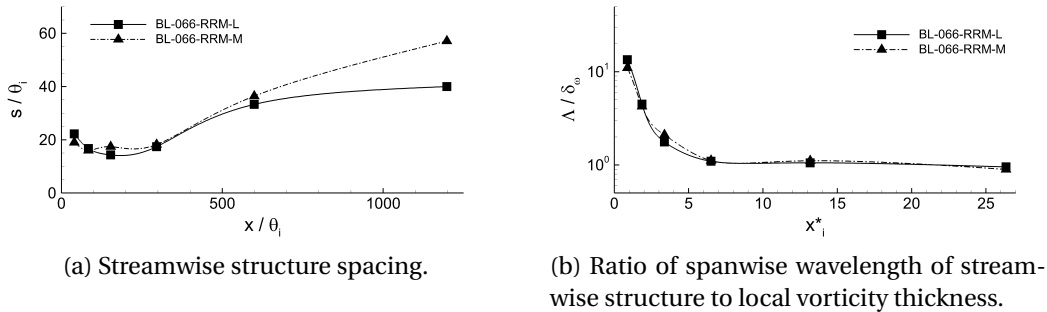


Figure 5.13: Streamwise vortex structure evolution.

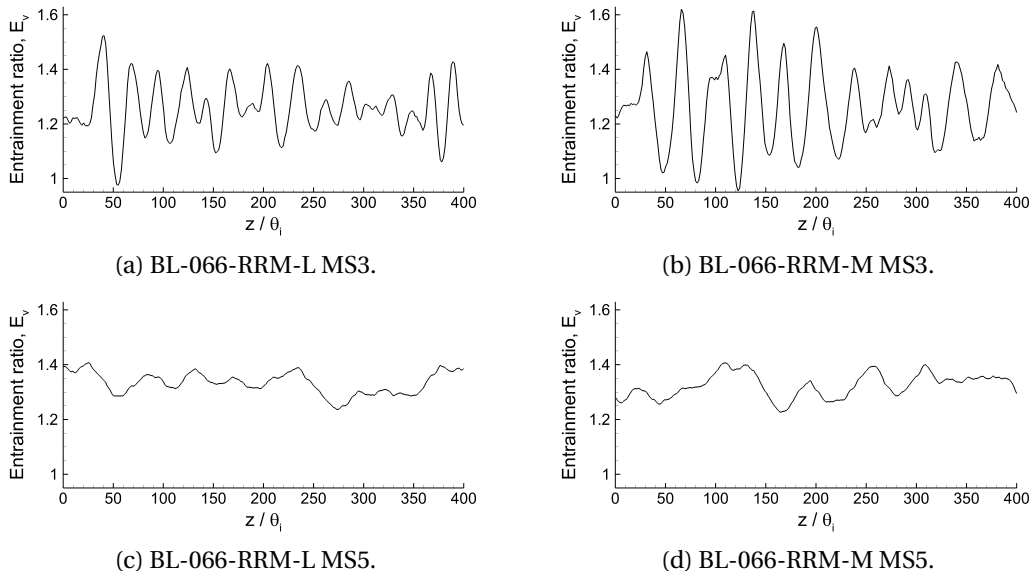


Figure 5.14: Entrainment ratio at measurement stations 3 and 5.

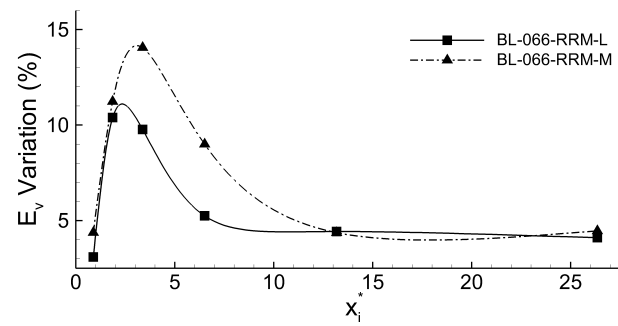


Figure 5.15: Streamwise development of the entrainment ratio variation.

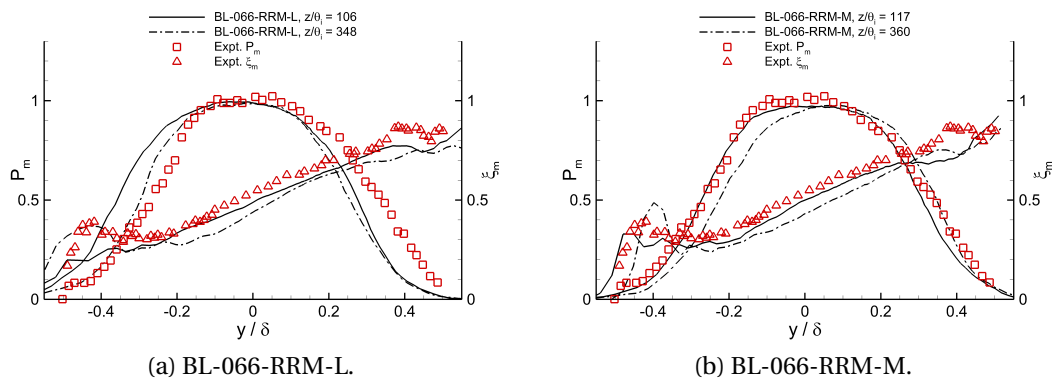


Figure 5.16: Mixed fluid statistics at measurement station 6.

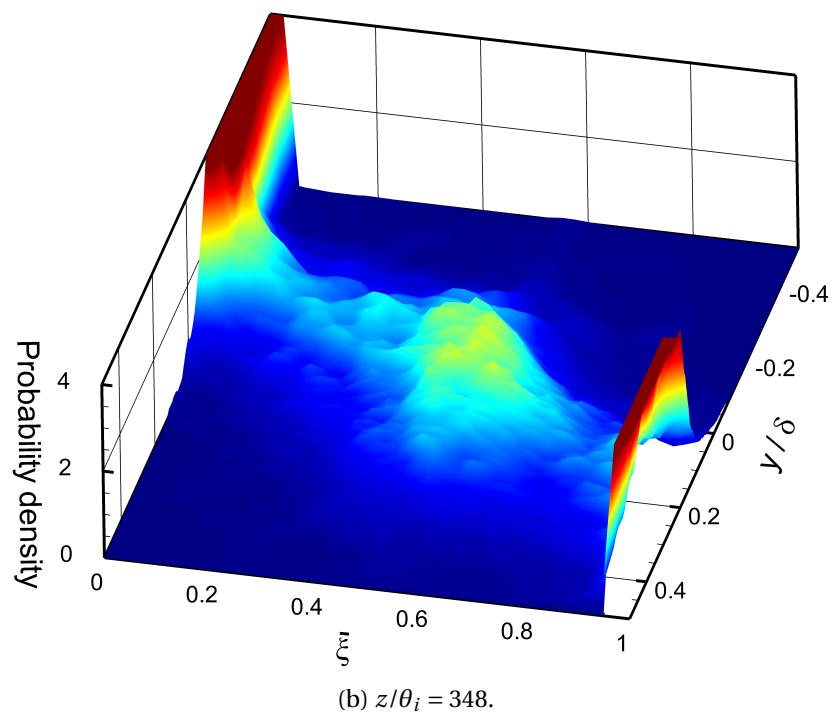
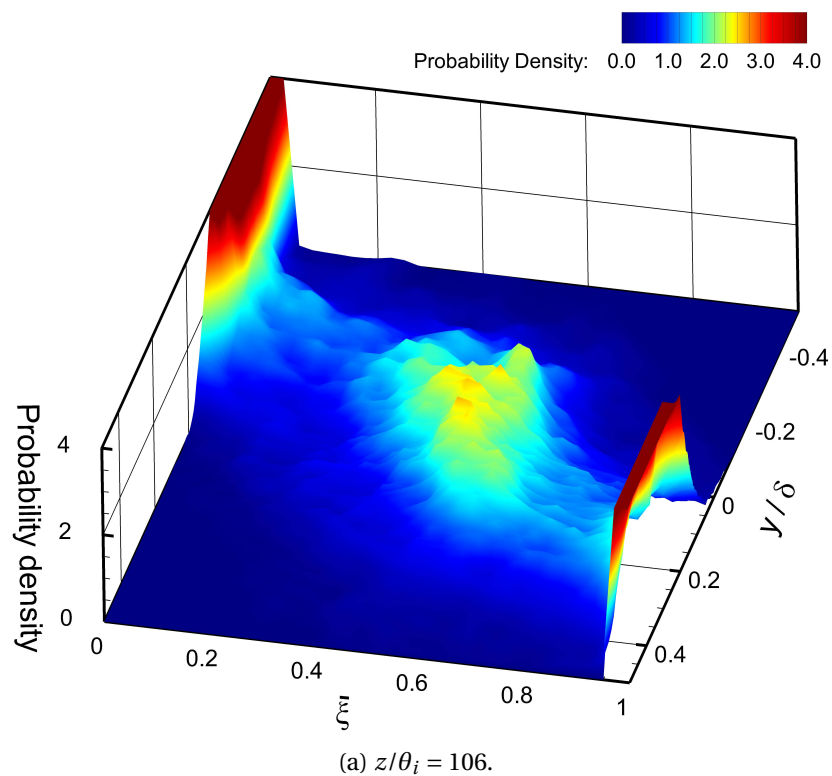


Figure 5.17: Probability density functions for BL-066-RRM-L at measurement station 6.

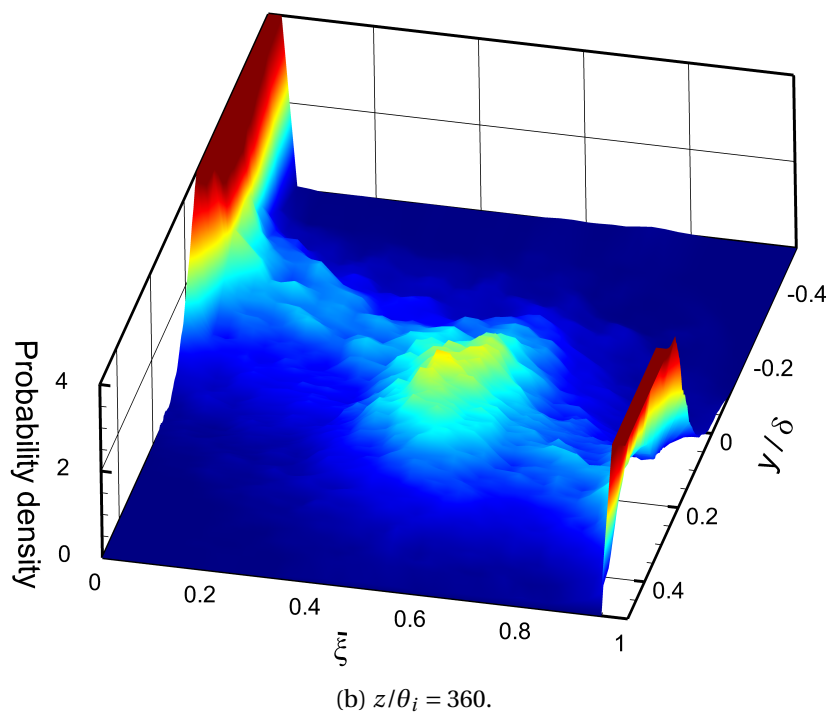
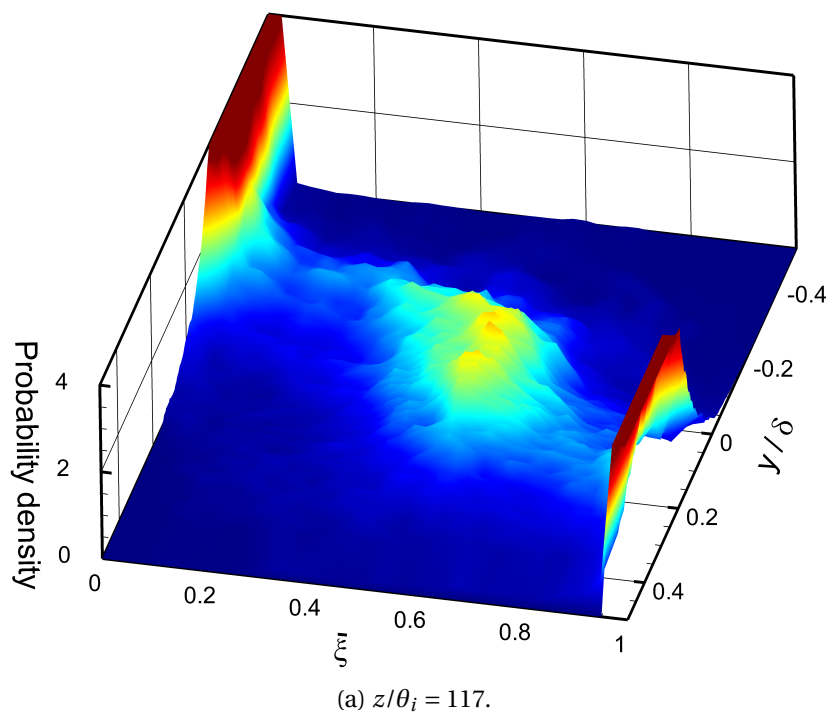
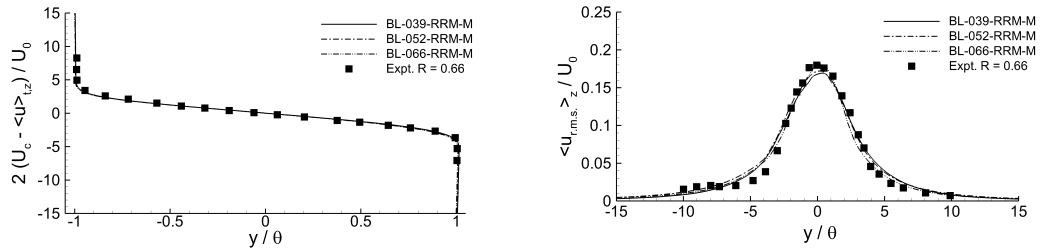
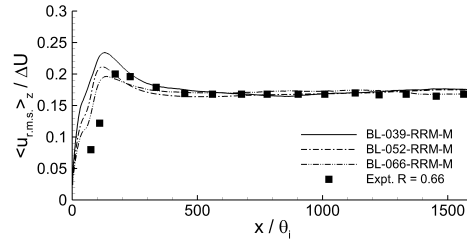


Figure 5.18: Probability density functions for BL-066-RRM-M at measurement station 6. For legend refer to Figure 5.17a.



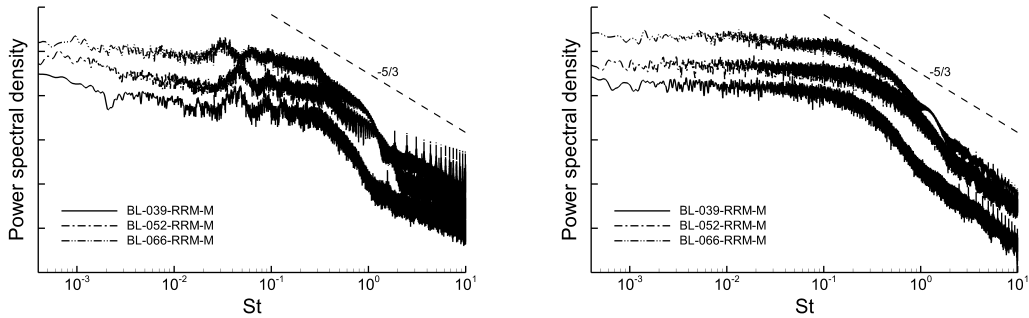
(a) Mean streamwise velocity at $x/\theta_i = 1000$.

(b) Streamwise velocity fluctuation at $x/\theta_i = 1000$.



(c) Maximum streamwise velocity fluctuation.

Figure 5.19: Mean flow statistics.



(a) $x/\theta_i = 44$.

(b) $x/\theta_i = 217$.

Figure 5.20: Power spectra density plots at $x/\theta_i = 44$ and $x/\theta_i = 217$. For clarity, spectra have been shifted along the vertical axis.

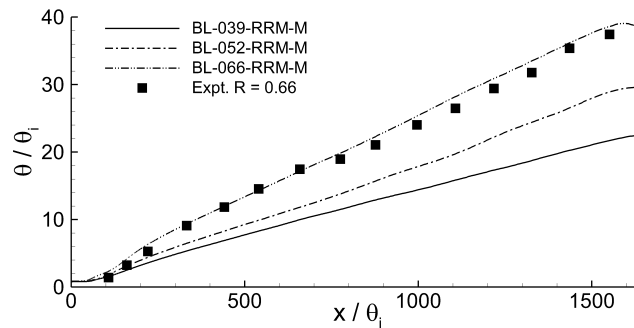


Figure 5.21: Local momentum thickness of the mixing layer.

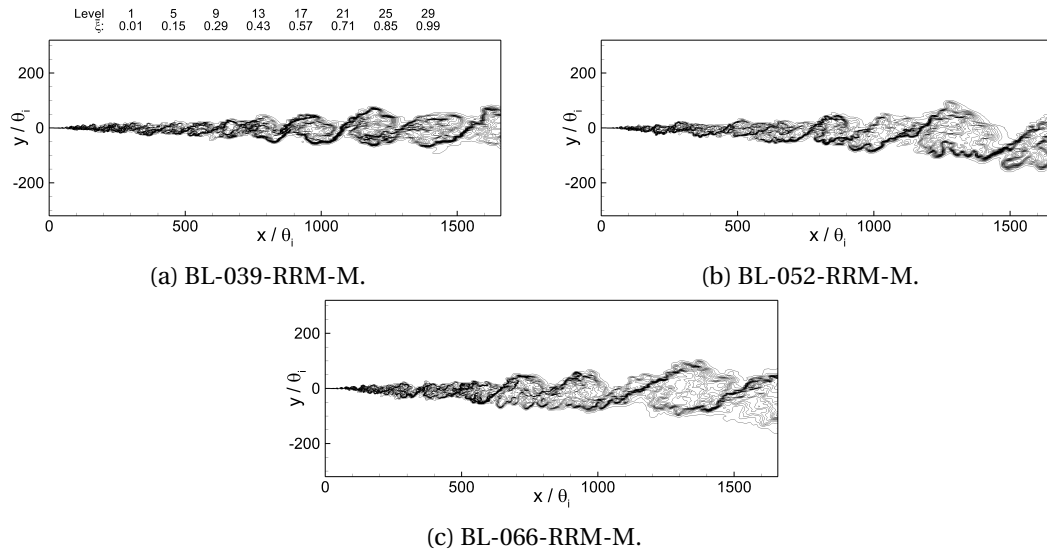


Figure 5.22: Single plane, passive scalar flow visualisations.

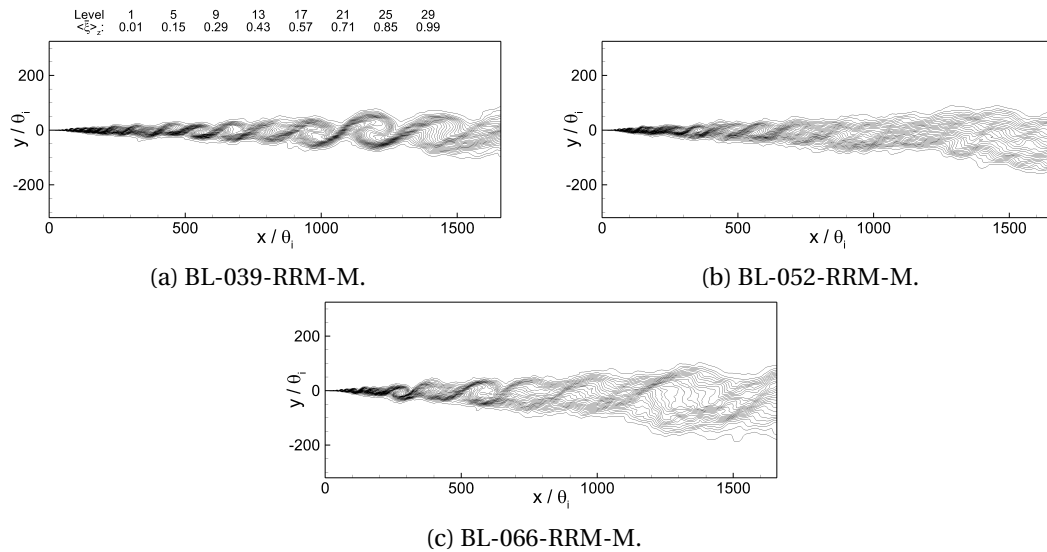


Figure 5.23: Spanwise averaged, passive scalar flow visualisations.

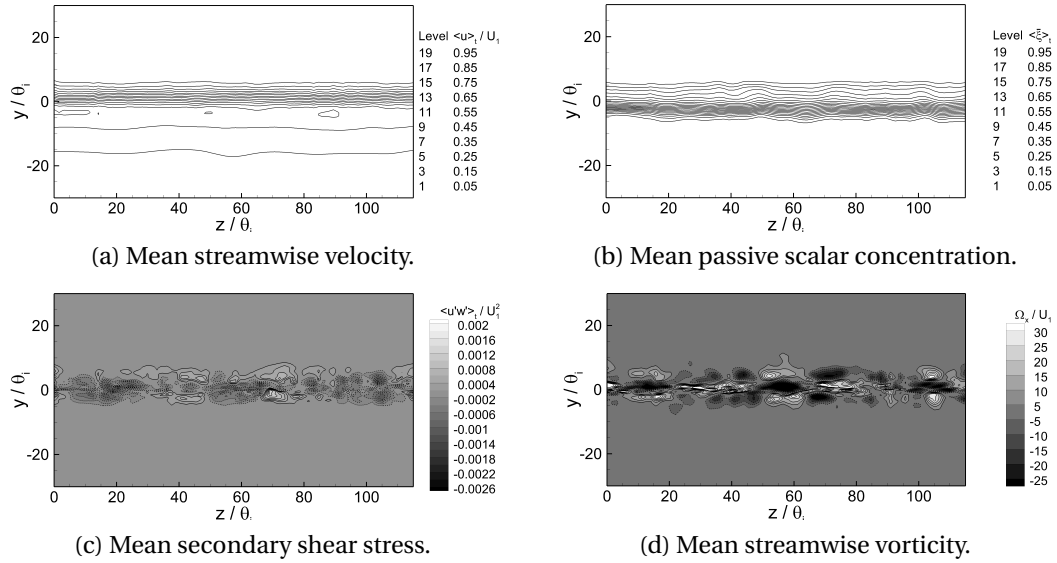


Figure 5.24: Cross-plane maps at measurement station 2 for BL-039-RRM-M.

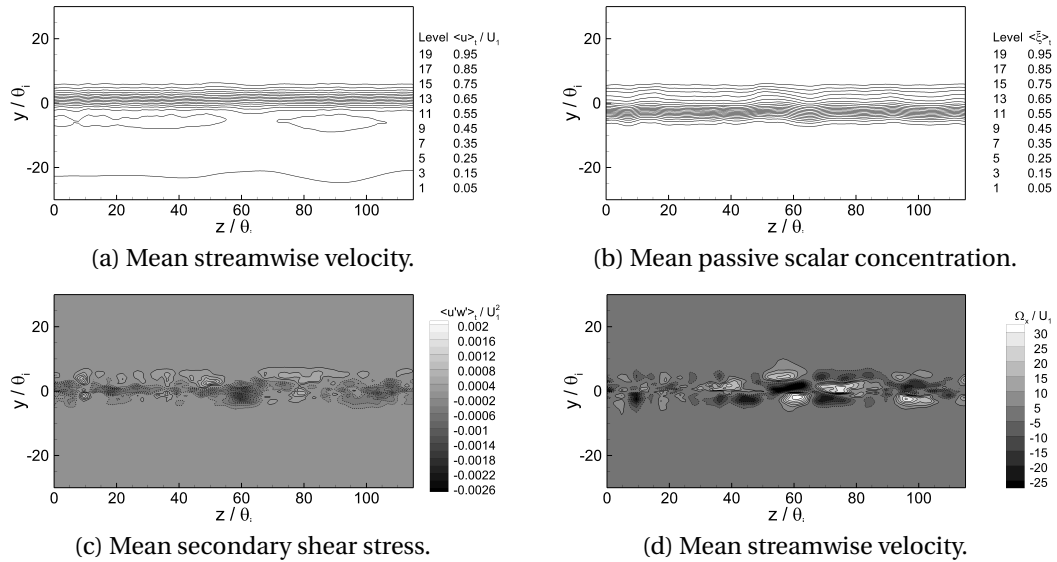


Figure 5.25: Cross-plane maps at measurement station 2 for BL-052-RRM-M.

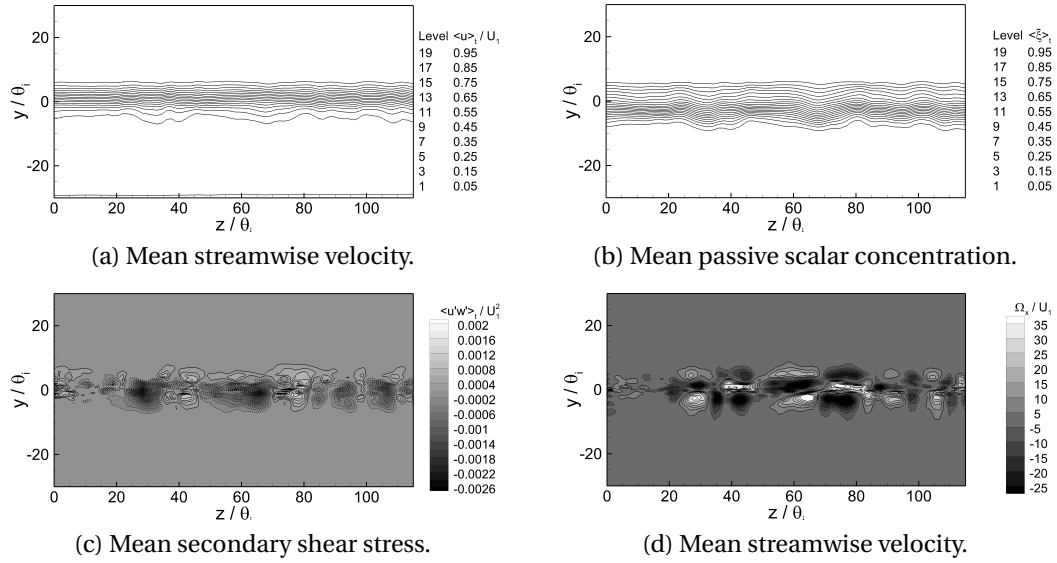


Figure 5.26: Cross-plane maps at measurement station 2 for BL-066-RRM-M.

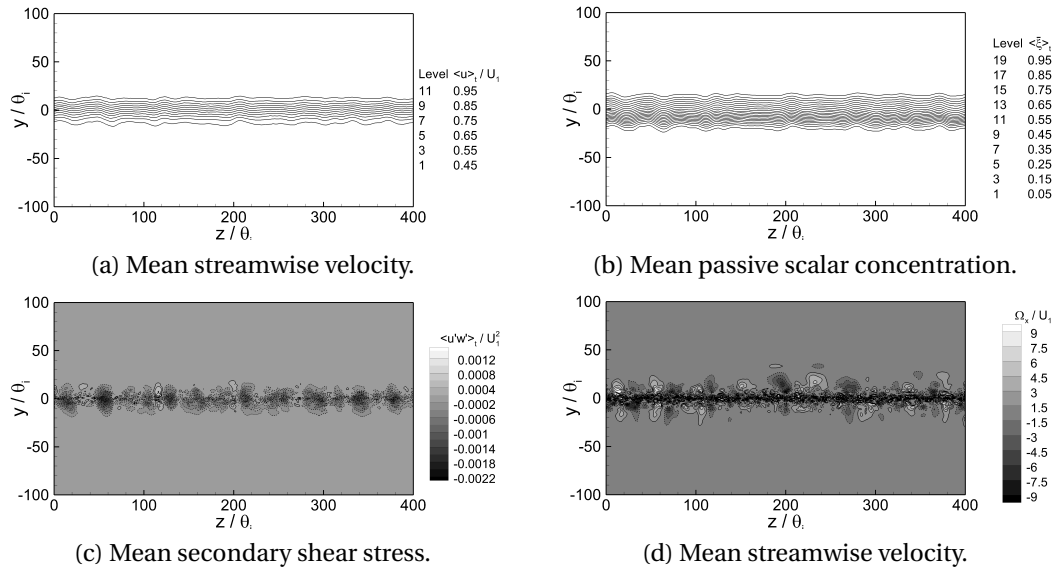


Figure 5.27: Cross-plane maps at measurement station 4 for BL-039-RRM-M.

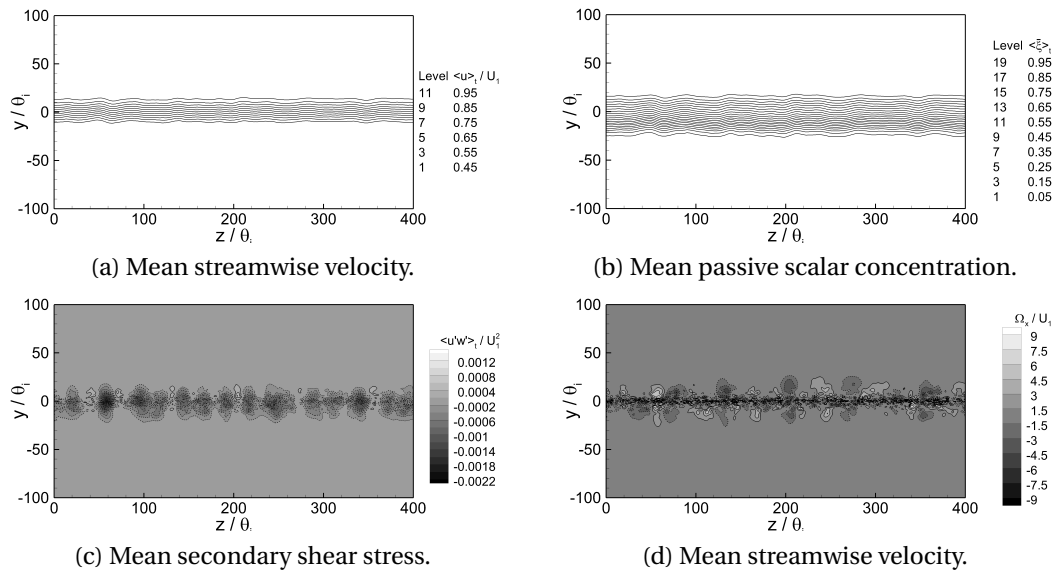


Figure 5.28: Cross-plane maps at measurement station 4 for BL-052-RRM-M.

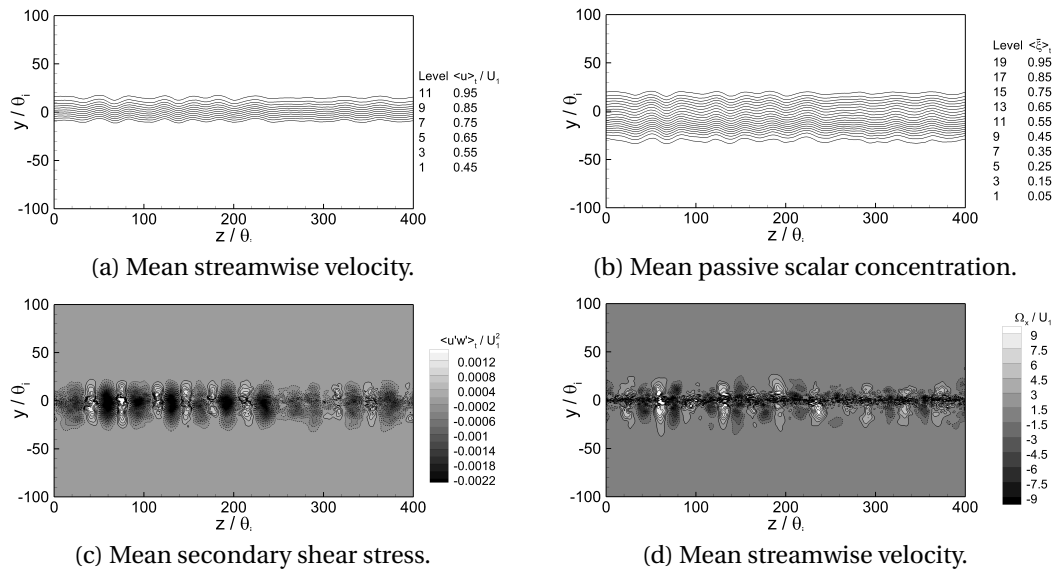


Figure 5.29: Cross-plane maps at measurement station 4 for BL-066-RRM-M.

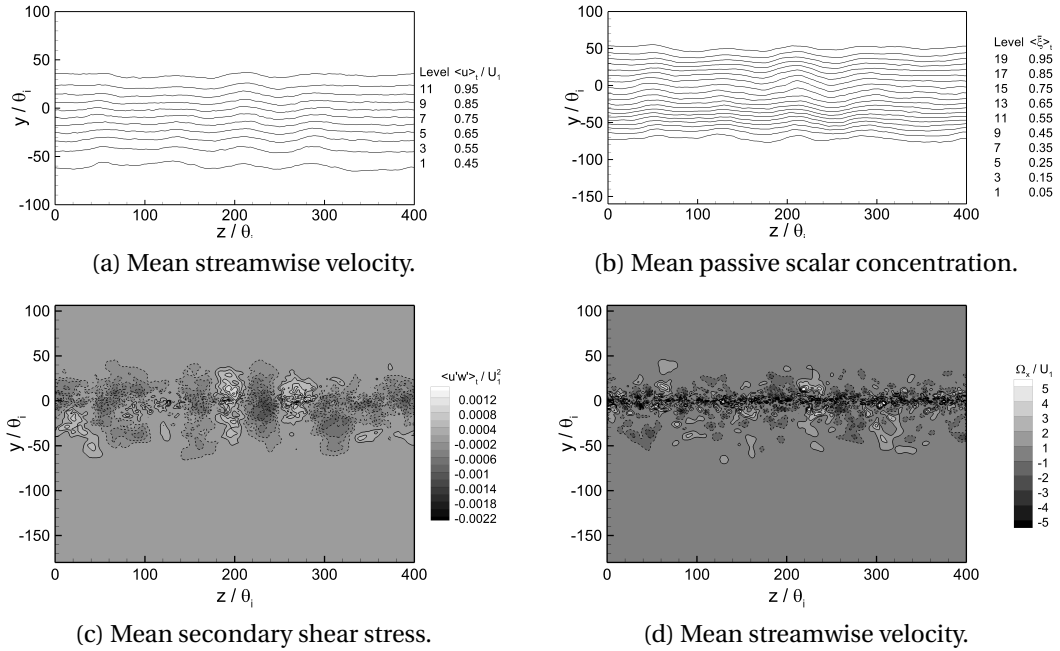


Figure 5.30: Cross-plane maps at measurement station 6 for BL-039-RRM-M.

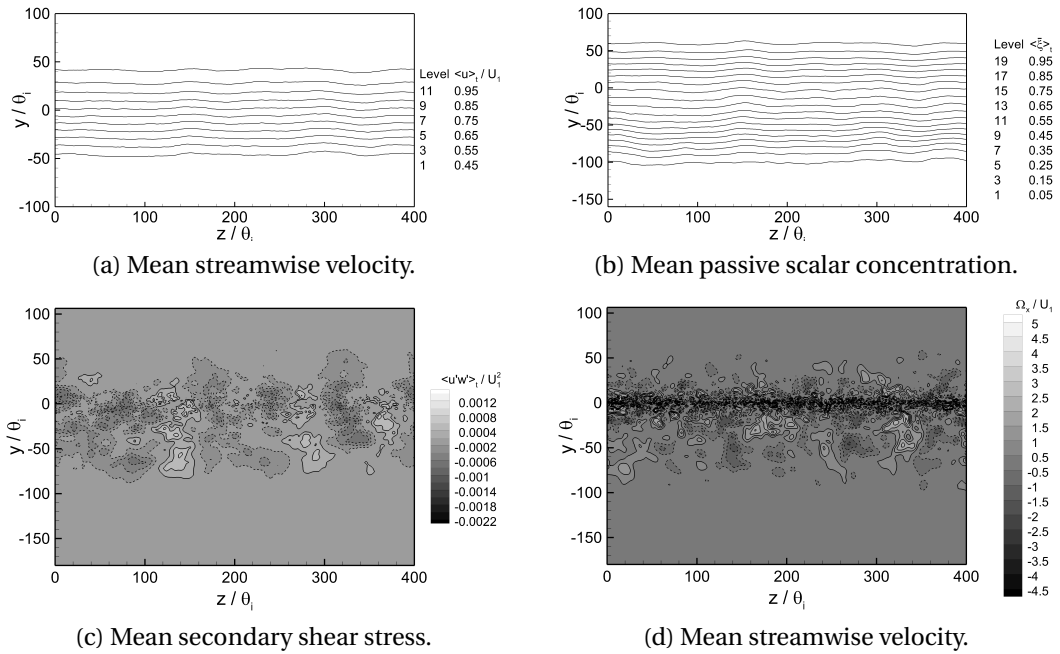


Figure 5.31: Cross-plane maps at measurement station 6 for BL-052-RRM-M.

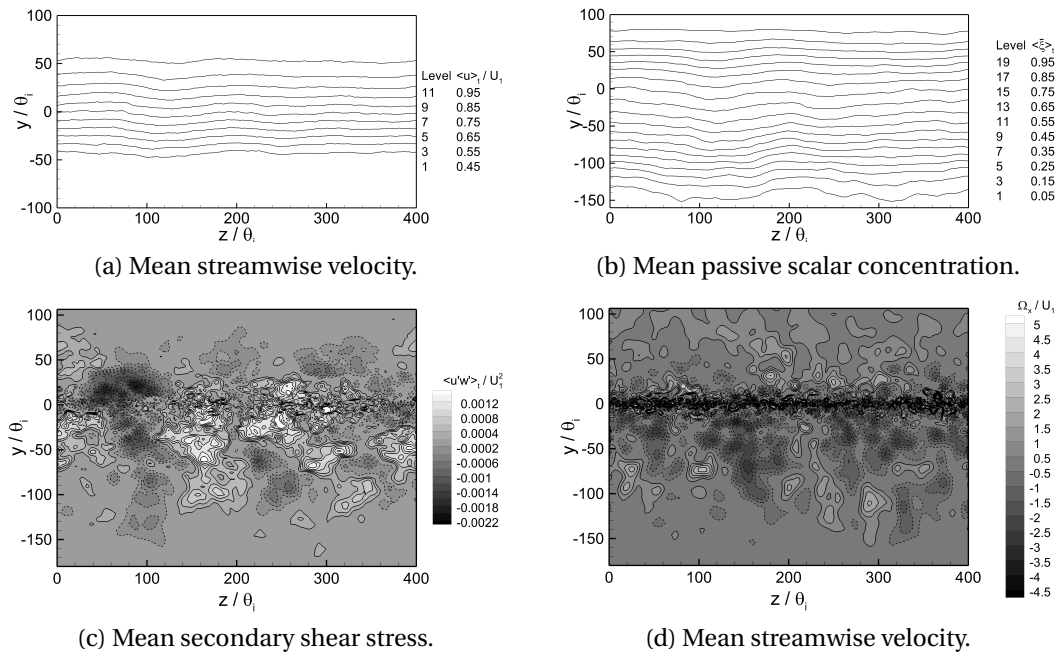


Figure 5.32: Cross-plane maps at measurement station 6 for BL-066-RRM-M.

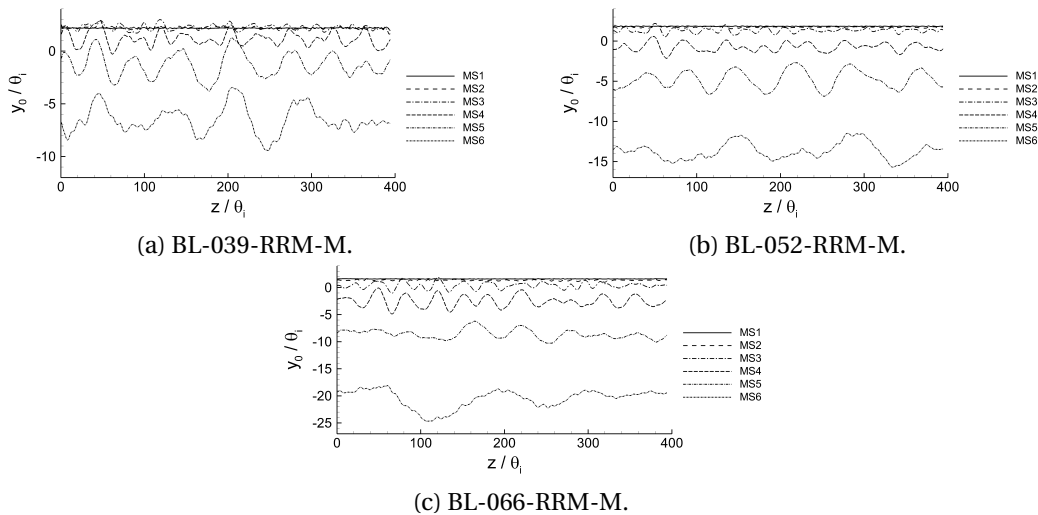


Figure 5.33: Centreline evolution at measurement stations 1 through 6.

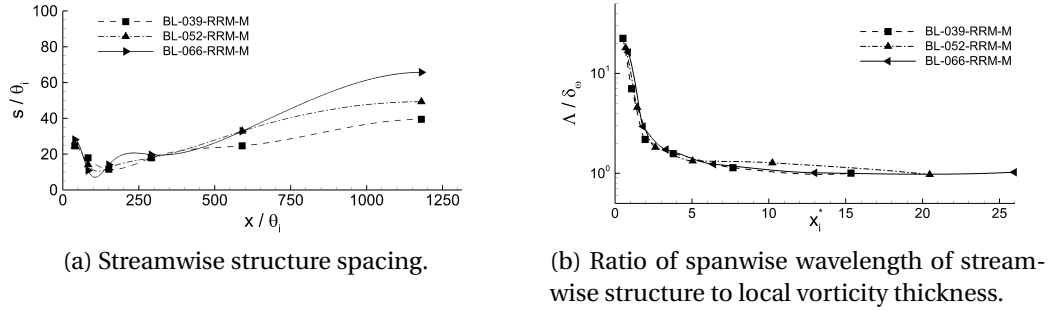


Figure 5.34: Streamwise vortex structure evolution.

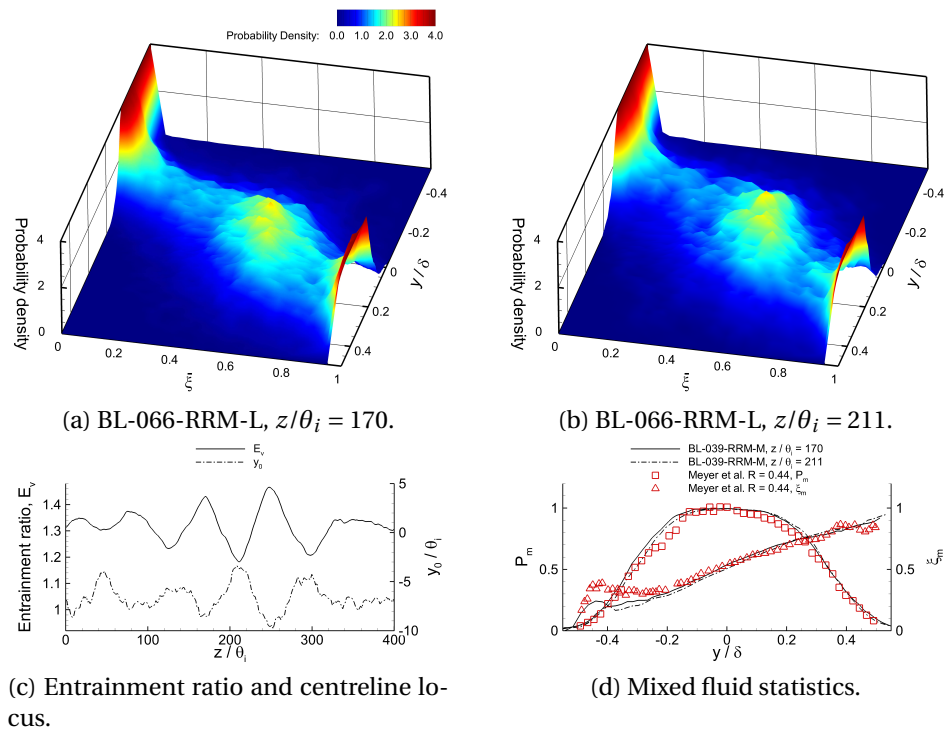


Figure 5.35: Passive scalar statistics of BL-039-RRM-M at measurement station 6.

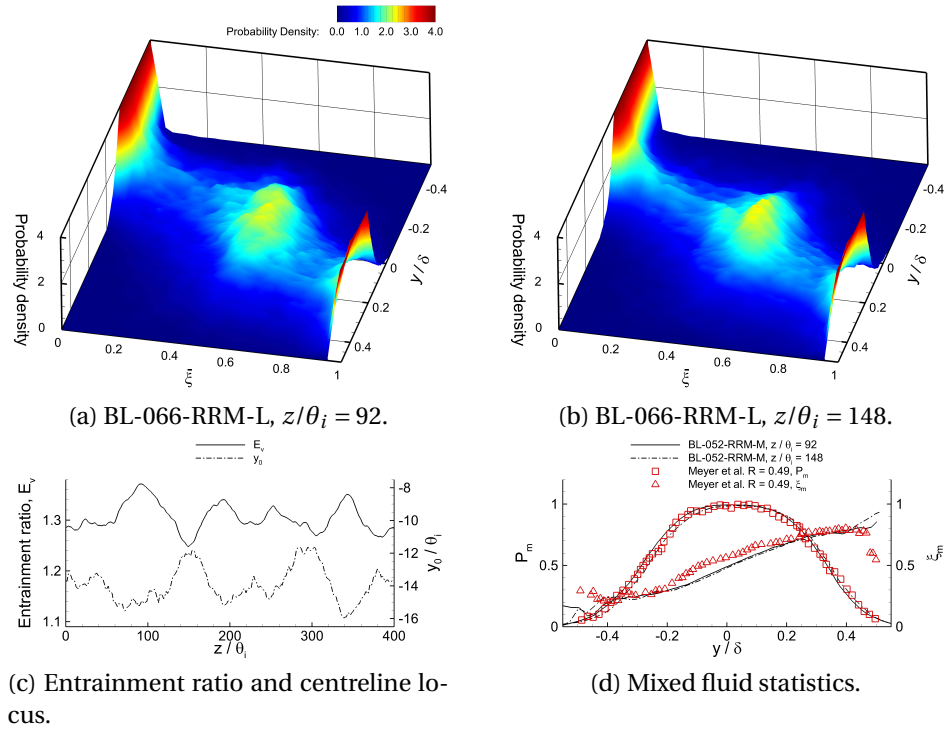


Figure 5.36: Passive scalar statistics of BL-052-RRM-M at measurement station 6.

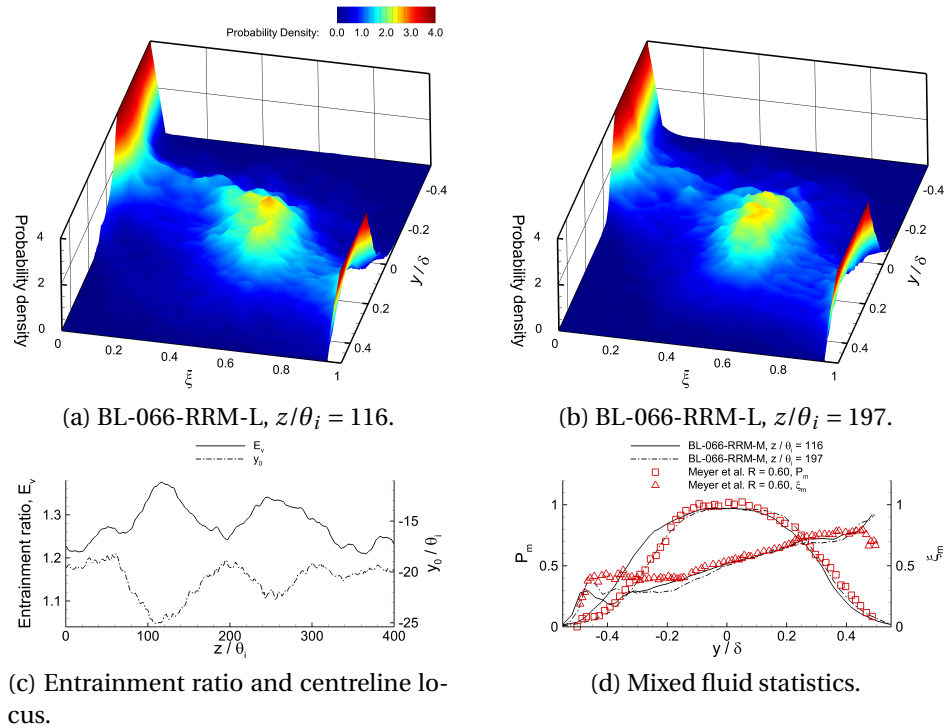
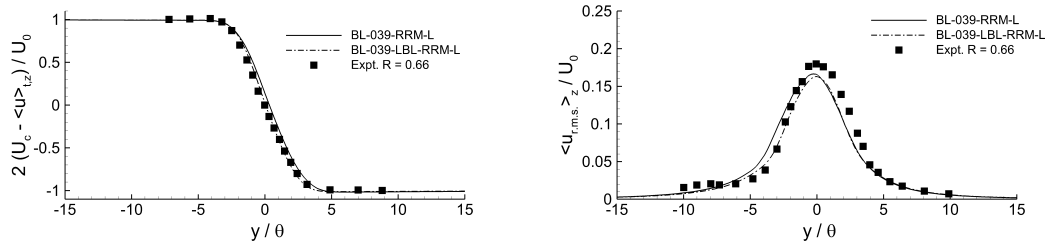
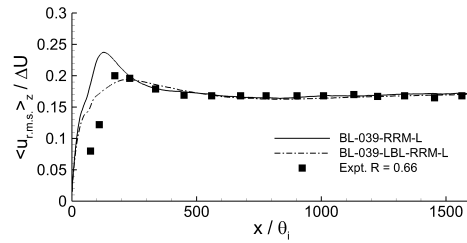


Figure 5.37: Passive scalar statistics of BL-066-RRM-M at measurement station 6.



(a) Mean streamwise velocity at $x/\theta_i = 1000$.

(b) Streamwise velocity fluctuation at $x/\theta_i = 1000$.



(c) Maximum streamwise velocity fluctuation.

Figure 5.38: Mean flow statistics.

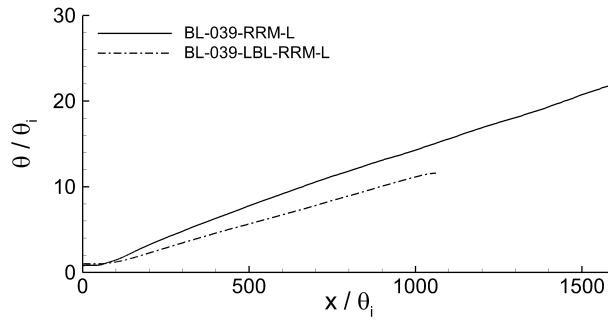
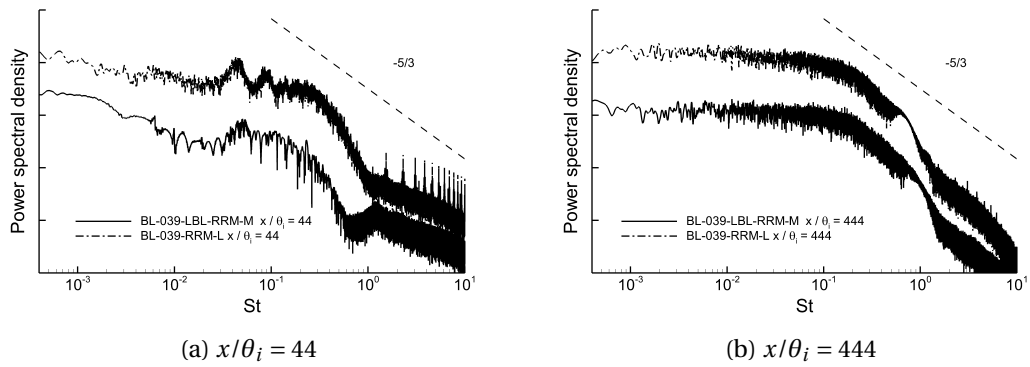


Figure 5.39: Local momentum thickness of the mixing layer.



(a) $x/\theta_i = 44$

(b) $x/\theta_i = 444$

Figure 5.40: Vertically shifted, power spectral density plots at $x/\theta_i = 44$ and $x/\theta_i = 444$.

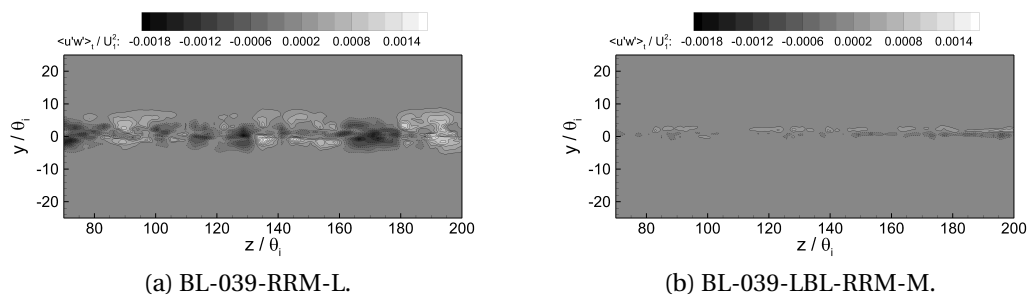


Figure 5.41: Secondary shear stress contour maps at measurement station 2.

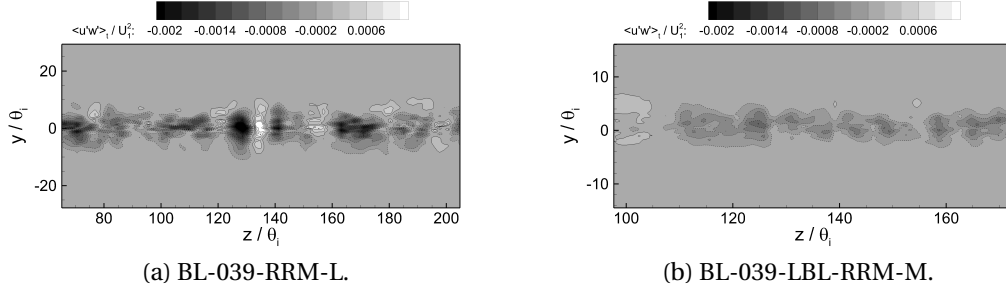


Figure 5.42: Secondary shear stress contour maps at measurement station 3.

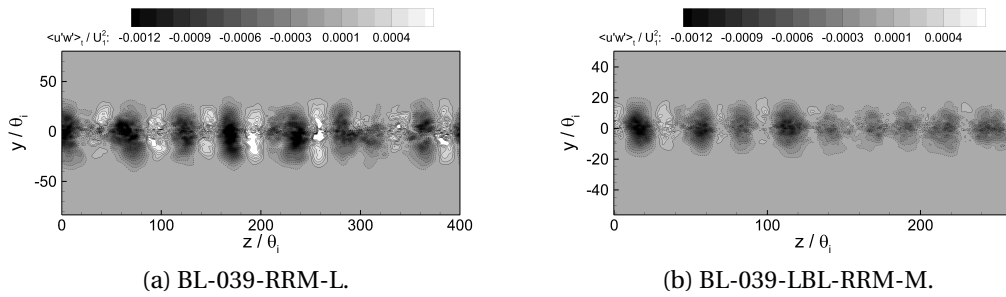


Figure 5.43: Secondary shear stress contour maps at measurement station 5.

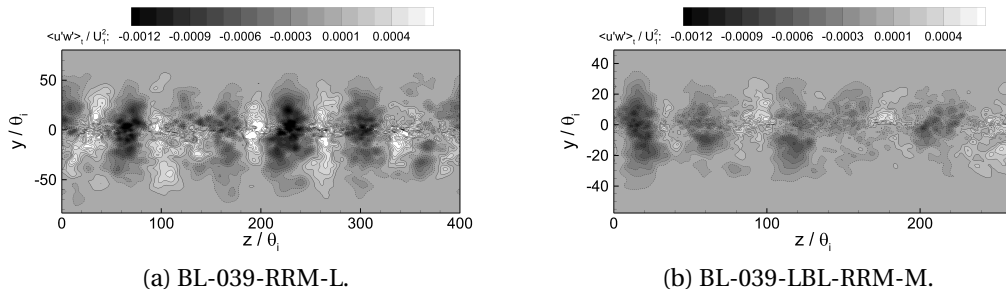


Figure 5.44: Secondary shear stress contour maps at measurement station 6.

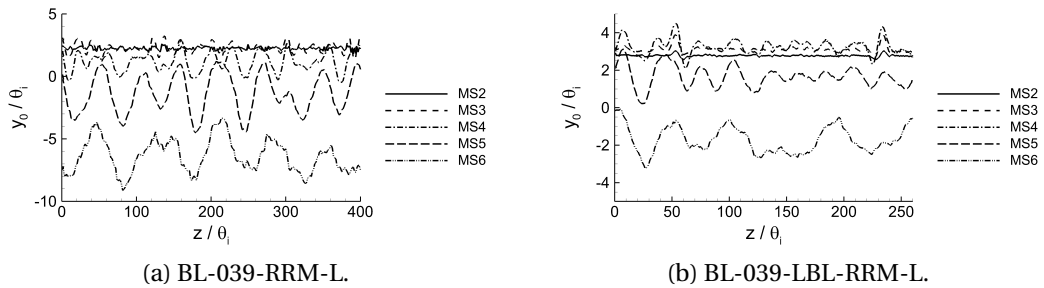
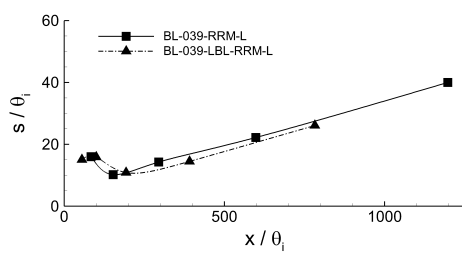
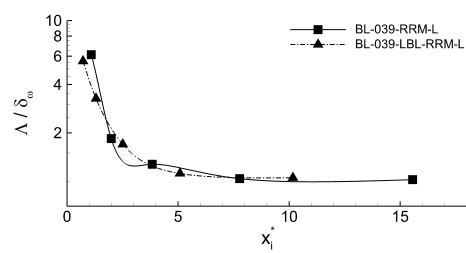


Figure 5.45: Centreline evolution at measurement stations 2 through 6.



(a) Streamwise structure spacing.



(b) Ratio of spanwise wavelength of streamwise structure to local vorticity thickness.

Figure 5.46: Streamwise vortex structure evolution.

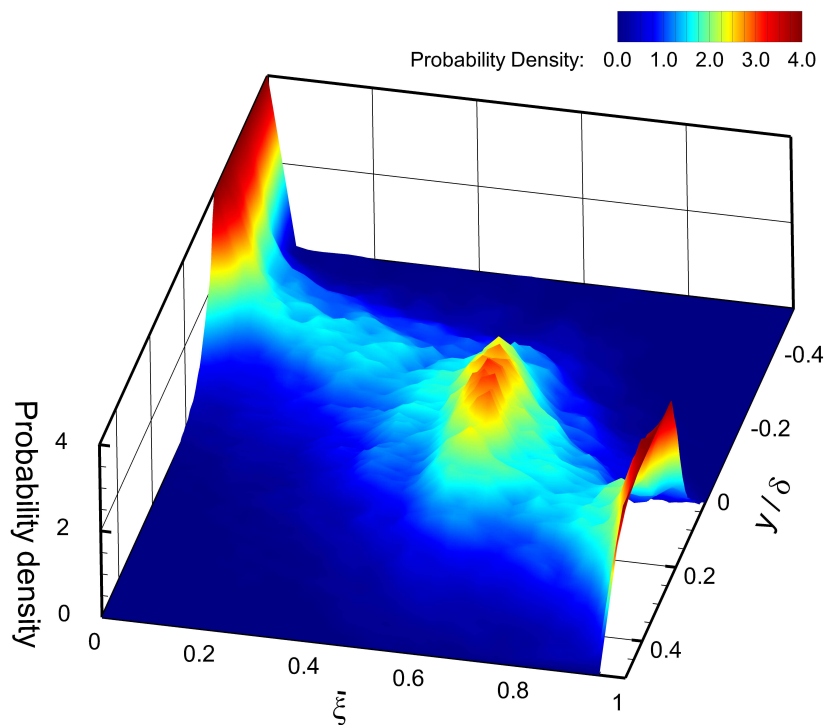
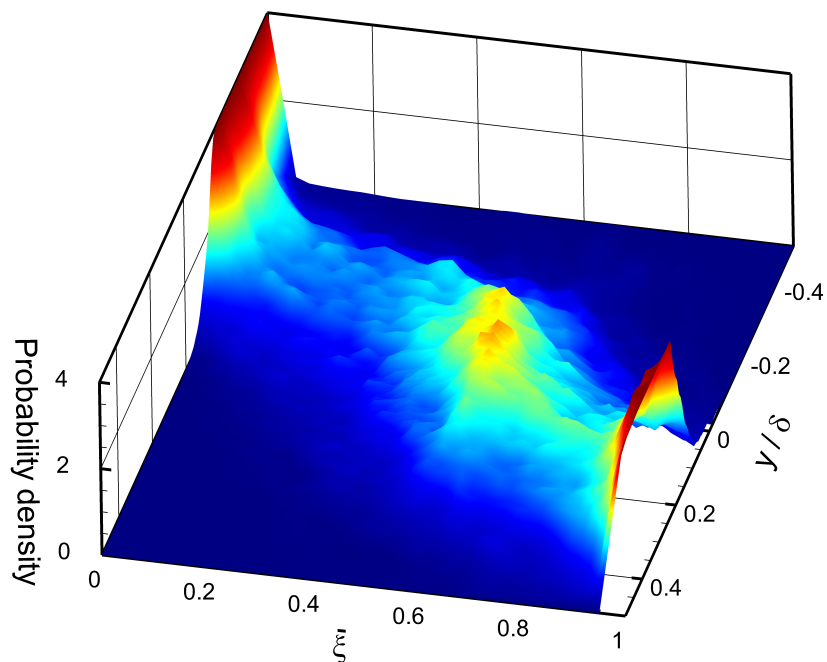
(a) BL-039-RRM-L, $z/\theta_i = 80$.(b) BL-039-RRM-L, $z/\theta_i = 220$.

Figure 5.47: Probability density functions at measurement station 6.

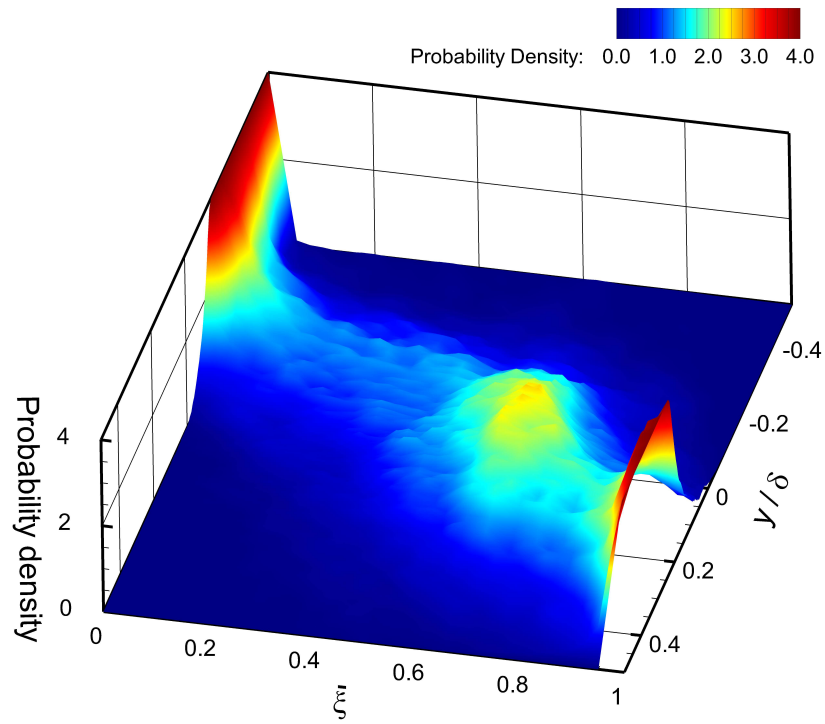
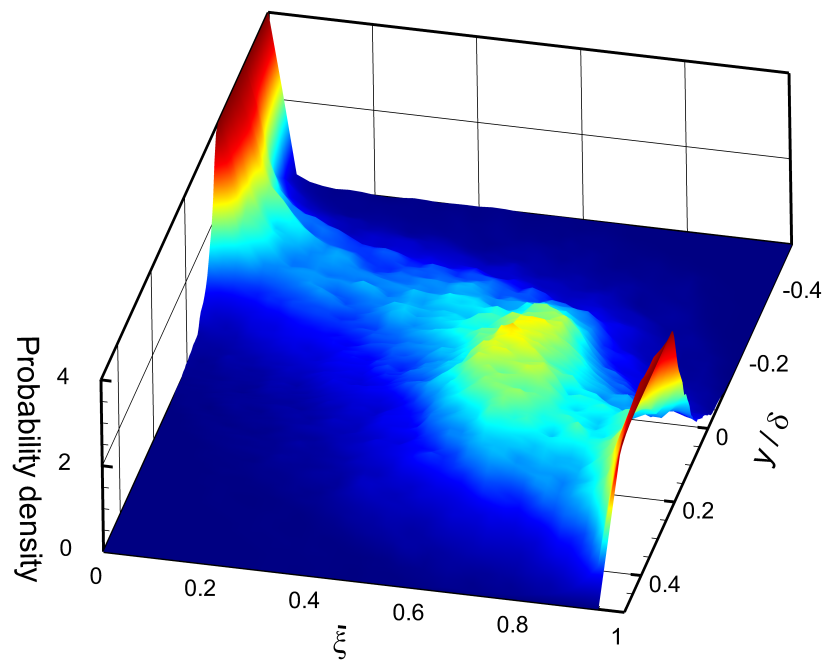
(a) BL-039-LBL-RRM-L, $z/\theta_i = 30$.(b) BL-039-LBLs-RRM-L, $z/\theta_i = 55$.

Figure 5.48: Probability density functions at measurement station 6.

Chapter 6

Elevated Inflow Fluctuation Magnitude Effects

6.1 Inlet Fluctuation Magnitude Effects

6.1.1 Introduction

The previous chapters have investigated a number of inlet parameters such as spatial correlation, and small changes in the boundary layer fluctuation magnitudes, as well as boundary layer momentum thickness. During those numerical experiments, the inlet boundary layer fluctuation magnitude was singled out for further investigation.

In this chapter, the effect of large boundary layer fluctuation magnitude changes is studied using large eddy simulations based on spatially correlated inlet fluctuations. Three numerical simulations with varying high-speed inlet boundary layer fluctuation magnitudes ranging from 2% to 10% u'_{max}/U_1 where U_1 is the high-speed inlet velocity.

Case	High-speed fluctuations	Low-speed fluctuations
BL-066-RRM-M	Fig. 6.1b	Fig. 6.1b
BL-066-RRM-H	Fig. 6.1c	Fig. 6.1b
BL-066-RRM-VH	Fig. 6.1d	Fig. 6.1b

Table 6.1: Simulation cases and inlet boundary layer fluctuation profiles.

6.1.2 Simulation Setup

The computational domain, grid and sub-grid scale model remain unchanged compared to Section 4.2.3. Three levels of inlet boundary layer fluctuations are compared. The different fluctuation levels are designated with the suffixes -M, -H and -VH, corresponding to maximum streamwise inlet fluctuation magnitude of 2%, 6.5% and 10% of U_1 , respectively. An overview of the simulation cases and their respective inlet boundary layer fluctuation magnitude profiles is given in Table 6.1. For a selected number of results the -L fluctuation intensity has been included for completeness. A complete presentation of results based on the -L dataset is found in Chapter 4.2.

The mean streamwise velocity profile specified at the inlet plane of the auxiliary upstream domain is shown in Figure 6.1a. A similar Blasius type inlet profile is imposed on the low-speed inlet plane. The inlet profiles are kept constant while the inlet boundary layer fluctuation magnitudes are varied. The inlet boundary layer momentum thickness is kept constant for all simulations.

The time step is chosen as $\Delta t = 6 \times 10^{-7}$, and the CFL number is kept below 0.35 for the entire duration of all simulations. Cross-plane ($y-z$) and flow visualisation data are recorded every 500 time steps which corresponds to a sampling frequency of 3.33kHz. Mean flow data has been computed from a minimum of 1000000 iterations equating to approximately 15 flow through times based on the convective velocity, $U_c = 0.5(U_1 + U_2)$ where U_1 and U_2 are the high- and low-speed inlet velocities, respectively. Cross-plane data is ensemble averaged from a minimum of 1200 instantaneous planes. The measurement stations are listed in Table 6.2.

Station	x (m)	x/θ_i	x_i^*
MS1	0.0180	40	0.88
MS2	0.0380	83	1.86
MS3	0.0690	151	3.37
MS4	0.1330	291	6.50
MS5	0.2695	590	13.17
MS6	0.5390	1180	26.35

Table 6.2: Measurement stations.

6.1.3 Results

6.1.3.1 Mean Flow Statistics

The mean streamwise velocity at $x/\theta_i = 1000$ is shown in Figure 6.2a. All simulations show self-similarity and agreement with reference data is very good. Mean streamwise velocity fluctuation magnitudes at $x/\theta_i = 1000$ are shown in Figure 6.2b. The predicted peak intensity is close to that of the reference data for all simulations. In the interface regions, the BL-066-RRM-M over-predicts the streamwise velocity fluctuation magnitude slightly. This over-prediction of the peak streamwise velocity fluctuation is commonly observed in LES of spatially evolving mixing layers [21].

Figure 6.2c shows the peak streamwise velocity fluctuation with downstream distance from the splitter plate trailing edge. BL-066-RRM-M shows best agreement with the reference data, both for the peak magnitude as well as the streamwise location of the peak. An increase in the inlet fluctuation level to the level of BL-066-RRM-H moves the peak fluctuation upstream to close proximity with the splitter plate but does not alter the peak magnitude. A further increase in the inlet fluctuation magnitude changes the shape noticeably. In the far-field, self-similar region of the mixing layer, all three simulations show very similar values for the fluctuation magnitude and capture the reference value well.

Power spectral density plots at two streamwise locations are shown in Figure 6.3. At $x/\theta_i = 44$, shown in Figure 6.3a, only BL-066-RRM-M shows a clear peak of the Strouhal number. This peak is located at $St \approx 0.0284$ which is close to the predicted

Case	k_o
BL-066-RRM-M	0.0358
BL-066-RRM-H	0.0305
BL-066-RRM-VH	0.0307
Browand & Latigo (lam.) [45]	0.0342
Browand & Latigo (turb.) [45]	0.0301

Table 6.3: Momentum thickness growth rates.

theoretical Strouhal number of $St = 0.0257$. BL-066-RRM-H and BL-066-RRM-VH are approaching the $-5/3$ slope indicative of turbulent flow. Power spectral density plots at $x/\theta_i = 219$ are shown in Figure 6.3b. All simulations show a $-5/3$ slope, indicative of a fully developed turbulent mixing layer.

The momentum thickness distribution from each simulation is shown in Figure 6.4. BL-066-RRM-M capture the experimental momentum growth well in the pre- and post-transition of the mixing layer. BL-066-RRM-H matches BL-066-RRM-M closely in the near field but starts to diverge at $x/\theta_i \approx 500$, producing a lower growth rate in the self-similar region. BL-066-RRM-VH grows at an almost constant rate, matching the growth rate of BL-066-RRM-H in the far field. Table 6.3 lists the momentum growth rates. For a laminar inlet boundary layer with a peak streamwise fluctuation magnitude of $2.5\% U_1$, the experiment reported a momentum growth rate constant of $k_o = 0.0342$. The peak inlet fluctuation magnitude of 2% in BL-066-RRM-M is slightly lower than that of the experiment. However, the growth rate constant is predicted well at $k_o = 0.0358$ which is only 4% higher than the reference value. The higher fluctuation simulations produce growth rate constant values of $k_o = 0.0305$ and $k_o = 0.0307$. These values are very close to the reference growth rate value of $k_o = 0.0301$ for a mixing layer developing from tripped inlet conditions [45].

While the mean streamwise velocity and mean streamwise velocity fluctuations are similar for all simulations, differences in the spectral density plots and momentum growth rates are observed. Mixing layer growth has been shown to be driven by the large scale primary vortices that make up the post-transition mixing layer. These vortices are analysed in detail in the next section.

6.1.3.2 Flow Structure

Figure 6.5 shows instantaneous spanwise averaged, and instantaneous single plane, passive scalar flow visualisations for BL-066-RRM-M. Large-scale structures are identifiable throughout the entire streamwise domain extent, and the large scale structures can easily be identified in the single plane flow visualisation, suggesting a high degree of spanwise regularity. Flow visualisations for BL-066-RRM-H are shown in Figure 6.6. Large scale vortices are visible in the pre- and post-transition of the mixing layer for the spanwise averaged and single plane visualisations. BL-066-RRM-VH passive scalar flow visualisations are shown in Figure 6.7. The main difference compared to the other simulations is seen in the vortex sheet which starts to develop from the trailing edge of the splitter plate. In the transition and post-transition region, the flow visualisations are qualitatively similar to those of the other simulations.

The underlying 3-D structures are investigated with perspective views in the transition and post-transition region of the mixing layer. Perspective views at measurement station 3 for BL-066-RRM-M, BL-066-RRM-H and BL-066-RRM-VH are shown in Figure 6.8. The upper and lower bounds of the mixing layer are defined by the passive scalar concentrations of $\bar{\xi} = 0.01$ and 0.99. The perspective view for BL-066-RRM-M is qualitatively different to those for BL-066-RRM-H and BL-066-RRM-VH. The primary vortices in BL-066-RRM-M are very regular the spanwise direction. Primary vortex structures and the braid regions separating them are easily discerned. In BL-066-RRM-H, shown in Figure 6.8b, the primary vortices show less spanwise regularity and local branching between the primary vortices is observed. Figure 6.8c shows the perspective view for BL-066-RRM-VH at MS3. The mixing layer is qualitatively similar to the one in BL-066-RRM-H but is more irregular still. The local branching observed in the BL-066-RRM-H, and BL-066-RRM-VH simulations has previously been observed in experiments [44], temporal [68] and spatial simulations based on idealised inlet conditions [21, 105, 65].

The perspective view for BL-066-RRM-M at MS4 is shown in Figure 6.9a. Most of the primary vortices are spanwise coherent. However, some local branching and tearing interactions are observed. The perspective views of BL-066-RRM-H and BL-066-RRM-VH are shown in Figure 6.9b and 6.9c, respectively. In both simulations

localised branching between the primary vortices is visible. The very high inlet fluctuations magnitudes in BL-066-RRM-VH produce primary vortices with a highly irregular iso-surface.

6.1.3.3 Streamwise Vortex Structure

To study the state of the boundary layers before it enters the main computational domain, data at an additional measurement station A (MSA), is recorded. This additional measurement station lies $26\theta_i$ upstream of the splitter plate trailing edge.

The mean streamwise vorticity planes at MSA are shown in Figure 6.10. Spatially stationary, streamwise vortices are present in all simulations. The spanwise wavelength and vertical size of the streamwise vortex structures decreases with an increase in the inlet fluctuation magnitude. The cause of this is that the recycling-rescaling method rescales the flow in the pre-cursor domain to match a desired spanwise averaged magnitude but the spatial evolution of the inlet fluctuations evolves ‘naturally’. This evolution appears to produce few and stronger vorticity clusters for low inlet fluctuation magnitudes and a large number of weaker vorticity clusters for high inlet fluctuation magnitudes.

The mean streamwise vorticity data at measurement station 2 are shown in Figure 6.11. Three-tiered vorticity clustering is present in BL-066-RRM-M and BL-066-RRM-H while the mean streamwise vorticity in BL-066-RRM-VH is qualitatively similar to that observed in the idealised simulations in Chapter 4.2. Cross examination of the vorticity shows that the vorticity clusters at MS2 have remained spatially stationary and can be directly linked to those observed at MSA, upstream of the splitter plate trailing edge.

Figure 6.12 shows the mean streamwise vorticity at measurement station 3. In BL-066-RRM-M and BL-066-RRM-H the vorticity has re-arranged itself from three-tiered clustering into a single row of counter rotating vortices. This re-arrangement has been observed in experiments [88] and temporally and spatially correlated numerical simulations [21]. When BL-066-RRM-M and BL-066-RRM-H are compared, it can be seen that the streamwise vortices in BL-066-RRM-H are much less clear than

those in BL-066-RRM-M. The mean streamwise vorticity levels for BL-066-RRM-VH are irregularly distributed and most of the vorticity appears to have been dissipated.

Mean secondary shear stress cross-plane maps at measurement station 5 are shown in Figure 6.13. The non-derivative nature of the mean secondary shear stress data makes it easier to identify spatially stationary streamwise vortices than in the differentiated mean streamwise vorticity data [88]. This allows for the identification of spatially stationary streamwise vortices in the post-transition region. Experimental studies have shown an anti-correlation between the secondary shear stress and the streamwise vorticity [88]. The mean secondary shear for BL-066-RRM-M is shown in Figure 6.13a. From the mean secondary shear stress clusters visible it is evident that the spatially stationary streamwise vortices continue to be important even in the far-field region of the mixing layer. A lack of clearly distinguishable clustering at MS3 in Figure 6.13b, shows that BL-066-RRM-H produces weakened stationary streamwise vortices in the pre-transition flow, which may, or may not, disappear in the far-field. For the mean secondary shear stress in BL-066-RRM-VH, shown in Figure 6.13c it is not possible to identify individual spatially stationary streamwise vortices.

From the cross-planes, it is clear that BL-066-RRM-M and BL-066-RRM-H produce spatially stationary streamwise vortices. However, it is unclear if a spatially stationary streamwise vortex structure exists in BL-066-RRM-VH. Quantitative evidence about the secondary structures is obtained from centreline loci plots, shown in Figure 6.14. This approach has also been used in experiments [88] and numerical simulations [21] to establish the presence and quantify the effects of spatially stationary streamwise vortices. Undulations of the centreline loci are visible at measurement stations 2 to 4 for BL-066-RRM-M and BL-066-RRM-H, shown in Figure 6.14a and 6.14b. These undulations indicate the presence of spatially stationary streamwise vortices. In contrast, the mixing layer centreline locus for BL-066-RRM-VH shows no undulations and is statistically two-dimensional. The mean streamwise vorticity and mean secondary shear stress planes, as well as the mixing layer centreline loci data, suggest that spatially stationary streamwise vortices are present in BL-066-RRM-M and BL-066-RRM-H. In the highest fluctuation case, it is unclear if spatially stationary streamwise vortex structures develop.

To study the effect of the inlet fluctuation magnitude on the spanwise wavelength,

the streamwise vortex structure spacing against the pairing parameter, x_i^* , is plotted in Figure 6.15. The streamwise vortex spacing is calculated by measuring the mean spacing between spatially stationary streamwise vortices in the mean secondary shear stress cross-plane data. Data by BL-066-RRM-VH is excluded as it is not possible to identify any spatially stationary streamwise vortex structures in the cross-plane data. The included reference data by Bell & Mehta [88] and Plesniak *et al.* [104] were recorded in the same experimental facility. From the graph, it is immediately evident that the increase of the inlet fluctuation magnitude leads to a reduced number of spatially stationary streamwise vortices and therefore an increase in the streamwise vortex structure spacing, s . The simulations reproduce the trend observed in the reference data of a spacing decrease with a subsequent spacing increase. The streamwise vortex spacing observed in BL-066-RRM-H is very similar to the data reported by Bell & Mehta [88].

From the presented data it is concluded that the effects of an increase of the inlet fluctuation level on the mixing layer are two-fold. In the near-field of the mixing layer, an increase of the fluctuation magnitude leads to an increase in the number of spatially stationary streamwise vortices and a reduced streamwise vortex size. During the first and second pairing events and the resulting streamwise vorticity rearrangement, the trend reverses, however. In the post-transition region of the mixing layer a higher inlet fluctuation level results in fewer spatially streamwise vortices.

6.1.3.4 Primary Structure Growth

The vertical size of a structure is defined as the vertical distance between the $\langle \bar{\xi} \rangle_z = 0.01$ and $\langle \bar{\xi} \rangle_z = 0.99$ concentration analogues in a vertical plane of the structure's centre of rotation. This type of analysis has been used in comparable numerical studies [21] as well as experimental studies of turbulent mixing layers [11]. In this study, the growth of individual primary vortices is studied by tracking the vertical size from their first appearance up until an interaction event with a neighbouring structure.

The primary structure growth tracks for BL-066-RRM-M are shown in Figure 6.16. Experimental studies have suggested that structures which grow continuously through

irrotational roll-up [98] or turbulent diffusion [99] do so with the square root of time [21]. This is shown to be true for the primary structures tracked in BL-066-RRM-M which grow at a high rate before their growth slows down and they start to interact with neighbouring structures. This square root of time growth is observed in the pre- and post-transition of the mixing layer. Similar observations have been made in other numerical simulations based on low level, physically correlated inlet fluctuations [21].

Structure growth tracks for BL-066-RRM-H are shown in Figure 6.17. Some of the tracked structures grow as the square root of time and others grow continuously and linearly. Continuous linear growth has been observed in experiments by D'Ovidio & Coats [11], in white noise type LES of a spatially evolving mixing layer by McMullan *et al.* [18] and in the idealised simulations in Chapter 4.2. The weakened streamwise vortices make some primary vortex structures grow as the square root of time in the near-field region, while the primary structure growth is largely of the continuous linear type in the far-field region.

The primary structure tracks for BL-066-RRM-VH are shown in Figure 6.18. As the fluctuation level is increased even further, the growth mechanism is exclusively of the continuous linear type. One of the commonalities between the idealised simulations by McMullan *et al.* [18], the idealised simulations in Chapter 4.2 and the presented very high-level fluctuation recycling-rescaling simulations is the lack of a spatially stationary streamwise vortex structure. The link between the spatially stationary streamwise vortices and primary structure growth is discussed in detail later in this chapter.

6.1.3.5 Passive Scalar Mixing

Instantaneous passive scalar planes for BL-066-RRM-M at measurement station 5 are shown in Figure 6.19. In the downstream braid, shown in Figure 6.19a, large undulations are visible such as the ones at $z/\theta_i = 160$ and 220. These 'mushroom' shaped undulations have been linked to spatially stationary streamwise vortex structures [64]. In the core of the structure, shown in Figure 6.19b, the mixing layer is made up of two interface zones and the structure core. Unmixed high speed and

low speed fluid can be seen as light and dark patches, respectively, near the interface zones. These patches of unmixed fluid, close to the opposing free stream, are evidence of the engulfment entrainment mechanism. The undulations observed in the downstream braid, depicted in Figure 6.19a, are visible in the low and high speed interface zones, particularly the one highlighted previously, at $z/\theta_i \approx 160$. After the structure passage, the mixing layer returns to a single interface zone, shown in Figure 6.19.

A primary structure passage for BL-066-RRM-H at measurement station 5 is visualised in Figure 6.20. In the downstream braid, shown in Figure 6.20a, five large undulations are visible. Cross-examination with Figure 6.13b shows how positive shear stress patches entrain low speed fluid into the high speed side, seen in the instantaneous plot as dark tongues of fluid reaching into the high-speed side. Similarly, negative clusters of secondary shear stress in Figure 6.13b, entrain high-speed fluid into the low-speed side of the mixing layer. The cross-plane taken in the core of the structure shows less spanwise coherence than that for BL-066-RRM-M. In Figure 6.20c the mixing layer has returned to a single interface zone. The undulations at $z/\theta_i \approx 100$ and 200 have remained spatially stationary.

The instantaneous passive scalar cross-planes for BL-066-RRM-VH are shown in Figure 6.21. Unlike the other two simulations, there is no qualitative difference between the braid and core plots. At any of the three depicted time instances, single interface zones and vortex cores are visible. Large undulations of the interface zones are visible, but they do not appear to be spatially stationary and can not be tracked through the time series.

The presented instantaneous passive scalar plots give qualitative, but no quantitative, evidence of the entrainment mechanism of the mixing layer. One quantitative measure of the entrainment behaviour is the spanwise averaged passive scalar concentration inside a typical primary structure core, shown in Figure 6.22. The difference in the passive scalar concentration lines is striking. The passive scalar concentration measurement in BL-066-RRM-M shows a reversal in the centre of the mixing layer. As the inlet fluctuation magnitude increases this phenomenon reduces and for BL-066-RRM-VH the passive scalar concentration distribution is quantitatively similar to that of BL-066-WN-L shown in Figure 4.58b. Similar passive scalar con-

Simulation	$E_{v,\min}$	$E_{v,\max}$	$E_{v,z}$
BL-066-RRM-M	1.21	1.38	1.28
BL-066-RRM-H	1.24	1.40	1.32
BL-066-RRM-VH	1.24	1.43	1.34

Table 6.4: Entrainment ratios at measurement station 6.

centrations plots have been reported in a simulation using white noise type inlet conditions by McMullan *et al.* [18].

The entrainment ratio and centreline loci at measurement station 4 are shown in Figure 6.23. In the interest of comparison, the vertical axis extents have been kept constant. The entrainment ratio and centreline locus in BL-066-RRM-M, shown in Figure 6.23a, are heavily undulated. The reduced number and strength of the spatially stationary streamwise vortices in BL-066-RRM-H and BL-066-RRM-VH lead to fewer and weaker undulations of the entrainment ratio and mixing layer centreline loci.

Figure 6.24 shows the entrainment ratio and centreline loci at measurement station 6. In the far-field region of the mixing layer, the entrainment ratio and centreline loci plots for the varying fluctuation levels are very similar. It has been suggested in experiments that the effect of the spatially stationary streamwise vortex structures is greatest in the near-field and the number and strength of the streamwise vortices decrease with streamwise distance [104]. In light of the shown differences in the spatially stationary streamwise structures in the simulations, this is a possible explanation for the large differences observed in the near-field and observed similarity in the post-transition region. Table 6.4 lists the maximum, minimum and spanwise averaged entrainment ratio values for the presented simulations at MS6. For the velocity ratio of $R = 0.66$ the Dimotakis entrainment model (Equation 2.10) predicts an entrainment ratio value of $E_v = 1.45$. This predicted value is slightly higher than observed in the simulations.

The standard deviation of the entrainment ratio as a function of downstream distance is shown in Figure 6.25. For BL-066-RRM-M the spanwise variation of the entrainment ratio peaks downstream of the roll up before decreasing and asymptoting to a value of $\approx 4\%$. As the inlet fluctuation magnitude increases the peak vari-

Simulation	$E_{v,\max}$	$E_{v,\min}$
BL-066-RRM-M	117	364
BL-066-RRM-H	253	340
BL-066-RRM-VH	350	30

Table 6.5: Chosen spanwise locations for mixed fluid statistics.

ation decreases to $\approx 5\%$ for BL-066-RRM-H. In the self-similar region, the value of the standard deviation of the entrainment ratio is similar to that of BL-066-RRM-M. The highest fluctuation magnitude tested produces no peak in the entrainment ratio and shows a slow increase in the variation until it asymptotes to an almost identical value as the other performed simulations.

For each simulation, mixed fluid statistics at two spanwise locations are reported. The spanwise locations have been chosen to correspond to an entrainment maximum and minimum. Table 6.5 lists the spanwise locations. The mixed fluid probability, P_m , and the average mixed fluid concentration, ξ_m , for BL-066-RRM-M at measurement station 6 are shown in Figure 6.26a. Experimental data by Meyer *et al.* [94], recorded at $R = 0.60$, $x_i^* = 28.1$, $Re_\delta = 103000$ is included for guidance purposes rather than a like-for-like comparison. In the engulfment entrainment mechanism unmixed fluid is entrained deep into the mixing layer, past the centreline producing a non-unity value for the mixed fluid probability at any vertical location. A peak value of $P_m = 0.989$ for BL-066-RRM-M in the centre of the mixing layer indicates that unmixed fluid can be found in the centre of the mixing layer, which suggests engulfment to be the dominating entrainment mechanism. Agreement with experimental data is also excellent in both interface zones, particularly for the peak entrainment measurement taken at $z/\theta_i = 117$. The average mixed fluid concentration, ξ_m , for BL-066-RRM-M shows a local concentration peak in the low-speed side of the mixing layer indicating the presence of unmixed high-speed fluid in the low-speed interface zone.

The P_m curve for BL-066-RRM-H at MS6 is shown in Figure 6.26b. The curve is much broader compared to BL-066-RRM-M. Of interest is the unity peak value of P_m , meaning that unmixed fluid does not penetrate far into the mixing layer core. The spanwise variation of P_m is also reduced compared to BL-066-RRM-M. The av-

eraged mixed fluid concentration shows no increase in high-speed fluid in the low-speed side of the mixing layer as observed in BL-066-RRM-M and the curves for both spanwise measurements are similar. This is a confirmation of the low spanwise variation seen in previous passive scalar measurements and suggests that no or only very weak spatially stationary streamwise vortex structures are present at MS6.

The mixed fluid data for BL-066-RRM-VH are shown in Figure 6.26c. The spanwise variation is minimal, and the mixed fluid probability is very broad compared to the other simulations. As with BL-066-RRM-H, the maximum P_m value is unity. The average mixed fluid concentration shows almost no spanwise variation and does not show an increase in the high-speed concentration in the low-speed interface zone. The broadening of the P_m curve that is seen with an increase in the inlet boundary layer fluctuation magnitude has previously been observed in an experimental study by tripping the high-speed boundary layer [86].

Figure 6.27 shows the probability density functions (p.d.f.'s) for BL-066-RRM-M at measurement station 6. The spanwise locations at which the p.d.f.'s have been obtained are listed in Table 6.5. Both p.d.f.'s are of the *non-marching* type. Experimental studies of mixing layers originating from laminar inlet conditions have reported predominantly *non-marching* p.d.f.'s [50, 60, 86]. The preferred concentration of 0.6 is very close to the value of $\xi = 0.6$ obtained in comparable experimental studies [50].

The p.d.f.'s for BL-066-RRM-H are shown in Figure 6.28. The p.d.f.'s at both spanwise locations are now of the *marching* type. *Marching* type p.d.f.'s have been reported by Batt [62]. However, at $z/\theta_i = 340$ there is a slight increase in the probability density value close to the high-speed inlet. With this local peak in the high-speed side the p.d.f.'s could be classed as *hybrid*. *Hybrid* type p.d.f.'s have been reported in experiments where one inlet stream was tripped [60]. The p.d.f.'s for BL-066-RRM-VH are shown in Figure 6.29. The p.d.f.'s at both spanwise locations are of the *marching* type.

6.1.4 Summary

The effect of the high-speed inlet boundary layer fluctuation magnitude has been investigated by performing large eddy simulations with a velocity ratio of $R = 0.66$ and varying inlet fluctuation magnitudes of 1.0% (-L), 2.0% (-M), 6.5% (-H) and 10.0% (-VH). All other simulation parameters have been kept constant.

It has been found that an increase in the inlet boundary layer fluctuation magnitude has strong effects on the spatially stationary streamwise vortex structure. An increase of the fluctuation level leads to decrease of the size of the streamwise vortices at the inlet plane of the domain. The lowest level fluctuation simulation shows the highest number of spatially stationary streamwise vortices. This number is reduced for the medium fluctuation level simulation and reduced further for the high fluctuation level simulation. The ‘very high’ level fluctuation simulation shows no evidence of spatially stationary streamwise vortices.

The inlet fluctuation level is shown to be critical for the number and strength of the spatially stationary, streamwise vortex structures in the near- and far-field of the mixing layer. The spanwise variation observed in the pre-transition and transition region of the mixing layer is highest in the lower inlet fluctuation simulations with fewer, but stronger spatially stationary streamwise vortices. In the highest inlet fluctuation simulation, the lack of spatially stationary streamwise vortices leads to very little spanwise variation.

It is also shown how the presence or lack of spatially stationary streamwise vortices affects the growth of the primary structures. For spatially stationary streamwise vortex containing simulations, the primary structures grow as the square root of time before interacting with neighbouring structures. In the highest inlet fluctuation simulations, most of the primary structures grow continuously and linearly.

The spatially stationary streamwise vortices are also shown to influence the passive scalar entrainment and mixing. Lasheras & Choi [64] have shown the spatially stationary streamwise vortices to be critical to mixing layer entrainment, particularly in the near-field. With an increase in the inlet fluctuation magnitude, a change from the engulfment to the nibbling entrainment mechanism is observed. This is evi-

dent in the mixed fluid statistics as well as the probability density functions (p.d.f.'s) which are of the *non-marching* type for the low and medium inlet fluctuation magnitude simulations and of the *hybrid* and *marching* type for the high and highest inlet fluctuation level simulations.

In the last section of this chapter, it will be investigated if the observed changes in the mixing layer with a velocity ratio of $R = 0.66$ are repeatable for the different velocity ratios of $R = 0.39$ and 0.52 .

6.2 Velocity Ratio Changes

6.2.1 Introduction

The previous section has shown how increasing the inlet boundary layer fluctuation magnitude reduces and eventually prohibits the growth of the spatially stationary streamwise vortex structure. In this section, it will be investigated if this phenomenon is also observed at different velocity ratios. Three velocity ratios of $R = 0.39$, 0.52 and 0.66 together with inlet fluctuation levels of -L, -M, -H and -VH are investigated.

6.2.2 Simulation Setup

The domain, grid and sub-grid scale models are evaluated in Section 4.2.3. The inlet boundary layer fluctuations are described in Section 6.1.2. Table 6.6 lists the simulations, the velocity ratio, R , and inlet fluctuation levels.

Case	R	High-speed fluctuations	Low-speed fluctuations
BL-039-RRM-L	0.39	Fig. 5.1b	Fig. 6.1a
BL-039-RRM-M	0.39	Fig. 6.1a	Fig. 6.1a
BL-039-RRM-H	0.39	Fig. 6.1b	Fig. 6.1a
BL-039-RRM-VH	0.39	Fig. 6.1c	Fig. 6.1a
BL-052-RRM-L	0.52	Fig. 5.1b	Fig. 6.1a
BL-052-RRM-M	0.52	Fig. 6.1a	Fig. 6.1a
BL-052-RRM-H	0.52	Fig. 6.1b	Fig. 6.1a
BL-052-RRM-VH	0.52	Fig. 6.1c	Fig. 6.1a
BL-066-RRM-L	0.66	Fig. 5.1b	Fig. 6.1a
BL-066-RRM-M	0.66	Fig. 6.1a	Fig. 6.1a
BL-066-RRM-H	0.66	Fig. 6.1b	Fig. 6.1a
BL-066-RRM-VH	0.66	Fig. 6.1c	Fig. 6.1a

Table 6.6: Simulation cases and inlet boundary layer fluctuation profiles.

6.2.3 Results

6.2.3.1 Mean Flow Statistics

The momentum thickness variations are shown in Figure 6.30. Table 6.7 lists the momentum growth rate constant, k_o (Equation 2.6) in the self-similar region. For all values of R the growth rate constants for the two lower inlet fluctuation magnitudes and the two higher fluctuation magnitudes are similar. The -L and -M inlet fluctuation magnitudes produce values of k_o similar to those reported by Browand & Latigo [45] for their laminar inlet case. The momentum growth rate constants in the -H and -VH inlet fluctuation levels are closer to the growth rate of the mixing layer developing from tripped inlet conditions in the Browand & Latigo experiments [45].

Experimental values for the vorticity growth rate, $\delta_\omega/(x-x_0)$, have traditionally shown very high spreads, something which has long been a subject of concern and possible reasons for this large spread have been suggested by numerous authors [13]. The structure of the boundary layer on the splitter plate and the level of the inlet fluctuation magnitudes are one of the suggested causes for the large spread [46, 45]. Figure 6.31 compares the vorticity growth rate as function of the velocity ratio, R .

Case	k_o
BL-039-RRM-L	0.0364
BL-039-RRM-M	0.0357
BL-039-RRM-H	0.0321
BL-039-RRM-VH	0.0319
BL-052-RRM-L	0.0354
BL-052-RRM-M	0.0345
BL-052-RRM-H	0.0319
BL-052-RRM-VH	0.0317
BL-066-RRM-L	0.0364
BL-066-RRM-M	0.0358
BL-066-RRM-H	0.0326
BL-066-RRM-VH	0.0323
Browand & Latigo (lam.) [45]	0.0342
Browand & Latigo (turb.) [45]	0.0301

Table 6.7: Momentum thickness growth rate constants.

The vorticity growth rates in the simulations are on the lower edge of the reported experimental values but inside the spread.

Quantitative evidence of the development of the spatially stationary streamwise vortex structures is produced from the mixing layer centreline locus plots. Figure 6.32 shows the mixing layer centreline with varying inlet fluctuation magnitudes at measurement station 6, located in the far-field, turbulent region of the mixing layer. The centreline data has been vertically shifted, and only the presence and number of undulations, are evaluated. For all velocity ratios an increase in the inlet fluctuation level leads to a decrease in the number, and strength of the spatially stationary streamwise vortices.

6.2.3.2 Primary Structure Growth

The results have indicated that the inlet fluctuation level plays a significant role in the number and strength of the spatially stationary streamwise vortices. In this part, the primary structure growth is investigated.

Case	$\delta_\omega/(\mathbf{x} - \mathbf{x}_0)$
BL-039-RRM-L	0.0667
BL-039-RRM-M	0.0652
BL-039-RRM-H	0.0634
BL-039-RRM-VH	0.0631
BL-052-RRM-L	0.0861
BL-052-RRM-M	0.0847
BL-052-RRM-H	0.0778
BL-052-RRM-VH	0.0756
BL-066-RRM-L	0.1137
BL-066-RRM-M	0.1112
BL-066-RRM-H	0.1026
BL-066-RRM-VH	0.1012

Table 6.8: Vorticity growth rate.

Typical primary structure growth tracks of the primary vortices in the $R = 0.39$ cases are shown in Figure 6.33. In the -L and -M fluctuation simulations the post-transition structures grow primarily as the square root of time. In BL-039-RRM-H some structures grow as the square root of time, and others grow with continuously and linearly. The primary vortices in the highest fluctuation simulation, -VH, grow predominantly continuously and linearly.

Similar observations are made in the $R = 0.52$ simulations. The growth of the primary structures in the -L and -M cases is fitted by a square root of time curve. The -H simulation is host to some structures which grow as the square root of time, but the majority show a continuous, linear growth. In the -VH the primary vortices grow linearly as they convect downstream before interacting with their downstream neighbour.

Primary structure growth tracks for $R = 0.66$ follow a similar trend and are discussed in detail Section 6.1.3.4.

6.2.3.3 Passive Scalar Mixing

Passive scalar statistics are shown for each velocity ratio and four fluctuation levels. The spanwise locations have been chosen correspond to an entrainment maximum.

The mixed fluid probability, P_m and average mixed fluid concentration, ξ_m , are shown in Figure 6.35. The included reference data by Meyer *et al.* [94] is of comparable values of R and streamwise locations. Previously presented results for $R = 0.66$ have shown non-unity peak values for P_m for the -L and -M inlet fluctuation levels and peak values of unity for the -H and -VH inlet fluctuation magnitudes. Figure 6.35a shows the P_m and ξ_m curves for $R = 0.39$. The -L and -M fluctuation levels produce non-unity values for P_m while -H and -VH produce a peak value of $P_m = 1$. The local peak of the mixed fluid concentration in the low speed region of the mixing layer gets weaker with an increase in the inlet fluctuation magnitude.

Similar observations are made for the passive scalar entrainment and mixing measurements for $R = 0.52$ in Figure 6.35b. The -L and -M fluctuation levels show good agreement with the reference data. The -H and -VH simulation cases show evidence of over-mixing. The broadening of the P_m curve observed at higher fluctuation level has previously been reported by comparable experimental studies of mixing layers developing from tripped inlet boundary layers [86]. The mixed fluid statistics for $R = 0.66$ are shown in Figure 6.35c. As is observed for $R = 0.39$ and 0.52, the -L and -M fluctuation level data matches the data by Meyer *et al.* [94] best. The lack of a spatially stationary streamwise vortex structure in the two highest fluctuation level simulations leads to over-mixing of the passive scalar.

The p.d.f. for BL-039-RRM-L, shown in Figure 6.36a, shows a clearly defined preferred concentration and the p.d.f. shape is of the *non-marching* type. This is also true for the p.d.f. for BL-039-RRM-M, shown in Figure 6.36b. However, compared to the lower inlet fluctuation simulation, the peak is broader and less well defined, but the p.d.f. is still of the *non-marching* type. As the inlet fluctuation magnitude increases further, the p.d.f. type changes to *marching* for BL-039-RRM-H and BL-039-RRM-VH, shown in Figure 6.36c and 6.36d, respectively.

Similar observations are made for the p.d.f.'s for the $R = 0.52$ simulations, shown in

Figure 6.37. The -L and -M inlet fluctuation magnitude simulations produce p.d.f.'s of the *non-marching* type with a clearly defined peak with a preferred concentration that is similar to values obtained in experimental mixing layers. For the higher fluctuation levels, -H and -VH, the p.d.f.'s are of the *marching* types, shown in Figure 6.37c and 6.37d, respectively.

6.2.4 Summary

In this section, the effect of large inlet fluctuation magnitude changes on varying velocity ratios has been investigated. In total three velocity ratio values of $R = 0.39$, 0.52 and 0.66 have been compared. It has been shown that observations made for $R = 0.66$ in previous sections hold true for two other values of the velocity ratio, $R = 0.39$ and 0.52 . For all values of R , an increase of the inlet fluctuation levels results in the weakening and eventual suppression of the development of the spatially stationary, streamwise oriented vortex structure. The lack of a spatially stationary, streamwise vortex structure leads to large-scale spanwise structures with an inherently 3-D geometry and an over-mixing of the passive scalar.

6.3 Discussion

Organised, large scale structures in the turbulent mixing layer have been a subject of academic interest ever since their discovery by Brown & Roshko [9]. While many researchers subsequently found the Brown & Roshko type structures in their experiments, others observed structures that were more three-dimensional and less spanwise coherent [106] and some suggested that the Brown & Roshko type structure was atypical and that the majority of coherent structures were three-dimensional with helical type interactions [44].

The simulations presented in this study show that white noise type, idealised inlet conditions lead to inherently 3-D primary, large scale structures with continuous linear growth, and a lack of spatially stationary, streamwise vortices. Passive scalar

data show evidence for the nibbling entrainment mechanism. Similar results have been observed in a DNS by Attili *et al.* [3]. Physically correlated, low-level inlet fluctuations produce spatially stationary, streamwise vortices which ride on top of the quasi 2-D primary vortex structures. The primary large-scale structures in the physically correlated simulations grow as the square root of time and passive scalar entrainment happens by engulfment.

Some of the confusion around passive scalar entrainment, and probability density function types, is the result of 2-D simulations, such as those by Zhou & Pereira [93], producing *non-marching* p.d.f.'s. However, this is a necessary consequence of 2-D simulations as the mixing layer growth is the result of primary structure interactions which are necessarily of the rotation-amalgamation behaviour due to the lack of the third dimension. During the rotation-amalgamation behaviour of the primary structures, fluid is entrained by engulfment which produces *non-marching* p.d.f.'s. Furthermore, the spanwise variation observed in experiments [103] and in physically correlated, 3-D simulations cannot be modelled in 2-D simulations. Whilst 2-D simulations are therefore superficially attractive, as they appear to model passive scalar entrainment well, they are not representative of the real flow and do not attain the 'correct' self-similar state [107].

In contrast, it is shown that physically correlated, low level inlet fluctuations produce spatially stationary, streamwise vortices. This results in primary structures which grow as the square root of time and are separated by thin braid regions. Interactions of the primary vortices are of the classical pairing type as described by Brown & Roshko [9]. Mixing layer entrainment is shown to be of the engulfment type which produces *non-marching* p.d.f.'s.

As the inlet fluctuation level is increased the spatially stationary streamwise vortex structure is weakened and eventually suppressed. The braid regions become thicker and branches between the primary structures are observed. The thick interconnecting braids are used to exchange spanwise vorticity [21] between the large-scale structures which now grow continuously and linearly as they convect downstream. A lack of classical pairings means that entrainment happens primarily by nibbling which produces *marching* p.d.f.'s. Increasing the inlet fluctuation level also reduces the mixing layer growth rate, in agreement with experiments by Karasso & Mungal [60]

and Pickett & Ghandhi [86] who observed similar effects when the inlet boundary layer was tripped. This is the first time that large-scale structure evolution, growth rate and probability density function shapes have been linked.

The presented findings strongly agree with Rogers & Moser [6] who suggested that

The link between the hydrodynamic structures and the character (*marching* or *non-marching* p.d.f.'s) of the scalar mixing is clear. *Non-marching* p.d.f.'s are expected whenever organized rollers with clean braid regions and 'classical' pairings dominate the layer. These are necessary to 'rapidly' distribute free-stream fluid throughout the thickness of the layer. The *marching* pdf, which one would expect from an eddy-viscosity model, occurs when the flow is not so well organized.

The data suggest that spatially stationary streamwise vortices are a categorising feature of the flow. If the spatially stationary streamwise vortices are present, structures grow as the square root of time, are spanwise coherent and p.d.f.'s are of the *non-marching* type. Flows which do not produce a secondary, streamwise oriented vortex structure produce spanwise incoherent structures, continuous linear growth and p.d.f.'s of the *marching* type. The current simulations show that a lack of a spatially stationary streamwise vortex structure can be achieved by using spatially and temporally correlated inlet fluctuations with high fluctuation magnitudes.

6.4 Conclusions

In this chapter, the effects of the fluctuation level present in the high-speed boundary layer on the mixing layer evolution have been investigated. It has been shown that changes in the inlet fluctuation magnitude have strong effects on a number of mixing layer aspects, including the growth rate, spatially stationary streamwise vortex structures and passive scalar entrainment and mixing.

An increase in the inlet fluctuation level increases the spatially stationary streamwise vortex structure wavelength and reduces their strength. This subsequently affects

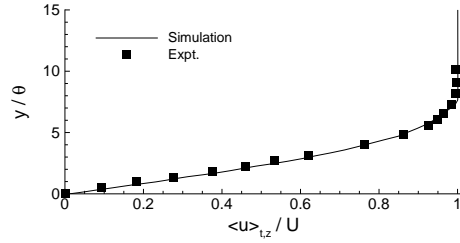
other mixing layer properties such as the growth rate and primary vortex growth mechanism. For lower fluctuation levels the primary structures grow as the square root of time as suggested by theoretical analysis [98, 99] and observed in comparable recycling-rescaling based simulations [21]. At high fluctuation levels the primary structures grow continuously and linearly as observed in experiments [11, 106].

The lack of spatially stationary streamwise vortex structures and the change in the primary structure growth mechanism also has a significant effect on the entrainment on the mixing of the passive scalar. Low and medium fluctuation magnitudes produce probability density functions of the *non-marching* type in line with experimental observations. High inlet fluctuation levels produce *marching* p.d.f.'s similar to experiments utilising inlet conditions with high boundary layer fluctuation levels [86].

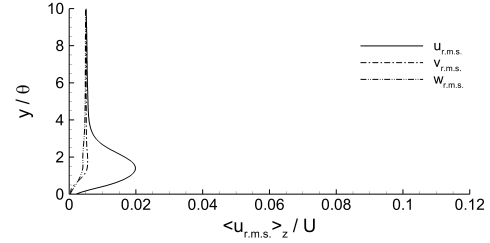
The second part of this chapter analysed three velocity ratios of $R = 0.39$, 0.52 and 0.66 . It is shown that the observations made in the for $R = 0.66$ in the post-transition region also hold true for the velocity ratios of $R = 0.39$ and 0.52 . Centreline plots show that the suppression effect of high inlet fluctuation magnitudes on the spatially stationary streamwise vortex structures is also observed for different velocity ratios. Mixing layer growth and large scale structure dynamics are similar to those observed for $R = 0.66$, which is also true for the passive scalar measurements.

The simulations show that the inlet boundary layer fluctuation magnitude has a strong effect on the plane mixing layer in the pre- and post-transition region. This chapter highlights the importance of inlet or initial conditions in experimental studies of the high Reynolds number mixing layer; an area which has not received a great amount of attention recently but could explain a large number of unexplained observations about mixing layers such as the large spread of reported mixing layer growth rates and differing probability density functions for mixing layers based on 'identical' bulk experimental parameters.

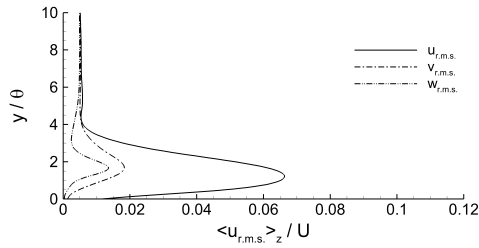
6.5 Figures



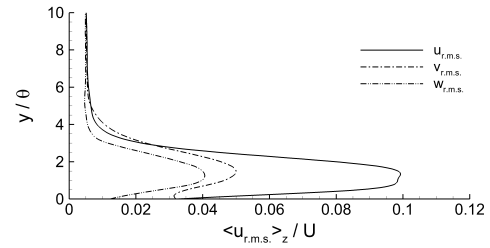
(a) Streamwise velocity inlet profile.



(b) Velocity fluctuations for BL-066-RRM-M.

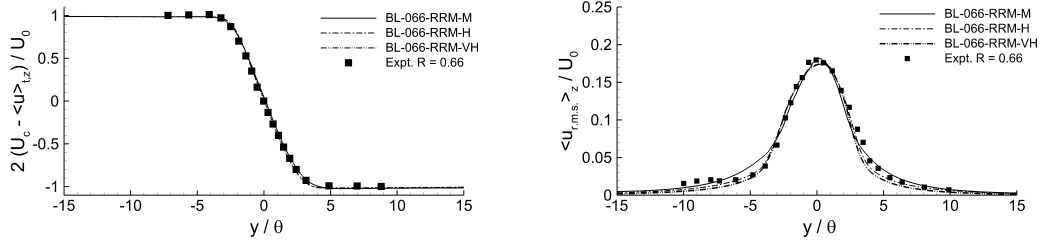


(c) Velocity fluctuations for BL-066-RRM-H.



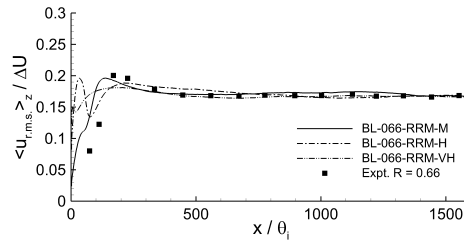
(d) Velocity fluctuations for BL-066-RRM-VH.

Figure 6.1: Streamwise velocity inlet profile and high-speed stream inflow fluctuation conditions.



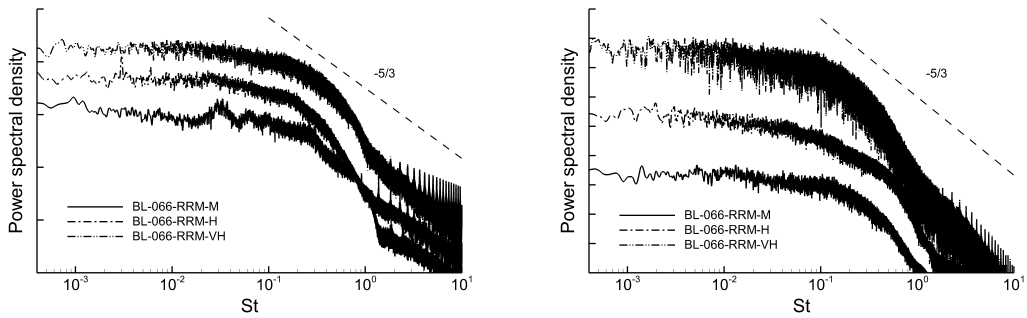
(a) Mean streamwise velocity at $x/\theta_i = 1000$.

(b) Streamwise velocity fluctuations at $x/\theta_i = 1000$.



(c) Maximum streamwise velocity fluctuation.

Figure 6.2: Mean flow statistics.



(a) $x/\theta_i = 44$

(b) $x/\theta_i = 219$

Figure 6.3: Power spectral density of streamwise velocity fluctuations. Power spectral density shifted along vertical axis for clarity.

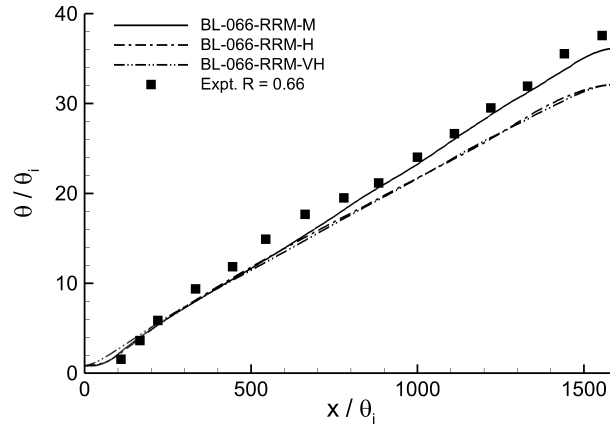


Figure 6.4: Local momentum thickness against downstream distance from the splitter plate trailing edge.

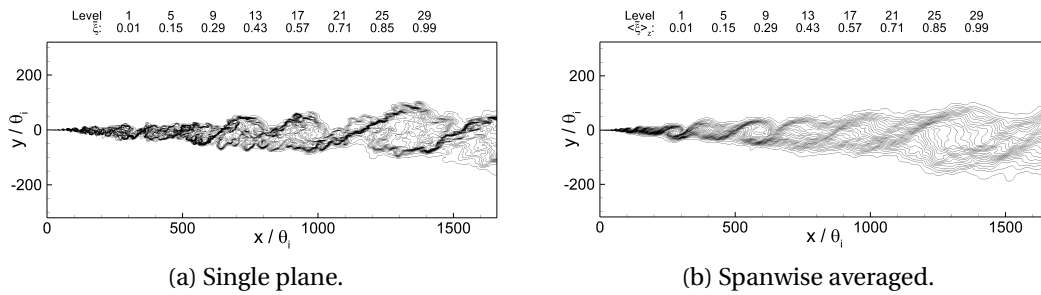


Figure 6.5: Instantaneous single plane and spanwise averaged passive scalar flow visualisations for BL-066-RRM-M.

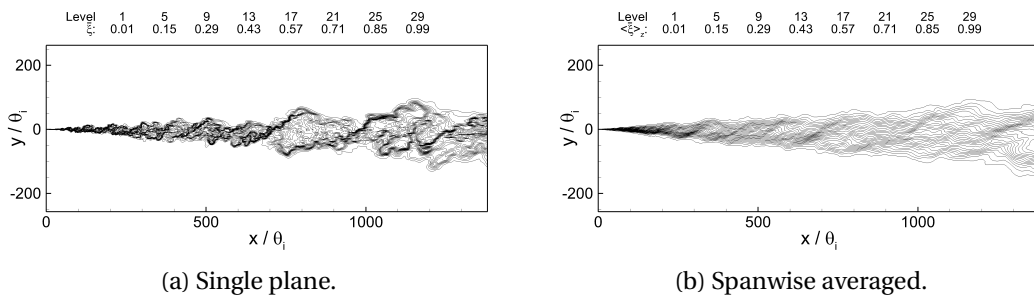


Figure 6.6: Instantaneous single plane and spanwise averaged passive scalar flow visualisations for BL-066-RRM-H.

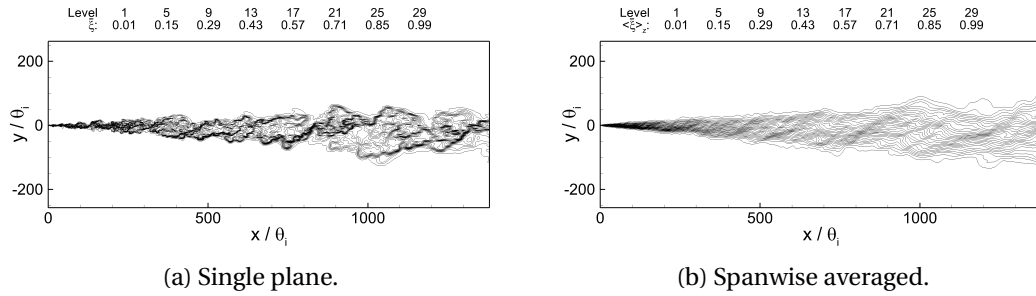


Figure 6.7: Instantaneous single plane and spanwise averaged passive scalar flow visualisations for BL-066-RRM-VH.

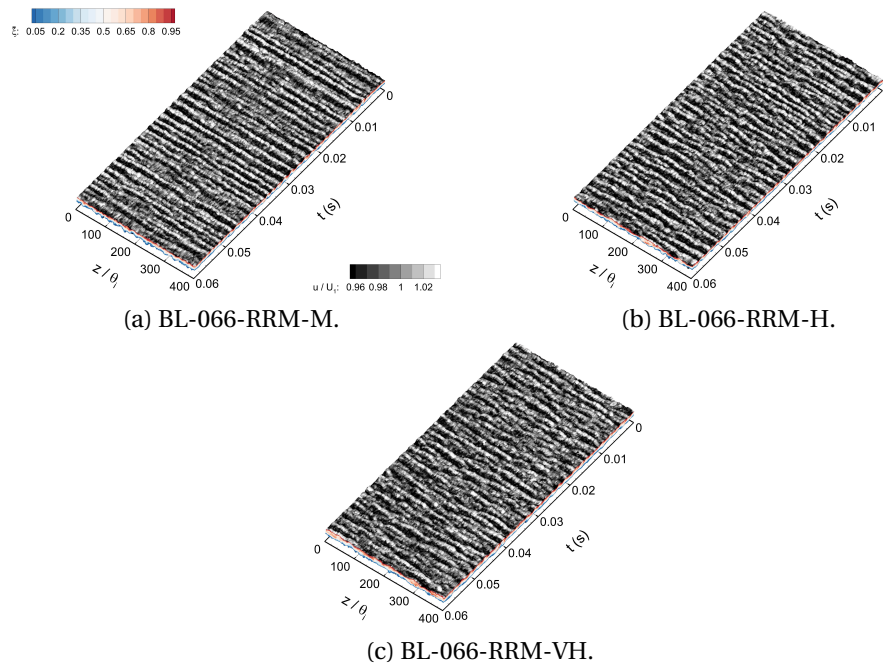


Figure 6.8: Perspective views at measurement station 3.

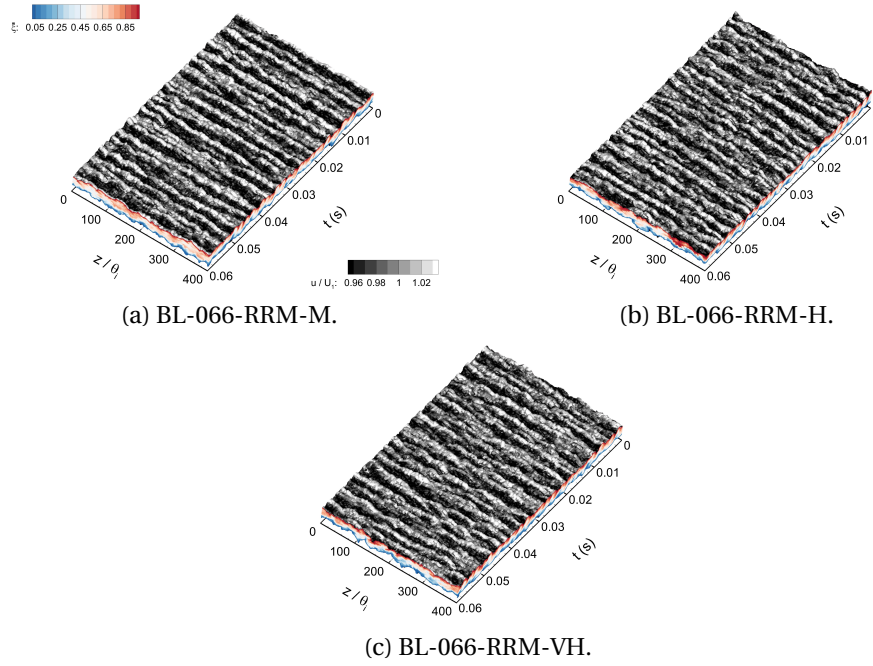


Figure 6.9: Perspective views at measurement station 4.

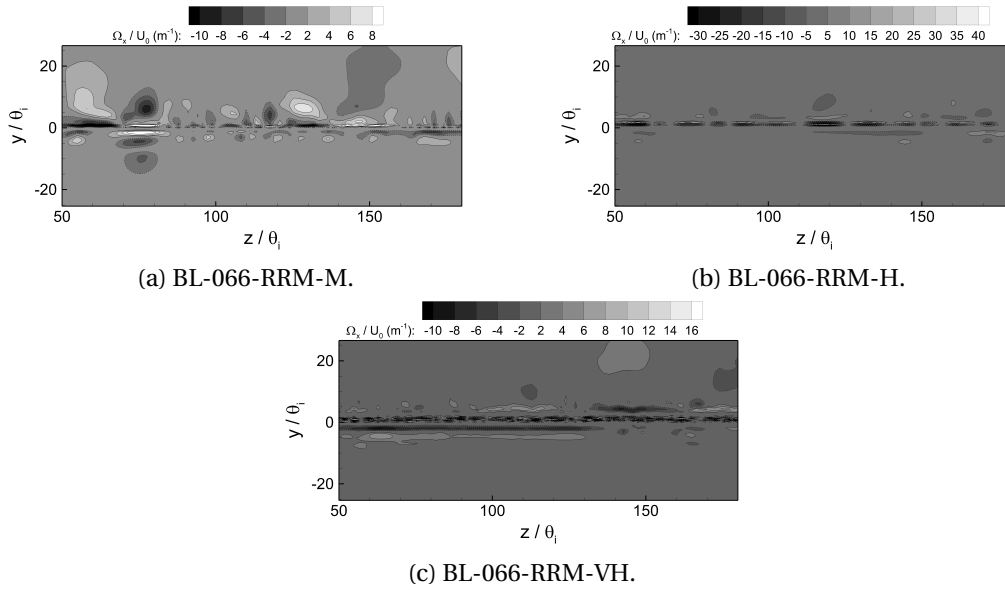


Figure 6.10: Cross-plane mean streamwise vorticity maps at measurement station A.

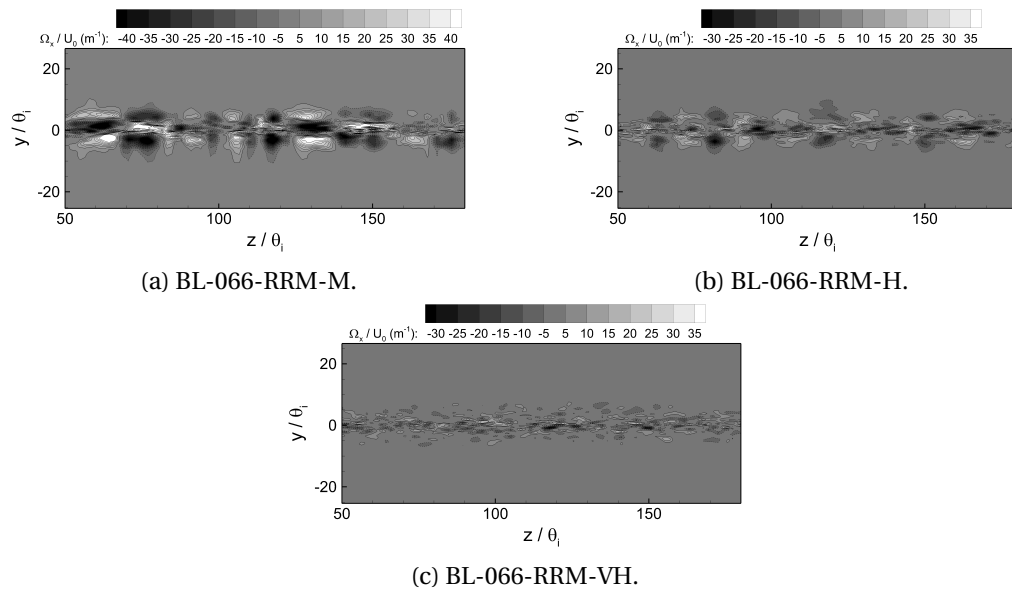


Figure 6.11: Cross-plane mean streamwise vorticity maps at measurement station 2.

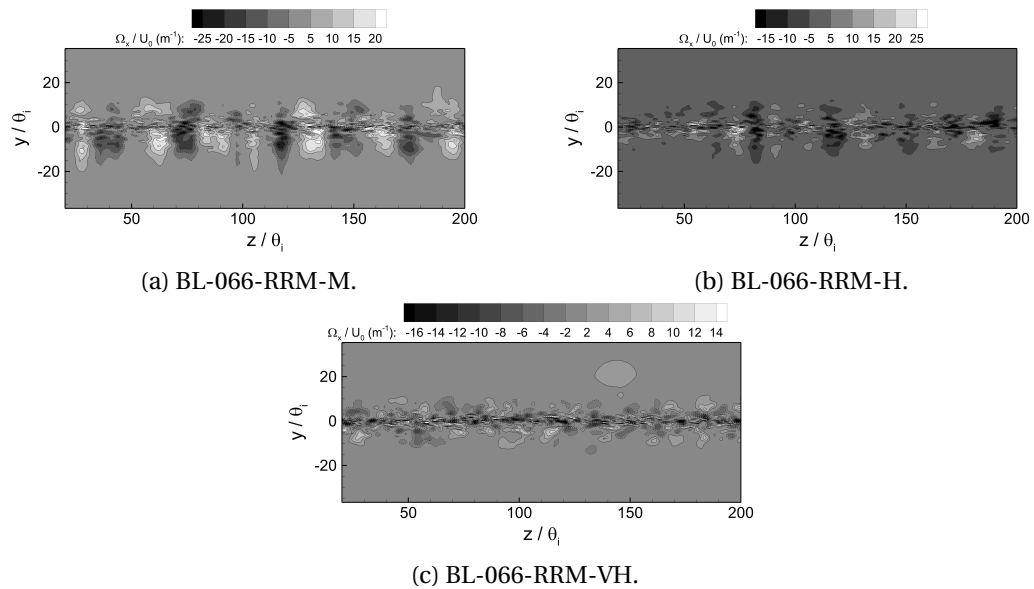


Figure 6.12: Cross-plane mean streamwise vorticity maps at measurement station 3.

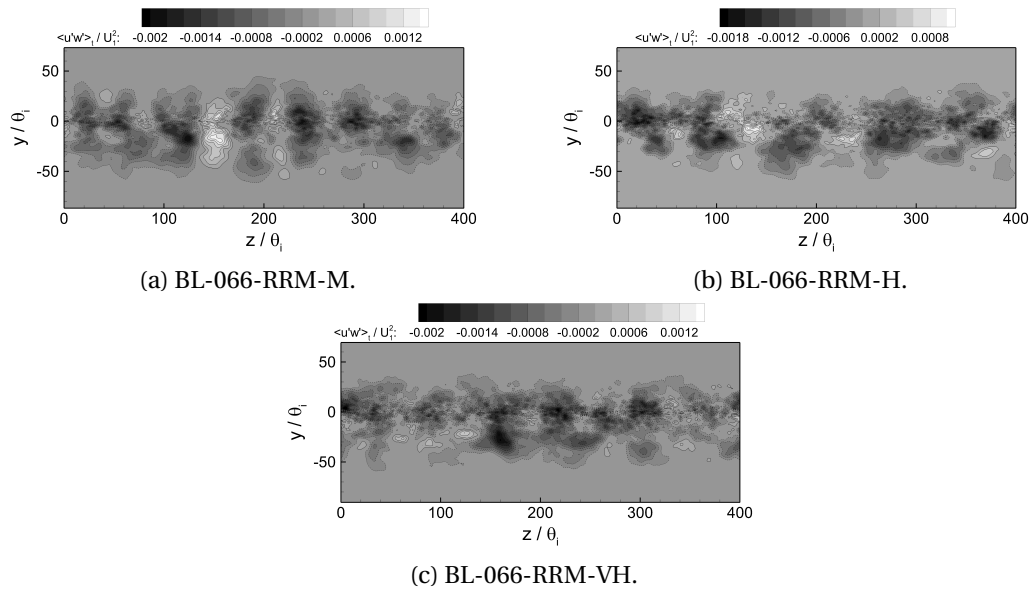


Figure 6.13: Cross-plane mean secondary shear stress maps at measurement station 5.

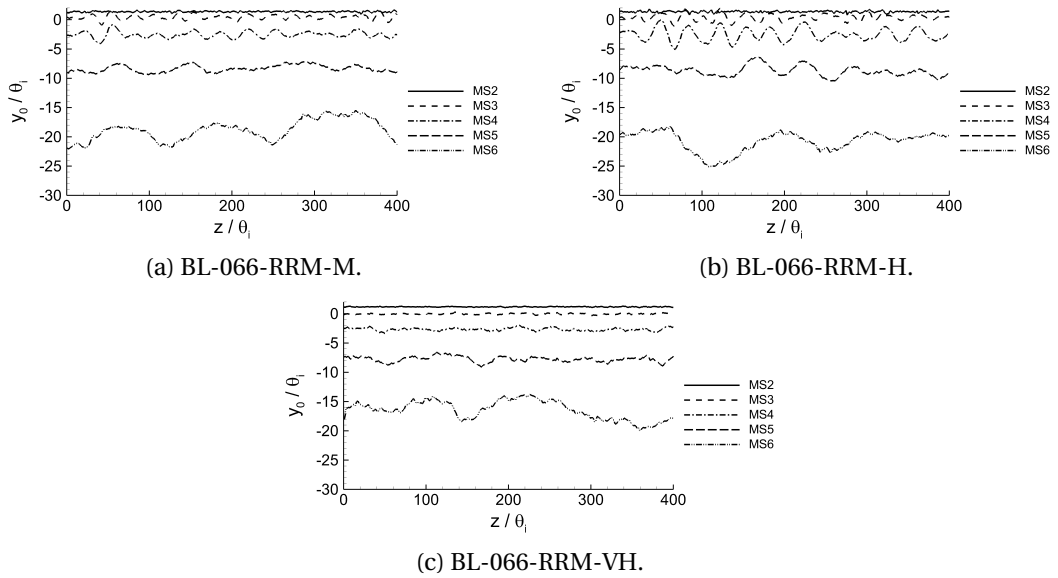


Figure 6.14: Centreline evolution at measurement stations 2 through 6.

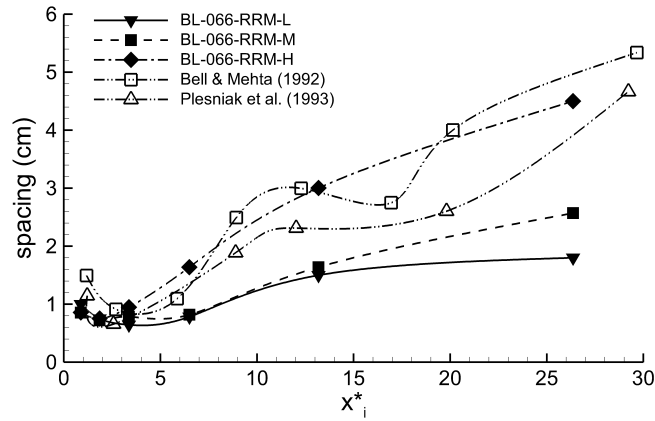


Figure 6.15: Streamwise vortex spacing. Included data by Bell & Mehta [88] and Plesniak *et al.* [104].

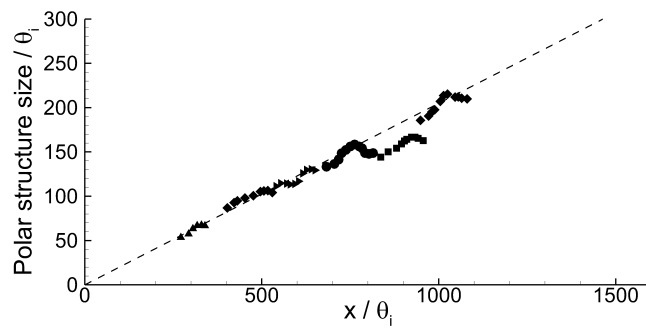


Figure 6.16: Primary structure growth for BL-066-RRM-M. Dashed line indicates the visual thickness of the mixing layer. Filled symbols denote square root of time growth.

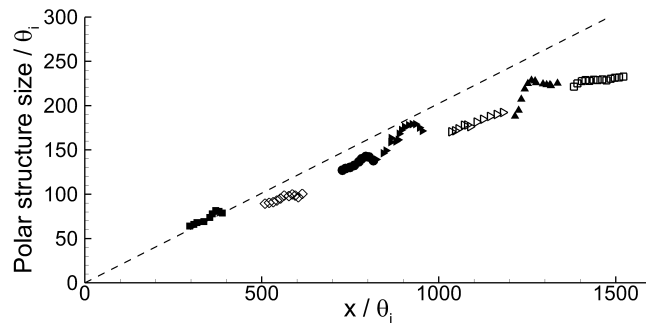


Figure 6.17: Primary structure growth for BL-066-RRM-H. Dashed line indicates the visual thickness of the mixing layer. Filled symbols denote square root of time growth.

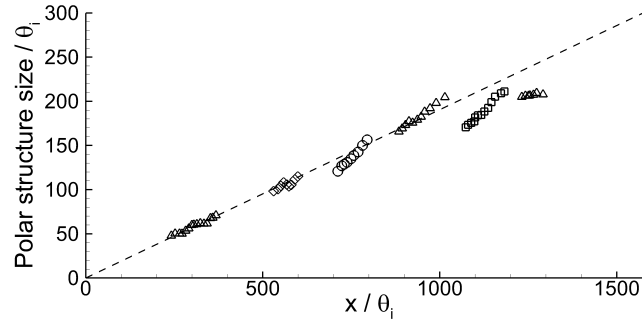


Figure 6.18: Primary structure growth for BL-066-RRM-VH. Dashed line indicates the visual thickness of the mixing layer. Filled symbols denote square root of time growth.

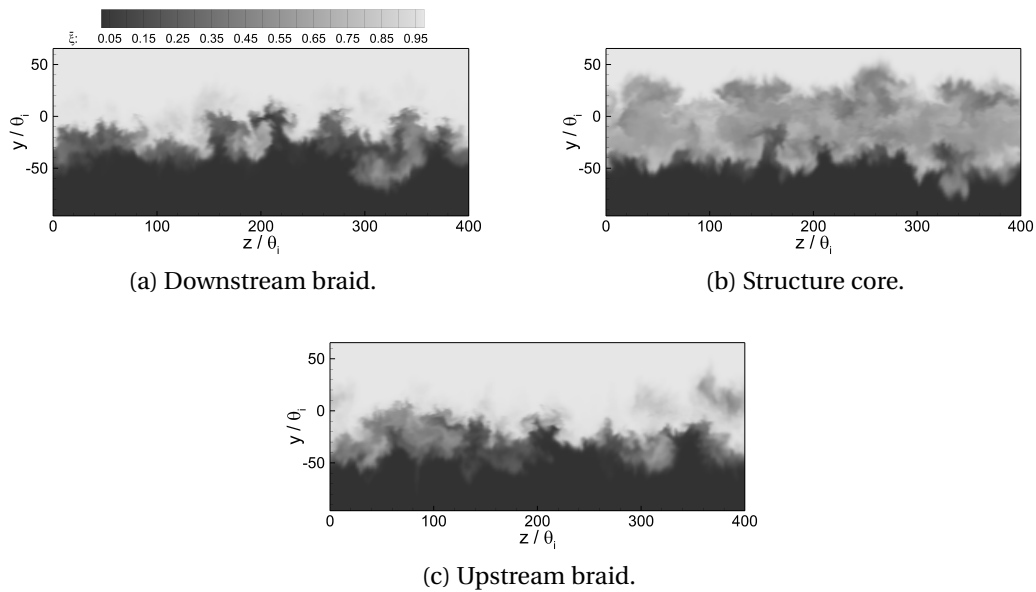


Figure 6.19: Primary structure passage for BL-066-RRM-M at measurement plane 5.

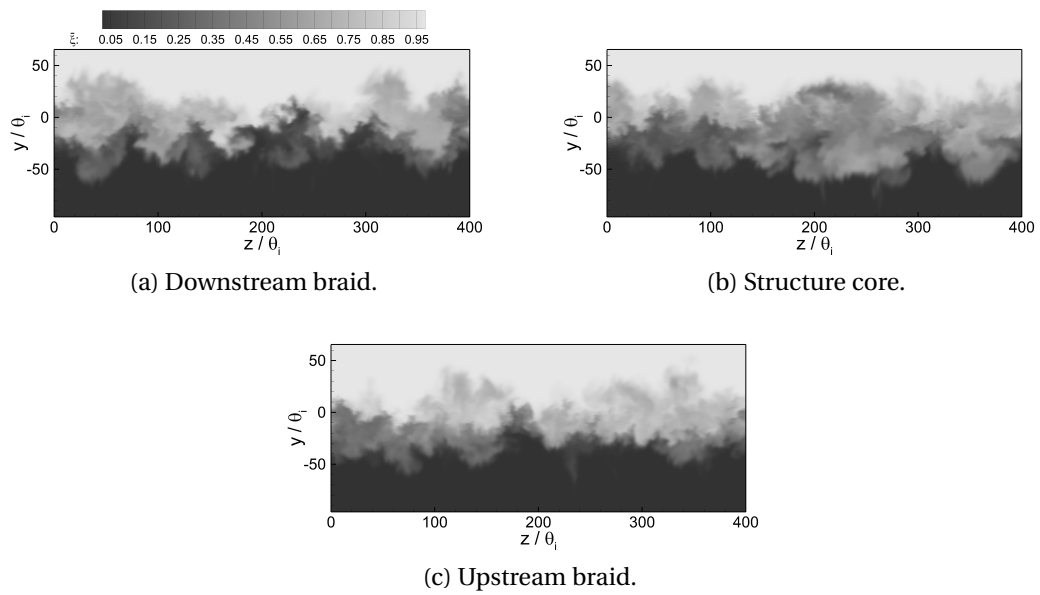


Figure 6.20: Primary structure passage for BL-066-RRM-H at measurement plane 5.

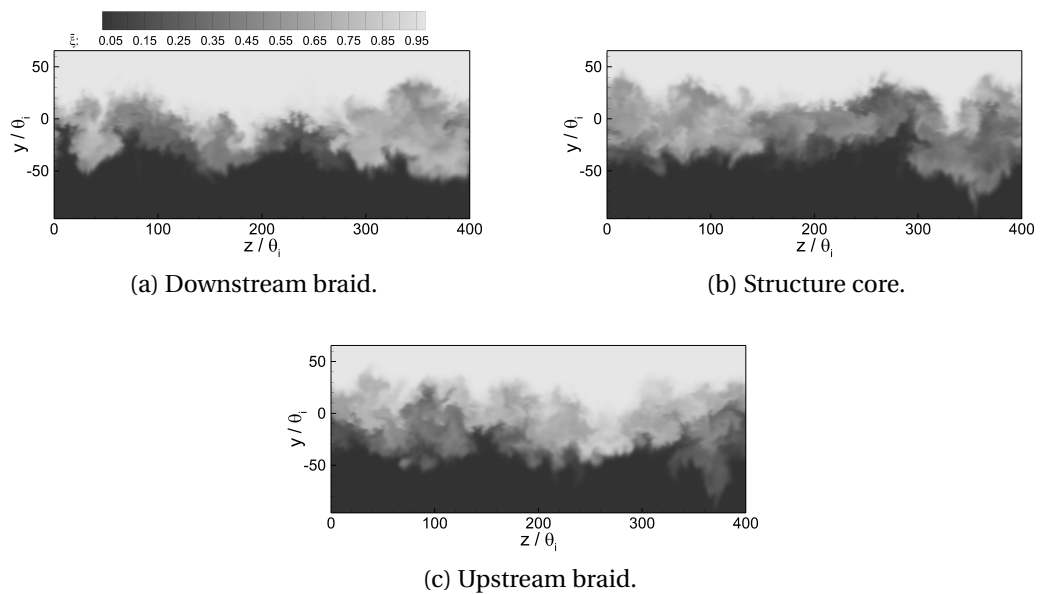


Figure 6.21: Primary structure passage for BL-066-RRM-VH at measurement plane 5.

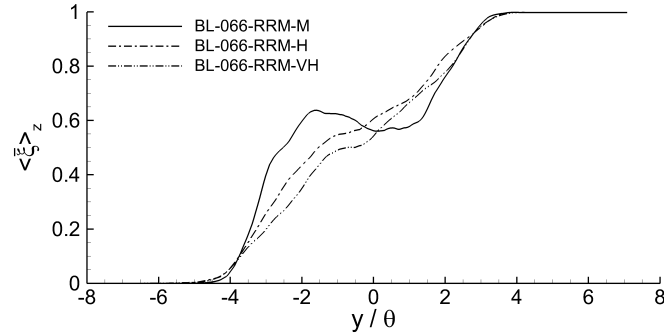


Figure 6.22: Typical spanwise averaged passive scalar concentration in a primary structure core at measurement station 5.

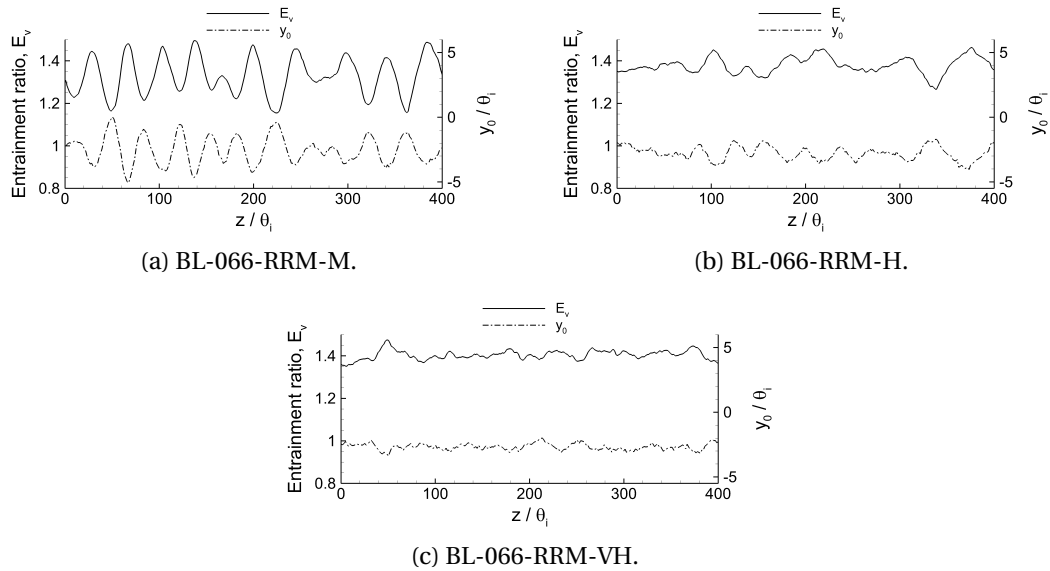


Figure 6.23: Entrainment ratio, E_v , and mixing layer centreline locus, y_0 , at measurement station 4.

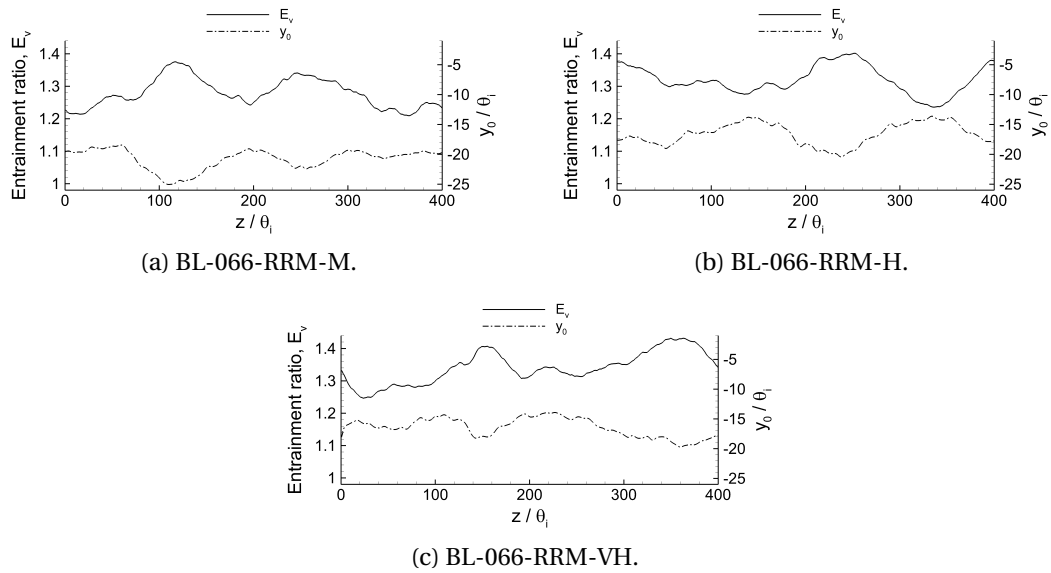


Figure 6.24: Entrainment ratio, E_v , and mixing layer centreline locus, y_0 , at measurement station 6.

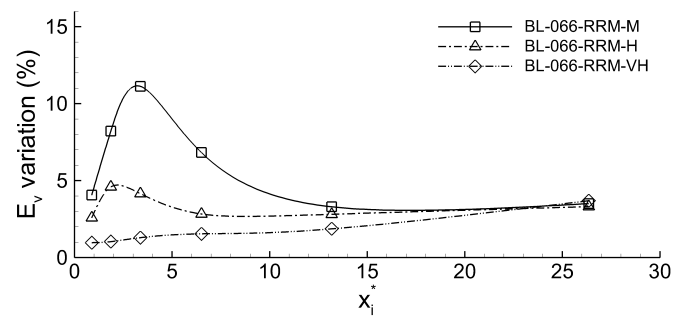


Figure 6.25: Standard deviation of the mixing layer entrainment ratio, E_v . Experimental data of Bell and Mehta [47] for the standard deviation of the mixing layer thickness.

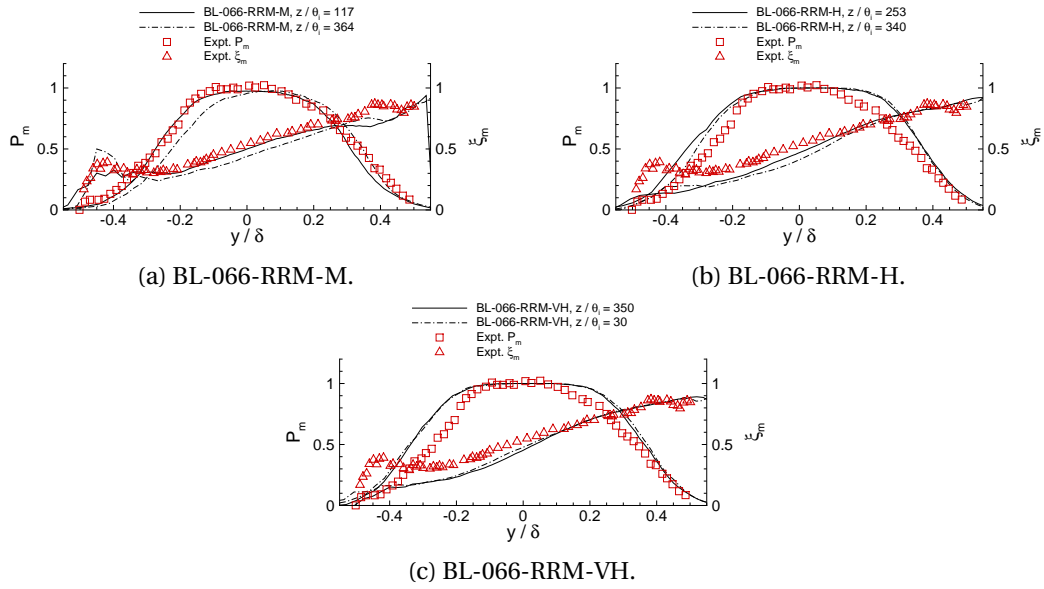


Figure 6.26: Mixed fluid probability, P_m , and average mixed fluid concentration, ξ_m at measurement station 6.

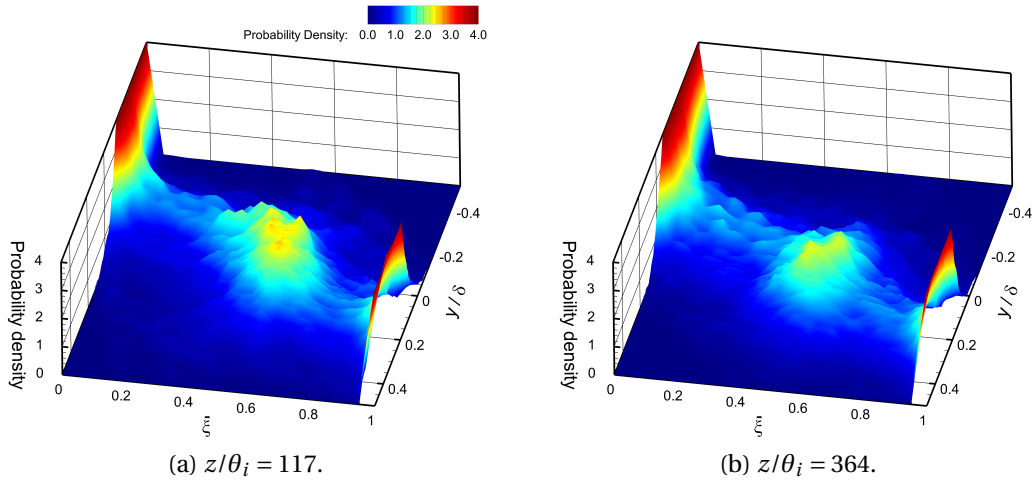


Figure 6.27: Probability density functions for BL-066-RRM-M at measurement station 6.

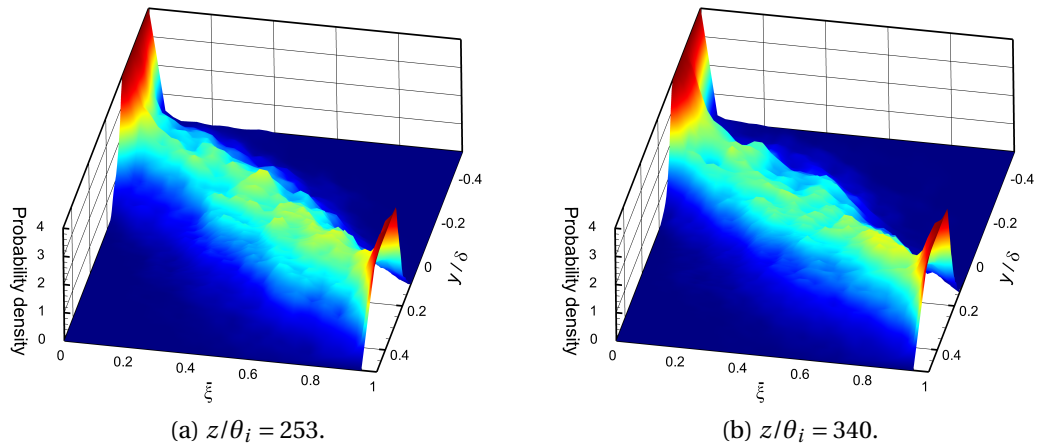


Figure 6.28: Probability density functions for BL-066-RRM-H at measurement station 6. For legend refer to Figure 6.27a.

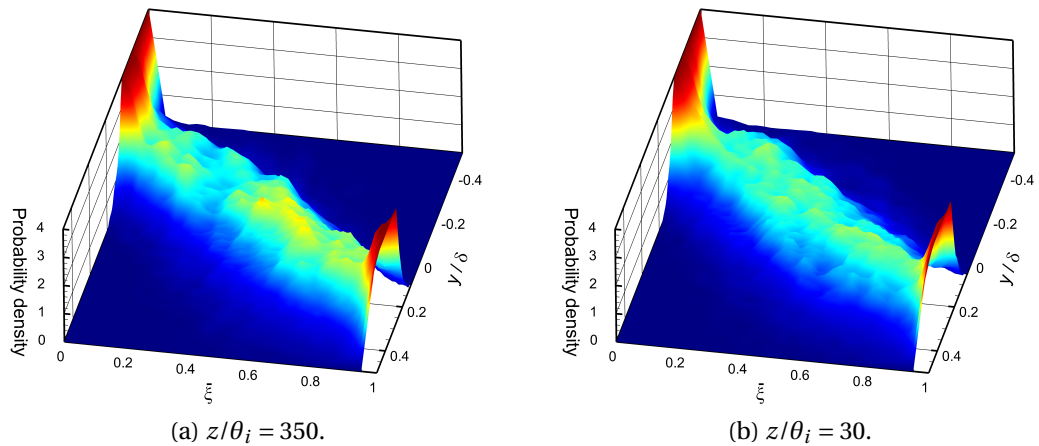


Figure 6.29: Probability density functions for BL-066-RRM-VH at measurement station 6. For legend refer to Figure 6.27a.

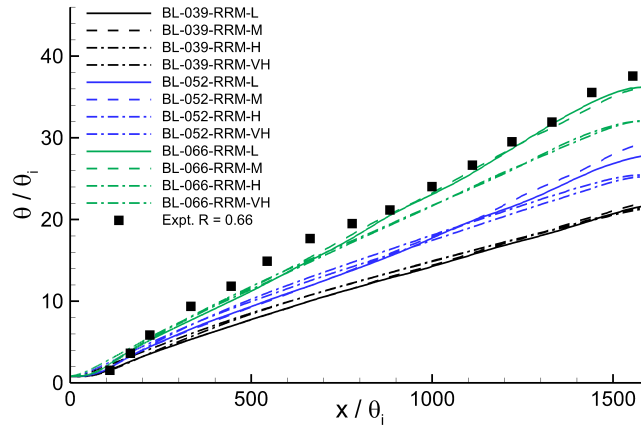


Figure 6.30: Local momentum thickness against downstream distance from the splitter plate trailing edge.

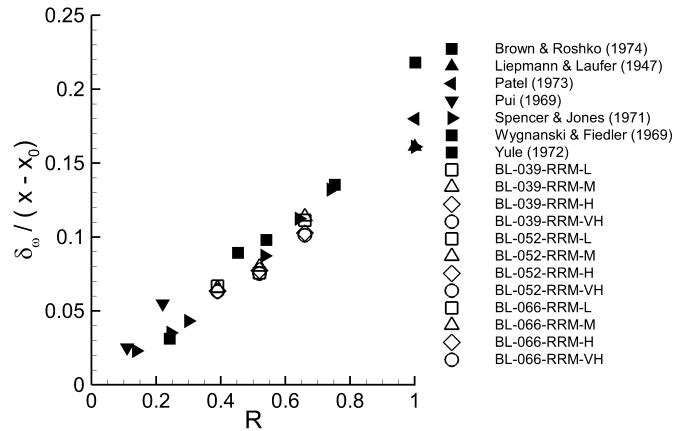


Figure 6.31: Vorticity growth rate as a function of velocity ratio.

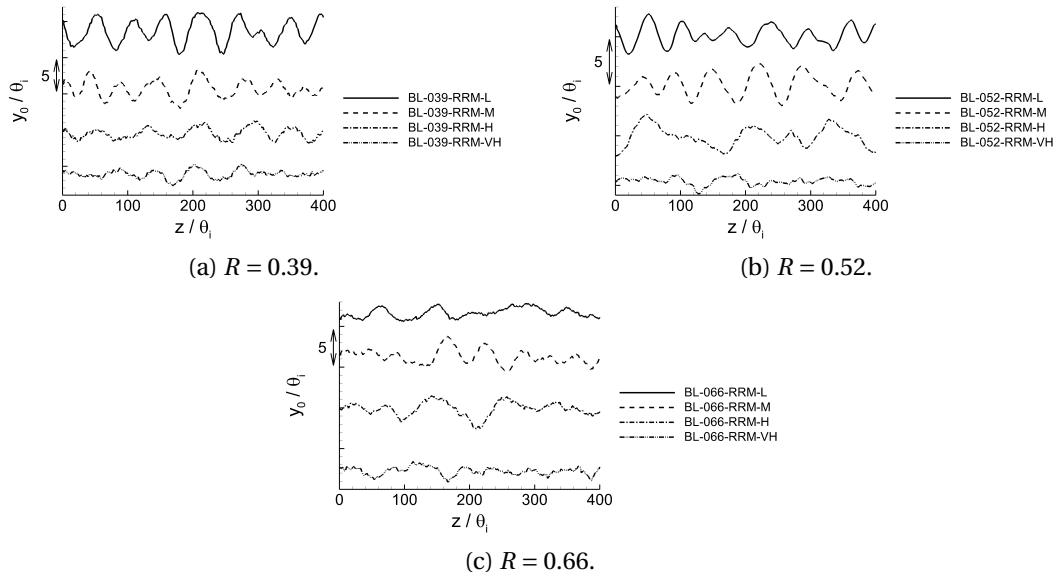


Figure 6.32: Mixing layer centreline at measurement station 6 for varying inlet fluctuation levels and velocity ratios. For clarity the centrelines have been shifted in the vertical axis.

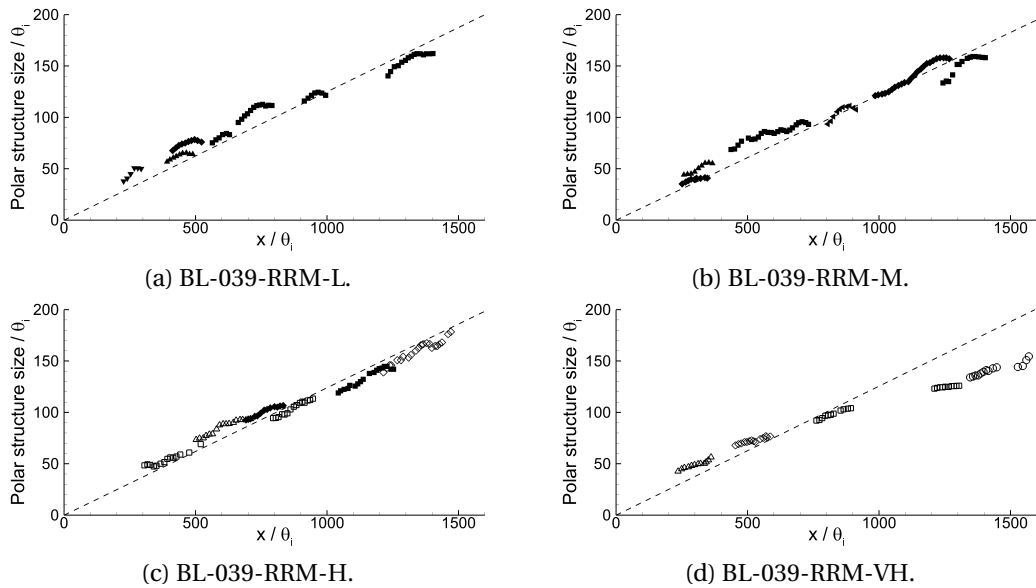


Figure 6.33: Primary structure growth tracks for $R = 0.39$ with varying inlet fluctuation magnitudes. Filled symbols denote square root of time growth.

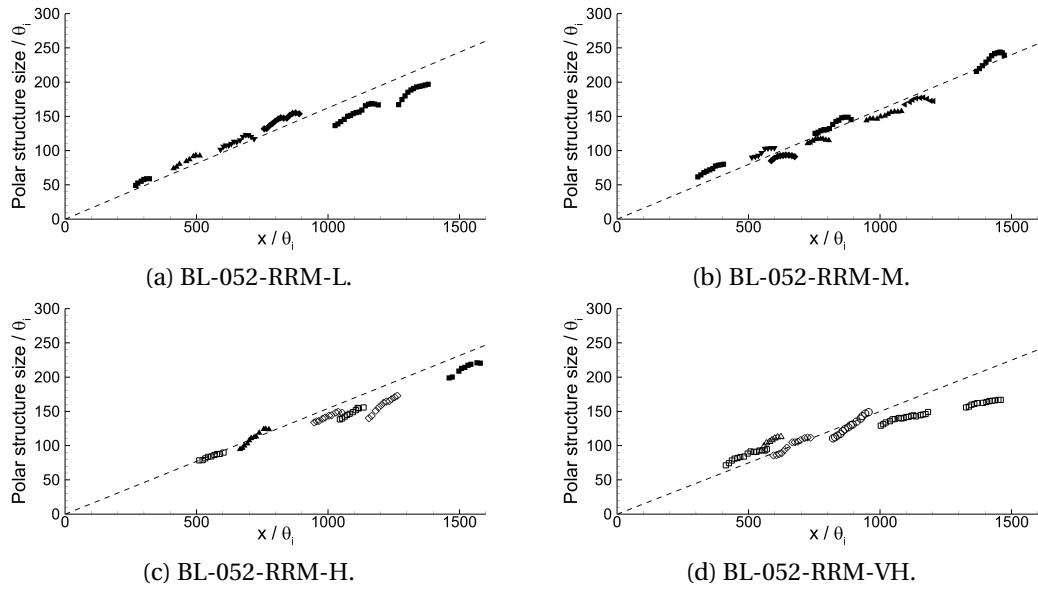


Figure 6.34: Primary structure growth tracks for $R = 052$ with varying inlet fluctuation magnitudes. Filled symbols denote square root of time growth.

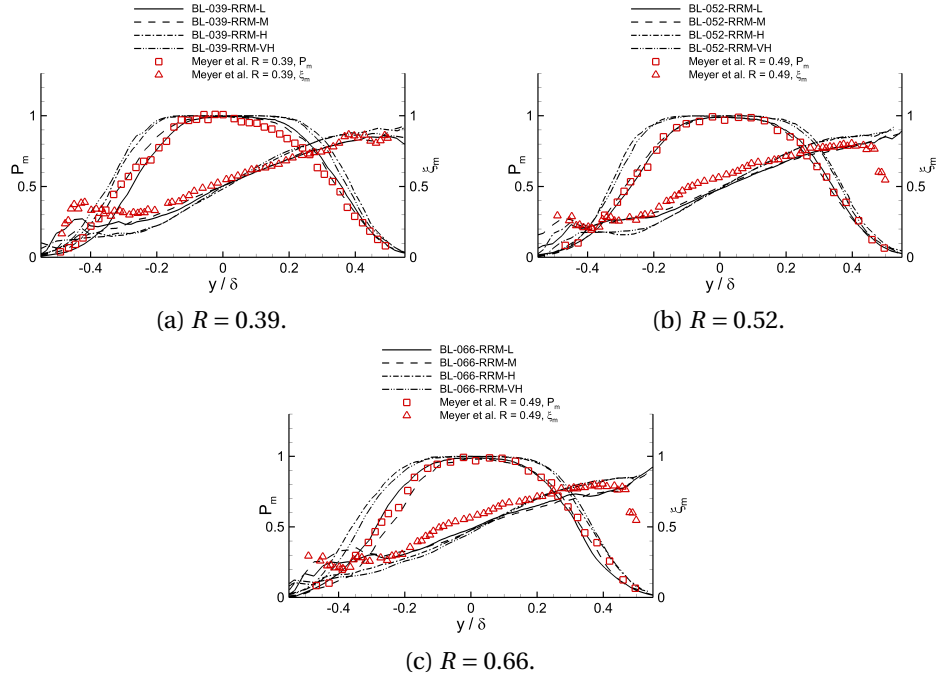


Figure 6.35: Mixed fluid probability, P_m , and average mixed fluid concentration, ξ_m , at measurement station 6.

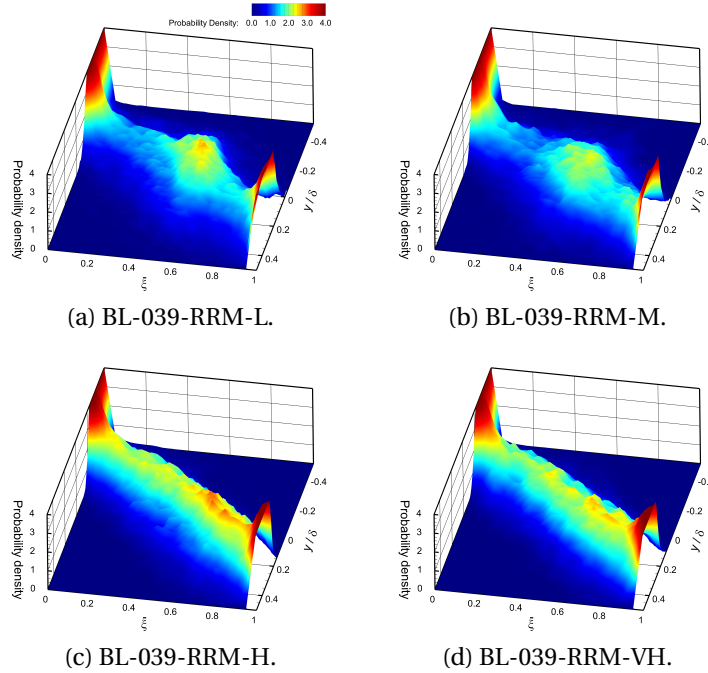


Figure 6.36: Probability density function for $R = 0.39$ at measurement station 6, taken at an entrainment maximum.

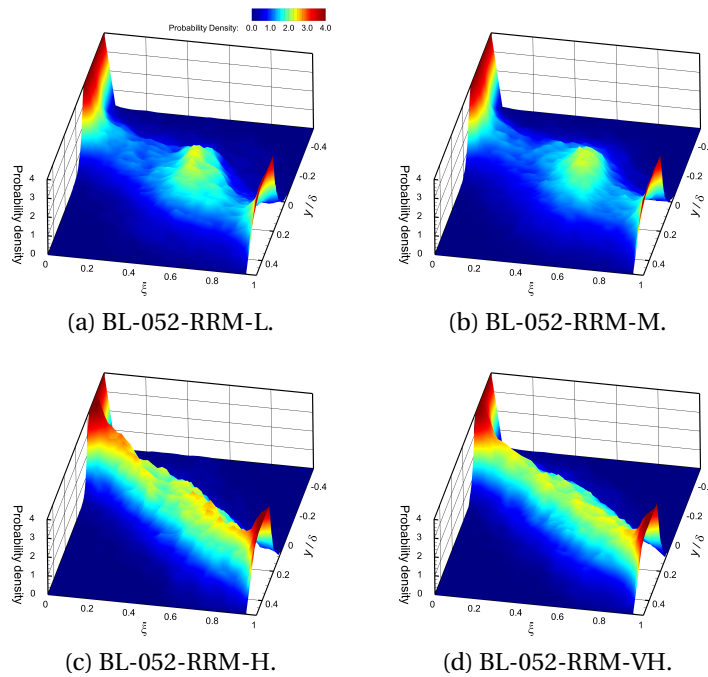


Figure 6.37: Probability density function for $R = 0.52$ at measurement station 6, taken at an entrainment maximum.

Chapter 7

Conclusions and Further Work

7.1 Conclusions

In this thesis, a Large Eddy Simulation (LES) code has been used to perform simulations of the plane mixing layer at low and high Reynolds numbers. The focus has been on the resolved scalar entrainment and mixing, large-scale coherent structures and spatially stationary streamwise vortices.

A low Reynolds number mixing layer simulation has been performed based on a dataset by Masutani & Bowman [59]. At the heart of these simulations stands the investigation of the temporal and spatial correlation of inlet boundary layer fluctuations. For this, a simulation using white noise (WN) type, idealised inlet conditions is compared with a simulation based on the recycling-rescaling (RRM) inlet fluctuation generation method by Xiao *et al.* [37]. It is shown how the temporal and spatial correlation of the inlet boundary layer fluctuations leads to the development of spatially stationary streamwise vortices in the RRM simulations. These streamwise oriented structures strongly affect the momentum and passive scalar fields of the flow. The probability density functions (p.d.f.'s) produced by the RRM simulations are of the *non-marching* type with a preferred concentration that is very close to that reported by the reference experiment while the WN simulations produce *marching* p.d.f.'s.

In the latter parts of this study, the high Reynolds number mixing layer, based on the experiments by Browand & Latigo [45], is studied using LES. In Chapter 4.2, the effects of the correlation of the inlet boundary layer fluctuations are studied, similar to what has been done for the low Reynolds number mixing layer in Chapter 4. The observations made for the low Reynolds number mixing layer also hold true for the high Reynolds number mixing layer. The RRM type simulations produce spatially stationary streamwise vortices which are not found in the WN simulations. The data suggest that the entrainment of the passive scalar in the RRM simulations is done by the engulfment entrainment mechanism, proposed by Dimotakis [56]. The RRM simulations show excellent agreement with passive scalar data for comparable mixing layers by Meyer *et al.* [94]. The p.d.f.'s in the RRM simulations are of the *non-marching* type, which is the p.d.f. type reported by Konrad [50] in their study of a comparably high Reynolds number mixing layer. The presented RRM simulations are the first three-dimensional LES to produce *non-marching* p.d.f.'s. The growth of the primary structures is studied by tracking the size of individual coherent structures during their lifetime, and it is found that the structures grow as the square root of time, in agreement with theoretical analysis [98, 99] and numerical simulations by McMullan & Garrett [21].

The white noise type simulations do not produce spatially stationary streamwise vortices and show overall worse agreement with the reference data. In particular, the passive scalar measurements fail to capture the pattern of mixing reported by Meyer *et al.* [94]. Passive scalar data suggests that entrainment in the white noise type simulations is done by the Corrsin & Kistler [57] nibbling entrainment mechanism.

The importance of the inlet fluctuation in the high Reynolds number mixing layer has been shown when the effects of temporal and spatial correlation of the inlet fluctuations have been studied in Chapter 4.2. In Chapter 5 mixing layer properties such as the velocity ratio, boundary layer thickness and small changes in the inlet fluctuation levels are investigated. The culminations of the results in Chapter 4.2 and 5 are the basis for a parametrised study of the inlet boundary layer fluctuation magnitude in Chapter 6. It is found that an increase in the inlet fluctuation levels increases the spanwise wavelength of the spatially stationary structures and reduces their strength. If the spatially stationary structures are weakened sufficiently, the

primary structures start to grow continuously and linearly. Simultaneously, the primary vortices go from a quasi-two-dimensional appearance in the low fluctuation level simulations, as observed by Brown & Roshko [9], to helical type pairings and a fully three-dimensional flow field in the high fluctuation simulations, as reported by D'Ovidio & Coats [11]. This is the first time that the inlet fluctuation level has been linked to the dynamics of the primary vortices.

Results show that passive scalar entrainment happens by engulfment, in agreement with Dimotakis [56], if spatially stationary streamwise vortices are present. However, in the high fluctuation level simulations, with a reduced number or complete lack of spatially stationary streamwise vortices, passive scalar entrainment is the result of the nibbling entrainment mechanism. This hypothesis is supported by passive scalar statistics and probability density functions which change from *non-marching* in the low fluctuation cases to *marching* in the higher fluctuation level simulations. Similar observations have been made in experiments by Picket & Gandhi [86]. The *marching* p.d.f. shape for the high fluctuation magnitude simulations is in agreement with *marching* p.d.f.'s produced by Batt [62] in an experiment with high fluctuation magnitudes. The finding that the shape of the p.d.f. in the low and high Reynolds number mixing layer can, effectively, be controlled using the inlet fluctuation level is novel and potentially highly relevant to industrial applications.

The simulations present the following findings relevant to future numerical and experimental studies:

- Spatially and temporally correlated inlet fluctuations are a critical requirement to produce accurate flow dynamics and passive scalar data.
- A lack of, or sufficiently weak, spatially stationary streamwise vortices changes the large scale structure growth mechanism from square root of time growth to continuous, linear growth.
- Very high boundary layer fluctuation magnitudes can weaken or prohibit the generation of spatially stationary streamwise vortices.
- The presence of spatially stationary, streamwise vortices is shown to heavily influence the mean momentum and passive scalar fields and result in a span-

wise dependence of the passive scalar statistics. This is in agreement with Bell *et al.* [103] who reported large spanwise variations in experiments and warned that significant misinterpretations regarding the mixing layer may be drawn on single span measurements.

- The inlet fluctuation magnitude can play a role in the explanation of the large spread of growth rates reported by experiments.

The most critical finding of this work is the discovery of the links between the inlet boundary layer fluctuation magnitude and spatially stationary, secondary streamwise oriented vortex presence, primary vortex growth mechanism and mixing layer entrainment mode. It has been demonstrated that control of the inlet boundary layer fluctuation magnitude effectively allows the control of the presence and number of secondary, spatially stationary, streamwise vortices. This control, in turn, can be used to alter the entrainment mechanism between the engulfment or nibbling type. Lastly, the ability to control the probability density function shape, resulting from the entrainment mechanism control, is of particular interest to the field of combustion modelling and prediction. Additionally the links established between the presence of secondary, streamwise oriented vortices and the primary vortex growth mechanism could help to explain some of the large spread of reported growth rates in experiments.

7.2 Further Work

This research has shown that physically correlated inflow fluctuations are essential, even for initially laminar flows. Initially turbulent plane mixing layers are also of interest. However, resolving the near wall flow structure in the turbulent boundary layer, combined with the large domain size requirement for turbulent mixing layers make these types of simulations extremely computationally intensive.

A logical next step is to use spatially and temporally correlated inlet fluctuations in LES of variable density mixing layers. This has been done by Wang *et al.* [108] for round jets. Agreement with experimental data was good, and strong streamwise

vorticity was observed in the helium jet case. LES of a variable density plane mixing layers by McMullan *et al.* [109] used white noise type inlet conditions. The white noise type inlet condition type lead to primary structures which grew continuously and linearly, and no spatially stationary streamwise vortices were present. An LES of a variable density plane mixing layer, based on recycling-rescaling inlet conditions is currently outstanding.

Of particular interest to engineering applications are exothermically reacting mixing layers. A plane mixing layer of this type has been studied by Hermanson *et al.* [110]. However, the simulation of an exothermic mixing layer remains extremely challenging. Some of the difficulties are the tracking of multiple species, modelling of sub-grid scale reactant mixing, changing densities due to heat release, and others. The variable density also affects computational stability and requires constant adjustments of modelling constants.

The inlet or initial conditions are a critical and integral part of any mixing layer experiment or simulation. Unfortunately, currently available experimental studies do not report adequate data about their inlet conditions. Often only the velocities, boundary layer thickness and free-stream fluctuation magnitudes are reported. These attributes are inadequate to fully describe the inlet conditions. Ideally, information about streamwise vorticity or even complete cross-plane measurements of the streamwise vorticity would be reported. The author appreciates the difficulty of obtaining such measurements but if LES is to advance there has to be certainty about what LES is trying to model. Further experiments which fully document the initial conditions of the mixing layer are required.

BIBLIOGRAPHY

- [1] J. P. Richter. *The notebooks of Leonardo da Vinci*. Courier Corporation, 2012.
- [2] Osborne Reynolds. An experimental investigation of the circumstances which determine whether the motion of water shall be direct or sinuous, and of the law of resistance in parallel channels. *Proceedings of the royal society of London*, 35(224-226):84–99, 1883.
- [3] Antonio Attili, Juan C Cristancho, and Fabrizio Bisetti. Statistics of the turbulent/non-turbulent interface in a spatially developing mixing layer. *Journal of Turbulence*, 15(10):555–568, 2014.
- [4] Michael M. Rogers and Robert D. Moser. The three-dimensional evolution of a plane mixing layer: the Kelvin-Helmholtz rollup. *Journal of Fluid Mechanics*, 243:183–226, 1992.
- [5] MM Rogers and RD Moser. Spanwise scale selection in plane mixing layers. *Journal of Fluid Mechanics*, pages 321–337, 1993.
- [6] M. M. Rogers and R. D. Moser. Direct simulation of a self similar turbulent mixing layer. *Physics of Fluids*, 6(2):903–923, 1994.
- [7] William K. George. Asymptotic Effect of Initial and Upstream Conditions on Turbulence. *Journal of Fluids Engineering*, 134(6):061203, 2012.
- [8] Paul E. Dimotakis. The mixing transition in turbulent flows. *Journal of Fluid Mechanics*, 409:69–98, 2000.

- [9] G. L. Brown and A. Roshko. On density effects and large structure in turbulent mixing layers. *Journal of Fluid Mechanics*, 64(04):775–816, 1974.
- [10] Miguel A. Hernan and Javier Jimenez. Computer Analysis of a High-Speed Film of the Plane Turbulent Mixing Layer. *Journal of Fluid Mechanics*, 119:323–345, 1982.
- [11] A. D’Ovidio and C. M. Coats. Organized large structure in the post-transition mixing layer. Part 1. Experimental evidence. *Journal of Fluid Mechanics*, 737:466–498, 2013.
- [12] RG BATT. Layer Some Measurements on the Effect of Tripping the Two-Dimensional Shear. *AIAA Journal*, (February):12–14, 1975.
- [13] D. Oster and I. Wygnanski. The Forced Mixing Layer Between Parallel Streams. *Journal of Fluid Mechanics*, 123:91–130, 1982.
- [14] J. Smagorinsky. General Circulation Experiments With the Primitive Equations. *Monthly Weather Review*, 91(3):99–164, 1963.
- [15] J.W. Deardorff. A numerical study of three-dimensional turbulent channel flow at large Reynolds numbers. *Journal of Fluid Mechanics*, 41(1970):453–480, 1970.
- [16] Richard W. Johnson. *The Handbook of Fluid Dynamics*. 1998.
- [17] F. Nicoud and F. Ducros. Subgrid-scale stress modelling based on the square of the velocity gradient tensor. *Flow, Turbulence and Combustion*, 62(3):183–200, 1999.
- [18] W. A. McMullan, S. Gao, and C. M. Coats. Organised large structure in the post-transition mixing layer. Part 2. Large-eddy simulation. *Journal of Fluid Mechanics*, 762:302–343, 2015.
- [19] M. Breuer. Numerical and modeling influences on large eddy simulations for the flow past a circular cylinder. *International Journal of Heat and Fluid Flow*, 19(5):512–521, 1998.

- [20] Massimo Germano, Ugo Piomelli, Parviz Moin, and William H. Cabot. A dynamic subgrid-scale eddy viscosity model. *Phys. Fluids A Fluid Dyn.*, 3(7):1760, 1991.
- [21] W. A. McMullan and S. J. Garrett. Initial condition effects on large scale structure in numerical simulations of plane mixing layers. *Physics of Fluids*, 28(1), 2016.
- [22] Holger Foysi, Juan P. Mellado, and S. Sarkar. Large-eddy simulation of variable-density round and plane jets. *International Journal of Heat and Fluid Flow*, 31(3):307–314, 2010.
- [23] C. Le Ribault. Large Eddy simulation of passive scalar in compressible mixing layers. *International Journal of Heat and Mass Transfer*, 51(13-14):3514–3524, 2008.
- [24] W Andrew McMullan and Gary J Page. Large Eddy Simulation of a Controlled-Diffusion Cascade Blade at Varying Flow Inlet Angles. *ASME Conference Proceedings*, 2009(48883):453–466, 2009.
- [25] Heinz Pitsch, Olivier Desjardins, Guillaume Balarac, and Matthias Ihme. Large-eddy simulation of turbulent reacting flows. *Progress in Aerospace Sciences*, 44(6):466–478, 2008.
- [26] Tayfun E Tezduyar, Sunil Sathe, Matthew Schwaab, and Brian S Conklin. Arterial fluid mechanics modeling with the stabilized space-time fluid-structure interaction technique. *International Journal for Numerical Methods in Fluids*, (October 2007):601–629, 2008.
- [27] D. J. Bodony and S. K. Lele. Current Status of Jet Noise Predictions Using Large-Eddy Simulation. *AIAA Journal*, 46(2):364–380, 2008.
- [28] Christophe Bogey and Christophe Bailly. Reprint of: On the importance of specifying appropriate nozzle-exit conditions in jet noise prediction. *Procedia IUTAM*, 1:38–43, 2010.
- [29] Hyun Kyu Suh, Seung Hyun Yoon, and Chang Sik Lee. Effect of Multiple Injection Strategies on the Spray Atomization and Reduction of Exhaust Emissions in a Compression Ignition Engine Fueled with Dimethyl Ether (DME). (X):1323–1332, 2010.

- [30] V. N. Prasad and A. R. Masri. LES Calculations of Auto-Ignition in a Turbulent Dilute Methanol Spray Flame. 0(December):18–21, 2012.
- [31] Vittorio Michelassi, Jan Wissink, and Wolfgang Rodi. Analysis of DNS and LES of Flow in a Low Pressure Turbine Cascade with Incoming Wakes and Comparison with Experiments. *Flow, Turbulence and Combustion*, 69(3-4):295–330, 2002.
- [32] V. Michelassi, J. Fröhlich, W. Rodi, and J. G. Wissink. Large-Eddy Simulation of Flow Around Low-Pressure Turbine Blade with Incoming Wakes. *AIAA Journal*, 41(11):2143–2156, 2003.
- [33] Bert Vreman, Bernard Geurts, and Hans Kuerten. Comparison of Numerical Schemes in Large-Eddy Simulation of the Temporal Mixing Layer. *International Journal for Numerical Methods in Fluids*, 22(4):297–311, 1996.
- [34] Peter R. Voke. Subgrid-scale modelling at low mesh reynolds number. *Theoretical and Computational Fluid Dynamics*, 8(2):131–143, 1996.
- [35] Yang Zhiyin. Large-eddy simulation: Past, present and the future. *Chinese Journal of Aeronautics*, 28(1):11–24, 2015.
- [36] W. A. McMullan. Influence of Spanwise Domain on the Large Eddy Simulation of an Idealised Mixing Layer. *7th AIAA Theoretical Fluid Mechanics Conference*, (June):1–17, 2014.
- [37] F. Xiao, M. Dianat, and J. J. McGuirk. LES of turbulent liquid jet primary breakup in turbulent coaxial air flow. *International Journal of Multiphase Flow*, 60:103–118, 2014.
- [38] G. R. Tabor and M. H. Baba-Ahmadi. Inlet conditions for large eddy simulation: A review. *Computers and Fluids*, 39(4):553–567, 2010.
- [39] C. Le Ribault, S. Sarkar, and S. a. Stanley. Large eddy simulation of evolution of a passive scalar in plane jet. *AIAA Journal*, 39(1999):1509–1516, 2001.
- [40] James W Deardorff. A numerical study of three-dimensional turbulent channel flow at large Reynolds numbers. *Journal of Fluid Mechanics*, 41(2):453–480, 1970.

- [41] G. N. Abramovich. The Theory of Turbulent Jets. page 109, 1963.
- [42] H.W. Liepmann and J. Laufer. Investigations of free turbulent mixing. *Liepmann, Hans, Wolfgang Laufer, John*, 1947.
- [43] I. Wygnanski and H.E. Fiedler. The two-dimensional mixing region. *Journal of Fluid Mechanics*, 41:327–361, 1970.
- [44] C. Chandrsuda, R. D. Mehta, a. D. Weir, and P. Bradshaw. Effect of free-stream turbulence on large structure in turbulent mixing layers. *Journal of Fluid Mechanics*, 85(04):693, 1978.
- [45] F. K. Browand and B. O. Latigo. Growth of the two dimensional mixing layer from a turbulent and nonturbulent boundary layer. *Physics of Fluids (1958-1988)*, 22(6):1011, 1979.
- [46] A. K. M. Fazle Hussain and A. Ray Clark. Upstream influence on the near field of a plane turbulent jet. *The Physics of Fluids*, 20(9):1416–1426, 1977.
- [47] James H. Bell and Rabindra D. Mehta. Measurements of the streamwise vortical structures in a plane mixing layer. *Journal of Fluid Mechanics*, 239:213–248, 1992.
- [48] P. A. Huerre, P.; Monkewitz. Absolute and convective instabilities in open shear layers. *Journal of Fluid Mechanics*, 159:151–168, 1985.
- [49] C. D. Winant and F. K. Browand. Vortex pairing : the mechanism of turbulent mixing-layer growth at moderate Reynolds number. *J. Fluid Mech.*, 63(02):237–255, 1974.
- [50] J. H. Konrad. An Experimental Investigation of Mixing in Two-Dimensional Turbulent Shear Flows with Applications to Diffusion-Limited Chemical Reactions, 1977.
- [51] R. Breidenthal. Chemically Reacting, Turbulent Shear Layer. 17(3):310–311, 1978.
- [52] Javier Jimenez. A spanwise structure in the plane shear layer. *Journal of Fluid Mechanics*, 132:319–336, 1983.

- [53] Javier Jimenez, Marta Cogollos, and Luis P Bernal. Perspective View of the Plane Mixing Layer. *Journal of Fluid Mechanics*, 152:125–143, 1985.
- [54] L. P. Bernal and A. Roshko. Streamwise vortex structure in plane mixing layers. *Journal of Fluid Mechanics*, 170:499–525, 1986.
- [55] Kevin C. Wiecek and Rabindra D. Mehta. Effects of velocity ratio on mixing layer three-dimensionality. *Experimental Thermal and Fluid Science*, 16(3):165–176, 1998.
- [56] Paul E. Dimotakis. Two-dimensional shear-layer entrainment. *AIAA Journal*, 24(11):1791–1796, 1986.
- [57] S. Corrsin and A. L. Kistler. Free-stream Boundaries of Turbulent Flows. 25(April), 1956.
- [58] J. E. Broadwell and R. E. Breidenthal. A simple model of mixing and chemical reaction in a turbulent shear layer. *Journal of Fluid Mechanics*, 125:397–410, 1982.
- [59] S. M. Masutani and C. T. Bowman. The structure of a chemically reacting plane mixing layer. *Journal of Fluid Mechanics*, 172:93–126, jan 1986.
- [60] P. S. Karasso and M. G. Mungal. Scalar mixing and reaction in plane liquid shear layers. *Journal of Fluid Mechanics*, 323(-1):23, 1996.
- [61] L. M. Pickett and J. B. Ghandhi. Passive scalar measurements in a planar mixing layer by PLIF of acetone. *Experiments in Fluids*, 31(3):309–318, 2001.
- [62] R. G. Batt. Turbulent mixing of passive and chemically reacting species in a low-speed shear layer. *Journal of Fluid Mechanics*, 82(01):53, 1977.
- [63] Lyle M. Pickett and Jaal B. Ghandhi. Combustion generated instabilities in a hydrocarbon-air planar mixing layer. *Combustion and Flame*, 129(3):324–341, 2002.
- [64] J. C. Lasheras and H. Choi. Three-dimensional instability of a plane free shear layer: an experimental study of the formation and evolution of streamwise vortices. *J. Fluid Mech.*, 315(1):175–221, 1988.

- [65] M. Lesieur, P. Comte, E. Lamballais, O. M. Etais, and G. Silvestrini. Large-eddy simulations of shear flows. *Journal of Engineering Mathematics*, 32:195–215, 1997.
- [66] Ralph W. Metcalfe, Steven A. Orszag, Marc E. Brachet, Suresh Menon, and James J. Riley. Secondary instability of a temporally growing mixing layer. *Journal of Fluid Mechanics*, 184:207–243, 1987.
- [67] Marcel Lesieur, Chantal Staquet, Pascal Le Roy, and Pierre Comte. The mixing layer and its coherence examined from the point of view of two-dimensional turbulence. *Journal of Fluid Mechanics*, 192:511, 1988.
- [68] Pierre Comte, Marcel Lesieur, and Eric Lamballais. Large- and small-scale stirring of vorticity and a passive scalar in a 3-D temporal mixing layer. *Physics of Fluids A: Fluid Dynamics*, 4(12):2761, 1992.
- [69] K. J. Nygaard and A. Glezer. Evolution of stream wise vortices and generation of small-scale motion in a plane mixing layer. *Journal of Fluid Mechanics*, 231:257–301, 1991.
- [70] Philippe R. Spalart. Direct simulation of a turbulent boundary layer up to $R\theta = 1410$. *Journal of Fluid Mechanics*, 187(-1):61, 1988.
- [71] Ahmed F Ghoniem and Kenneth K. Ng. Numerical study of the dynamics of a forced shear layer. 706(1987), 1986.
- [72] W.B. Yang, H.Q. Zhang, C.K. Chan, and W.Y. Lin. Large eddy simulation of mixing layer. *Journal of Computational and Applied Mathematics*, 163(1):311–318, 2004.
- [73] A. Roshko. Errata: Structure of Turbulent Shear Flows: A New Look. *AIAA Journal*, 15(5):0768c–0768c, 1977.
- [74] a.M. Baig and R.E. Milane. Vortex-In-Cell and Probability Density Function Approach for a Passive Scalar Field in a Mixing Layer. *International Journal of Computational Fluid Dynamics*, 18(3):247–263, 2004.
- [75] P. Bradshaw, D. H. Ferriss, and R. F. Johnson. Turbulence in the noise-producing region of a circular jet. *Journal of Fluid Mechanics*, 19(04):591–624, 1964.

- [76] A. K. M. Fazole Hussain. Coherent structures and turbulence. *Journal of Fluid Mechanics*, 173(-1):303, 1986.
- [77] Denis Veynante and Luc Vervisch. Turbulent combustion modeling. *Progress in Energy and Combustion Science*, 28(3):193–266, 2002.
- [78] W.A. McMullan. Spanwise domain effects on the evolution of the plane turbulent mixing layer. *International Journal of Computational Fluid Dynamics*, 29(6-8):333–345, 2015.
- [79] B Vremen, Bernard Geurts, Hans Kuerten, Bert Vreman, Bernard Geurts, and Hans Kuerten. Large-eddy simulation of the turbulent mixing layer. *Journal of Fluid Mechanics*, 339(-1):357–390, 1997.
- [80] G Dufour, N Gourdain, F Duchaine, O Vermorel, and T Poinso. Numerical Investigations in Turbomachinery : A State of the Art. Large Eddy Simulation Applications. *VKI Lecture Series*, pages 21–25, 2009.
- [81] N. Tauveron. Simulation of a compressor cascade with stalled flow using Large Eddy Simulation with two-layer approximate boundary conditions. *Nuclear Engineering and Design*, 240(2):321–335, 2010.
- [82] S. N. Hug and W. A. McMullan. Resolved Scalar Mixing in Large Eddy Simulations of a Low Reynolds Number Plane Mixing Layer. In *22nd AIAA Computational Fluid Dynamics Conference*, Reston, Virginia, jun 2015. American Institute of Aeronautics and Astronautics.
- [83] S H Lo, Peter Ryal Voke, and NICOLE JACQUELINE Rockliff. Three-dimensional vortices of a spatially developing plane jet. *International Journal of Fluid Dynamics*, 4(1):1–20, 2000.
- [84] W. A. McMullan, S. Gao, and C. M. Coats. The effect of inflow conditions on the transition to turbulence in large eddy simulations of spatially developing mixing layers. *International Journal of Heat and Fluid Flow*, 30(6):1054–1066, 2009.
- [85] Patrick J Roache. *Computational fluid dynamics*. Hermosa publishers, 1972.

- [86] L. M. Pickett and J. B. Ghandhi. Passive scalar mixing in a planar shear layer with laminar and turbulent inlet conditions. *Physics of Fluids*, 14(3):985–998, 2002.
- [87] D. H. Wood and P. Bradshaw. A turbulent mixing layer constrained by a solid surface; part 1, measurements before reaching the surface. *Journal of Fluid Mechanics*, 122(-1):57–89, 1982.
- [88] James H. Bell and Rabindra D. Mehta. Measurements of the streamwise vortical structures in a plane mixing layer. *Journal of Fluid Mechanics*, 239:213–248, 1992.
- [89] M. M. Koochesfahani and P. E. Dimotakis. Laser-Induced Fluorescence Measurements of Mixed Fluid Concentration in a Liquid Plane Shear Layer. *AIAA Journal*, 23(11):1700–1707, 1985.
- [90] M. M. Koochesfahani and P. E. Dimotakis. Mixing and chemical reactions in a turbulent liquid mixing layer. *Journal of Fluid Mechanics*, 170(-1):83, 1986.
- [91] L-S. Huang and C-M. Ho. Small scale transition in a plane mixing layer. *J. Fluid Mech.*, 210:475–500, 1990.
- [92] Dennis A. Yoder, James R. Debonis, and Nicholas J. Georgiadis. Modeling of Turbulent Free Shear Flows. *Aiaa-2013-2721*, (August):38, 2013.
- [93] X. Y. Zhou and J. C. F. Pereira. Large Eddy Simulation (2D) of a Reacting Plan Mixing Layer Using Filtered Density Function. *Flow Turbul. Combust.*, 64(m):279–300, 2000.
- [94] T. R. Meyer, J. C. Dutton, and R. P. Lucht. Coherent structures and turbulent molecular mixing in gaseous planar shear layers. *Journal of Fluid Mechanics*, 558:179–205, 2006.
- [95] W. A. McMullan and S. J. Garrett. The Effect of Initial Conditions on Streamwise Vortices in the Plane Turbulent Mixing Layer. *22nd AIAA Computational Fluid Dynamics Conference*, pages 1–18, 2015.
- [96] C. Bogey and C. Bailly. Influence of nozzle-exit boundary-layer conditions on the flow and acoustic fields of initially laminar jets. *Journal of Fluid Mechanics*, 663:507–538, 2010.

- [97] Peter A. Monkewitz. Subharmonic resonance, pairing and shredding in the mixing layer. *Journal of Fluid Mechanics*, 188(-1):223, 1988.
- [98] J Jimenez. On the visual growth of a turbulent mixing layer. *Journal of Fluid Mechanics*, 96(3):447–460, 1980.
- [99] D. W. Moore and P. G. Saffman. The density of organized vortices in a turbulent mixing layer. *J. Fluid Mech.*, 69(3):465, 1975.
- [100] Joseph Mathew, Inga Mahle, and Rainer Friedrich. Effects of compressibility and heat release on entrainment processes in mixing layers. *Journal of Turbulence*, 9(July 2014):37–41, 2008.
- [101] N. D. Sandham and R. D. Sandberg. Direct numerical simulation of the early development of a turbulent mixing layer downstream of a splitter plate. *Journal of Turbulence*, 10(1):1–17, 2009.
- [102] Antonio Attili and Fabrizio Bisetti. Statistics and scaling of turbulence in a spatially developing mixing layer at $Re \lambda = 250$. *Physics of Fluids*, 24(3), 2012.
- [103] J. H. Bell, M. W. Plesniak, and R. D. Mehta. Spanwise averaging of plane mixing layer properties. *AIAA journal*, 30(3), 1992.
- [104] M. W. Plesniak, J. H. Bell, and R. D. Mehta. Effects of small changes in initial conditions on mixing layer three-dimensionality. pages 286–288, 1992.
- [105] Y. Wang, M. Tanahashi, and T. Miyauchi. Coherent fine scale eddies in turbulence transition of spatially-developing mixing layer. *International Journal of Heat and Fluid Flow*, 28(6):1280–1290, 2007.
- [106] F. K. Browand and T. R. Troutt. A note on spanwise structure in the two-dimensional mixing layer. *Journal of Fluid Mechanics*, 97(04):771–781, 1980.
- [107] W. A. McMullan, S. Gao, and C. M. Coats. A comparative study of inflow conditions for two- and three-dimensional spatially developing mixing layers using large eddy simulation. *International Journal for Numerical Methods in Fluids*, (October 2007):601–629, 2007.

- [108] Ping Wang, Jochen Fröhlich, Vittorio Michelassi, and Wolfgang Rodi. Large-eddy simulation of variable-density turbulent axisymmetric jets. *International Journal of Heat and Fluid Flow*, 29(3):654–664, 2008.
- [109] W. A. McMullan, C. M. Coats, and S. Gao. Analysis of the variable density mixing layer using Large Eddy Simulation. (June):1–19, 2011.
- [110] J.C. Hermanson, M.G. Mungal, and P.E. Dimotakis. Heat Release Effects on Shear-Layer Growth and Entrainment. *AIAA journal*, 25(4):578–583, 1987.